Linear Parameter-Varying Modelling and Robust Control of Variable Cam Timing Engines

Ali Umut Genç

Wolfson College
Cambridge

A dissertation submitted to the
University of Cambridge for
the degree of Doctor of Philosophy

November 2002

In memory of my father

İsmail Hakkı Genç

UNIVERSITY OF CAMBRIDGE

Hopkinson Lab
Department of Engineering
Trumpington Street
Cambridge CB2 1PZ
United Kingdom

Abstract

In this thesis the air-fuel ratio (AFR) control problem is investigated for a gasoline, port fuel injected, twin-independent variable cam timing engine. A complete parameter-varying AFR path model is proposed and identified. In order to separate the effects of the fuel and air on the measured AFR, gaseous fuel experiments are performed as well as gasoline ones. It is shown that variable cam timing not only alters the air flow into the cylinders but also the fuel flow. A reliable cylinder air charge model that can predict the transient behaviour of the air charge entering the cylinder is identified with the help of the gaseous fuel experiments. Moreover, a global nonlinear identification scheme is proposed and successfully implemented to identify the wall-wetting dynamics modelled as a slow and a fast fuel puddle. The resulting parameter-varying model is able to predict the observed AFR transients induced by variable cam timing very accurately.

The second half of the thesis reviews the linear parameter-varying (LPV) controller design techniques in the context of $\mathscr{H}_\infty$ loop shaping controller design, which is the main controller synthesis paradigm in this thesis. The identified AFR model can be approximated with a linear fractional transformation (LFT) model varying with manifold pressure and valve timings. The LFT AFR path model allows the use of any LPV controller design technique for AFR controller synthesis. Experimental evaluation of the designed LTI and LPV $\mathscr{H}_\infty$ loop shaping AFR controllers reveals that the LPV controller offers up to 50 % improvements in AFR regulation performance without any feedforward action. Further improvements in performance are obtained by introducing feedforward elements into the controllers. The testing of the final controllers under various conditions including rapid transients has revealed that when coupled with a well designed feedforward controller both the LPV and LTI controllers perform equally well.

Keywords: Variable cam timing engines, air-fuel ratio control, gaseous fuel, wall-wetting,

$\mathscr{H}_\infty$ loop shaping, LPV control, LFT systems, gain scheduling, nonlinear identification, robust control.

Preface

It has been four years and few months since I had been to Cambridge for the first time for an interview with Keith and Nick on a sunny August day. My Ph.D. "adventure" has been a great experience and challenge. As with any adventure I have made many friends on the way and they all in one way or the other contributed to this piece. I would like to take this opportunity to acknowledge the help and support of the few.

Firstly, I would like to express my gratitude to my supervisor, Professor Keith Glover who not only guided me throughout this research but also provided reassurance during difficult times.

Professor Nick Collings has been an excellent adviser and a creative experimentalist; propane experiments wouldn't have taken place without his lead. Special thanks should go to Dr. Richard Ford who had been an excellent R.A. and a friend. He helped me with both engine testing and related control issues. Performing engine tests on a daily basis wouldn't be possible without the excellent support of technicians in the department. Particular thanks to Dave Gautrey, John Harvey, Trevor Parsons and Michael Underwood. The custom soft and hardware for engine control was developed at the Advanced Powertrain Group Ford Motor Co. Special thanks to Julian Hodgson for the technical support during the commissioning of the VCT engine.

Thanks to Merten Jung, Christos Papageorgiou, George Biskos, Dr. Eric Kerrigan, Dr. Kelvin Halsey, and Dr. Rahmi Öklü who helped me proof read this thesis; the number of typos and missing "the"s have been significantly reduced. My co-workers and the faculty in the control and engines-emissions-control groups deserve a mention since they have always been friendly and helpful: thank you all. Special thanks to Dr. Michael Cantoni and Dr. George Papageorgiou who were always willing to help me with any problem.

The area of this study was proposed by Mr. Derek Eade and Mr. Andy Scarisbrick of Ford Motor Co. whose generous funds financed my Ph.D. and together with the Engineering and Physical Sciences Research Council (EPSRC) financed the engine test facilities. I am very grateful for their support.

I have had many good friends in Cambridge who made my stay richer and more fun. I will miss for sure never-ending discussions with Dr. Polykarpos Papadopoulos, damn funny "geyik"s with Abdülkadir Hallaç, and the all-is-perfect attitude of Merten Jung. I also enjoyed and had great fun (and always lost) on each "rgf" poker club night.

My mum does not speak English so, "Bana hep destek ve sevgi veren anneme, aramızdan zamansız ayrılan babama ve çılgın kızkardeşime beni hiç bir zaman yalnız bırakmadıkları için minnettarım". Finally, Dicle Kortantamer has been great company during the good and bad times; without her support it would have been too difficult.

A. Umut Genç

Cambridge, November 2002

As required by University Statute, I hereby declare that this dissertation is the result of my own work and includes nothing which is the outcome of work done in collaboration except where specifically indicated in the text.

This dissertation contains no more than 65,000 words and 150 figures.

Contents

List of Figures

List of Tables

Notation and Acronyms

ENGINE

Acronyms

AFR	Air-Fuel Ratio
ATDC	After Top Dead Centre
BDC	Bottom Dead Centre
EGO	Exhaust Gas Oxygen
EGR	Exhaust Gas Recirculation
EVC	Exhaust Valve Closing
EVO	Exhaust Valve Opening
FAR	Fuel-Air Ratio
FPW	Fuel Injection Pulse Width
IVC	Inlet Valve Closing
IVO	Inlet Valve Opening
MAF	Mass Air Flow
MAP	Manifold Absolute Pressure
OCV	Oil Control Valve
OVL	Valve Overlap
PFI	Port Fuel Injection
rpm	Revolutions per Minute
SI	Spark Ignition
TDC	Top Dead Centre
TI-VCT	Twin Independent VCT
TP	Throttle Position
VCT	Variable Cam Timing

VVT	Variable Valve Timing
WOT	Wide Open Throttle

Symbols

$\dot{m}_{at}$	Throttle MAF
$\dot{m}_{ac}$	Cylinder MAF
m_{fi}	Injected fuel mass
m_{fc}	Fuel mass sucked into cylinders
m_{ff}	Fuel film mass
τ	Fuel film evaporation constant
$\mathcal{X}$	Fuel film deposition constant
P_m	MAP
λ	AFR relative to stoichiometric
ϕ	equivalence ratio, $\phi = \lambda^{-1}$
ϕ_c	ϕ in cylinder
ϕ_x	ϕ in exhaust
T_s	Sampling time
N	Engine speed in rpm

CONTROL

Acronyms

LFT	Linear Fractional Transformation
LMI	Linear Matrix Inequality
LQG	Linear Quadratic Gaussian
LTI	Linear Time-Invariant
LPV	Linear Parameter-Varying
LTR	Loop Transfer Recovery
MIMO	Multiple Input Multiple Output
PI	Proportional-Integral
PV	Parameter-Varying
RHP	Right Half Plane
SISO	Single Input Single Output
2DOF	Two Degree-of-Fredoom

Fields of Numbers

$\mathbb{R}$	real numbers

$\mathbb{R}_+$	strictly positive real numbers
j	the imaginary unit, i.e. $j = \sqrt{-1}$
$\mathbb{C}$	complex numbers
$\mathbb{C}_+$	open right-half plane

Relational Symbols

$:=$	defined by
$\approx$	approximately equal to

Matrix Operations

0	zero matrix of compatible dimensions
I	identity matrix of compatible dimensions
I_n	identity matrix of dimension $n \times n$
A'	complex conjugate transpose of matrix A
$A^{-'}$	denotes $\left(A^{-1}\right)'$ or equivalently $(A')^{-1}$
$\mathrm{diag}(A_1, A_2, \ldots, A_n)$	block-diagonal matrix with matrices A_i on the main diagonal
$\mathcal{F}_l\,(P, Q)$	lower linear fractional transformation of matrices P and Q
$\mathcal{F}_u\,(P, Q)$	upper linear fractional transformation of matrices P and Q
$A > 0$	hermitian matrix $A = A'$ with strictly positive eigenvalues
$A < 0$	hermitian matrix $A = A'$ with strictly negative eigenvalues
$A < B$	denotes $(A - B) < 0$

Function Spaces

$\mathscr{L}_2$	space of square integrable functions on $j\mathbb{R}$ including ∞
$\mathscr{H}_2$	subspace of functions in $\mathscr{L}_2$ that are analytic in $\mathbb{C}_+$ and uniformly square integrable along $\Re(s) = \alpha$ for all $\alpha \in \mathbb{R}_+$
$\mathscr{H}_\infty$	subspace of functions in $\mathscr{L}_\infty$ that are analytic and bounded in $\mathbb{C}_+$
prefix $\mathscr{R}$	subspace of real-rational functions, e.g. $\mathscr{RL}_2$, $\mathscr{RL}_\infty$

Measures of Size

$\overline{\sigma}(A)$	largest singular value of matrix A
$\underline{\sigma}(A)$	smallest singular value of matrix A
$\lvert x \rvert$	modulus (or magnitude) of $x \in \mathbb{C}$
$\lVert x \rVert$	Euclidean norm of $x \in \mathbb{C}^n$
$\lVert G \rVert_2$	two-norm of $G \in \mathscr{RL}_2$

$\|G\|_\infty$	infinity-norm of $G \in \mathscr{RL}_\infty$

Shorthand Notation

$\begin{pmatrix} * \\ * \end{pmatrix}' \begin{pmatrix} P + (*) & S \\ * & R \end{pmatrix} \begin{pmatrix} T \\ V \end{pmatrix}$	denotes the matrix $\begin{pmatrix} T \\ V \end{pmatrix}' \begin{pmatrix} P + P' & S \\ S' & R \end{pmatrix} \begin{pmatrix} T \\ V \end{pmatrix}$
$\left[\begin{array}{c\|c} A & B \\ \hline C & D \end{array}\right]$	shorthand for state space realisation $C\,(\sigma I - A)^{-1}\,B + D$, $\sigma = s, z$
$\bullet$	do not care

1 Introduction

Automobile manufacturing is one of the biggest industries around the globe. Increasingly severe competition forces automobile manufacturers to reduce cost while at the same time having to meet increasing tight, and therefore expensive emissions legislation. Coupled with this is a requirement, via pressures on CO_2 reduction and customer needs, for improved quality in terms of fuel efficiency and vehicle safety. These objectives are interrelated in fact usually conflicting. For example, lean-burn technology can improve fuel consumption significantly but at the same time it reduces the three-way catalyst conversion efficiency. The opposing requirements of the modern automobiles can be met in different ways such as by improving the existing designs, by increased (mechanical) complexity or by introducing completely new designs. Hybrid engines, fuel cells, gasoline direct injection and variable valve timing (VVT) are some of the new technologies available today. However, since these innovations come with increased complexity they require more demanding control capability.

Variable cam timing (VCT) is one of these new technologies introduced recently in the production engines. It offers the potential to achieve better fuel economy, emission levels and engine torque response. However, it can also cause a significant transient disturbance to the engine torque output adversely affecting driveability, and air-fuel ratio (AFR) degrading catalyst conversion efficiency. Thus, realising the full potential of the VCT engines requires a well-designed control system. This thesis investigates one particular control problem in VCT engines: the so called AFR control problem. The main objectives of the thesis are threefold:

i. Propose and validate appropriate identification and modelling methods for the AFR path in the VCT engines as an extension of the standard mean value engine models.

ii. Introduce and apply the recently developed linear parameter-varying controller design methods to the AFR control problem in a unified and systematic framework.

iii. Encourage the use of the advanced robust control theory in real life control problems.

The AFR controller design problem investigated in this thesis focuses on the regulation of the AFR signal at the exhaust manifold i.e. before the catalyst under warm operating conditions. Issues such as cold start emissions or regulation of the oxygen storage state of the catalyst in order to improve the emissions are not investigated in the thesis (although VCT has ability in this aspect). After a brief introduction to gasoline engines the rest of the chapter discusses the AFR control problem and VCT engines in detail.

1.1 Gasoline Engines

Although they are slowly losing ground to the diesel engines as shown in Figure 1.1, gasoline engines are still the main power plant for automobiles. The gasoline engine (also called spark ignition (SI) engine, Otto engine or petrol engine) is one type of internal combustion engine. The purpose of internal combustion engines is to produce mechanical power from the chemical energy contained in the fuel. Four stroke cycle gasoline engines are mainly used in the automobile applications. The sequence of events in a four stroke gasoline engine are:

- *Intake:* The intake stroke, which starts with the piston at the top extreme position and ends with the piston at the bottom extreme position, draws fresh mixture into the cylinder.

- *Compression:* During the compression stroke the air-fuel mixture is compressed to a small proportion of its initial volume (usually 9-11:1).

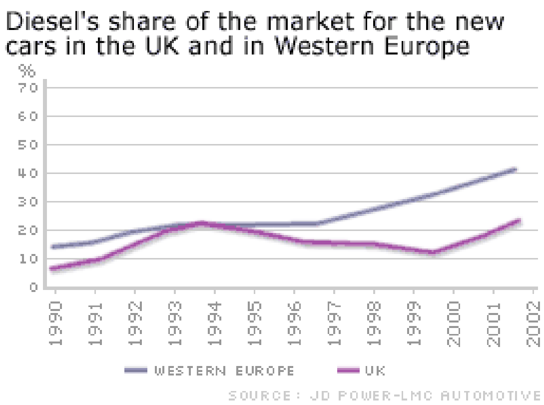

Figure 1.1 Market share of diesel in Europe (Source: JD Power-LMC automotive)

- *Power (Expansion):* During the power stroke, which starts with the piston near the top (minimum volume) position and ends with the piston near the bottom (maximum volume) position, the high pressure high temperature gases push down the piston and do work on the rotating crank.

- *Exhaust:* Unburned and burned gases are expelled from the cylinder during the exhaust stroke.

In current gasoline engines fuel is injected into each inlet port near the inlet valve, which is called port fuel injection (PFI), and the premixed charge is drawn into the cylinders and ignited. PFI gasoline engines have high power output, yet they suffer from lower compression ratio, low thermal efficiency and high fuel consumption when compared with the diesel or gasoline direct injection engines. The main causes of these drawbacks are knock and spontaneous ignition limits, high throttling and limited AFR operation range. The PFI gasoline engines run at stoichiometric AFR at most loads. A *stoichiometric* AFR denotes a chemically correct proportion of air and fuel so that there is just enough oxygen for conversion of all the fuel into completely oxidised products. For current gasoline fuel, the stoichiometric AFR by weight is approximately 14.6. A more useful measure is the *relative AFR (or lambda)*,

$$\lambda = \frac{AFR_{actual}}{AFR_{stoich}} \tag{1.1}$$

or its inverse the *equivalence ratio* (normalised fuel-air ratio (FAR))

$$\phi = \lambda^{-1} = \frac{FAR_{actual}}{FAR_{stoich}} \tag{1.2}$$

Then, a lean mixture gives $\lambda > 1 (\phi < 1)$ and a rich mixture gives $\lambda < 1 (\phi > 1)$.

1.2 Air-Fuel Ratio Control

In our ever-more-mobile society, reducing the vehicle pollution is an environmental imperative. The tail pipe emissions contribute greatly to the air pollution and are also the primary cause of the air pollution in most urban areas. The main automotive air pollutants are carbon monoxide (CO), nitrogen oxides (NO_x), hydrocarbons (HC), particulates, and carbon dioxide (CO_2). CO is a poisonous gas that displaces oxygen from the blood. At high concentrations it is fatal and at lower concentrations it can exacerbate heart problems. NO_x react with HC in the sunlight to form ozone and photochemical smog. Moreover, it can increase respiratory illnesses and is a contributor to acid rain. Ozone causes breathing difficulties and damages plants due to its acidity. Diesel engines

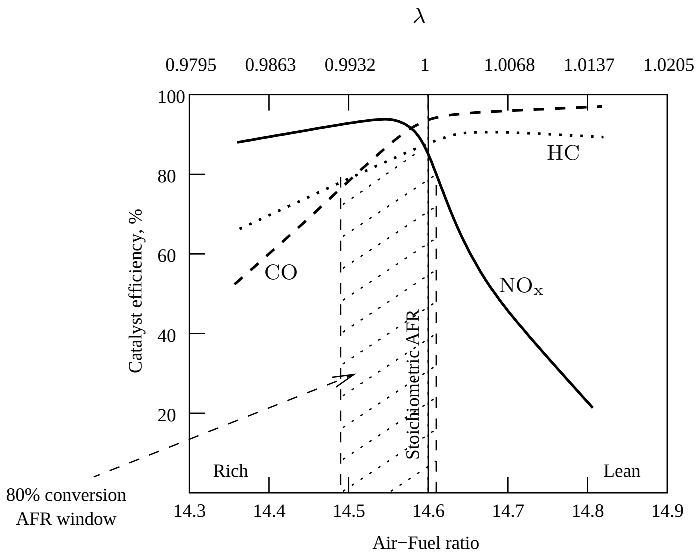

Figure 1.2 Catalyst conversion efficiency for NO_x, CO and HC [Hey88]

are responsible for the majority of ultrafine particulates (less than one micron in diameter). Ultrafine particulates are suspected to be linked to increased rates of premature death since they are able to penetrate deep into the lung where they may enter interstitial tissue, causing severe respiratory inflammation and acute pulmonary toxicity [DLM98]. Finally, CO_2 is the final product of all combustion processes and a major contributor to the greenhouse effect [Pea01].

Several devices have been developed to reduce the pollutants from the exhaust gases in the engine exhaust system. They include catalytic converters and thermal reactors for the CO, HC, NO_x, and traps or filters for the NO_x and particulates. The catalytic converter is contained in a suitable closure in the exhaust system, which contains the autocatalyst, a ceramic or metallic substrate with an active coating incorporating alumina, ceria and other oxides and combinations of the precious metals: platinum, palladium and rhodium. The substrate can be protected from vibration and shock by a resilient ceramic or metallic mat. The autocatalysts can be either an oxidation or a three-way type. The oxidation catalysts convert the CO and HC to CO_2 and water. They decrease the mass of diesel particulate emissions via the reaction of hydrocarbons which would otherwise condense/adsorb onto particles, but have little effect on the NO_x and particulate number. The three-way catalysts can simultaneously oxidise the CO and HC to CO_2 and water while reducing the NO_x to nitrogen. They are able to reduce the emissions of HC, CO and NO_x by more than 98 % provided that the engine operates within a very narrow scatter range

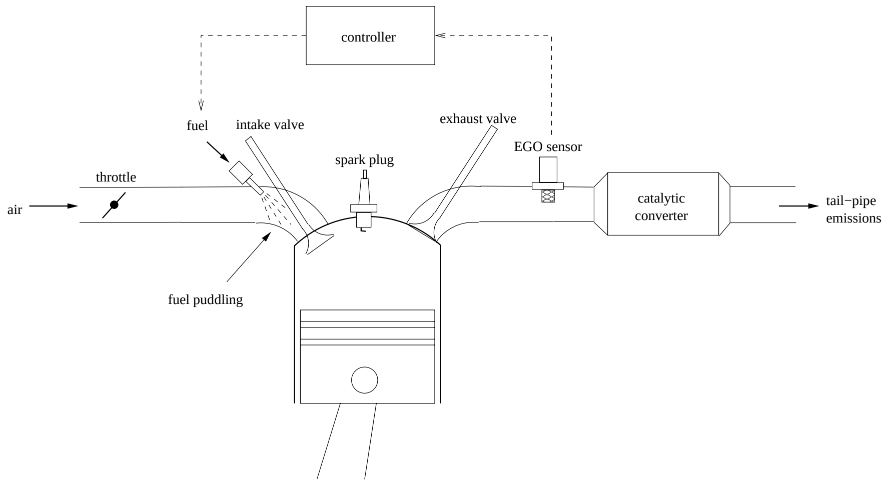

Figure 1.3 Closed-loop AFR control system

(<1%) centred around the stoichiometric AFR ($\lambda = 1$) as depicted in Figure 1.2 [Bau99]. Since maintaining the AFR in this restricted range under all operating conditions is a very difficult task for open loop fuel systems, closed-loop control of the AFR has been introduced. This system relies on a closed-loop control system to consistently maintain the AFR mixture entering the engine within the optimal range known as the AFR window. An oxygen sensor (lambda sensor) in the exhaust system is used to monitor the AFR of the exhaust gas composition.

The AFR (lambda) closed-loop control systems incorporating a catalytic converter, such as the one depicted in Figure 1.3, are very effective in cleaning the exhaust gases from the SI engines. The lambda sensor monitors the AFR composition in the exhaust and the amount of injected fuel is manipulated by the control system to maintain the measured lambda at unity. The throttle is controlled by the driver in a conventional SI engine and constitutes the main disturbance on the AFR signal. The dynamic behaviour of the AFR system is also strongly affected by the fuel dynamics such as the fuel puddle in the inlet port. The fuel puddle dynamics describe the fact that even in a fully warmed-up engine a significant fraction of the fuel injected in each cycle impinges onto the inlet port wall and valves, and enters the cylinder in subsequent cycles through evaporation and dribble. The delays in the AFR path such as the transport delay or injection delay put fundamental limitations on the achievable speed of response by a feedback control system. This necessitates a feedforward element in the AFR control system in order to enhance the controller's speed. Unfortunately, a feedforward controller has no robustness against the uncertainty in the system and therefore requires high fidelity models to perform satisfactorily.

Engine dynamics are nonlinear and operating point dependent. So-called mean value engine models have been developed for the engine control system analysis and synthesis purposes [Dob80, Pow87, PC87, HS90, MH92, CM00]. These models are nonlinear in general. Usually linearised models are derived from the original nonlinear model at different operating points and linear control systems are designed for the linearised models. Although this approach has been shown to work in practice, further improvements in the feedback controller performance can only be achieved if a nonlinear controller such as a linear parameter-varying controller is designed for the nonlinear engine model. A more detailed discussion of the mean value engine models for the AFR control and the related literature review will be presented in Chapter 3.

The classical approach to the AFR control is to design simple proportional-integral (PI) controllers at fixed operating points and to schedule the controller gains across the operating envelope [Kie88]. Describing function analysis is used to analyse the limit cycle properties caused by the sensor nonlinearities and time delays in the loop. The performance of this controller can be enhanced by introducing an open-loop control map (a simple feedforward element). Sliding mode feedback controllers have been developed as an alternative to the PI controllers [CH88]. The main advantage of these controllers is that they have certain stability and robustness guarantees when state measurements are available. An LQG/LTR controller for combined AFR and engine speed control in a limited speed range is published in [OG93]. Several other design methods are applied to the AFR control problem such as feedback linearisation [BBC95, Guz95, XYM98] and $\mathscr{H}_\infty$ loop shaping [Bra96].

However, engine control applications, including the AFR control, have been dominated by observer based control systems. The main reason for using an observer/estimator is to improve the AFR regulation during transients by replacing the conventional empirical feedforward control with a model-based approach. The linear and nonlinear estimation theories (such as Extended Kalman Filtering, adaptive observers) have applied to the mean value models to get observers/estimators [PFC98, KRU98, CVH00]. Sliding mode observers are developed in [CH98] as an extension of the sliding mode controllers.

The above short review of the AFR control is not exhaustive and a comprehensive review can be found in [HL01].

1.3 Variable Cam Timing

Valves control the breathing of engines. The timing of the breathing, i.e. the timing of the air intake and exhaust, is controlled by the shape and phase angle of the cams. To optimise the breathing whether from the point of view of volumetric efficiency, or emissions control,

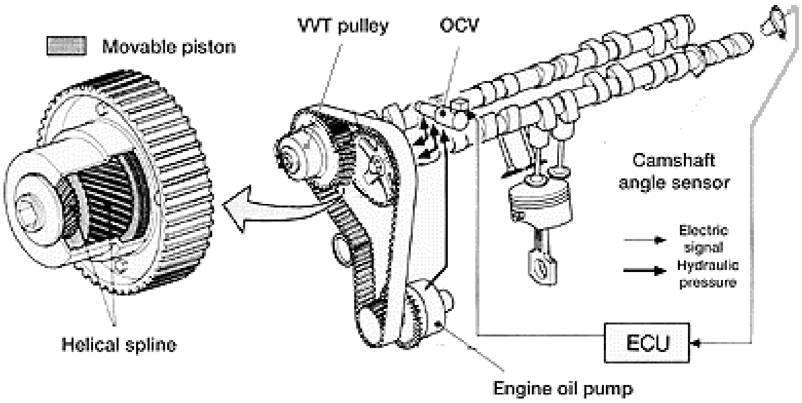

Figure 1.4 Toyota VCT Mechanism

or combustion stability especially at cold start engines require different valve timings at different conditions. In conventional SI engines the valve timing is, roughly speaking, a tradeoff between the idle stability and wide-open-throttle (WOT) performance. Many improvements in engine operation in terms of idle quality, WOT performance, part-load emissions and fuel economy can be achieved, if the valve timings could be optimised for each engine speed and load. For example, the overlap between the intake stroke and exhaust stroke should be increased in order to improve performance as the manifold pressure increases, i.e. wider throttle openings, and as the engine speed increases. Briefly, this is because the residual gases from the previous cycle will be more effectively removed with increased overlap at these conditions.

VVT can be achieved in different ways [MWU$^+$96]. The simplest mechanism called VCT is depicted in Figure 1.4.[1] The VCT alters the phase between the cam shaft and the crankshaft. It consists of an oil control valve, a position sensor and the VCT pulley. Oil control valve regulates the amount of oil pressure in the VCT pulley. This mechanism can make the cam shaft retard/advance to any angle between the maximum limits. There are 4 different types of VCT in double-over-head-cylinder engines:

- Intake Only (phasing only the intake cam);
- Exhaust Only (phasing only the exhaust cam);
- Twin Equal (phasing the intake and the exhaust cams equally);

[1] http://www.billzilla.org/vvtvtec.htm

- Twin Independent (phasing the intake and the exhaust cams independently).

Twin independent (TI) VCT provides the most advantages among these at the cost of increased complexity. It can improve the part-load fuel consumption and emissions as well as the idle quality, cold start emissions and WOT performance [LCS96]. In the following some advantages provided by TI-VCT are discussed in more detail.

Idle Quality

At idle the TI-VCT mechanism can be used to reduce or more correctly maintain a desired quality of the residual gas fraction in the cylinder to maintain the idle stability. Too little residual gas has a detrimental effect on NO_x production, and a limited amount has virtually no effect on stability. In fact during warm-up, a certain quantity of hot residuals is beneficial from the point view of encouraging fuel evaporation. As noted above, in a fixed valve timing engine the amount of overlap at idle is a trade-off between the idle quality and high speed power. The TI-VCT can reduce the valve overlap when required without compromising high speed power. The improved idle quality from reduced overlap could allow the engine to operate at lower idle speeds without losing stability. For example, [Ma88] shows that a 200 rpm reduction in idle speed from 800 rpm translates to 6.1% improvement in the fuel consumption.

Part-load Emissions

Increasing the valve overlap at part-load increases the amount of residual gas trapped in the cylinder. This functions as an internal exhaust gas recirculation (EGR) mechanism and reduces HC as well as the NO_x emissions. The NO_x reduction is due to the reduced combustion temperatures but HC reduction mainly results from another opportunity to burn unburnt HC from the previous cycle. The same level of reduction of the HC emissions cannot be achieved with external EGR [MWU+96]. The reason for this is that most of the unburnt HC comes from the piston top land. This comes out last, so residuals left in the cylinder are much richer in HC than the rest of the exhaust. Therefore trapping more residuals with valve timing is more effective as reacting the previous cycle HC. Moreover, when both cams are significantly retarded the NO_x and HC emissions are determined by the exhaust valve closing (EVC) timing, and are independent of the overlap [LCS96, p. 678].

Part-Load Fuel Consumption

The intake valve closing (IVC) timing and the duration of valve overlap are the main parameters governing the fuel efficiency at part-load. Retarding the IVC more into the compression stroke reduces the intake stroke pumping losses due to the higher manifold pressures for a given load. However, it also reduces the effective compression ratio and temperature near the end of compression stroke, limiting the fuel consumption benefit of the late IVC. This can be offset by enlarging the valve overlap since it increases the amount of internal EGR [LCS96]. At high loads the late IVC allows unthrottled control of the engine pumping, which reduces the intake stroke pumping work. Moreover, the late IVC retards the valve overlap period more into the intake stroke and consequently increases internal EGR.

WOT Performance

At low speeds the volumetric efficiency can be improved with the early IVC, which results in more charge being trapped in the cylinder. On the other hand, at high speeds and loads the late IVC increases the volumetric efficiency. This is because cylinder pressure at bottom dead centre (BDC) is lower than the manifold pressure at high speeds and loads due to the beneficial effects of "suction" from the exhaust stream momentum, and therefore more charge can be sucked into the cylinder with the late IVC after BDC [Asm82]. Furthermore, the late EVC at high speed helps scavenging process and enhances volumetric efficiency even more. However, the late EVO also increases the pumping losses during the first part of the exhaust stroke. Note that the improvements at WOT performance can be converted to a fuel economy advantage by lowering the axle ratio to maintain the same performance [Ma88].

1.3.1 Control Issues in VCT engines

In order to achieve the full potential benefits of the TI-VCT engine, the cam phasing must be altered continuously across the operating envelope as discussed in the previous section. While the TI-VCT improves the engine emissions and fuel efficiency, it also causes undesired transients in torque response and AFR. This is because the cam phasing affects the manifold pressure, which affects the amount of air sucked into the cylinders, the fuel film dynamics at the port walls (to be shown in this thesis) and the residual gas fraction in the cylinders. Therefore feedback control is necessary to reject the undesired transients and maintain the smooth torque response and stoichiometric AFR.

There are three main control issues in VCT engines. The first one is the control of the VCT actuators. The response of the cam actuators must be fast enough to provide good transient torque response at high loads. In fact, the cams must ideally be moved to the standard valve timings as fast as the manifold filling dynamics (in the order of 150 msec) [SGL95]. It is shown in [GGF01] that the VCT actuators have a static nonlinearity and an integrator in their system dynamics. By identifying a nonlinear model of the actuators a nonlinear controller that inverts the static nonlinearity can be designed.

Experimental results indicate that such a controller can achieve superior performance over its linear counterparts.

The second important control problem in a VCT engine is the control of engine torque response. The VCT engines should have a torque response similar to the torque response of a conventional engine. There have been few publications in the literature on torque management of the Twin Equal VCT engines. In [JF97, JFSC98] a nonlinear feedforward strategy, in which the VCT disturbance on the torque response is rejected by an electronic throttle or an air bypass valve, is proposed. Since there is no feedback element in their design, the performance of the feedforward controller solely depends on the accuracy of the models used. In [HSFB97, HFS99] the torque response is regulated together with the AFR and VCT actuators by a multivariable controller. The torque measurement and electronic throttle are assumed available in these studies.

The third and most important one for this study is **the AFR control problem** in a VCT engine. Although the VCT mechanism reduces the engine emissions, a three-way catalyst is still needed in VCT engines to satisfy the stringent emission regulations. Minimising the effects of the VCT and throttle disturbances on the AFR is crucial in order to maintain the high conversion efficiency of the catalyst. A predictive linear feedback-and-feedforward controller is designed in [GCFV99] to reject the VCT, throttle and engine speed disturbances on the AFR in a Twin Equal VCT engine. The engine model is obtained by a black-box identification method. In another study the control Lyapunov function methodology is applied to regulate the AFR and torque response in a variable intake valve timing engine [KG00]. Other studies propose a linear MIMO LQG controller for the regulation of the VCT actuators, torque response and AFR around an operating point [HSFB97, HFS99]. A review of the VCT control algorithms can be found in [JM02]. In all of the aforementioned studies of the AFR control problem in VCT engines mean value engine models are used to analyse the problem and design controllers. These mean value models include only the air path dynamics and the effect of the VCT on the cylinder air charge. On the other hand it is known that the fuel path dynamics such as the fuel puddle parameters vary with the manifold pressure, engine speed and inlet temperature. Therefore it is likely that the VCT mechanism affects the fuel path dynamics in the AFR problem as well as the air path dynamics. The modelling and identification of the fuel path dynamics for the AFR control problem is one of the main objectives of this thesis and will be presented in Chapter 3. It will be shown that the effect of the VCT on the fuel path dynamics must be modelled for tight regulation of the AFR in TI-VCT engines.

1.4 Thesis Layout

The layout of the thesis is as follows:

Chapter 2 Transient VCT Disturbances on AFR An experimental investigation of the variations in the AFR path caused by the VCT mechanism is presented. Both gasoline fuel and gaseous fuel experiments are performed in order to show that not only the cylinder air flow, but also the cylinder fuel flow varies under the transient VCT disturbances.

Chapter 3 Modelling and Identification of the AFR Path The standard mean value engine modelling and identification methods are extended to the TI-VCT engines while a critical review of the standard methods are given. A global identification framework for the identification of the wall-wetting dynamics is proposed and a nonlinear parameter-varying AFR path model at a constant engine speed ($1500rpm$) is identified.

Chapter 4 LFT Representation of the AFR Path Model The LFT framework in control theory is described and an LFT approximation of the identified nonlinear AFR path model is constructed for controller synthesis purposes.

Chapter 5 Robust Control System Design The necessary $\mathscr{H}_\infty$ robust control theory is introduced in the linear matrix inequality framework. The LTI $\mathscr{H}_\infty$ robust control techniques are extended to the LPV case and a review of the available LPV controller synthesis methods is presented in a systematic and unified framework. Two illustrative examples are included to give a comparison of the synthesis methods discussed in this chapter.

Chapter 6 AFR Control System Design The design of the LTI and LPV $\mathscr{H}_\infty$ loop shaping controllers for the AFR control problem in the TI-VCT engines is presented. The performance of the controllers are investigated both through simulations and extensive engine tests across the entire operating envelope.

Chapter 7 Conclusions The main conclusions, contributions and future research proposals of this thesis are discussed in this chapter.

Appendices In three separate appendices details of the engine testing facilities, excitation signals used for linear identification and the $\mathscr{H}_\infty$ loop shaping design framework are discussed.

2

Transient VCT Disturbances on AFR

It is well known from the literature that varying the valve timings by VCT mechanism disturbs the AFR signal and that even less surprisingly, varying the IVO and/or EVC timing changes the amount of air entering the cylinders [HSFB97, JFSC98, HFS99]. However, it is unknown from the literature if and how variations in the valve timings perturb the amount of fuel entering the cylinders. In the following an answer to this questions will be sought through experiments.

Engine tests are performed by exciting the AFR loop via either IVO or EVC timing. This allows the dissociation and assessment of independent transient effects of either the IVO or EVC on the AFR signal. One difficulty of this experiment is that it does not indicate the extent of AFR deviations arising from variations in cylinder air flow and cylinder fuel flow. It is difficult to separate the effects of air and fuel flows on AFR partly because of the wall-wetting dynamics of the gasoline fuel in the inlet port of the cylinder. To attempt to circumvent the wall-wetting dynamics, gaseous fuel (propane) instead of gasoline fuel is also used in the same set of experiments. The comparison of the data obtained from the gasoline and propane fuel experiments under the same operating conditions helps separate the effects of the cylinder air flow and cylinder fuel flow on AFR deviations during VCT transients. In the following terms AFR and lambda will be used interchangeably to refer the normalised AFR.

2.1 Gasoline Experiments

Effects of the IVO and EVC timing on the AFR signal are investigated in separate engine tests. The experiments are performed at $1500rpm$ with constant throttle angle and fuel injection. A square wave reference is applied to the valve timings and measurements are sampled every event (180 crank angle degrees). Units of time axis can be converted from

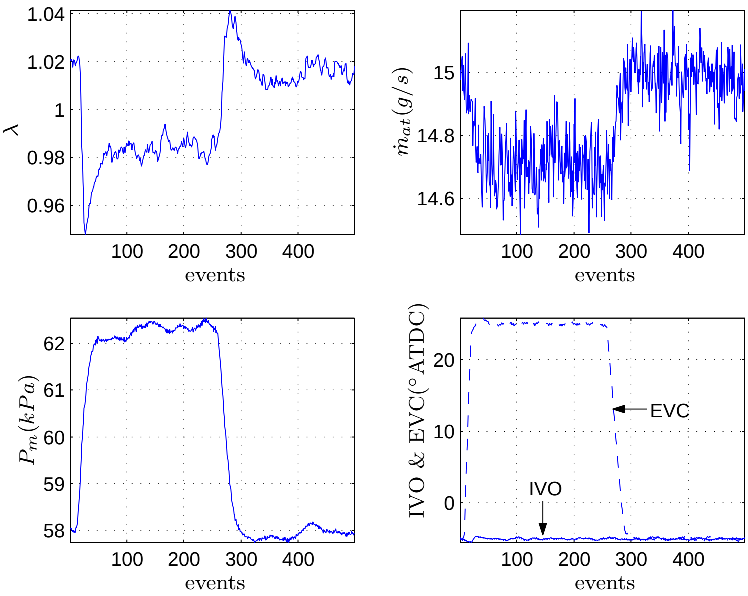

Figure 2.1 Transient EVC disturbance on AFR (gasoline experiment)

engine events to seconds through the following scale: 100 events equals to 2 seconds at $1500rpm$. During the experiments, the AFR signal is measured at the exhaust of cylinder 1 by a wide-range lambda sensor. All the data presented in this chapter are averaged over 6 measurements to obtain representative responses.

Figure 2.1 shows a transient disturbance on the lambda signal when the valve overlap is varied between $0°$ and $30°$ by exciting the EVC timing with a square wave reference (IVO is fixed at $-5°$ ATDC). Throttle mass air flow (MAF) $\dot{m}_{at}$, manifold air pressure (MAP) P_m, and the valve timing traces are also included in the figure. It is observed that EVC causes significant transient deviations in the measured AFR. When the overlap is increased by retarding EVC from $-5°$ to $25°$, volumetric efficiency is reduced as the throttle MAF trace indicates. This causes a rich spike in the lambda trace at around event 30. The increase in MAP is due to the fact that the cylinder MAF is quicker to respond to the change in EVC than the throttle MAF. Hence, there is a short period during which less air is sucked into the cylinder than the air entering the manifold via the throttle. This causes the rich spike in lambda and the increase in MAP. Similarly when the overlap is reduced by advancing EVC from $25°$ to $-5°$, a lean spike is observed at around event 270. The cause of the lean spike can be explained using similar arguments, i.e. advancing EVC increases the volumetric efficiency and this in turn reduces MAP via a positive spike in the cylinder MAF. This analysis shows that the transient EVC disturbances on the AFR signal can be explained by only analysing the changes in the air path dynamics without

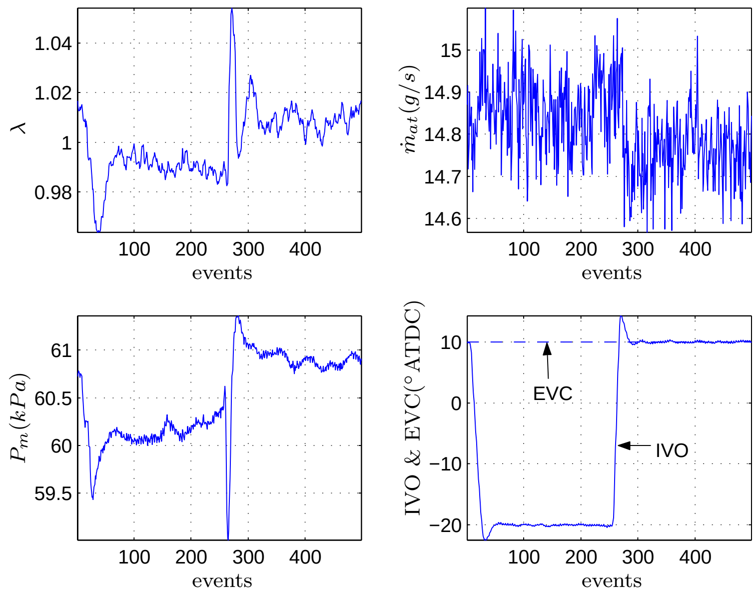

Figure 2.2 Transient IVO disturbance on AFR (gasoline experiment)

considering any possible effects of the fuel flow dynamics.

A similar experiment is performed by exciting the IVO timing with a square wave reference and keeping the EVC timing fixed at 10° ATDC. Figure 2.2 shows that exciting IVO like EVC causes significant transient spikes in the AFR. Extending the overlap into the exhaust stroke by advancing IVO timing from 10° to −20° increases the volumetric efficiency, as the slight increase in the throttle MAF trace hints. Thus it is expected that there should be a lean spike in the lambda trace at around event 30, if one uses similar arguments to the previous EVC experiment case, yet there is a rich spike in the measurement instead. Another unexpected behaviour is observed when the overlap is reduced to zero by retarding IVO from −20° to 10°, i.e. a lean spike in lambda at around event 270. On the other hand, the MAP trace supports the throttle MAF behaviour, because when the throttle MAF increases, MAP decreases as in the case of EVC disturbance. Yet the lambda trace has its spikes in opposing directions to that which would be expected from the air flow dynamics. This suggests that there is an extra dynamic effect in the measurements that is related to neither throttle MAF nor MAP dynamics.

The gasoline experiments above show that not all the transient VCT disturbances on the AFR signal can be explained by the changes in the air path dynamics. In particular the transient IVO disturbance on AFR cannot be explained by changes in the air flow dynamics caused by IVO. If the variations in the cylinder MAF cannot explain the observed AFR behaviour, it must be the cylinder fuel flow dynamics that are governing the observed behaviour. The next section will reveal the transient behaviour of the cylinder MAF under the VCT excitation through gaseous fuel (propane) experiments in order to understand how the fuel dynamics behave during the VCT transients.

2.2 Propane Experiments

The same experiments described above are performed with propane as the fuel rather than gasoline. A constant amount of propane is injected into the inlet port of cylinder 1 only. The rate of injection is independent of MAP as the propane injector consisted of a choked orifice located very close to the injection point. The following assumptions are satisfied for the propane experiments,

- There is no wall-wetting dynamics for propane;
- The amount of propane fuel entering the cylinder 1 at each event is almost constant and independent of MAP.

The first assumption can be made since propane is a gaseous fuel. The second assumption requires a careful examination. During the propane fuel experiments the rest of the cylinders are run on gasoline through the fuel injectors. If the injected propane stays in the inlet port 1 the assumption would hold and the cylinder propane flow would be independent of MAP. However, if some of the propane leaks back into the intake manifold, the assumption would not hold anymore. This is because the propane leaked into the manifold would form a premixed air-fuel composition in the intake manifold and the overall propane flow into the cylinder 1 would depend on MAP. Moreover, this premixed air-fuel composition would also disturb the AFR composition in other cylinders. Since no such abnormality in the AFR measurements of the other cylinders are observed during the tests, it is concluded that the second assumption holds as well. These two conditions are required to ensure that the cylinder fuel flow is constant during the experiments. This means that any variations in the observed lambda trace are due to the variations in the cylinder MAF in the following experiments.

Figure 2.3 compares the results of the propane and gasoline experiments for the same reference excitation in the EVC timing. Very small differences between the throttle MAF, MAP, and valve timing traces of the two experiments show that they are performed essentially under the same conditions. Moreover, almost identical lambda traces confirm that the lambda transient is caused only by the variations in the cylinder MAF as explained in the previous section. Note that such a small difference between the lambda traces is only possible, if there is no significant change in the wall-wetting dynamics under this particular EVC disturbance. However, this observation does not suggest that there is no

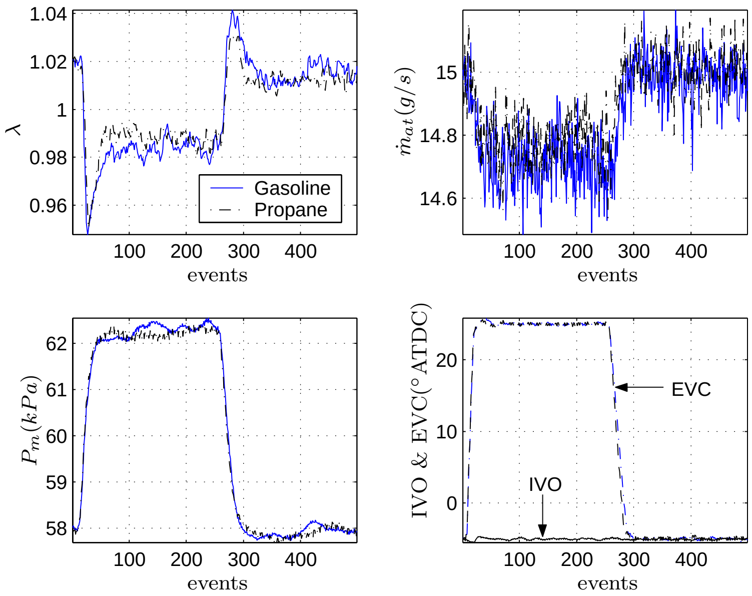

Figure 2.3 Transient EVC disturbance on AFR signal (propane experiment)

wall-wetting dynamics for gasoline fuel but only indicates that the wall-wetting dynamics do not change under the EVC excitation.

Figure 2.4 compares the propane and gasoline experiments for the IVO disturbance case. The lambda behaviour for the propane is just what would be expected from changing air path dynamics. The increase in the overlap by advancing the IVO timing from 10° to −20° improves the volumetric efficiency as the throttle MAF trace indicates, and this in turn causes a lean spike in the propane lambda trace at around event 30. Similarly, a rich spike is observed in the propane lambda trace when the overlap is reduced by retarding IVO at around event 270. Therefore, for the propane experiments all the transient VCT disturbances (varying EVC or IVO) on AFR can be explained by changes in the air path dynamics only. This is an expected result and confirms that the two assumptions made above for propane experiments are true.

The observed lambda behaviour under the IVO excitation in the gasoline experiment can be explained with the help of the results of the propane experiment, which show explicitly the variations in the cylinder MAF during VCT transients. Note that the measured lambda trace for the propane fuel can be considered as the normalised cylinder MAF trace. The disagreement between the measured lambda behaviour for the gasoline fuel and the one for the propane fuel at transients indicates a significant contribution of wall-wetting dynamics in the observations. In particular, the rich spike in the lambda trace for the gasoline fuel (solid line in the top left plot of Figure 2.4) at around event 30 can only be

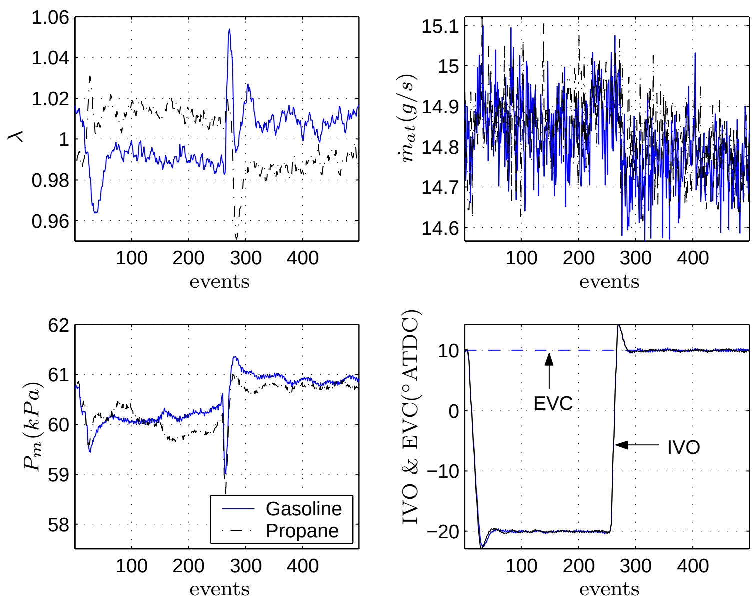

Figure 2.4 Transient IVO disturbance on AFR signal (propane experiments)

explained with a big increase in the cylinder fuel flow when the normalised cylinder MAF is going through a positive transient as indicated by the measured lambda trace for the propane fuel (dashed-dotted line in the top left plot of Figure 2.4). Since the injected fuel is constant during the experiments, the extra fuel can only come from the fuel puddle itself. This implies a decrease in the fuel puddle size at around event 30. Similarly, a lean spike in the lambda trace for the gasoline fuel at around event 270 while the normalised cylinder MAF is going through a negative transient shows a significant reduction in the cylinder fuel flow. This indicates an increase in the fuel puddle size at around event 270.

So far only the transient behaviour of the results shown in Figure 2.4 has been discussed since it is the main focus of this work. However there is some steady state inconsistency in the measurements. In particular throttle MAF readings are in disagreement with the gasoline lambda readings, i.e.when throttle MAF increases the gasoline lambda goes rich at steady state and vice versa. Note that this is a very unexpected behaviour since the fuel injection timings were constant during the experiments. The data presented in Figures 2.3- 2.4 suggest that the propane lambda readings are reliable as they agree with all the other sensor measurements. This raises the question whether the injected fuel was really constant during the experiment shown in Figure2.4. One possibility is that there was a hysteresis in the fuel pressure control valve which is referenced to manifold pressure. Thus pressure spikes in Figure 2.4 in MAP could cause slight changes in injected fuel amount. This discussion is not exhaustive and further work is definitely required in order

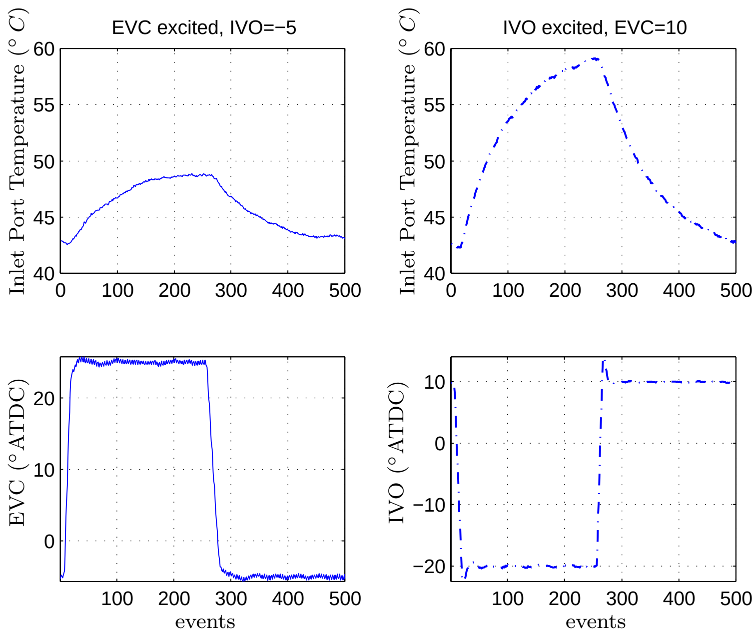

Figure 2.5 Variations in the inlet port temperature at $40kPa$ under VCT excitation

to determine the causes of this steady state mismatch in the measurements. However this problem will not be further pursued in this work due to strict time limitations.

It is evident from the above experiments that varying the valve overlap via the IVO timing has a significant effect on the fuel puddle size, whereas varying it via the EVC timing has a negligible one. This difference cannot be explained by variations in either the throttle MAF or MAP dynamics. A possible explanation is given below. During the experiments the gas temperature around the inlet port of the cylinder 1 is also measured by a thermocouple (K-type/insulated/$0.5mm$) as depicted in Figure 2.5. The measurements show that both the EVC and IVO timing change the inlet port temperature. In particular increasing the valve overlap increases the inlet port temperature, since there is more back flow of residual gases into the inlet port and intake manifold. However, data also show that early IVO causes a much bigger change in the port temperature than the late EVC for the same overlap change, especially at low loads. With early IVO, the piston is moving upwards for the most of the overlap period and is pushing the residual gases into the intake manifold. On the other hand, with late EVC, the piston is moving downwards for most of the overlap, and therefore pulling the residual gases into the cylinder. Such a difference in the amount of residual gas pushed back into the inlet port can explain the smaller increase in the temperature by retarding EVC. Furthermore, the fact that the EVC excitation causes smaller variations in the port temperature can explain why exciting EVC does not change the fuel puddle size as much. Note that it is expected that the actual mean temperature variation of the gas around the intake valves would be larger since the measurements were taken 4-5cm upstream from the injectors. Also there must be a cyclic temperature variation which is not resolved with the thermocouple here due to the time constant of the thermocouple (appeared to be around 0.3-0.4s). Higher frequency response temperature measurements by a faster sensor might reveal other effects.

2.3 Comments

The propane experiments give a clear indication of the normalised cylinder MAF behaviour during the VCT transients. This will give us confidence later on, when the validation of the cylinder MAF model will be performed against the traces from the propane experiments. The gasoline and propane experiments together not only show that the VCT mechanism causes significant transient deviations in AFR but also indicate that the fuel puddle size varies significantly during the IVO timing transients. The empirical evidence showing that the fuel puddle size changes with the valve timings especially with the IVO timing is the first published result indicating significant changes in the wall-wetting dynamics under VCT transients to the author's knowledge. Furthermore, the experiments indicate that even a perfect cylinder MAF predictor alone cannot achieve a tight transient AFR control in a TI-VCT engine due to significant variations in the cylinder fuel flow rate during the transients. Such a change in fuel flow cannot be compensated for without an accurate wall-wetting model, which must predict the variations in the fuel puddle parameters with the valve timings. Hence further investigation of the AFR path in TI-VCT engines is imperative, if a satisfactory transient AFR control is to be accomplished. The results of this chapter have recently been published in [GFGC02].

3

Modelling and Identification of the AFR Path

Empirical results of the previous chapter have shown that both air-and fuel dynamics play an important role in shaping the transient AFR behaviour under the VCT disturbances. These dynamics and their relationships with the valve timings must be captured by an AFR path model if good AFR regulation is desired. This chapter presents a mean value AFR path model and proposes schemes for identification of its parameters, for which both local (linear) and global identification methods are employed.

A mean value engine model describes the engine dynamics with limited bandwidth, equivalent to considering the mean behaviour of the state variables over engine events. So-called standard mean value engine models exist in the literature for PFI engines [HS90, MH92, CM00]. They usually include the models of the air flows, intake manifold, wall-wetting of the fuel, torque generation and engine speed. Early publications also include models for the carburetor and fuel flow in the intake manifold [Dob80, Pow87, PC87].

There are two types of relationships in a mean value engine model. The first type is the very fast dynamics that achieve equilibrium in a few engine events. Such dynamics are usually ignored and static mappings (look-up tables or polynomial regression fittings) are used to describe them. For example, the relationship from throttle position (TP) and MAP to throttle MAF is considered as instantaneous in the mean value model. The second type of relationships are relatively slow processes with time constants around tens or hundreds of engine events. They are described by differential equations and constitute the state variables of the engine model. In general most of the flows (apart from fuel flow), torque and emission generations are modelled as instantaneous relationships. On the other hand, the manifold pressure, fuel puddle (film) mass and engine speed (denoted as N) are the most common state (dynamic) variables in the mean value engine model.

Engine models can be constructed either in the time domain or crank angle domain. It is possible to transform a differential equation in one domain to another with the knowledge

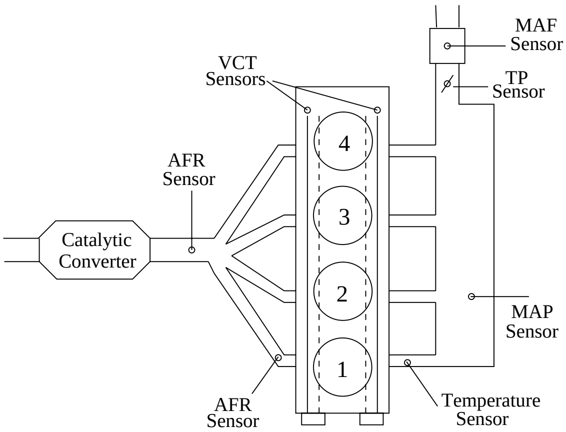

Figure 3.1 Main sensors used in the AFR path identification

of engine speed

$$\frac{d\theta}{dt} = 6N, \tag{3.1}$$

where θ is in crank angle degrees, t is in seconds and N is in rpm. Since many engine processes are periodic in the crank angle domain, identification of the models in this domain has advantages over identification of models in the time domain. For example, most of the dynamics vary less in the crank angle domain than in the time domain [CC86]; this is very desirable when identifying a parameter-varying model. Therefore, the AFR path model for the TI-VCT engine will be constructed in the crank angle domain with a sampling angle of 180 crank angle degrees, i.e. an engine event. Such models are also known as event based discrete-time mean value engine models.

Figure 3.1 shows a sketch of the positions of the main sensors used in the identification of the AFR path. More detailed information about the engine and facilities can be found in Appendix A. The next section will present the identification and partial validation of the air path dynamics, which are composed of the throttle MAF, cylinder MAF and MAP dynamics. Section 3.2 will expose the identification and partial validation of the fuel path dynamics, which are composed of the injection delay, wall-wetting dynamics, transport delay, gas mixing, and the lambda sensor dynamics. Local linear identification methods are used for identifying the parameters of the fuel path except for the wall-wetting parameters, which are identified by a global identification scheme. Finally, the complete AFR path model will be validated under transient VCT operation in Section 3.3. Note that all the identification and validation experiments are performed at $1500 rpm$.

3.1 Air Path Dynamics

It is common to identify the air flow characteristics of the engine through steady state measurements at different operating points. In a VCT engine operating points are defined by the manifold pressure, valve timings, and engine speed. Table 3.1 shows the valve timings tested during the steady state engine measurements. In total, 28 different valve timings are tested. Two valve timings, IVO=$-20°$/EVC=$29°$ and IVO=$-25°$/EVC=$29°$, are not tested since the large valve overlaps of these timings cause misfires at low manifold pressures. At each valve timing combination, a staircase reference is applied to the throttle position, shown in the bottom plot of Figure 3.2, in order to cover 13 different manifold pressure points between $30kPa$ and $70kPa$ at a fixed engine speed of $1500rpm$.

3.1.1 Throttle Mass Air Flow

The throttle MAF model is based on a one-dimensional steady, isentropic, compressible flow equation for flow across an orifice [Hey88, pp. 304-308]. However, the throttle MAF is not a true one-dimensional flow and information reflecting this fact is contained in the discharge coefficient, which is determined experimentally and is a function of TP and the pressure ratio across the throttle body.

In general the discharge coefficient is determined through steady state engine tests and flow area is described via the physical dimensions of the throttle body. However a simpler approach is taken here: throttle MAF is determined via a regression fitting of TP, measured in volts, and P_m given by

$$\begin{aligned} \dot{m}_{at}(k) =& a_0 + a_1 TP(k) + a_2 P_m(k) + a_3 TP(k) P_m(k) \\ &+ a_4 TP^2(k) + a_5 P_m^2(k) + a_6 TP^3(k) + a_7 P_m^3(k) \end{aligned} \tag{3.2}$$

The Figure 3.2 shows a sample steady state engine measurement if IVO=5° and EVC=29°. The quality of the fit can be seen from the predicted throttle MAF in the

IVO (° ATDC)	EVC (° ATDC)	N (rpm)
15	29	1500
5	20	
-5	10	
-15	0	
-20	-10	
-25		

Table 3.1 Valve timings for the steady state identification experiments

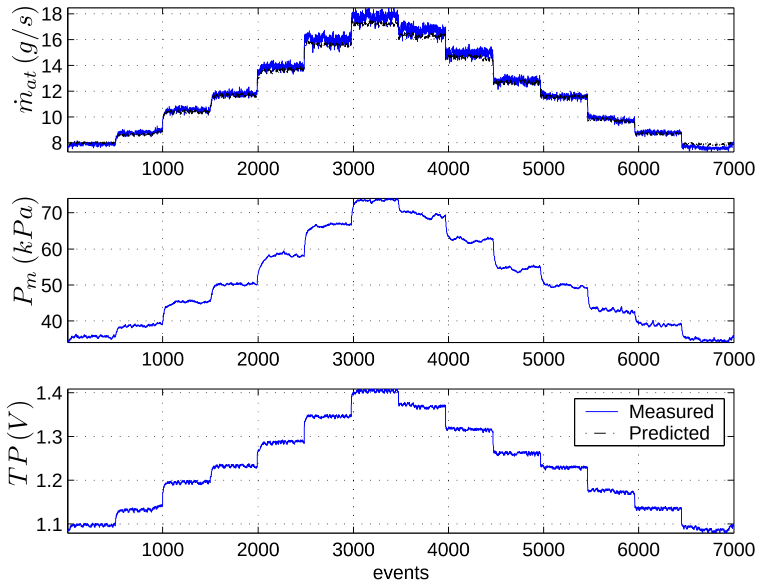

Figure 3.2 A sample steady state engine test for IVO=5°and EVC=29°

top plot. Although, the figure shows that the model has a good steady state fit, the transient accuracy of the model needs to be checked against the independent validation data to make sure that the transient throttle MAF behaviour is captured correctly.

The overall measurements and the fitted surface are plotted in Figure 3.3, where the quality of the fit can be seen. In fact, the worst case error between the model and data is no larger than 2.6 %.

Transient Validation

It is an established assumption for mean value models that the throttle MAF is governed by the throttle position and manifold pressure. In a VCT engine variations in valve timings change the manifold pressure and therefore the throttle MAF. It is important that the proposed model can predict the transient behaviour observed in the measured throttle MAF induced by the VCT mechanism through the manifold pressure correctly. In order to confirm this, the throttle flow model is validated against independent transient data, which are averaged over 4 measurements to improve the signal-to-noise ratio. The first validation data are shown in Figure 3.4, in which the EVC timing follows a square reference signal while the IVO timing is fixed at $-5°$ ATDC. Although there is some offset in the prediction, the transient behaviour of the actual data is captured in the model.

The final transient validation is performed for the IVO excitation, while EVC is fixed at 10° ATDC. The model again correctly predicts actual behaviour shown in Figure 3.5, which reveals that, at low loads, IVO excitation does not affect the throttle MAF.

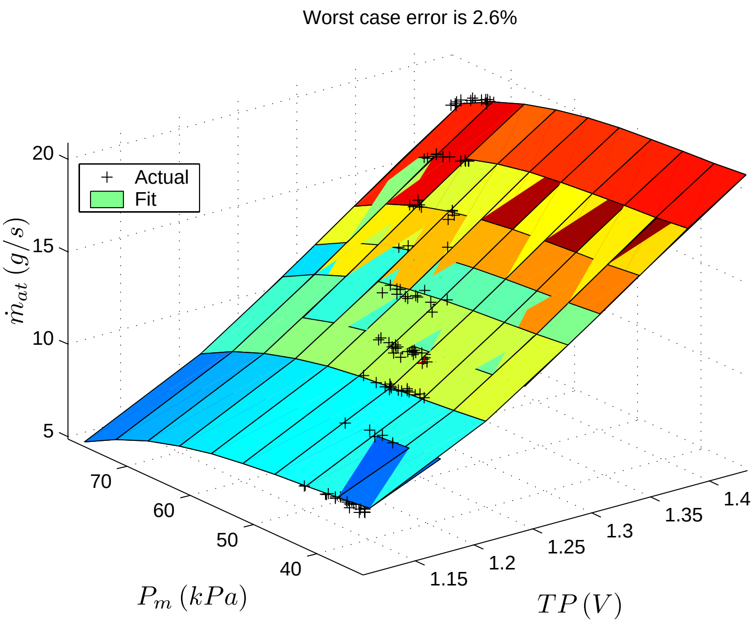

Figure 3.3 Steady state measurements of the throttle MAF and the model fit

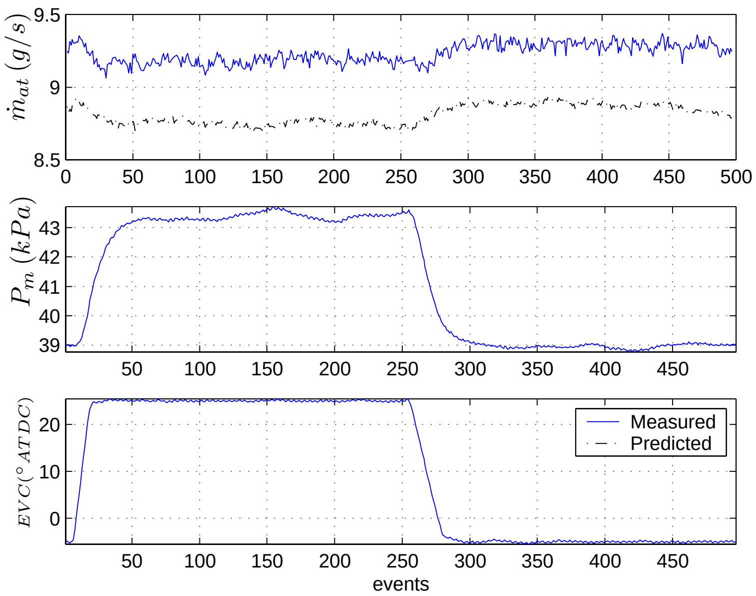

Figure 3.4 Transient validation of the throttle MAF (EVC excitation)

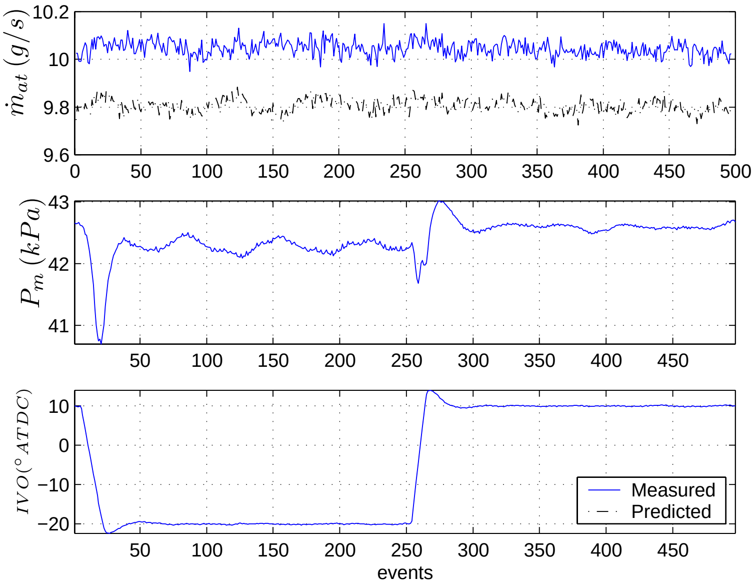

Figure 3.5 Transient validation of the throttle MAF model (IVO excitation)

3.1.2 Cylinder Mass Air Flow

For a conventional PFI engine the cylinder MAF is considered to be the main disturbance for the AFR loop, hence its precise modelling is essential. Conventional steady state engine measurements are capable of describing the engine breathing performance with remarkable accuracy even during fast transient operation, despite the complex nature of the pulsating air flow out of the manifold. It is common to model cylinder MAF by the so-called speed-density formulation [MH92, CVH00], in which the volumetric efficiency is mapped as a function of the manifold pressure, ambient pressure and ambient temperature. For a dual-equal VCT engine, the cylinder MAF is modelled as a polynomial in cam phasing, manifold pressure and engine speed in [SCGF98]. Here, a slightly different polynomial approach is proposed. The data used for cylinder MAF identification are the same as the steady state data used for the throttle MAF identification above (see Table 3.1 and Figure 3.2). Figure 3.6 shows that the manifold pressure is the main factor determining the amount of air sucked into cylinders when the engine speed is constant. On the other hand, the valve timings seem to mainly vary the offset of this almost linear relationship. Each plot shows how the cylinder MAF characteristics varies with MAP and IVO timing at a fixed EVC timing. The solid lines, which change significantly with the valve timings, are the fitted quadratic polynomials for each valve timing. Thus, the cylinder MAF is modelled as a quadratic in MAP, where the coefficients are functions of the valve timings

$$\dot{m}_{ac}(k) = l_{0_a}(k) + l_{1_a}(k)P_m(k) + l_{2_a}(k)P_m^2(k) \tag{3.3}$$

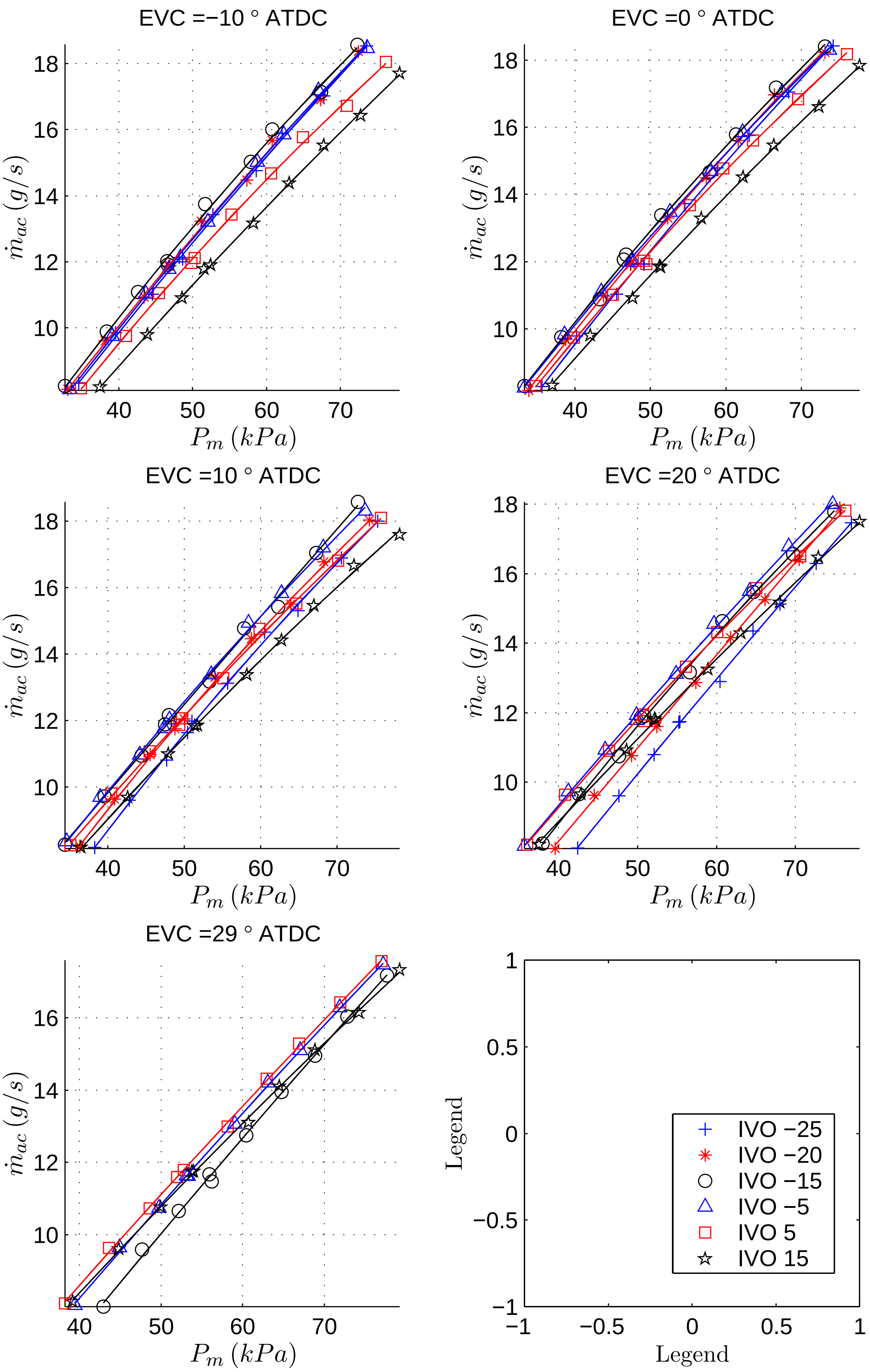

Figure 3.6 Identification data and the model fit for $\dot{m}_{ac}$

and

$$l_{i_a}(k) = f_i(IVO(k), EVC(k)), \qquad i = 0, 1, 2.$$

Note that a quadratic model is used to ensure that even the weak second order effects are captured by the model. Each coefficient l_{i_a} is a complicated nonlinear function of the valve timings IVO and EVC. They are depicted in Figure 3.7. The plots on the left column show the identified raw surfaces of coefficients with respect to valve timings, whereas the ones on the right show the same surfaces but smoothed. The identified coefficient surfaces have multiple maxima, which make them difficult to model precisely without using high order polynomials. The dominant term is l_1 as expected and its value is fairly smooth across the valve timing envelope. On the other hand, the values of the l_0 and l_2 terms seem to vary significantly with valve timings. In order to maximise the accuracy of the model, the coefficients l_{i_a} are stored in look-up tables.

Finally, the identified cylinder MAF surfaces are plotted in Figure 3.8, where each surface is given for a fixed EVC timing. The main trends in cylinder MAF model are:

i. MAP is the main factor in determining the cylinder MAF;

ii. Retarding EVC from $-10°$ to $29°$ reduces the flow;

iii. IVO has a more complicated effect, almost quadratic, on the cylinder MAF and moving IVO to both ends reduces the flow;

The identification is deemed to be successful with a worst case error of 2.3 % between the model and data.

Transient Validation

The accurate modelling of the cylinder MAF is very crucial in building a reliable AFR path model of the TI-VCT engine. The transient validation of the cylinder MAF model is achieved by comparing the model predictions with the lambda traces of the propane experiments discussed in the previous chapter. Recall that the lambda traces from the propane experiments represent the transient behaviour of the normalised cylinder MAF. The first validation data are given in Figure 3.9 for varying EVC and IVO=-5°. For a good model the empirical lambda trace should be a delayed and low-pass filtered form of the predicted normalised cylinder MAF. This is due to the transport delay and extra dynamics at the exhaust such as the lambda sensor dynamics which cause the low-pass filtering. Figure 3.9 shows that the prediction of the model is precise both during retarding and advancing of the EVC timing.

The second transient validation, where data is again taken from the previous propane experiments, is done against the IVO timing excitation with EVC=10°. The transient

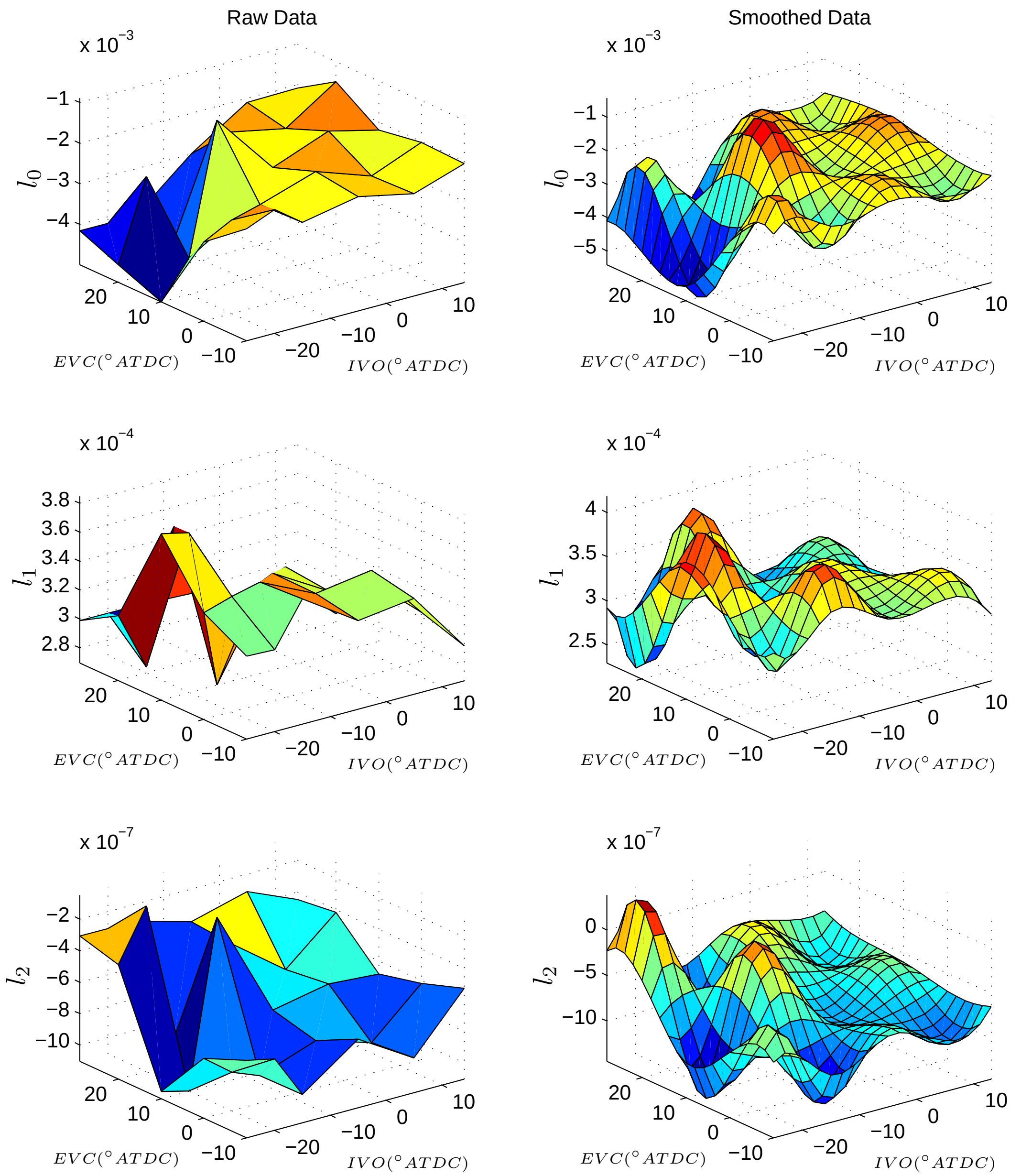

Figure 3.7 Coefficients of the quadratic cylinder MAF model

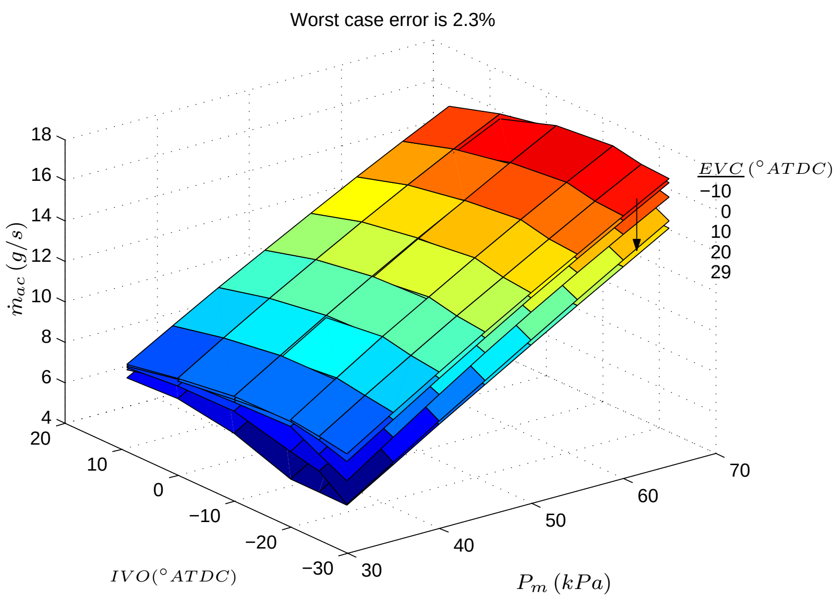

Figure 3.8 Identified cylinder MAF surfaces

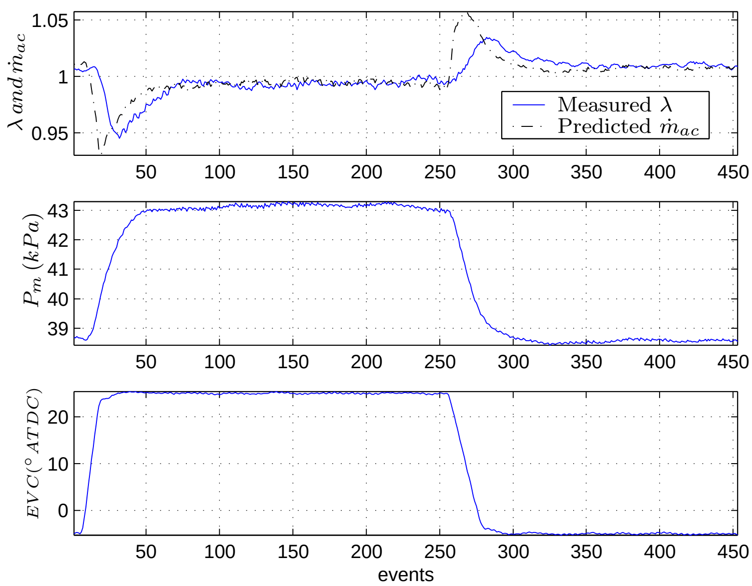

Figure 3.9 Transient validation of the cylinder MAF model (EVC excitation)

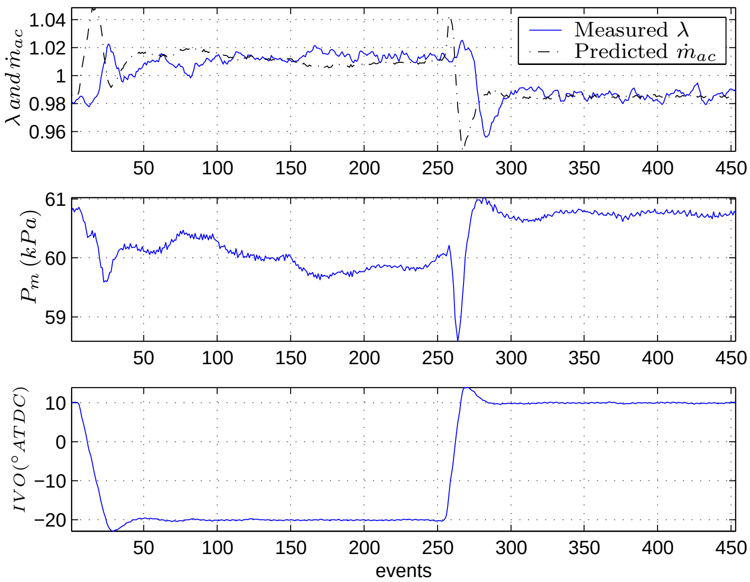

Figure 3.10 Transient validation of the cylinder MAF model (IVO excitation)

agreement between the measured lambda and the predicted normalised cylinder MAF is accurate in the sense that measured lambda looks like a filtered form of the predicted air flow as can be seen in Figure 3.10. The model predicts precisely not only the positive spike in the normalised cylinder MAF when IVO is advanced but also the negative spike when IVO is retarded. These transient validation results increase the confidence in the proposed cylinder MAF model defined in (3.3).

3.1.3 Intake Manifold Model

The true nature of the air dynamics in the intake manifold is very complex. The intake manifold consists of a plenum with individual runners feeding branches which lead to individual cylinders. It is common in AFR control applications to use a lumped parameter model and assuming uniform pressure and temperature. The most common mean value model of the intake manifold is the isothermal filling-emptying model [Hey88, MH92], where manifold pressure is the only state variable. Such a model can be derived by applying conservation of mass and the ideal gas law. Isothermal models assume that the intake manifold temperature is known and constant.

More recent studies in [CM00, Hen01] also propose adiabatic manifold models, where both the conservation of mass and energy are applied in order to derive the governing equations. The main difference between the isothermal and adiabatic models is an extra differential equation describing the dynamics of intake manifold temperature in the adiabatic models. Adiabatic models assume both the manifold pressure and manifold temperature as time-varying, but assume negligible heat transfer between the manifold and its environment. On the other hand, isothermal models assume a constant manifold temperature throughout the inlet manifold. In [CM00] it is shown that better predictions of the air flow dynamics can be achieved, if the adiabatic manifold models are employed.

Here the first approach is taken and the event based discrete-time filling-emptying intake manifold model is used to describe the manifold dynamics as

$$P_m(k+1) = P_m(k) + \frac{T_s R T_m}{6 N V_m} \left(\dot{m}_{at}(k) - \dot{m}_{ac}(k) \right), \tag{3.4}$$

where T_s is sampling time in events, V_m is the manifold volume, and T_m is the manifold temperature in Kelvin. Since both the throttle MAF and cylinder MAF have already been modelled, the intake manifold model can be used without any further engine tests by substituting the appropriate values of the parameters in (3.4). However, the accuracy of the model should be validated.

Transient Validation

The manifold engine model is validated against three different transient excitations. Note that all the presented validation data are averaged over 4 measurements. The first set of validation data shown in Figure 3.11 is taken from an engine test where the EVC timing is excited by a square wave reference signal as before. Although there is some offset in the predictions, the model captures both the MAP and throttle MAF transients accurately. The transient validation data for IVO excitation are depicted in Figure 3.12. Again some steady state errors are present in the predictions but the transient characteristics of the data are captured well by the model. In the final validation test it is investigated whether the model can predict the variations in MAP under TP excitation with constant valve timings. Once again the model predictions of the MAP and throttle MAF agree with the observed transient behaviour well in Figure 3.13.

The validation of the manifold model completes the mean value modelling of the air path dynamics for the AFR control problem. The partial validation of the transient accuracy of each model for different excitations gives promising results and increases the confidence in the use of the model for designing a feedforward controller. Note that neither of the MAF models take into account the ambient air temperature. Hence steady state errors are expected in the models' predictions when the ambient air temperature is different from its value during the identification tests.

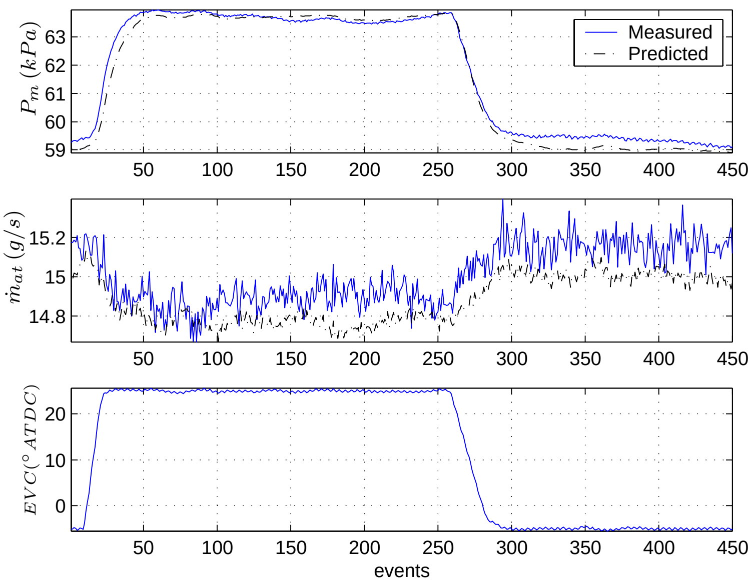

Figure 3.11 Transient validation of the intake MAP model (EVC excitation)

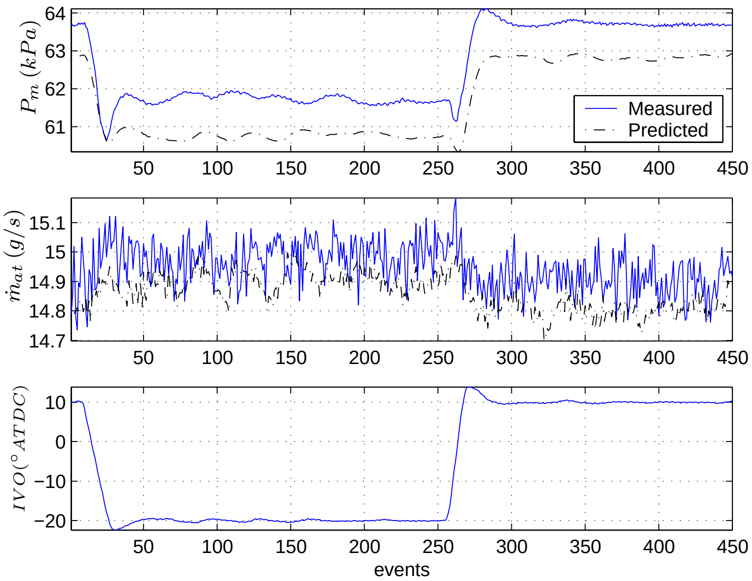

Figure 3.12 Transient validation of the intake MAP model (IVO excitation)

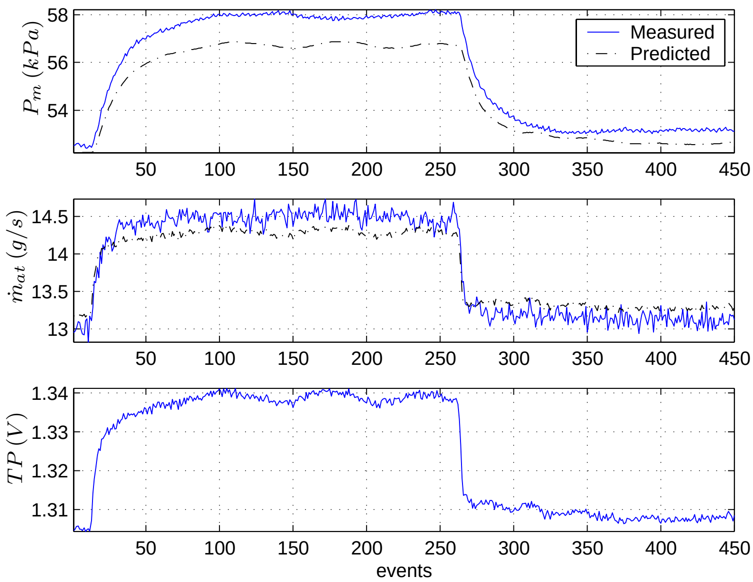

Figure 3.13 Transient validation of the intake MAP model (TP excitation)

3.2 Fuel Path Dynamics

The fuel path, depicted in Figure 3.14, is composed of the injection delay, wall-wetting dynamics, transport delay, gas mixing dynamics and lambda sensor dynamics. The injection fuel pulse-width is denoted as FPW in the following. Note that the model output is chosen as ϕ rather than λ in order to have the controller input FPW entering the model linearly. The injection delay is the time between the sampling of the lambda sensor by engine control unit (ECU) and the time at which the in-cylinder AFR builds up to its final value. This delay is important, because any disturbance that may alter the AFR during this period cannot be compensated for by the controller. The injection delay depends on three parameters [CVH00]:

- Computation duration: This is the time it takes for the ECU to compute one step of the control strategy.
- Injection duration: The flow out of the injector is constant and it is the duration of the injection pulse that determines the quantity of fuel injected. This pulse is usually between 12 and 450 crank-angle degrees.
- Start of injection delay: In order to achieve low emissions, the quality of air-fuel mixture is also important, i.e. as much fuel as possible should enter into the cylinders in vapour form. As the heat from the intake air is negligible compared to the heat absorbed from the walls, injecting most of the fuel on closed intake valves is a

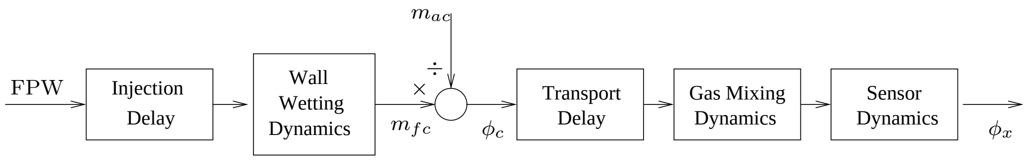

Figure 3.14 Fuel path dynamics for one cylinder

requirement.

The transport delay, which has constant and variable parts, is the main delay in the loop. The constant part is around two engine events long and is due to the compression and expansion strokes. The variable part is the time it takes for the burned gases in the cylinders to have an impact on the lambda sensor once the exhaust valves are open. This delay is inversely proportional to the MAF. Overall the transport delay varies from three events to several events depending on the engine speed and manifold pressure (also called engine load).

The wall-wetting dynamics describe the fact that not all the injected fuel enters into the cylinder immediately. Some of the fuel impinges onto the inlet port wall and enters the cylinder gradually through evaporation and dribble. The model proposed by Aquino [Aqu81] is widely quoted in the literature [HO81, TG93, PD93], and can be described in discrete-time as:

$$m_{ff}(k+1) = (1-\tau)m_{ff}(k) + \mathcal{X}m_{fi}(k) \tag{3.5}$$

$$m_{fc}(k) = \tau m_{ff}(k) + (1-\mathcal{X})m_{fi}(k) \tag{3.6}$$

The input to the model is the injected fuel mass m_{fi} and the output is the fuel mass entering into the cylinder m_{fc}. A fraction $\mathcal{X}$ of the injected fuel is deposited on the walls to increase the fuel puddle mass in the intake port together with a portion $1-\tau$ of the fuel puddle itself. At the same time, a fraction τ of the fuel puddle mass evaporates and enters into the cylinder together with the remainder portion $1-\mathcal{X}$ of the injected fuel. Note that this model satisfies conservation of mass and therefore makes no contribution at steady state. A second order wall-wetting model with three parameters has been introduced by Turin et al. [TCG94]. Wall-wetting models with two fuel puddles have been published in [OG94,ORG97]. In a multi-cylinder PFI engine there are as many wall-wetting dynamics as the number of the cylinders in the engine. Thus, a model with multiple parallel systems should be considered. A simplified multiplexing fuel path model for a 4-cylinder engine is shown in Figure 3.15. This model can predict the resonance modes in the frequency response of the AFR path caused by the multiplexing nature of a multi-cylinder engine.

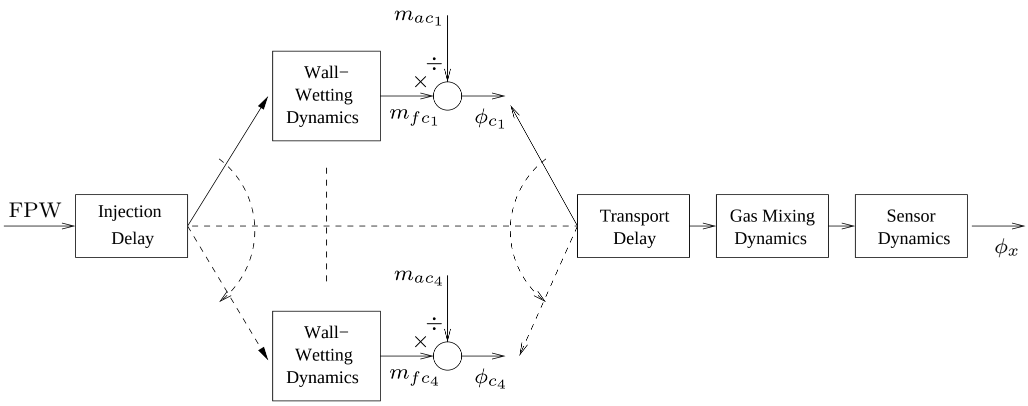

Figure 3.15 Fuel path dynamics for a 4-cylinder engine

The gas mixing dynamics describe the mixing of the gases in the exhaust manifold. The existence of this effect is shown in [ORG97]. These dynamics have more significant effect on the measurements when the sensor is located further down in the exhaust system.

A wide-range lambda sensor has also a substantial dynamic effect on the AFR signal. It is usually modelled as a first order transfer function, even though the actual process itself is fairly nonlinear [Jur95, Chapter 6]. In [TG93] it is reported that the sensor dynamics are of second order and change from under-damped to over-damped with increasing load.

3.2.1 Model Structure

Model structure selection is a crucial part of the identification process. It is essentially an iterative process during which different model structures are tried until satisfactory results are achieved. In the case of the fuel path identification the following decisions need to be made:

- **Number of fuel puddles**: Most of the published modelling effort of the wall-wetting dynamics assume a single fuel puddle as in (3.5)-(3.6). However, more recent studies show that a better description of the dynamics can be achieved with a wall-wetting model that has two fuel puddles [OG94, ORG97]. In such models a slow and a fast fuel puddle model are used to get good modelling at both low and high frequencies.

- **Structure of the gas mixing dynamics**: Studies done in ETH, Zürich, show that the gas mixing dynamics in the exhaust system behaves like a low-pass filter before

<table>
<tr><th>Test number</th><th>OVL (degrees)</th><th>IVO (° ATDC)</th><th>EVC (° ATDC)</th><th>P_m (kPa)</th><th>N (rpm)</th></tr>
<tr><td>1</td><td>15</td><td>-5</td><td>10</td><td>30</td><td rowspan="11">1500</td></tr>
<tr><td>2</td><td>0</td><td>-5</td><td>-5</td><td rowspan="5">40</td></tr>
<tr><td>3</td><td>15</td><td>-5</td><td>10</td></tr>
<tr><td>4</td><td>30_e</td><td>-5</td><td>25</td></tr>
<tr><td>5</td><td>30_i</td><td>-20</td><td>10</td></tr>
<tr><td>6</td><td>35</td><td>-25</td><td>10</td></tr>
<tr><td>7</td><td>0</td><td>-5</td><td>-5</td><td rowspan="5">60</td></tr>
<tr><td>8</td><td>15</td><td>-5</td><td>10</td></tr>
<tr><td>9</td><td>30_e</td><td>-5</td><td>25</td></tr>
<tr><td>10</td><td>30_i</td><td>-20</td><td>10</td></tr>
<tr><td>11</td><td>35</td><td>-25</td><td>10</td></tr>
</table>

Table 3.2 Operating points of the fuel path identification experiments

the lambda sensor [ORG97,ORSG98]. However, whether or not these dynamics vary with the operating point should be investigated together with the order of the filter.

- **Structure of the lambda sensor dynamics**: The order of the sensor transfer function and whether or not the dynamics vary with the operating point should be investigated.

Answers to these questions are sought through performing different types of identification experiments and analysing the empirical data. The operating points, at which the experiments are performed, are given in Table 3.2. The valve overlap is denoted as OVL in the table. At each operating point only the amount of fuel injection is varied in order to excite the fuel path. The valve timings are varied from no overlap to increased overlap values with different valve timing combinations. For example 30° of overlap can be achieved by either retarding EVC or advancing IVO. Both cases are included in the experiments and are labelled as 30_e for retarded EVC and 30_i for advanced IVO. Furthermore, the experiments are repeated at different manifold pressures to investigate the effect of the load in the fuel path as well as the effect of the VCT. Only one overlap timing is tested at $30kPa$, because it is not possible to increase the overlap further at very low loads without causing engine misfires.

Step responses of the fuel path dynamics are measured by exciting the fuel injectors with a square wave FPW. The peak to peak magnitude of the FPW is kept around 8 % of its nominal value to achieve local linearity in the input-output data. The AFR deviations are measured by a wide-range lambda sensor at the exhaust of cylinder 1. Moreover,

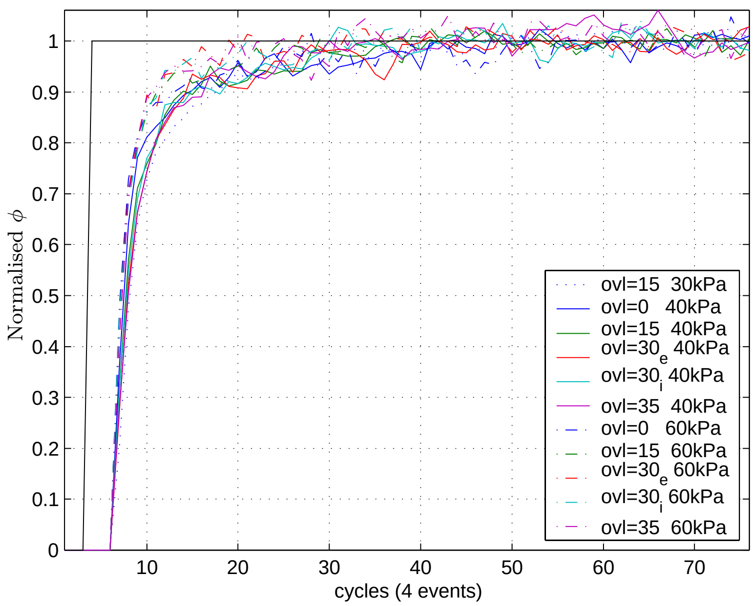

Figure 3.16 Normalised step responses of the fuel path

the data are averaged over many measurements to get a representative response. The normalised ϕ step responses are plotted in Figure 3.16, where each step response is an average of 26 steps. All the responses have second order over-damped characteristics with a delay as expected. The data show variations in step responses with operating point. It is observed that the speed of the response is dependent on both the manifold pressure and valve timings. For example, as the load increases the responses get faster.

Although step responses are useful to observe the low frequency characteristics of the system such as time delay, dominant time constant, rise and settling times, they do not contain much information about the higher frequency dynamics. An ideal excitation for a wide-range frequency identification is a sum of sinusoids [Lju99, p. 423]. Hence, further experiments are performed by exciting the fuel injectors with a sum of sinusoids FPW. Details of how to construct such an excitation signal are given in Appendix B. The measurements are taken by a wide-range lambda sensor after the confluence point of the exhaust runners, i.e. these measurements represent the mean behaviour of the four cylinders rather than just one. The measured frequency response of the fuel path at different operating points are given in Figure 3.17. The frequency responses are calculated via a Fourier analysis of the input-output data. It is seen that the magnitudes and phases of the responses have substantial variations at high frequencies ($> 0.1 rad/event$). As the MAP increases the response gets faster as evident from the decreasing phase, which is a direct result of the shorter transport delays at high manifold pressures. Moreover, the

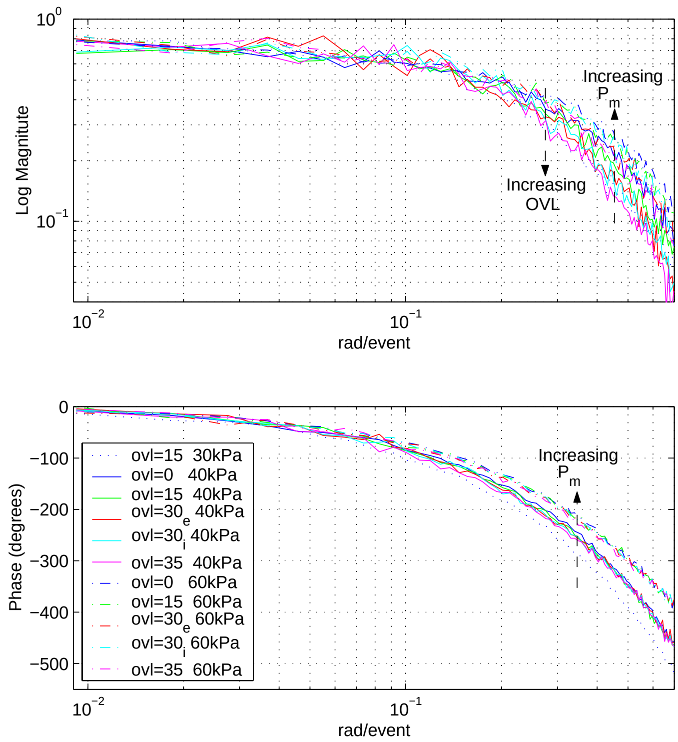

Figure 3.17 Identified frequency responses of the fuel path at different operating points

large overlaps reduce the system gain while increasing MAP amplifies it at high frequencies. Both the step responses and frequency responses show that the fuel path dynamics are strongly operating point dependent at both low and high frequencies.

The final data presented for the discussion of the model structure are given in Figure 3.18. It shows the lambda deviations measured at the exhaust of cylinder 1 when the AFR loop is excited by the IVO timing as in Figure 3.10. The dashed line shows the predicted normalised cylinder MAF by the model developed in Section 3.1.2. As discussed earlier the lambda response is opposite of what would be expected from the cylinder MAF, which can only be due to a significant and sudden change in the fuel puddle mass. This indicates that the wall-wetting dynamics governing this transient are as fast as the cylinder MAF dynamics.

The results of the 3 different tests have been presented above, each revealing different information at different frequency ranges. The variations in the step responses show that the low frequency dynamics of the fuel path are operating point dependent. This can be modelled as a slow fuel puddle that describes the variations in the settling times of the step responses. Moreover, the data also expose the variations in the mid and high frequency characteristics. This suggests parameter dependent models for the gas mixing and sensor

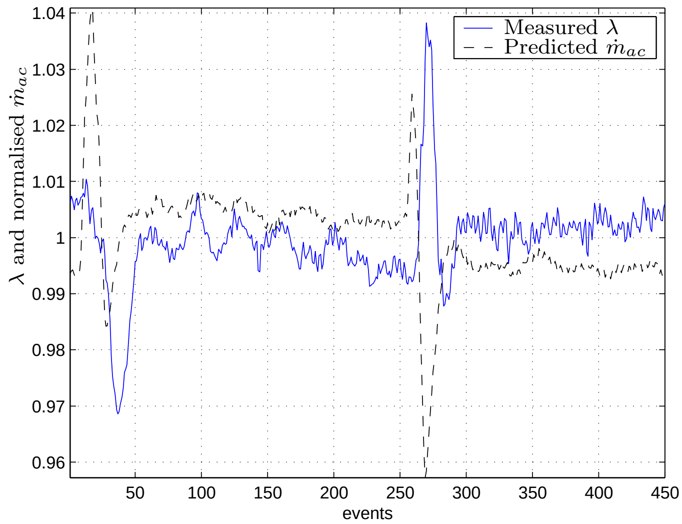

Figure 3.18 Measured lambda and predicted normalised cylinder MAF

dynamics. Figure 3.18 further indicates that the wall-wetting dynamics can be as fast as the cylinder MAF dynamics. This can be modelled with a fast fuel puddle model in the wall-wetting dynamics. Therefore, a model containing two fuel puddles is proposed for describing the wall-wetting dynamics in the event based discrete-time

$$G_{ww}(z) = \left(\frac{\mathcal{X}_s \tau_s}{z - (1 - \tau_s)} + \frac{\mathcal{X}_f \tau_f}{z - (1 - \tau_f)} + 1 - \mathcal{X}_s - \mathcal{X}_f \right), \tag{3.7}$$

where $\mathcal{X}_s$ and τ_s are the slow fuel puddle parameters, $\mathcal{X}_f$ and τ_f are the fast fuel puddle parameters and z is the shift operator in the event based discrete time. Note that this model satisfies the conservation of mass and has unity steady state gain.

Both the gas mixing and sensor dynamics are assumed to be parameter-varying first order transfer functions. Their combined dynamics are modelled as a single transfer function of second order

$$G_x(z) = \frac{1 + \xi_1 + \xi_2}{z^2 + \xi_1 z + \xi_2}, \tag{3.8}$$

where, ξ_1 and ξ_2 are operating point dependent coefficients. This can be interpreted as a second order parameter-varying filter with unity steady state gain.

The transport delay in the loop is modelled as a delay in the event based continuous-time domain, due to the time-varying nature of the transport delay with MAP

$$e^{-j\omega d T_s}, \tag{3.9}$$

where d is the delay in engine events and T_s is the sampling time in engine events. The injection delay at $1500rpm$ is assumed to be two engine events. The overall fuel path dynamics can be written as

$$G_{fp}(z) = g_0 G_x(z) G_{ww}(z) e^{-j\omega d T_s}, \tag{3.10}$$

where g_0 is a scalar constant, which allows for variations in the steady state gain of the model if necessary. This transfer function describes the fuel path dynamics from injectors to the measured equivalence ratio ϕ (not λ) when the cylinder MAF is constant and is suitable for linear identification. Moreover, this model describes the fuel path dynamics of a single cylinder but is only an approximation for the fuel path dynamics of a multi-cylinder engine since $G_{ww}(\cdot)$ does not include the multiplexing dynamics.

3.2.2 Local Linear or Global Identification

Since the dynamics of the fuel path are operating point dependent parameter-varying models will be identified. There are two different approaches that can be taken for the identification of the fuel path model.

- **Local linear identification**: The parameters of the model are identified at different operating points by exciting the injectors. The amplitude of the excitation is kept small to assure the linearity of the input-output data. Once the parameter sets are obtained for all of the operating range, each parameter set is described by a regression function of the some measurable parameters similar to what has been done for the air path dynamics. The main advantage of this approach is that linear identification methods are well-developed and easily applicable. However, there is no guarantee that the interpolation of the local identified dynamics will capture the global (nonlinear) behaviour of the real system.

- **Global identification**: This method requires assigning a structure to each parameter in the model beforehand. Once the model and parameter structures are chosen, the model parameters are identified in one step for the whole operating envelope. The quality of the identification data is crucial for the success of this method. Moreover, the data should also reflect the real operation of the system. Once good global data are captured, a nonlinear optimisation routine can be used in order to get the model parameters. The main difficulties of this approach are twofold. Firstly, one has to to guess the right structure for the parameter variations in the model. Secondly, one has to design the right experiment for collecting the appropriate identification data. Both of these problems require a good knowledge of the process to be identified, whereas most of the local identification methods can be applied without even assigning a model structure (black/gray box methods).

In a standard PFI engine without VCT, the wall-wetting parameters are identified by local linear identification methods [HVK+93, ST95, ORSG98]. In [HVK+93] the wall-wetting parameters are modelled as a function of the manifold temperature. In [ST95] the engine cooling temperature and engine speed are found to be the most important influences on $\mathcal{X}$ and τ. The difference between identifying a local linear model and a global model for the wall-wetting dynamics is discussed in [SLOG00], where numerical integration of the local fuel puddle parameters is employed to get a global model of the wall-wetting dynamics (Interpolation of the local parameters is not suggested for recovering the global behaviour in this study).

A mixed approach is taken in this thesis: the dynamics of the gas mixing, lambda sensor and delay are identified through the local linear methods, since only the variation of linear dynamics are required. On the other hand, a global identification method is preferred for identifying the wall-wetting dynamics for which not only linear dynamics but also nonlinear effects such as the variation of the fuel puddle mass with the valve timings are required to be modelled. An Aquino type model capturing the variation in the fuel puddle size when m_{fi} is constant will be used. For simplicity consider the first order Aquino model (3.5)-(3.6) at steady state

$$m_{ff} = (1-\tau)m_{ff} + \mathcal{X}m_{fi},$$

which implies that

$$m_{ff} = \frac{\mathcal{X}}{\tau}m_{fi} \tag{3.11}$$

This means that when m_{fi} is constant the fuel film mass m_{ff} will only change through $\mathcal{X}$ and τ in the model. Although it is not expected that this model will predict the real value of the fuel film mass, it can certainly simulate the behaviour of the fuel film under VCT disturbances if the correct variations of $\mathcal{X}$ and τ with respect to the valve timings can be identified. According to the author's experience, this is a hard and tricky task if the local linear identification methods are used. However with the right global identification scheme a satisfactory model describing the variations of the wall-wetting parameters with respect to VCT can be obtained. This will be presented later on in Section 3.2.5.

3.2.3 Delay, Gas Mixing and Sensor Dynamics

The frequency response data of Figure 3.17 are used for the identification of the delay, gas mixing and sensor dynamics. Since the data describe the frequency response of the complete full path, the model (3.10) is used in the identification. A nonlinear least squares optimisation routine is employed to minimise the difference between the measured complex frequency response and the one predicted by the model (3.10). The identification cost is defined as

$$\min_{\Theta} \sum_{w=\pi/\mathcal{T}_M}^{\pi/\mathcal{T}_m} \left[(\mathcal{D}(e^{jwT_s}) - G_{fp}(e^{jwT_s}))F(e^{jwT_s}) \right]^2 \tag{3.12}$$

where $\Theta = [\mathcal{X}_s, \tau_s, \mathcal{X}_f, \tau_f, \xi_1, \xi_2, d, g_o]^T$ is the parameter vector, $\mathcal{T}_M$ and $\mathcal{T}_m$ are the longest and shortest period of the sinusoidal present in the input excitation signal, $\mathcal{D}(e^{j\omega T_s})$ is the measured frequency response data and $F(z)$ is a frequency weighting function. $F(z)$ is chosen such that the errors at frequencies larger than $0.1 rad/event$ are penalised more severely in the cost. The parameter vector Θ is identified for the 11 different operating points shown in Table 3.2. Figure 3.19 shows the predictions of the identified models at two different operating points. In both cases the measured responses are predicted with good accuracy especially at high frequencies as dictated by $F(z)$. The corresponding time domain responses are depicted in Figure 3.20, in which the difference between the actual

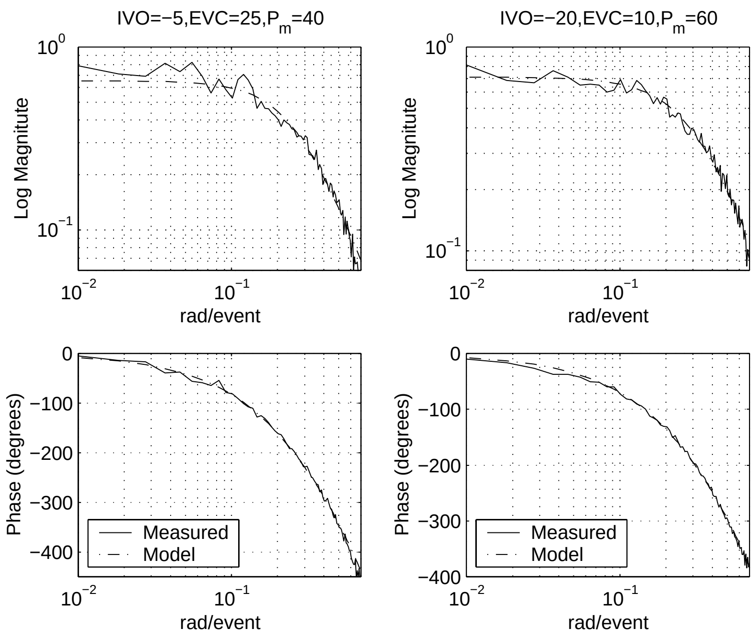

Figure 3.19 Measured and predicted frequency responses at two different operating points

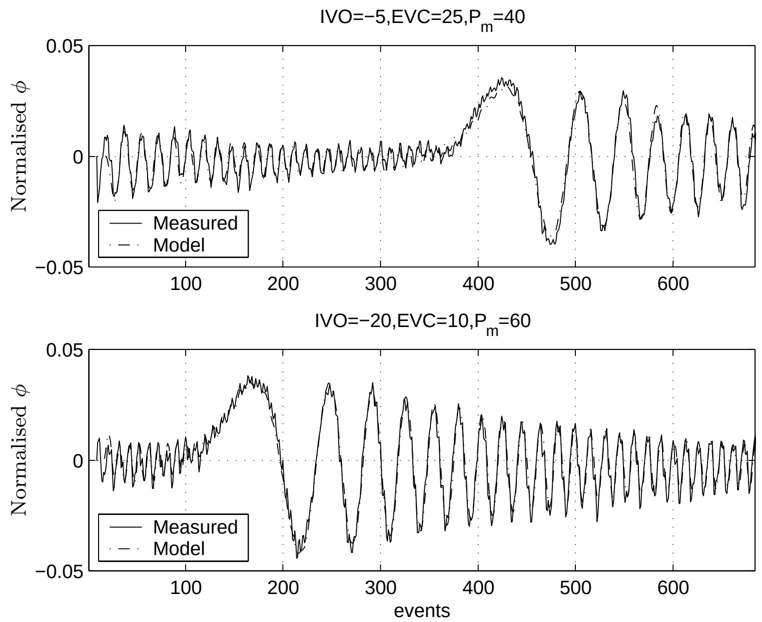

Figure 3.20 Measured and predicted time responses at two different operating points

responses and the predicted ones are hardly noticeable. One implication of the good fit in the time responses is that the input-output data is indeed linear in a local sense. Above results show that the proposed model (3.10) is adequate and can capture the local dynamics precisely. Next the identified parameters of the model will be presented.

Transport Delay

The identified values of the transport delay are plotted against the MAP and valve overlap in Figure 3.21. The transport delay strongly depends on the MAP, because as the pressure increases the speed of the flow in the exhaust system increases, and this shortens the transport delay. A slight dependence on the OVL can also be seen in the figure: as the overlap increases the transport delay decreases. Therefore the transport delay is modelled as an affine function of the MAP and OVL

$$d(k) = l_{0_d} + l_{1_d} P_m(k) + l_{2_d} OVL(k), \tag{3.13}$$

which defines the surface plotted in Figure 3.21. The modelled surface predicts the measured values with a worst case error no more than 5.4 %.

Gas mixing and Sensor Dynamics

The identified parameters of the second order transfer function,

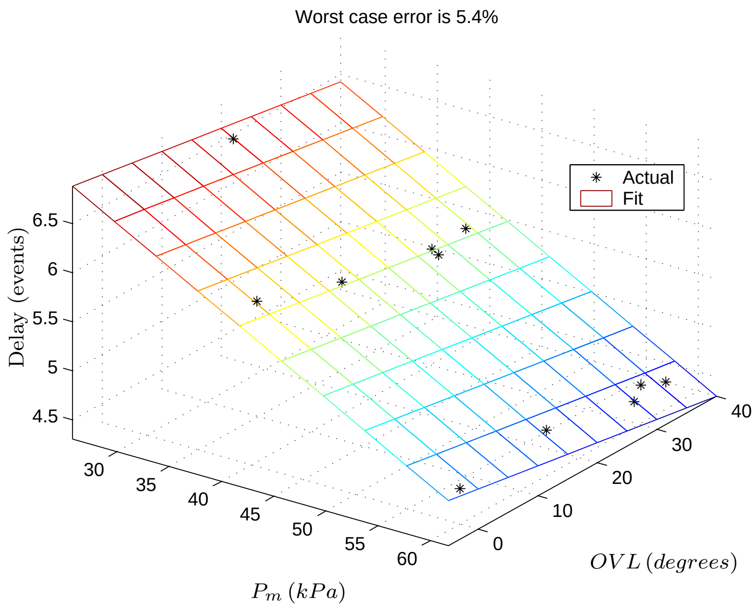

Figure 3.21 Variation of the transport delay with valve overlap and manifold pressure

$$G_x(z) = \frac{1+\xi_1+\xi_2}{z^2+\xi_1 z+\xi_2}$$

describing the gas mixing and sensor dynamics are presented in Figure 3.22 and Figure 3.23. The identified parameters ξ_1 and ξ_2 are modelled as affine functions of the MAP and OVL

$$\begin{aligned} \xi_1 &= l_{10_x} + l_{11_x} P_m(k) + l_{12_x} OVL(k), \\ \xi_2 &= l_{20_x} + l_{21_x} P_m(k) + l_{22_x} OVL(k). \end{aligned} \tag{3.14}$$

The significance of the variations in the parameters can be interpreted by analysing the change in the pole locations of $G_x(\cdot)$ with respect to the MAP and OVL. The modelled surfaces show that increasing the MAP increases ξ_1 but decreases ξ_2. Such a change in ξ_1 and ξ_2 moves the poles closer to the origin as shown in Table 3.3. This also increases the system gain at high frequencies because in a discrete-time system dynamics become faster as the poles move closer to the origin. On the other hand, increasing the OVL, which reduces the value of ξ_1 but increases the value of ξ_2, moves the poles closer to the unit circle as shown in Table 3.4. This in turn reduces the system gain and increases the phase of the system. All these predictions of the identified parameter varying model agree well with the highlighted trends presented in Figure 3.17.

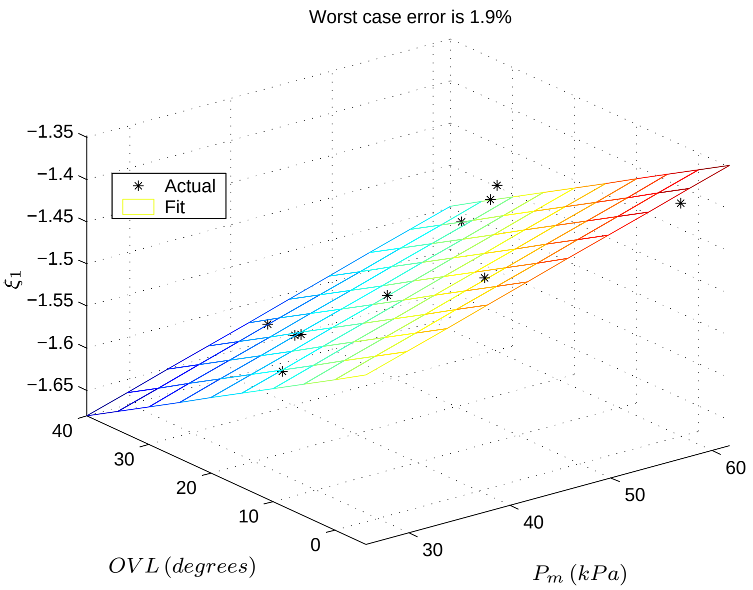

Figure 3.22 Variation of ξ_1 with the valve overlap and manifold pressure

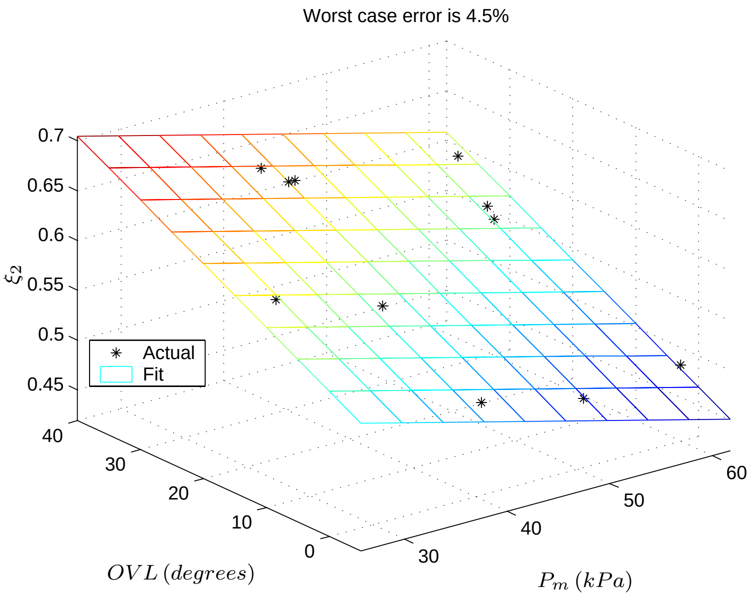

Figure 3.23 Variation of ξ_2 with the valve overlap and manifold pressure

P_m	OVL	Pole Locations
40	15	$\lvert 0.7582 \pm j0.0654 \rvert = 0.7610$
50	15	$\lvert 0.7399 \pm j0.0702 \rvert = 0.7432$
60	15	$\lvert 0.7216 \pm j0.0701 \rvert = 0.7250$

Table 3.3 Variation of the poles of G_x with the manifold pressure

P_m	OVL	Pole Locations
50	0	$\lvert 0.7064 \pm j0.0307 \rvert = 0.7071$
50	15	$\lvert 0.7399 \pm j0.0702 \rvert = 0.7432$
50	30	$\lvert 0.7734 \pm j0.0817 \rvert = 0.7777$

Table 3.4 Variation of the poles of G_x with the valve timings

3.2.4 Injector Calibration

So far the fuel path dynamics have been identified independent of the air path dynamics since the cylinder MAF is kept constant during the engine tests. However, global identification of the wall-wetting dynamics requires designing experiments during which not only the fuel flow but also the air flow changes significantly. Under varying cylinder MAF conditions the measured ϕ,

$$\phi_c = \frac{m_{fc}}{m_{ac}},$$

depends on both m_{fc} and m_{ac}, where ϕ_c refers to the in-cylinder ϕ rather than its exhaust value ϕ_x. In order to predict ϕ_c and ϕ_x not only the input FPW but also the amount of fuel injected m_{fi} is required. This subsection aims at developing a relationship between the FPW and m_{fi}.

One way of calibrating the injectors is to perform steady state engine tests. Different manifold pressures are visited at $\lambda = 1$ and the corresponding values of the throttle MAF and input FPW are recorded. They are plotted in the left column of Figure 3.24. There is an affine relationship between FPW and the throttle MAF. This can be used to get another affine relationship from the FPW to the injected fuel flow m_{fi} because at steady state and unity lambda, $\dot{m}_{at} = \dot{m}_{ac} \approx 14.6\dot{m}_{fi}$. The right column of Figure 3.24 shows this affine relationship between FPW and $\dot{m}_{fi}$. Therefore the following affine models are both valid:

$$\dot{m}_{fi} = l_{10_i} + l_{11_i} FPW, \tag{3.15}$$

$$m_{ac_F} = l_{20_i} + l_{21_i} \dot{m}_{ac}. \tag{3.16}$$

The second equality above is the affine relationship shown on the left column of Figure 3.24. It describes the conversion from $\dot{m}_{ac}$ in grams per seconds to m_{ac_F} in micro seconds.

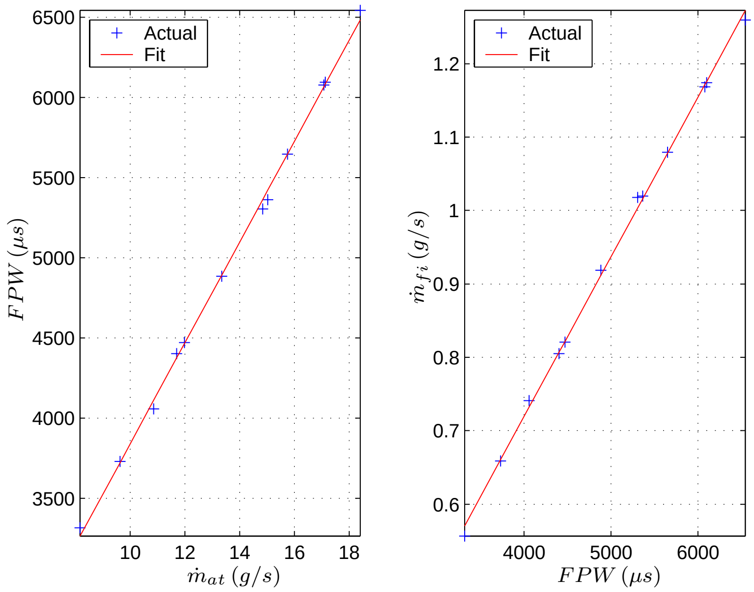

Figure 3.24 Injector calibration data

Both of these conversions are valid for the calibration of the injectors since AFR is a dimensionless number. In the rest of this thesis m_{ac_F} will be used in order to calculate estimates of ϕ or λ.

3.2.5 Wall-Wetting Dynamics

The calibration of the injectors completes the identification of the AFR path model apart from the wall-wetting dynamics. It has already been shown in (3.11) that the variation of the fuel puddle mass with VCT can be modelled if the relative variation of $\mathcal{X}$ and τ with respect to each other can be identified during the VCT transients.

Recall that $\mathcal{X}$ and τ parameters of the slow and fast fuel puddles have already been identified for different valve timings in Section 3.2.3 as they are part of the parameter vector Θ in optimisation (3.12). Unfortunately, the interpolation of the wall-wetting parameters obtained by the local linear identification method fails to predict the variations in the fuel film mass, even though the models predict the local linear behaviour very well, as shown in Figures 3.19 and 3.20. Therefore, a global identification scheme is proposed in the following to model the wall-wetting dynamics and variations in the fuel film mass.

The proposed framework for the global identification scheme is depicted in Figure 3.25, in which the complete AFR path model is used. The inputs to the model are the FPW, IVO, EVC and MAP, and the output is the equivalence ratio at the exhaust measured by the lambda sensor. Once the appropriate input-output data are collected, the nonlinear

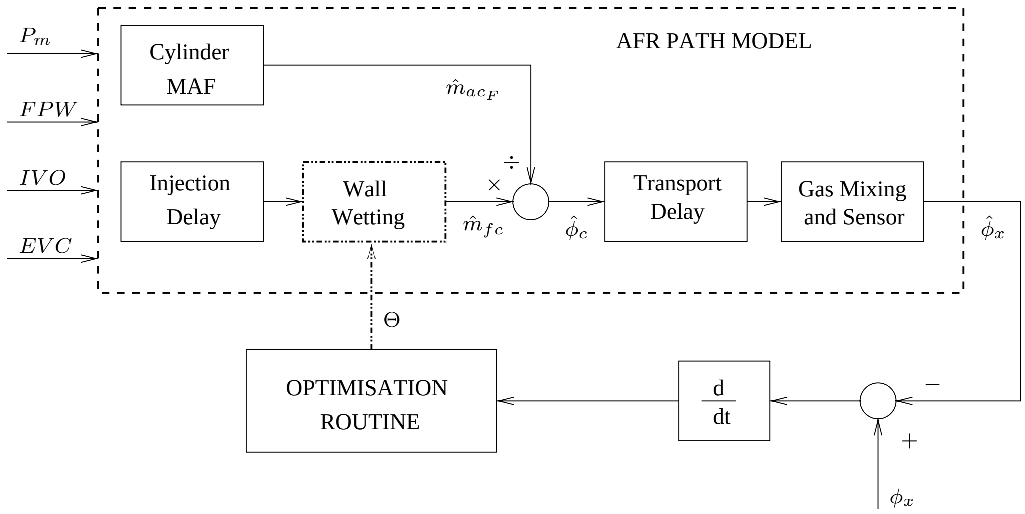

Figure 3.25 Global identification framework for wall-wetting dynamics

optimisation routine calculates the parameters of the wall-wetting model to minimise the identification cost (recall that the rest of the model have already been identified). The parameterisation of the wall-wetting transfer function

$$G_{ww}(z) = \left(\frac{\mathcal{X}_s \tau_s}{z - (1 - \tau_s)} + \frac{\mathcal{X}_f \tau_f}{z - (1 - \tau_f)} + 1 - \mathcal{X}_s - \mathcal{X}_f \right)$$

has to be determined in order to proceed with the identification process. After a few trials the following parameterisation, which is inspired by the empirical data, is found to be satisfactory

$$\begin{aligned} \tau_s &= l_{10_s} + l_{11_s} P_m \\ \mathcal{X}_s &= l_{20_s} + l_{21_s} P_m \\ \tau_f &= l_{10_f} + l_{12_f} EVC + l_{13_f} IVO \\ \mathcal{X}_f &= l_{20_f} + l_{22_f} EVC + l_{23_f} IVO \end{aligned} \tag{3.17}$$

Since it has been observed that there is a fast variation in the fuel film mass with the valve timings not with the manifold pressure, the fast fuel puddle parameters are modelled as functions of EVC and IVO. On the other hand, since no such variations are observed for the slow fuel puddle under VCT transients, its parameters are modelled as functions of the manifold pressure instead. This is because the manifold pressure is an indicator of the engine load and known to affect the fuel film evaporation rate.

The global identification framework is implemented in MATLAB/Simulink environment, which requires realisation of the parameter-varying transfer functions $G_{ww}(z)$ and

$G_x(z)$ in the state-space form. The next subsection discusses the details of how a realisation of a parameter-varying transfer function may affect the input-output behaviour of the system.

State-Space Realisation of the Parameter-Varying Transfer Functions

There are two parameter-varying (PV) transfer functions in the AFR path model. The PV wall-wetting model is to be identified and the PV gas mixing and sensor model has already been identified. During this study it is noticed that a PV system has an interesting property due its time-varying nature, i.e. the ability to change its output even if the input excitation is constant. This property is useful and desirable in the case of modelling the wall-wetting dynamics, for which the fuel flow out of the film changes even if the injected fuel is constant due to the varying valve timings. However, such a change of the output value when the input signal is constant is not desirable for the gas mixing and sensor dynamics. The underlying principles of the system and observations show that the sensor output signal should only change when the input signal changes, or at least this is the desired operation of the sensor. Therefore care has to be taken when obtaining a state-space realisation of the gas mixing and sensor model. The following realisation of $G_x(z)$ satisfy the desired properties, i.e. its output only changes when the input changes.

$$\begin{aligned} G_x(z) &= \frac{1+\xi_1+\xi_2}{z^2+\xi_1 z+\xi_2} \\ &= \left[\begin{array}{c|c} A_x(\xi) & B_x(\xi) \\ \hline C_x & 0 \end{array}\right] \\ &= \left[\begin{array}{cc|c} 0 & 1 & 0 \\ -\xi_2 & -\xi_1 & 1+\xi_1+\xi_2 \\ \hline 1 & 0 & 0 \end{array}\right]. \end{aligned} \tag{3.18}$$

This can be seen by the fact that the matrix product $(I - A_x(\xi))^{-1}B_x(\xi)$ and the steady state output Y_{ss}

$$Y_{ss} = C_x(I - A_x(\xi))^{-1}B_x(\xi)U_{ss}$$

are independent of ξ.

On the other hand, the wall-wetting transfer function can be realised as

$$G_{ww}(z) = \left[\begin{array}{cc|c} 1-\tau_s & 0 & \mathcal{X}_s \\ 0 & 1-\tau_f & \mathcal{X}_f \\ \hline \tau_s & \tau_f & 1-\mathcal{X}_s-\mathcal{X}_f \end{array}\right], \tag{3.19}$$

where the states of the realisation represent the fuel film masses. Furthermore, for a 4-cylinder engine with identical wall-wetting dynamics at each port, the state-space realisation with the multiplexing effect takes the form

$$G_{ww}(z) = \left[\begin{array}{cccc|c} 0 & 1-\tau_s & 0 & 0 & \mathcal{X}_s \\ I_3 & 0 & 0 & 0 & 0 \\ 0 & 0 & 0 & 1-\tau_f & \mathcal{X}_f \\ 0 & 0 & I_3 & 0 & 0 \\ \hline 0 & \tau_s & 0 & \tau_f & 1-\mathcal{X}_s-\mathcal{X}_f \end{array}\right]. \tag{3.20}$$

In this realisation the states 1 through 4 represent the four slow fuel puddle masses and the states 5 through 8 represent the four fast fuel puddle masses. Both the single or 4-cylinder state-space realisations have their outputs m_{fc} changing under the parameter variations even if the input fuel flow is constant.

Identification Algorithm

The natural error for the identification scheme may be the difference between the actual equivalence ratio and the predicted equivalence ratio, yet such a choice tries to optimise the steady state accuracy as well as the transient accuracy. Since the transient accuracy is what is required to model the fast fuel film variations under rapid VCT disturbances, the error is defined as the derivative of the difference between the actual equivalence ratio and the predicted equivalence ratio. Hence the identification cost can be written as

$$\epsilon^T \epsilon = \left[\frac{d}{dt}(\underline{\phi}_x - \hat{\underline{\phi}}_x)\right]^T \left[\frac{d}{dt}(\underline{\phi}_x - \hat{\underline{\phi}}_x)\right] \tag{3.21}$$

where $\underline{\phi}_x$ is the measured equivalence ratio vector, $\hat{\underline{\phi}}_x$ is the predicted equivalence ratio vector and $\frac{d}{dt}$ is the derivative operator in the event based discrete-time domain.

It is important that the identified dynamics are stable. This can be assured by putting simple constraints on the poles of $G_{ww}(z)$ such as

$$|1-\tau_s| < 1 \text{ and } |1-\tau_f| < 1.$$

However, the locations of the zeros of the wall-wetting model are also very important. The identified PV wall-wetting model must be invertible, i.e. all of its zeros must be inside the unit circle in z-domain, since the feedforward controller design for the AFR control usually involves inverting the wall-wetting transfer function. The zeros of $G_{ww}(z)$ are given by the roots of the following quadratic in z

$$\begin{aligned} N_{ww}(z) =& (1-\mathcal{X}_s-\mathcal{X}_f)z^2 + [-2(1-\mathcal{X}_s-\mathcal{X}_f) + \tau_s(1-\mathcal{X}_f) + \tau_f(1-\mathcal{X}_s)]\, z \\ &+ [(1-\mathcal{X}_s-\mathcal{X}_f) - \tau_s(1-\mathcal{X}_f) - \tau_f(1-\mathcal{X}_s) + \tau_s\tau_f] \end{aligned} \tag{3.22}$$

The root locations of this quadratic in z-domain can be checked by Jury's stability test [Oga87], which states that for a quadratic of the form

$$N(z) = n_0 z^2 + n_1 z + n_2$$

all the roots of $N(z)$ are inside the unit circle in z-domain, if the following conditions hold

$$\begin{aligned}
&|n_2| < |n_0| \\
&N(1) > 0 \\
&N(-1) > 0.
\end{aligned} \tag{3.23}$$

Considering all the above requirements the identification objective can be written as

$$\begin{gathered}
\min_{\Theta} \left[\frac{d}{dt}(\underline{\phi}_x - \hat{\underline{\phi}}_x)\right]^T \left[\frac{d}{dt}(\underline{\phi}_x - \hat{\underline{\phi}}_x)\right] \\
\text{subject to} \\
0 < \tau_s < 1, \quad 0 < \mathcal{X}_s < 1, \\
0 < \tau_f < 1, \quad 0 < \mathcal{X}_f < 1, \\
-\tau_f(1 - \mathcal{X}_s) - \tau_s(1 - \mathcal{X}_f) + \tau_s\tau_f < 0, \\
[-2(1 - \mathcal{X}_s - \mathcal{X}_f) + \tau_s(1 - \mathcal{X}_f) + \tau_f(1 - \mathcal{X}_s)] - \tau_s\tau_f < 0,
\end{gathered} \tag{3.24}$$

where $\Theta = [l_{10_s}\, l_{11_s}\, l_{20_s}\, l_{21_s}\, l_{10_f}\, l_{12_f}\, l_{13_f}\, l_{20_f}\, l_{22_f}\, l_{23_f}]^T$ is the parameter vector and the last two constraints are derived from (3.23). In its above form this identification objective can be solved by a nonlinear least squares algorithm whenever the identification data are available.

Global Data

The identification data are collected via an experiment designed to cover the relevant operating envelope of the TI-VCT engine at 1500 rpm. The experiment is repeated 3 times and the mean responses are presented in the following. Figure 3.26 shows both the excitation signals and measured variables, where the lambda measurements are taken after the confluence point of the exhaust runners. The trajectories of the input signals TP, FPW, IVO and EVC are predetermined. In particular the TP and FPW are synchronised to keep the lambda at around unity during the experiment. Moreover the TP excitation is chosen as a staircase signal to cover the manifold pressures from $40kPa$ to $60kPa$. At each TP step, IVO and EVC are moved through a series of steps consecutively to simulate the VCT transients likely to occur during the real operation of the engine. First the IVO is moved aggressively to change the overlap, while the EVC is kept constant at 10° ATDC. Following this the IVO is fixed at −5° ATDC, and the EVC is moved rapidly through a series of steps. As observed in the lambda trace these trajectories cause significant transient deviations (up to 6 %) in the exhaust AFR, as intended, and cover most of the engine operating envelope. Since the lambda measurements are of 4 cylinders, the multiplexing model of the wall-wetting dynamics (3.20) is used in the optimisation cost.

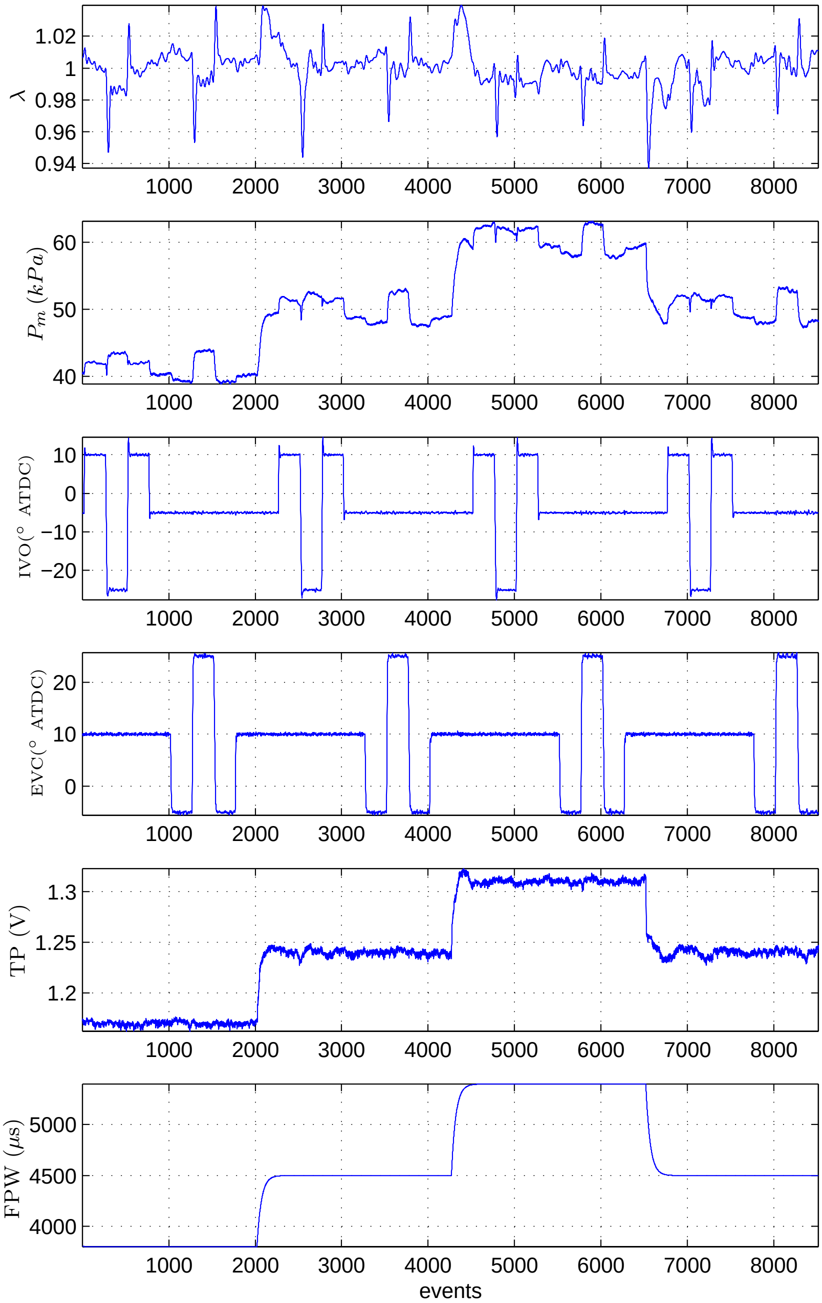

Figure 3.26 Global data for the identification of the wall-wetting dynamics

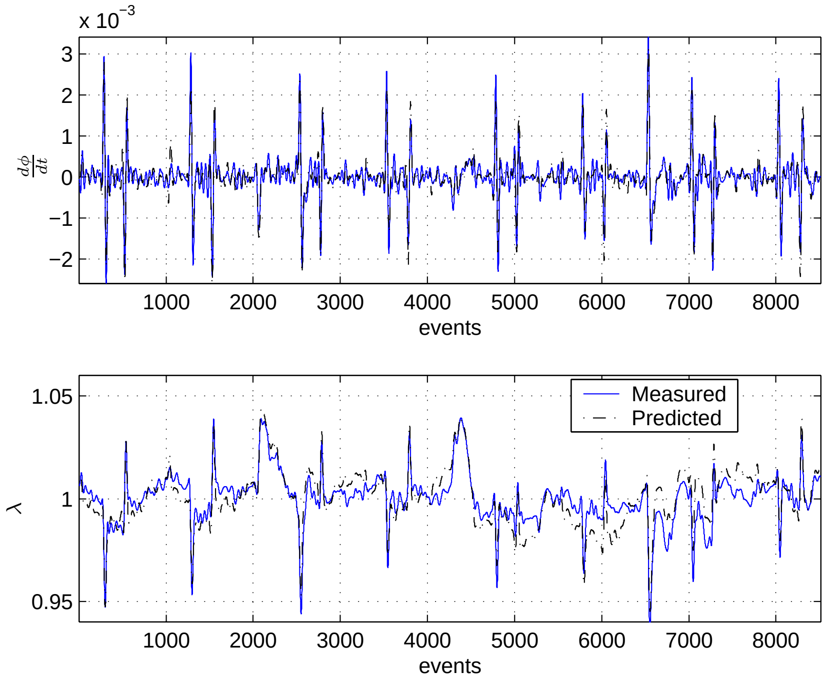

Figure 3.27 Measured and predicted trajectories of the $\frac{d\phi}{dt}$ and lambda

Results

The proposed global identification scheme is implemented with the data presented above and its results are discussed in the following. Figure 3.27 shows the actual $\frac{d}{dt}\phi$ and lambda traces together with their predicted values by the identified global model. From the top plot it is clear that only the significant transients are penalised in the identification error. This allows good modelling of the transient behaviour of the system while tolerating the errors in the slow dynamics since a feedback scheme can compensate for the modelling errors in the slow dynamics with ease. Furthermore, a good fit of the model predictions for both the $\frac{d}{dt}\phi$ and lambda is an evidence of a successful identification of the system dynamics by the proposed algorithm.

The identified trajectories of the fast fuel puddle parameters are plotted in Figure 3.28. The top two traces depict the identified $\mathcal{X}_f$ and τ_f. It is observed in these two traces that not only the IVO timing but also the EVC timing significantly affect the fast fuel parameters. However, the inspection of the predicted m_{fc} trace (third row in the figure) reveals that only the IVO transients cause large spikes in the m_{fc} around its nominal value. These spikes around the nominal fuel injection value are indications of the variations in the fuel puddle size caused by the VCT transients. Thus the identified fast fuel puddle parameters predict the previously observed phenomena in Chapter 2, i.e. although both

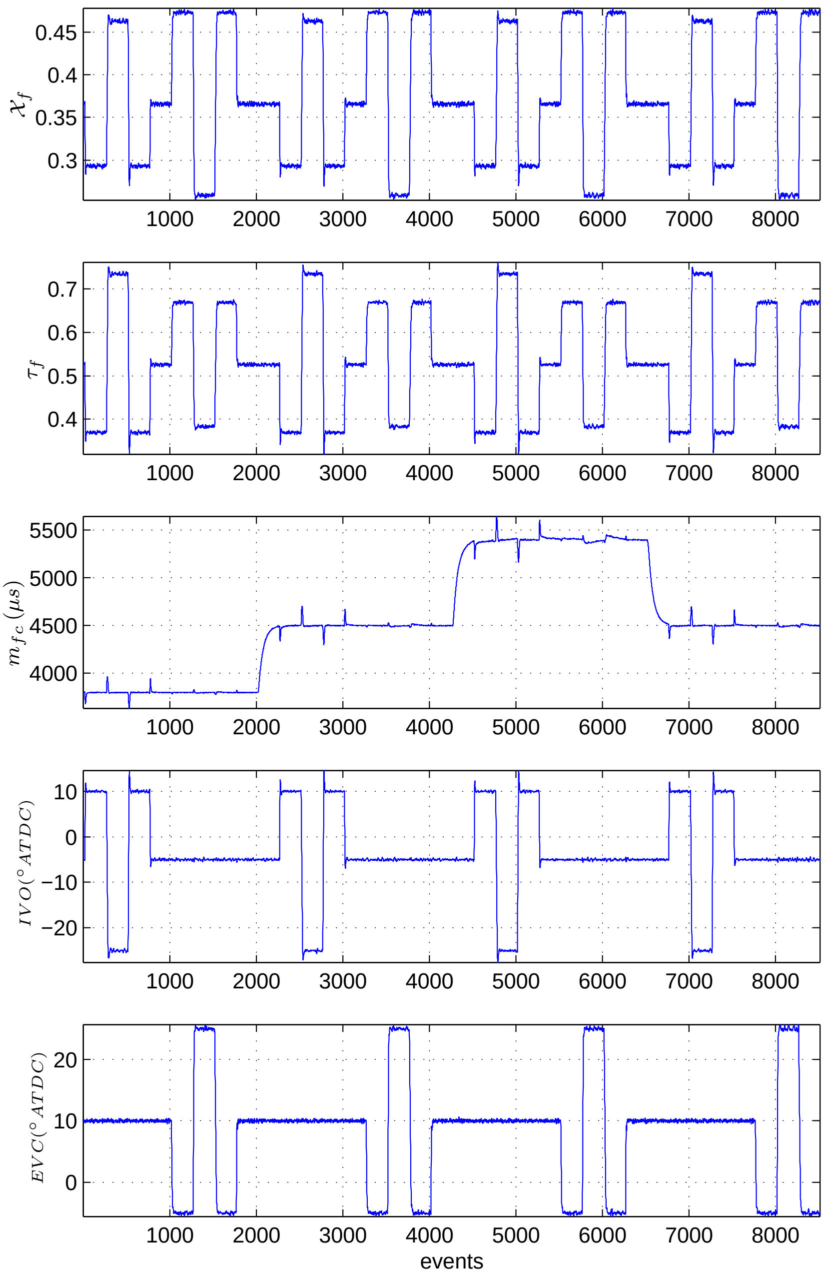

Figure 3.28 Identified trajectories of the fast fuel puddle parameters

IVO and EVC transients cause AFR deviations, only the IVO transients have a significant effect on the fuel film size. Note that there are also some tiny spikes caused by the EVC in the m_{fc} trace, yet they are almost negligible compare to the IVO induced spikes.

The identified parameter surfaces of the fast fuel puddle are given in Figures 3.29 and 3.30, which expose the variations in $\mathcal{X}_f$ and τ_f with respect to the valve timings. Both parameter surfaces have the same trends: retarding the EVC makes the parameters smaller, whereas advancing the IVO makes the parameters larger.

The above results are very convincing in the sense that the identified model can capture the observed fast fuel puddle dynamics, but it is not yet clear why only the parameter variations caused by IVO change the m_{fc} in the model. The answer to this question is hidden in (3.11), which suggests that the fuel puddle mass is proportional to $\frac{\mathcal{X}_f}{\tau_f}$ at steady state. This ratio is plotted in Figure 3.31 for further investigation. The large variations in the $\frac{\mathcal{X}_f}{\tau_f}$ are seen under the IVO excitation but the variations under the EVC excitation are much smaller. This explains why the IVO excitation causes significant transients in the predicted m_{fc} trace. Moreover, Figure 3.31 hints that the identified model captures the variations in the fuel film size by shaping the $\frac{\mathcal{X}_f}{\tau_f}$ ratio rather than the individual values of $\mathcal{X}_f$ and τ_f. The relationship between the $\frac{\mathcal{X}_f}{\tau_f}$ and fuel film size is further evident when the m_{fc} trace in Figure 3.28 is compared with the $\frac{\mathcal{X}_f}{\tau_f}$ trace in Figure 3.31. It shows that any positive (negative) step in the $\frac{\mathcal{X}_f}{\tau_f}$ cause a negative (positive) spike in the m_{fc} trace as expected.

The identified trajectories of the slow fuel puddle parameters are shown in Figure 3.32. It shows that the parameter variations in the slow fuel puddle model are much smaller than the parameter variations in the fast fuel puddle model. Although the slow fuel parameters are inversely proportional with the manifold pressure, they do not affect the m_{fc}, but tiny deviations in m_{fc} can be seen at high loads around event 6000.

The identified values of the $\mathcal{X}_s$ and τ_s with respect to the manifold pressure are plotted in Figure 3.33. It shows that both parameters are inversely proportional with MAP. The inverse proportionality of the evaporation constant with the MAP agrees with the physical fact that the evaporation is helped by lower pressures [SLOG00].

Finally, the zeros of the identified PV wall-wetting transfer function (of a single cylinder) are plotted in Figure 3.34. The zeros of the PV transfer function always stay in the unit circle as constrained by the optimisation scheme. This ensures that the PV transfer function remains invertible over all of the operating envelope. Therefore a feedforward control scheme can easily be designed by inverting the identified PV wall-wetting model.

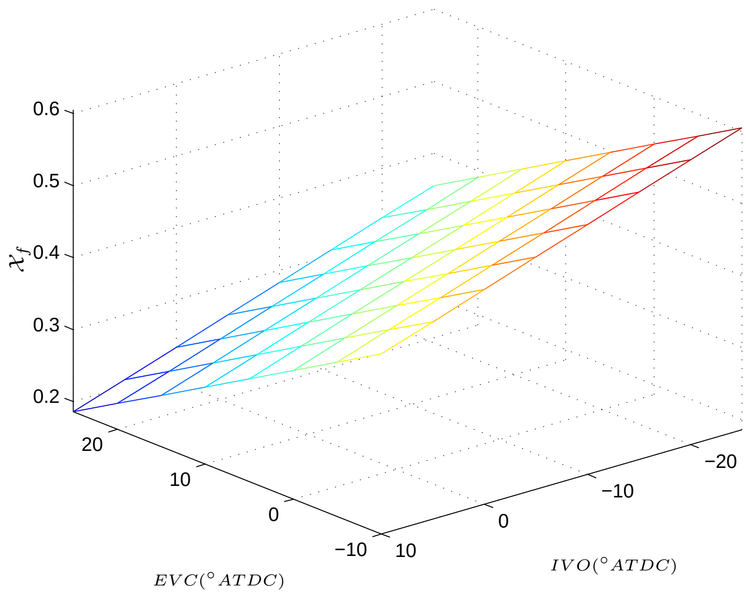

Figure 3.29 Variation of $\mathcal{X}_f$ with the valve timings

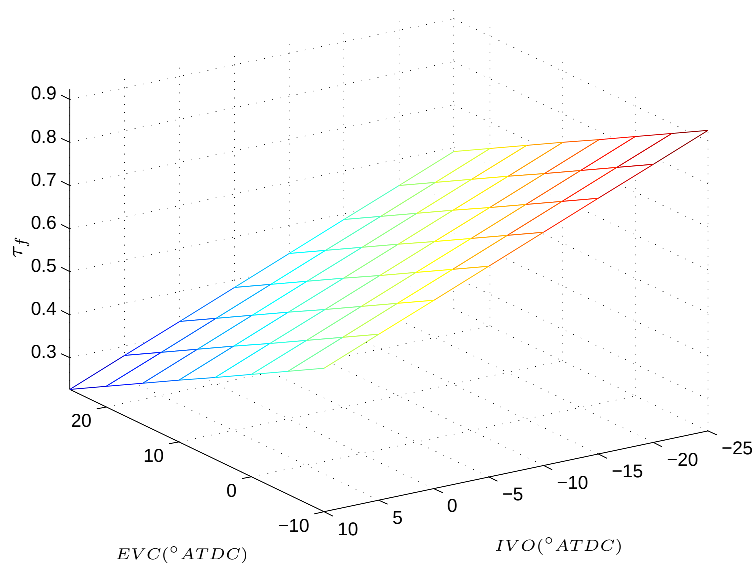

Figure 3.30 Variation of τ_f with the valve timings

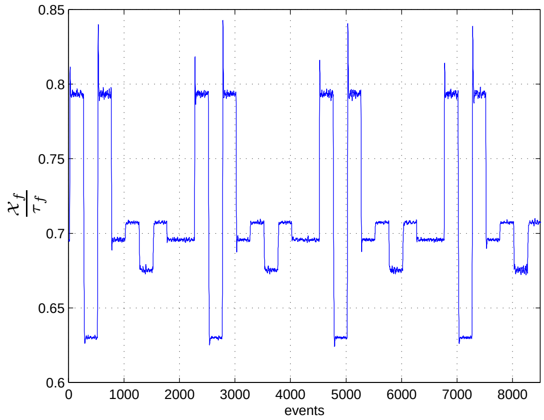

Figure 3.31 Variation of $\frac{\mathcal{X}_f}{\tau_f}$ during the identification experiment

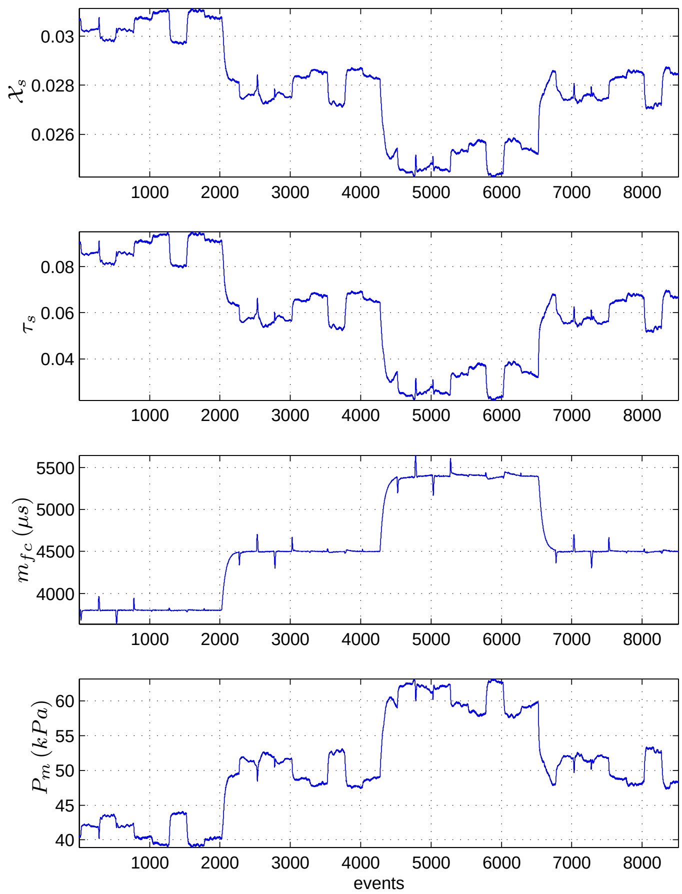

Figure 3.32 Identified trajectories of the slow fuel puddle

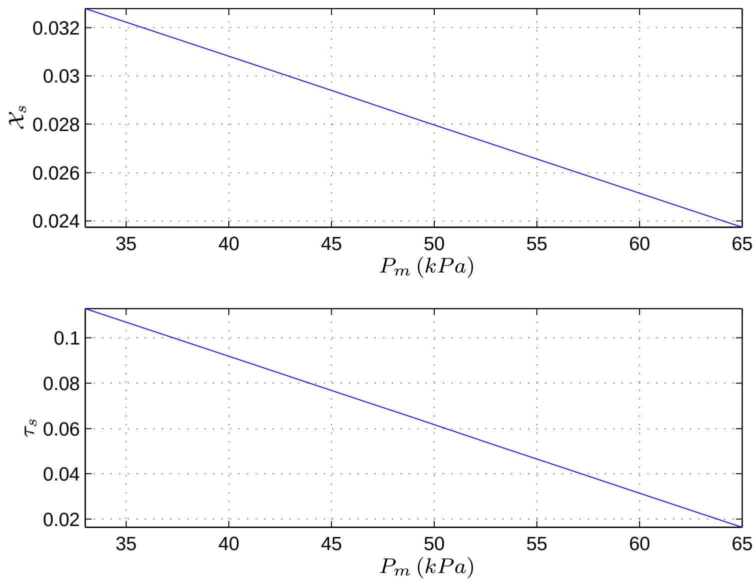

Figure 3.33 Variation of $\mathcal{X}_s$ and τ_s with the manifold pressure

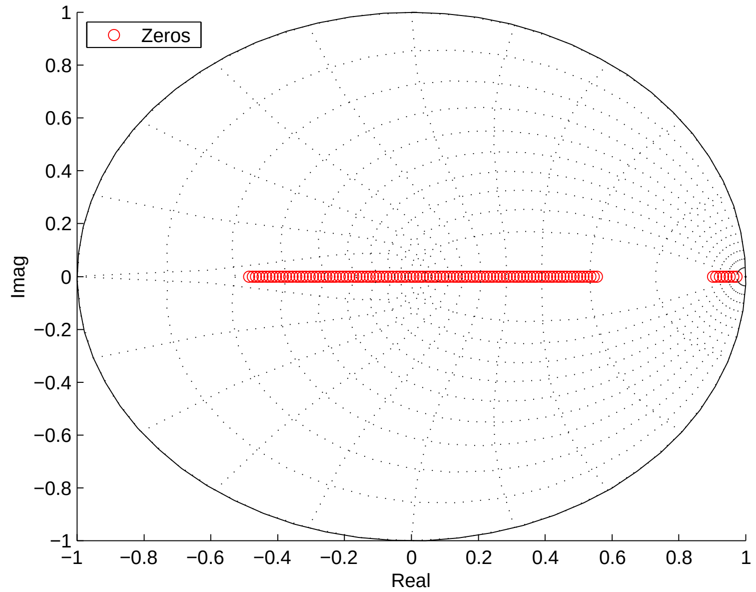

Figure 3.34 Zeros of $G_{ww}(z)$

3.3 Transient Validation of the AFR Model

Validation is defined as a process of determining how well one system replicates the properties of some other system or, more generally, any comparison between the representation of a system and some specified criteria.[1] The validation of a model cannot be separated from the purpose for which it is designed and used. This section validates the identified AFR path model under the VCT and FPW transients at constant MAP.

EVC Excitation

In common with previous tests, the valve timings are excited with a square wave reference signal in order to facilitate a higher signal-to-noise ratio in the data. For the first validation test the EVC timing is excited between $-5°$ and $25°$ at around $60kPa$. The top plot of Figure 3.35 shows:

- the measured λ,
- the predicted λ,
- the normalised predicted cylinder MAF m_{ac},
- the inverse of the normalised predicted cylinder fuel flow m_{fc}^{-1}.

The inverse of the m_{fc} is plotted in order to see its effect on the λ directly. As the EVC is retarded the predicted m_{ac} goes through a large negative transient, i.e. negative (positive) in the sense that it would cause a rich (lean) spike in the lambda signal. At the same time the predicted m_{fc}^{-1} follows a smooth tiny positive transient, slightly negative at first. A positive (negative) transient in the m_{fc}^{-1} trace means less (more) fuel leaves the fuel film. When the EVC is advanced, the m_{ac} goes through a positive spike, while the m_{fc}^{-1} follows a slow negative bump. The final predicted λ, after going through the identified delay, gas mixing and sensor dynamics, fits well with the measured λ. Hence, the model can predict the fact that the fuel film size does not change, although the $\mathcal{X}_f$ and τ_f change significantly. On the other hand, variations in the slow fuel puddle parameters cause smooth transients in the m_{fc}^{-1}. This complements the predicted m_{ac} response to increase the fitting of the predicted λ when the response is settling down. This can be considered as another supporting evidence for a slow fuel puddle in the wall-wetting dynamics.

IVO Excitation

Another validation experiment is performed to test the model's predictions under the IVO excitation. Figure 3.36 shows the measured and predicted parameters of the model. The

[1]Web Dictionary of Cybernetics and Systems, http://pespmc1.vub.ac.be/ASC/indexASC.html

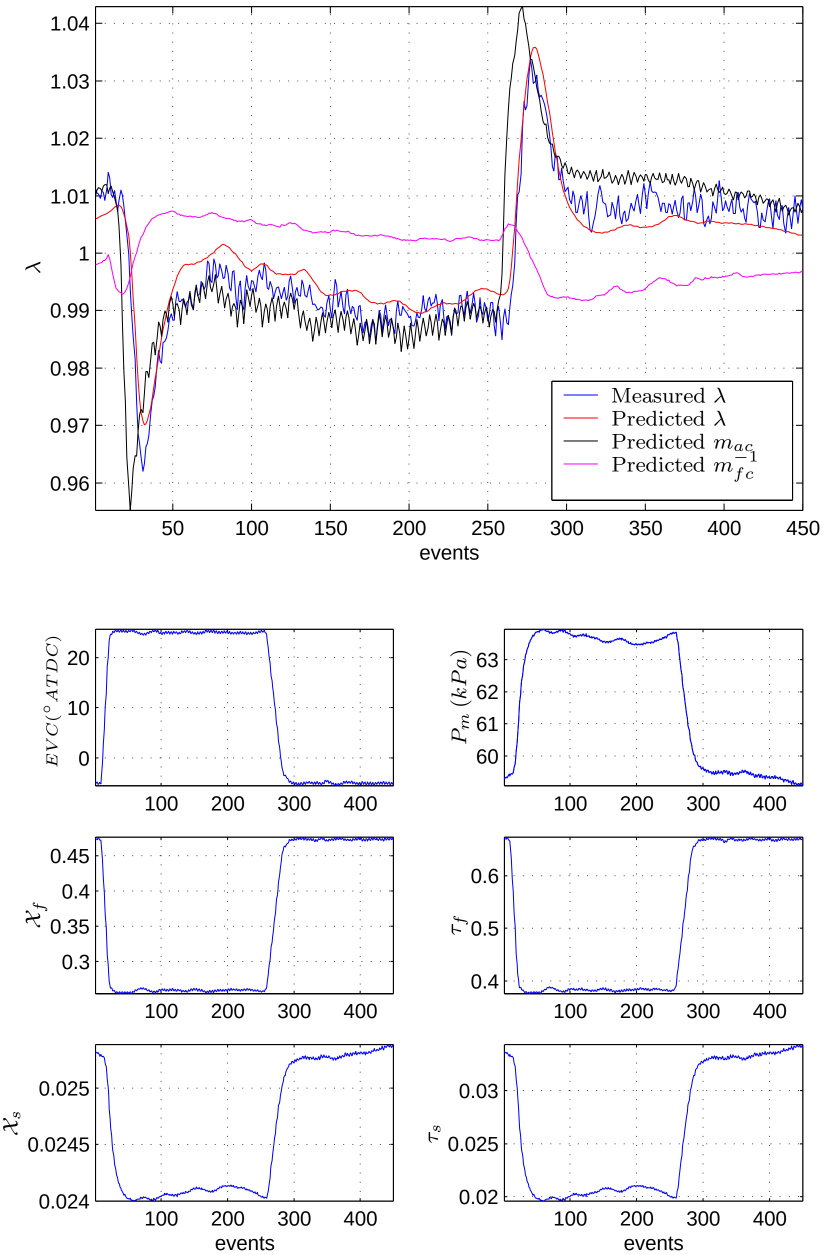

Figure 3.35 Transient validation of the AFR path model (EVC excitation)

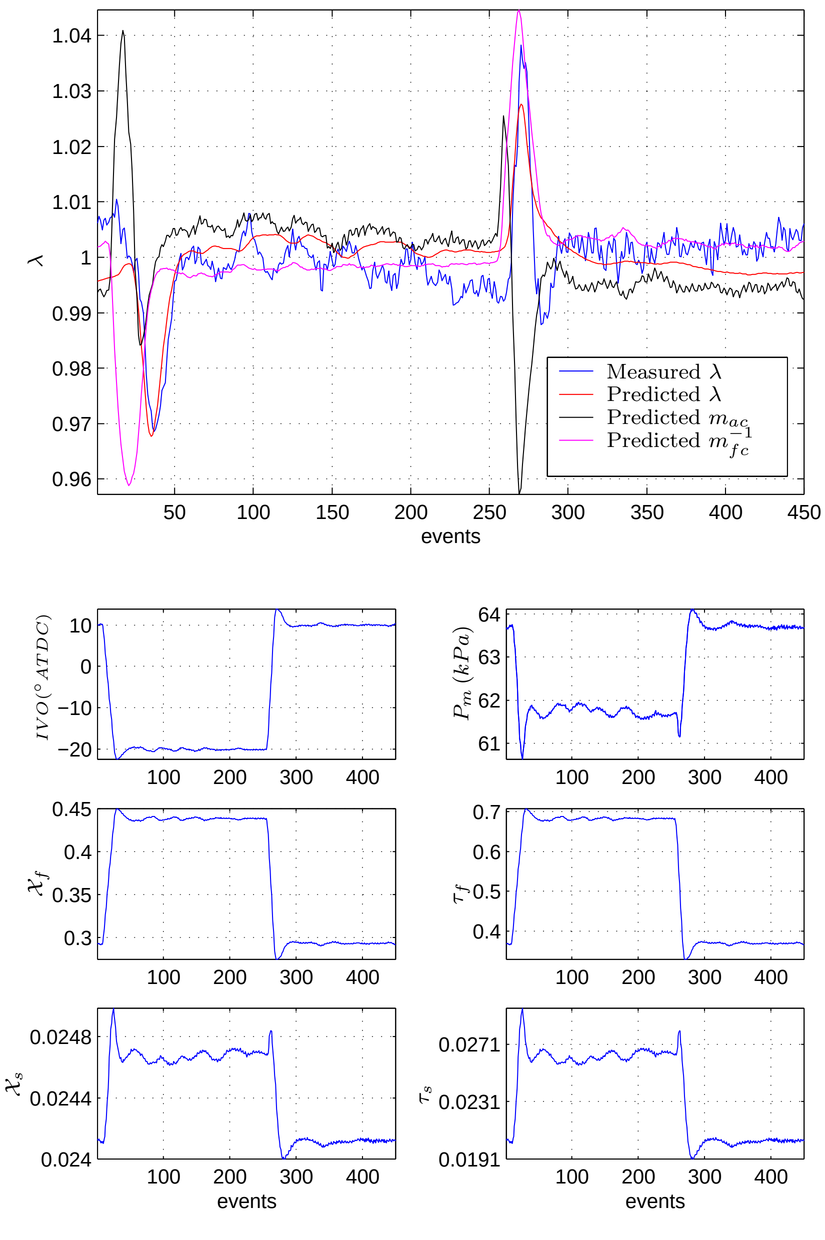

Figure 3.36 Transient validation of the AFR path model (IVO excitation)

IVO timing is changed between 10° and −20° in a square wave manner. This causes first a positive and then a negative (positive-negative) spike in the m_{ac}, while the m_{fc}^{-1} goes through a large single negative transient. The combined effect is that the negative m_{fc}^{-1} spike cancels the positive m_{ac} spike and causes a rich λ transient. This matches the measured λ accurately. When the IVO is retarded the m_{ac} goes through a positive-negative transient, while the m_{fc}^{-1} follows a single lean spike. It can be seen that the final predicted λ accurately models the actual λ. All the fuel transients in the model are due to the changes in the fast fuel puddle parameters. Moreover, the slow fuel puddle parameters do not change much since the variations in the MAP are small under the IVO excitation.

FPW Excitation

The final validation test is performed under a FPW excitation, where the injected fuel is changed in a square wave form. The average responses and model predictions are plotted in Figure 3.37. Since during this test all the input excitations apart from the FPW are constant, the wall-wetting dynamics are almost frozen as the predicted values of the fuel puddle parameters indicate. The high frequency engine induced noise can be seen in the measurements. The slow oscillation present in the normalised predicted m_{ac} around its nominal value is due to the oscillation in the MAP trace. The measured λ is predicted well by the model during the FPW excitation and this confirms that the model can also satisfactorily capture the frozen (linear) dynamics of the AFR path.

3.4 Comments

The AFR path of a TI-VCT engine is modelled and identified in this chapter by mostly following conventional methods. The two main contributions of the chapter are:

i. A new formulation for the cylinder MAF in a TI-VCT engine is proposed and validated in Section 3.1.2. The new formulation has a more intuitive form than the standard regression form.

ii. A global identification scheme that can capture the nonlinear behaviour of the system is proposed for the identification of the wall-wetting dynamics. Furthermore, a parameter-varying wall-wetting model for a TI-VCT engine has been identified using the proposed scheme and partially validated in Section 3.2.5 and Section 3.3 for the first time to author's knowledge as far as the published literature is concerned. This is an improvement on the widely accepted local linear identification methods.

Since the identified model is a parameter-varying one, it might be interesting to see how well the recently developed linear parameter-varying identification methods would perform on the TI-VCT engine [LP96, MMP99]. In addition to the AFR path dynamics,

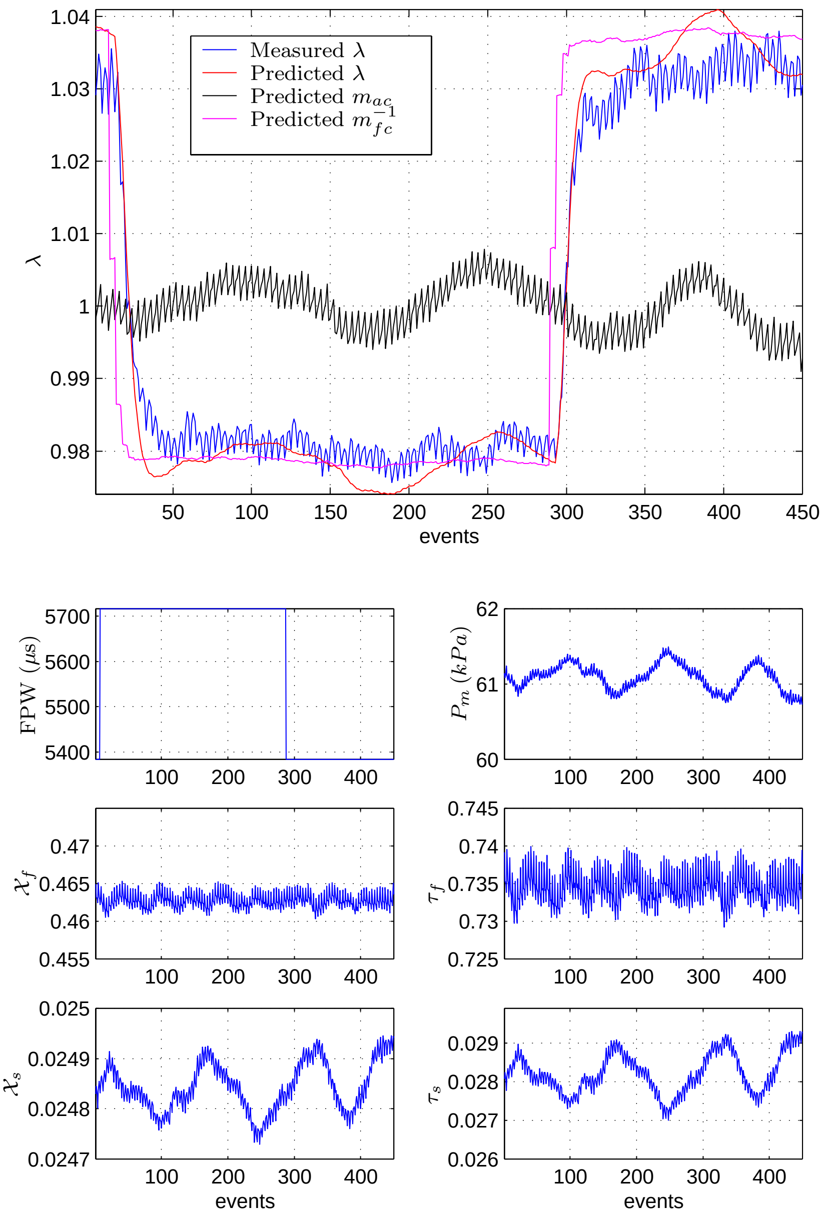

Figure 3.37 Transient validation of the AFR path model (FPW excitation)

VCT actuators' dynamics also play an important role in the AFR control problem. The modelling and identification of the TI-VCT actuators has been published in [GGF01].

4

LFT Representation of the AFR Path Model

Linear fractional transformations play an important role in the control theory by providing a framework that unifies many interesting and challenging control problems. Suppose $P \in \mathbb{C}^{(p_1+p_2)\times(q_1+q_2)}$ is a complex matrix partitioned as

$$P = \begin{bmatrix} P_{11} & P_{12} \\ P_{21} & P_{22} \end{bmatrix}, \tag{4.1}$$

with $P_{11} \in \mathbb{C}^{p_1 \times q_1}$ and $P_{22} \in \mathbb{C}^{p_2 \times q_2}$. Then, given $Q_l \in \mathbb{C}^{q_2 \times p_2}$ and $Q_u \in \mathbb{C}^{q_1 \times p_1}$,

- the lower linear fractional transformation (LFT) is defined by

$$\mathcal{F}_l\left(P, Q_l\right) := P_{11} + P_{12}Q_l(I - P_{22}Q_l)^{-1}P_{21}, \tag{4.2}$$

- the upper LFT is defined by

$$\mathcal{F}_u\left(P, Q_u\right) := P_{22} + P_{21}Q_u(I - P_{11}Q_u)^{-1}P_{12}, \tag{4.3}$$

provided that the required inverses exist. The motivation for the terminologies "lower" and "upper" LFTs should be clear from the diagram representations of $\mathcal{F}_l\left(P, Q_l\right)$ and $\mathcal{F}_u\left(P, Q_u\right)$ given in Figure 4.1. Interconnections of LFTs are again LFTs. This is a fundamental property of LFTs and is one reason why they are so important in the control theory. Details of the algebraic properties of LFTs can be found in [DPZ91] and [ZDG96].

General affine state space uncertainty is a special class of state space models with unknown coefficients. In the following we will show how this type of uncertainty can be represented via the LFT formulae with respect to an uncertain parameter matrix so that perturbations enter the system in a feedback form. Consider a linear system that is

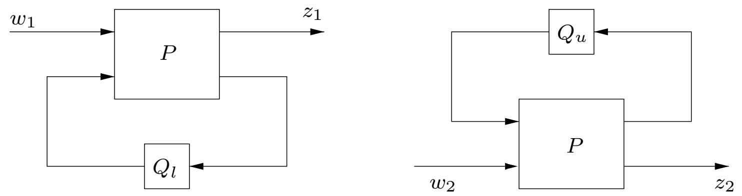

Figure 4.1 Diagrammatic representations of $\mathcal{F}_l(P, Q_l)$ and $\mathcal{F}_u(P, Q_u)$

parameterized by k uncertain parameters with the following state space data

$$M := \begin{bmatrix} A + \sum_{i=1}^{k} \rho_i \tilde{A}_i & B + \sum_{i=1}^{k} \rho_i \tilde{B}_i \\ C + \sum_{i=1}^{k} \rho_i \tilde{C}_i & D + \sum_{i=1}^{k} \rho_i \tilde{D}_i \end{bmatrix}, \tag{4.4}$$

where nominal plant data is given by (A, B, C, D) and the parametric uncertainty in the model is represented by ρ_i and $(\tilde{A}_i, \tilde{B}_i, \tilde{C}_i, \tilde{D}_i)$. Such a system can be written as

$$M = \mathcal{F}_l(P, \Delta), \tag{4.5}$$

where $\Delta = diag[\rho_1 I, \cdots, \rho_k I]$. To achieve this with the smallest possible size of repeated blocks, let q_i denote the rank of the matrix

$$\tilde{P}_i := \begin{bmatrix} \tilde{A}_i & \tilde{B}_i \\ \tilde{C}_i & \tilde{D}_i \end{bmatrix}, \tag{4.6}$$

for each i. Then $\tilde{P}_i$ can be written as

$$\tilde{P}_i = \begin{bmatrix} L_i \\ W_i \end{bmatrix} \begin{bmatrix} R_i \\ Z_i \end{bmatrix}', \tag{4.7}$$

and,

$$\rho_i \tilde{P}_i = \begin{bmatrix} L_i \\ W_i \end{bmatrix} [\rho_i I_{q_i}] \begin{bmatrix} R_i \\ Z_i \end{bmatrix}', \tag{4.8}$$

therefore M can be written as

$$M = \begin{bmatrix} A & B \\ C & D \end{bmatrix} + \begin{bmatrix} L_1 & \cdots & L_k \\ W_1 & \cdots & W_k \end{bmatrix} \begin{bmatrix} \rho_1 I_{q_1} & & \\ & \ddots & \\ & & \rho_k I_{q_k} \end{bmatrix} \begin{bmatrix} R_1' & Z_1' \\ \vdots & \vdots \\ R_k' & Z_k' \end{bmatrix}, \tag{4.9}$$

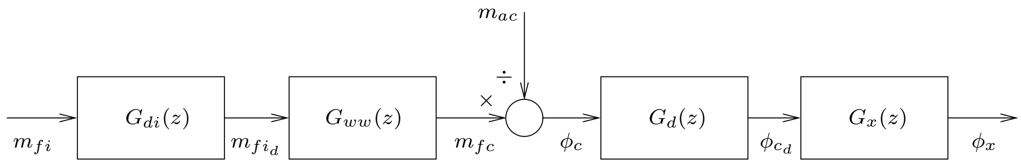

Figure 4.2 Identified AFR path model

i.e.

$$\begin{aligned} M &= \mathcal{F}_l\left(\left[\begin{array}{cc|ccc} A & B & L_1 & \cdots & L_k \\ C & D & W_1 & \cdots & W_k \\ \hline R'_1 & Z'_1 & 0 & \cdots & 0 \\ \vdots & \vdots & \vdots & \ddots & \vdots \\ R'_k & Z'_k & 0 & \cdots & 0 \end{array}\right], \begin{bmatrix} \rho_1 I_{q_1} & & \\ & \ddots & \\ & & \rho_k I_{q_k} \end{bmatrix}\right) \\ &= \mathcal{F}_l\left(P, \Delta\right) \end{aligned} \tag{4.10}$$

Above procedure will be used in order to put the identified AFR path model shown in Figure 4.2 into an LFT form by exploiting the affine parameter dependence of its subblocks. The final LFT model will be an approximation of the identified nonlinear model since some of the submodels such as the transport delay or cylinder MAF do not accept LFT formulations and approximate representations have to be used. The LFT model of the AFR path will play an important role in Chapter 6 when advanced robust controllers will be designed for the AFR control problem in the TI-VCT engines.

4.1 Injection Delay

The injection delay is assumed to be 2 events at 1500 rpm. Its state space representation in the event based discrete-time domain takes the following form

$$\begin{aligned} G_{di}(z) &= \left[\begin{array}{c|c} A_{di} & B_{di} \\ \hline C_{di} & D_{di} \end{array}\right] \\ &= \left[\begin{array}{cc|c} 0 & 1 & 0 \\ 0 & 0 & 1 \\ \hline 1 & 0 & 0 \end{array}\right]. \end{aligned} \tag{4.11}$$

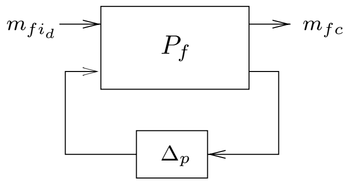

Figure 4.3 LFT representation of the wall-wetting dynamics

4.2 Wall-Wetting Dynamics

The wall-wetting dynamics of a single cylinder have been modelled as

$$G_{ww}(z) = \left(\frac{\mathcal{X}_s \tau_s}{z - (1 - \tau_s)} + \frac{\mathcal{X}_f \tau_f}{z - (1 - \tau_f)} + 1 - \mathcal{X}_s - \mathcal{X}_f \right).$$

If identical wall-wetting dynamics are assumed for each cylinder, the state space representation of the wall-wetting dynamics for a 4-cylinder engine can be described in the following form

$$\begin{aligned} G_{ww}(z) &= \left[\begin{array}{c|c} A_f & B_f \\ \hline C_f & D_f \end{array} \right] \\ &= \left[\begin{array}{cccc|c} 0 & 1 - \tau_s & 0 & 0 & \mathcal{X}_s \\ I_3 & 0 & 0 & 0 & 0 \\ 0 & 0 & 0 & 1 - \tau_f & \mathcal{X}_f \\ 0 & 0 & I_3 & 0 & 0 \\ \hline 0 & \tau_s & 0 & \tau_f & 1 - \mathcal{X}_s - \mathcal{X}_f \end{array} \right]. \end{aligned} \tag{4.12}$$

Using the parametrisation of the fuel puddle parameters introduced in Section 3.2.5

$$\begin{aligned} \tau_s &= l_{10_s} + l_{11_s} P_m, \\ \mathcal{X}_s &= l_{20_s} + l_{21_s} P_m, \\ \tau_f &= l_{10_f} + l_{12_f} EVC + f_{13_s} IVO, \\ \mathcal{X}_f &= l_{20_f} + l_{22_f} EVC + f_{23_f} IVO, \end{aligned}$$

(4.12) can be put into a lower LFT form as shown in Figure 4.3

$$G_{ww}(z) = \mathcal{F}_l \left(P_f, \Delta_p \right), \tag{4.13}$$

where

$$P_f = \left[\begin{array}{cccc|cccc} 0 & 1-l_{10_s} & 0 & 0 & l_{20_s} & 1 & 0 & 0 \\ I_3 & 0 & 0 & 0 & 0 & 0 & 0 & 0 \\ 0 & 0 & 0 & 1-l_{10_f} & l_{20_f} & 0 & 1 & 1 \\ 0 & 0 & I_3 & 0 & 0 & 0 & 0 & 0 \\ \hline 0 & l_{10_s} & 0 & l_{10_f} & 1-l_{20_s}-l_{20_f} & -1 & -1 & -1 \\ 0 & -l_{11_s} & 0 & 0 & l_{21_s} & 0 & 0 & 0 \\ 0 & 0 & 0 & -l_{12_f} & l_{22_f} & 0 & 0 & 0 \\ 0 & 0 & 0 & -l_{13_f} & l_{23_f} & 0 & 0 & 0 \end{array}\right],$$

$$\Delta_p = \begin{bmatrix} P_m & 0 & 0 \\ 0 & EVC & 0 \\ 0 & 0 & IVO \end{bmatrix}.$$

4.3 Transport Delay

Recall that the transport delay is modelled as a delay in the event based continuous-time domain. A time delay in the continuous-time is an infinite-dimensional system and not representable by a rational transfer function. An n'th order approximation of a time delay d may be obtained by putting n first-order Padé approximations in series

$$e^{-ds} \approx \frac{\left(1 - \frac{d}{2n}s\right)^n}{\left(1 + \frac{d}{2n}s\right)^n}. \tag{4.14}$$

An equivalent approximation in the event based discrete-time domain can be calculated via a bilinear transformation of the form (Tustin's transformation)

$$s = \frac{2}{T_s}\frac{1-z^{-1}}{1+z^{-1}}. \tag{4.15}$$

Substituting (4.15) into (4.14) yields the n'th order delay approximation in the discrete-time domain

$$e^{-ds} \approx \frac{\left(nT_s - d + (nT_s + d)z^{-1}\right)^n}{\left(nT_s + d + (nT_s - d)z^{-1}\right)^n}. \tag{4.16}$$

Consider the case with $T_s = 1$ and $n = 2$

$$\begin{aligned} e^{-ds} &\approx \left(\frac{2 - d + (2+d)z^{-1}}{2 + d + (2-d)z^{-1}}\right)^2 \\ &= \left(\frac{2-d}{2+d} \quad \frac{z + \frac{2+d}{2-d}}{z + \frac{2-d}{2+d}}\right) \cdot \left(\frac{2-d}{2+d} \quad \frac{z + \frac{2+d}{2-d}}{z + \frac{2-d}{2+d}}\right) \end{aligned} \tag{4.17}$$

If one of the terms above can be put into an LFT form, then overall expression can be written as an LFT since multiplication of LFTs are still LFTs. Define each term in (4.17) as

$$
\begin{aligned}
e^{-d's} &:= \left(\frac{2-d}{2+d} \quad \frac{z+\frac{2+d}{2-d}}{z+\frac{2-d}{2+d}} \right) \\
&= \theta \quad \frac{z+\theta^{-1}}{z+\theta} \\
&= \left[\begin{array}{c|c} -\theta & 1+\theta \\ \hline 1-\theta & \theta \end{array} \right] \\
&= \mathcal{F}_l \left(\left[\begin{array}{c|cc} 0 & 1 & 1 \\ \hline 1 & 0 & 1 \\ -1 & 1 & 0 \end{array} \right], \theta \right),
\end{aligned} \tag{4.18}
$$

where

$$\theta = \frac{2-d}{2+d}. \tag{4.19}$$

Moreover, θ also can be expressed as an LFT in d

$$\theta = \mathcal{F}_l \left(\begin{bmatrix} 1 & -1 \\ 1 & -1/2 \end{bmatrix}, d \right). \tag{4.20}$$

Recall that the transport delay d is parameterised as

$$d = l_{0_d} + l_{1_d} P_m + l_{2_d} OVL.$$

Substituting OVL=EVC$-$IVO, the above affine relationship also takes an LFT representation

$$d = \mathcal{F}_l \left(\begin{bmatrix} l_{0_d} & l_{1_d} & l_{2_d} & -l_{2_d} \\ 1 & 0 & 0 & 0 \\ 1 & 0 & 0 & 0 \\ 1 & 0 & 0 & 0 \end{bmatrix}, \Delta_p \right), \tag{4.21}$$

Finally, LFTs (4.18), (4.20) and (4.21) can be combined to get an LFT representation of $e^{-d's}$ in terms of P_m, EVC and IVO as depicted in Figure 4.4

$$e^{-d's} = \mathcal{F}_l \left(P_d, \Delta_p \right). \tag{4.22}$$

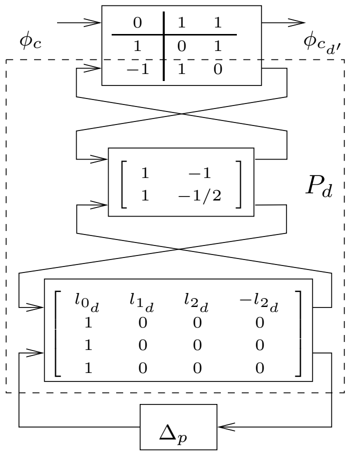

Figure 4.4 LFT representation of $e^{-d's}$

Hence, the second order approximation of the transport delay can be written as

$$\begin{aligned} e^{-ds} &\approx e^{-d's}.e^{-d's} \\ &= G_d(z) \\ &= \mathcal{F}_l\left(P_d, \Delta_p\right)\mathcal{F}_l\left(P_d, \Delta_p\right) \end{aligned} \tag{4.23}$$

Note that the higher order LFT approximations of the transport model can be obtained by applying the above procedure for $n > 2$.

4.4 Gas Mixing and Sensor Dynamics

The identified gas mixing and sensor dynamics are modelled as a parameter-varying transfer function

$$\begin{aligned} G_x(z) &= \frac{1+\xi_1+\xi_2}{z^2+\xi_1 z+\xi_2} \\ &= \left[\begin{array}{c|c} A_x & B_x \\ \hline C_x & D_x \end{array}\right] \\ &= \left[\begin{array}{cc|c} 0 & 1 & 0 \\ -\xi_2 & -\xi_1 & 1+\xi_1+\xi_2 \\ \hline 1 & 0 & 0 \end{array}\right], \end{aligned} \tag{4.24}$$

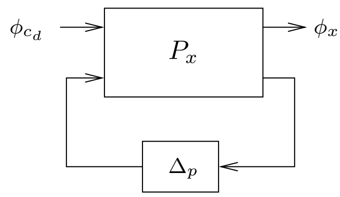

Figure 4.5 LFT representation of the gas mixing and sensor dynamics

with the following parameterisation

$$\begin{aligned}\xi_1 &= l_{10_x} + l_{11_x} P_m + l_{12_x} OVL\\ \xi_2 &= l_{20_x} + l_{21_x} P_m + l_{22_x} OVL.\end{aligned}$$

This parameter-varying transfer function can be written as shown in Figure 4.5

$$G_x(z) = \mathcal{F}_l\left(P_x, \Delta_p\right), \tag{4.25}$$

where

$$P_x = \left[\begin{array}{cc|cccc} 0 & 1 & 0 & 0 & 0 & 0\\ -l_{20_x} & -l_{10_x} & 1 + l_{20_x} + l_{10_x} & 1 & 1 & 1\\ \hline 1 & 0 & 0 & 0 & 0 & 0\\ -l_{21_x} & -l_{11_x} & l_{21_x} + l_{11_x} & 0 & 0 & 0\\ -l_{22_x} & -l_{12_x} & l_{22_x} + l_{12_x} & 0 & 0 & 0\\ l_{22_x} & l_{12_x} & -l_{22_x} - l_{12_x} & 0 & 0 & 0 \end{array}\right].$$

4.5 Cylinder Mass Air Flow

The cylinder MAF model developed and identified in Section 3.1.2 is a highly nonlinear function of P_m, EVC and IVO. Such a model would require a high order LFT representation for an accurate description. Moreover, the cylinder MAF does not enter the fuel path transfer function depicted in Figure 4.2 linearly because

$$\phi_c = \frac{m_{fc}}{m_{ac_F}} = m_{fc} m_{ac_F}^{-1}, \tag{4.26}$$

whereas the inverse of the cylinder MAF $m_{ac_F}^{-1}$ is linear in the model and can be considered as a parameter-varying gain in the loop. Therefore, an affine approximation of the $m_{ac_F}^{-1}$ is computed

$$m_{ac_F}^{-1} \approx M_{vlg} := l_{0_{af}} + l_{1_{af}} P_m + l_{2_{af}} EVC + l_{3_{af}} IVO. \tag{4.27}$$

Figure 4.6 shows the affine surfaces of (4.27) for fixed values of the EVC varying between -10° and 29° ATDC. The affine model has moderate accuracy with a worst case error

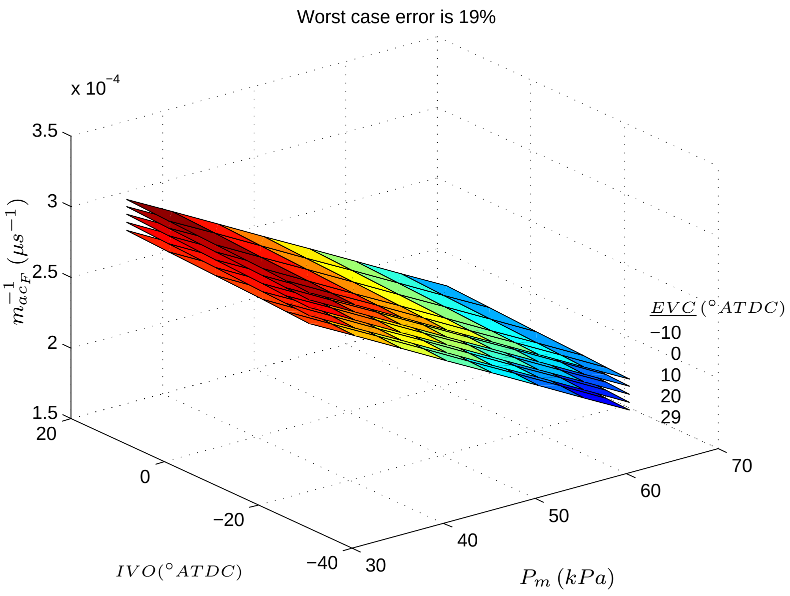

Figure 4.6 LFT approximation of $m^{-1}_{ac_F}$

no more than 19%. Note that the injector calibration data identified in Section 3.2.4 is used in order to convert the cylinder MAF output $\dot{m}_{ac}$ from "gram per seconds" to "micro seconds" before computing the affine approximation of $m^{-1}_{ac_F}$. This makes the units of the m_{fc} and $m^{-1}_{ac_F}$ compatible before the calculation of the ϕ_c in the AFR path model. The affine approximation of $m^{-1}_{ac_F}$ can also be written in LFT form

$$M_{vlg} = \mathcal{F}_l\left(\begin{bmatrix} l_{0_{af}} & l_{1_{af}} & l_{2_{af}} & l_{3_{af}} \\ 1 & 0 & 0 & 0 \\ 1 & 0 & 0 & 0 \\ 1 & 0 & 0 & 0 \end{bmatrix}, \Delta_p\right). \tag{4.28}$$

Note that the LFT approximation of the cylinder air charge will be only used for feedback controller synthesis, for estimation purposes and feedforward controller design the original full nonlinear air charge model will be used.

4.6 Overall AFR Path

Since the interconnections of the LFTs are again LFTs, the nonlinear AFR path model can be approximated in an LFT form by combining the individual LFT representations of the transfer functions in Figure 4.2

$$\begin{aligned} G_\phi(z) &= G_x(z)G_d(z)M_{vlg}G_{ww}(z)G_{di}(z) \\ &= \mathcal{F}_l\left(P_x,\Delta_p\right)\mathcal{F}_l\left(P_d,\Delta_p\right)\mathcal{F}_l\left(P_d,\Delta_p\right)\mathcal{F}_l\left(P_M,\Delta_p\right)\mathcal{F}_l\left(P_f,\Delta_p\right)G_{di} \\ &= \mathcal{F}_l\left(P_\phi,\Delta_\phi\right), \end{aligned} \tag{4.29}$$

where $P_\phi \in \mathbb{R}^{30\times 30}$ has 14 states, 16 inputs and 16 outputs, Δ_ϕ =diag[$P_m I_5$,EVCI_5,IVOI_5] $\in \mathbb{R}^{15\times 15}$ and G_ϕ is a transfer function with 14 states, 1 input and 1 output.

4.7 Comments

The identified nonlinear AFR path model has been approximated with an LFT model in this chapter. Apart from the transport delay and inverse of the cylinder MAF, all of the submodels in the AFR path model identified in Chapter 3 have been exactly described in the LFT framework. The LFT AFR path model will allow us to analyse and synthesise feedback controllers for the AFR control problem using the powerful tools of the advanced robust control theory introduced in Chapter 6. The loss of accuracy in the model will be compensated by designing controllers that have appropriate robustness properties. Furthermore, the full nonlinear AFR path model will be used in the design of a feedforward controller in order to improve the performance further.

5

Robust Control System Design

This chapter introduces some concepts of the robust control theory that are necessary to design the final AFR controller of this thesis. Preceding chapters have revealed an AFR path model that is both uncertain and highly operating point dependent. Uncertainty in a model is inherent and cannot be diminished. This can be seen from the validation data provided in Section 3.3. Even though the identified model predicts the system response accurately, it cannot match it exactly. The uncertainty in a model gets even larger when it is used at operating points different than the operating points the identification experiments were performed. The inherent mismatch between a system and its model is one of the main motivations for using feedback since feedback can reduce the effect of the uncertainty on the closed-loop system. In addition to the uncertainty in the model, the disturbances acting on the AFR signal such as the valve timings or throttle position can only be rejected by a feedback controller. The ability to reject disturbances is another main motivation for using feedback control systems. The sensible design requirements for a basic feedback system are discussed in Section 5.1 in terms of stability and disturbance rejection performance. Design guidelines for the classical loop shaping framework are also presented in this section.

Even though mere use of the feedback improves the robustness of the closed-loop system, only in the robust control theory the uncertainty in the model is explicitly taken into account during the design process. Section 5.2 introduces $\mathscr{H}_\infty$ robust control theory together with the $\mathscr{H}_\infty$ loop shaping design paradigm[1]. The $\mathscr{H}_\infty$ loop shaping controller design is chosen as the main controller synthesis tool in this thesis since it combines the essential ideas of the classical loop shaping with the modern ideas of robust control theory in a convenient way. The $\mathscr{H}_\infty$ control theory is exposed in a linear matrix inequalities (LMIs) framework as LMI techniques apply not only to standard $\mathscr{H}_\infty$ control problems

[1]Details of the $\mathscr{H}_\infty$ loop shaping design paradigm is presented in Appendix C

but also to more difficult control problems such as the robust gain-scheduling controller design.

Inherent uncertainty and multiple disturbances are not the only difficulties in the AFR control problem in TI-VCT engines. The AFR path dynamics vary significantly with the operating point and an AFR controller has to cope with these variations without much degradation of its performance and robustness. Such variations in dynamics may be handled in two ways. The first approach is to treat the variations as uncertainties and techniques developed in Section 5.2 can be used. The second approach is to treat them as measurable parameter variations in the model and recently developed linear parameter-varying (LPV) controller design ideas can be used. Although the first option produces simple controllers, superior robustness and performance can only be achieved through the second option. The wide variety of techniques in LPV $\mathscr{H}_\infty$ controller design are presented in Section 5.3 as an extension of the LMI framework exposed in Section 5.2 in a unified and systematic manner as much as possible. The presentation of the LMI techniques in this chapter closely follows the lines of [SW99, Det01].

Remark 5.1 *The $\mathscr{H}_\infty$ control theory and LPV methods introduced in this chapter are for continuous-time systems. They can be applied to the discrete-time systems by converting the discrete-time parameters to continuous-time parameters through a mapping such as the Tustin's (bilinear) transformation. Once the controller design is completed in the continuous-time domain, the controller parameters in the discrete-time are obtained by applying the inverse transformation. The Tustin's (bilinear) transformation is used in this thesis as the mapping tecnique since it can be shown that $\mathscr{L}_2$ gain for an LPV system is preserved under the Tustin's transformation whenever the LPV system accepts an LFT formulation (see Section 5.3.2 for further details).*

5.1 Typical Closed-Loop Requirements

The first requirement of a feedback system is well-posedness and stability of the interconnected system of plant G and controller K. A feedback system is said to be well-posed if all closed-loop transfer matrices are well-defined and proper. If a transfer matrix is bounded at infinite frequency, it is called a proper transfer matrix.

Lemma 5.1 *(Well-Posedness) The feedback system in Figure 5.1 is well-posed if and only if*

$$I + K(\infty)G(\infty) \tag{5.1}$$

is invertible [ZDG96, Lemma 5.1].

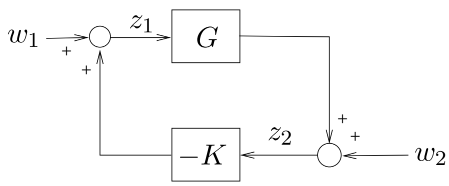

Figure 5.1 Interconnected system

Furthermore, if the transfer functions from all the inputs to all the internal signals are stable, the closed-loop system is said to be internally stable.

Lemma 5.2 *(Internal Stability) The system in Figure 5.1 is internally stable if and only if each transfer function in*

$$T_{\left[\begin{smallmatrix} w_1 \\ w_2 \end{smallmatrix}\right] \to \left[\begin{smallmatrix} z_1 \\ z_2 \end{smallmatrix}\right]} = \begin{bmatrix} (I+KG)^{-1} & -(I+KG)^{-1}K \\ (I+GK)^{-1}G & (I+GK)^{-1} \end{bmatrix} \tag{5.2}$$

is stable [ZDG96, Lemma 5.3].

Internal stability guarantees that all internal signals in a system are bounded provided that the input signals are bounded.

In addition to stability conditions, there are several performance requirements of a typical closed-loop system shown in Figure 5.2 with the plant input disturbance w_1, plant output disturbance w_2 and sensor noise w_3, controller output u, plant input u_p and measured output y, performance signals z_1 and z_2. In general a controller is designed to minimise the effect of the disturbance signals on the error signals. Given that the system is internally stable, individual effects of each disturbance on the performance signals can be expressed as follows:

$$z_1 = y = T_o(r - w_3) + S_oGw_1 + S_ow_2 \tag{5.3}$$

$$z_2 = u = KS_o(r - w_3) - KS_ow_2 - T_iw_1 \tag{5.4}$$

$$r - y = S_o(r - w_2) + T_ow_3 - S_oGw_1 \tag{5.5}$$

$$u_p = KS_o(r - w_3) - KS_ow_2 + S_iw_1, \tag{5.6}$$

where $L_o = GK$ is the *output loop transfer function*, $L_i = KG$ is the *input loop transfer function*, $S_o = (I + L_o)^{-1}$ is the *output sensitivity matrix*, $S_i = (I + L_i)^{-1}$ is the *input sensitivity matrix*, $T_o = I - S_o$ is the *output complementary sensitivity function* and $T_i = I - S_i$ is the *input complementary sensitivity function*. The above equations show

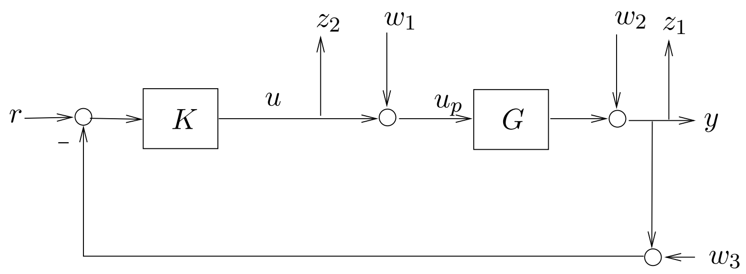

Figure 5.2 Standard feedback configuration

the fundamental relationships between the input and output signals in a feedback system and reveal some important insights for the controller design such as:

$$\begin{aligned}
&\overline{\sigma}(S_o) \ll 1, && \text{for } w_2 \text{ rejection at } y\\
&\overline{\sigma}(S_oG) = \overline{\sigma}(GS_i) \ll 1, && \text{for } w_1 \text{ rejection at } y\\
&\overline{\sigma}(S_i) \ll 1, && \text{for } w_1 \text{ rejection at } u_p\\
&\overline{\sigma}(S_iK) = \overline{\sigma}(KS_o) \ll 1, && \text{for } w_2 \text{ rejection at } u_p.
\end{aligned}$$

Furthermore, it can be shown that for rejecting w_2 at y, and w_1 at u_p following implications hold,

$$\overline{\sigma}(S_o) \ll 1 \Longleftrightarrow \underline{\sigma}(GK) \gg 1,$$
$$\overline{\sigma}(S_i) \ll 1 \Longleftrightarrow \underline{\sigma}(KG) \gg 1.$$

Finally, the following approximations hold, when $\underline{\sigma}(GK) \gg 1$ or $\underline{\sigma}(KG) \gg 1$, and G and K are square and invertible:

- $\overline{\sigma}(S_oG) \approx \frac{1}{\underline{\sigma}(K)}$. Hence, for disturbance rejection at y the output loop gain, $\underline{\sigma}(GK)$, should be large in the frequency range where w_2 is significant and the singular values of the controller K and $\underline{\sigma}(GK)$ should be large in the frequency range where w_1 is significant.

- $\overline{\sigma}(KS_o) \approx \frac{1}{\underline{\sigma}(G)}$. Good performance at plant input u_p requires large input loop gain, $\underline{\sigma}(KG)$, in the frequency range where w_1 is significant, and large plant singular values and large $\underline{\sigma}(GK)$ in the frequency range where w_2 is significant. However, we cannot affect the singular values of the plant, thus they impose a limitation on the design.

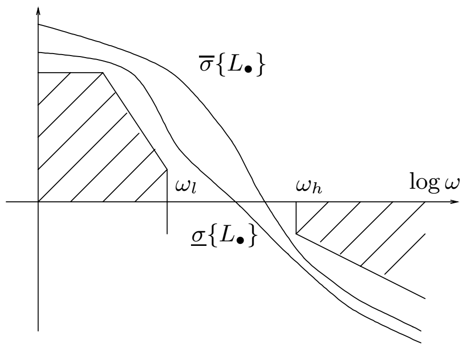

Figure 5.3 Singular values of a typical loop shape

Note that good disturbance rejection at the plant output does not necessarily imply good disturbance rejection in the plant input. Satisfying all these performance requirements is not an easy task since there are several performance/stability tradeoffs and design limitations:

- For example *robust closed-loop stability* in the case of multiplicative uncertainty requires that the loop gain should be small at the frequencies where the *uncertainty* is significant.
- Good *disturbance rejection* requires high loop gain over the frequency range where the disturbance is significant, whereas good *noise rejection* necessitates low loop gain in the frequency range where the noise is substantial, which is revealed in (5.3). Hence, noise rejection at low frequency conflicts with disturbance rejection.
- The *controller gain* should not be very large in the frequency range where the loop gain is small in order not to saturate the actuators, which is implied by (5.4).
- The shape of the sensitivity function is constrained by *RHP zeros* and the control power available. Similarly, the shape of the complementary sensitivity function is constrained by *RHP poles* and the control power available.

Above implications and requirements can be summarised in terms of the shape of the singular values of the loop gain as shown in Figure 5.3. Briefly, a good nominal design requires high loop gain at low frequency and low loop gain at high frequency and a smooth transition between them. The desired loop shape in the figure forms the basis of the loop shaping design procedure which simply finds a controller K that shapes the loop transfer function L in a way that the loop gains satisfy all the performance conditions at low frequency and all the robustness requirements at high frequency as discussed above. The details of the loop shaping controller design are presented in [ZDG96, pp. 134-135].

Unfortunately, the designer must shape not only the magnitude but also the phase of the loop for achieving stability and performance requirements in the classical loop shaping (but not in the $\mathscr{H}_\infty$ loop shaping). This makes the classical loop shaping design procedure arduous to apply for difficult systems such as non-minimum phase plants, unstable plants or MIMO systems.

5.2 $\mathscr{H}_\infty$ Control with Linear Matrix Inequalities

A linear matrix inequality is a matrix inequality of the form

$$F(x) := F_0 + \sum_{i=1}^{m} x_i F_i > 0 \text{ (or } \geq 0),$$

where $x := [x_1\, x_2 \cdots x_m]' \in \mathbb{R}^m$ is the vector of decision variables and the matrices $F_i = F_i'$ are given. Thus LMIs as given above are convex constraints on the variable x. Multiple LMIs $F^1(x) > 0, \cdots, F^p(x) > 0$ may be combined into a single LMI to give $\mathrm{diag}[F^1(x), \cdots, F^p(x)] > 0$. A wide variety of problems in systems and control theory can be written as optimisation problems with LMI constraints such as the matrix scalings problems or multi-objective control problems [PZPB91, BBFE93, SGC97, AT00]. An historical account of the LMIs in control is presented in [BF94]. Analytic solutions to these LMIs generally do not exist, but efficient numerical methods are available to find a feasible solution [GNLC95]. Some nonlinear convex inequalities can be converted into LMI form using Schur Complements. The following lemma states such an equivalence.

Lemma 5.3 *(Schur Complement) Suppose that $P = P' \in \mathbb{C}^{n\times n}$, $R = R' \in \mathbb{C}^{m\times m}$ and $S \in \mathbb{C}^{n\times m}$. Then*

$$R < 0 \text{ and } P - SR^{-1}S' < 0 \quad \Leftrightarrow \quad \begin{bmatrix} P & S \\ S' & R \end{bmatrix} < 0.$$

[GA94, Lemma 3.2]

The generic framework for synthesis of optimal $\mathscr{H}_\infty$ control problems is depicted in Figure 5.4. The standard closed-loop system as given in Figure 5.2 can be always put into this generic framework.

The plant P represents the generalised plant and takes the following state space form,

$$\begin{pmatrix} \dot{x} \\ \hline z \\ y \end{pmatrix} = \left(\begin{array}{c|cc} A & B_w & B_u \\ \hline C_z & D_{zw} & D_{zu} \\ C_y & D_{yw} & 0 \end{array}\right) \begin{pmatrix} x \\ \hline w \\ u \end{pmatrix} \tag{5.7}$$

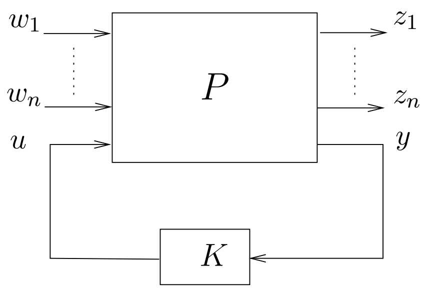

Figure 5.4 LFT control system synthesis framework

where $w = [w_1 \cdots w_m]'$ and $z = [z_1 \cdots z_m]'$. In this framework the controller K is designed to achieve some bound on the closed-loop transfer function $T = \mathcal{F}_l\,(P, K)$ in some measure. Various measures are available for bounding T such as $\mathscr{H}_2$ and $\mathscr{H}_\infty$ norms. The $\mathscr{H}_2$ performance bound is useful to handle stochastic aspects such as the measurement noise and random disturbances. On the other hand the $\mathscr{H}_\infty$ performance bound, which is used for the robust controller analysis and synthesis, is convenient to enforce robustness to model uncertainty and to express frequency-domain specifications such as bandwidth, low-frequency gain, and roll-off. For a more complete discussion of various measures for performance specifications refer to [SGC97].

The analysis results are presented for the closed-loop system T with the following state space form,

$$\begin{aligned} z &= Tw \\ &= \left[\begin{array}{c|c} \mathcal{A} & \mathcal{B} \\ \hline \mathcal{C} & \mathcal{D} \end{array}\right] w. \end{aligned} \tag{5.8}$$

Definition 5.1 *(Quadratic Performance) The system (5.8) is said to have quadratic performance with respect to the performance index*

$$P_p = \begin{pmatrix} Q_p & S_p \\ S_p' & R_p \end{pmatrix}, \; and\; R_p \geq 0 \tag{5.9}$$

if it is asymptotically stable and if there exists an $\beta > 0$ such that:

$$\int_0^\infty \begin{pmatrix} w(t) \\ z(t) \end{pmatrix}' P_p \begin{pmatrix} w(t) \\ z(t) \end{pmatrix} dt \leq -\beta \left\|w\right\|^2, \; for\, every\, w \in \mathscr{L}_2 \tag{5.10}$$

[Sch00, Section 3.2].

The quadratic performance specification is rather general and covers some well-known cases for special choices of the index P_p. For instance, choosing $Q_p = 0$, $S_p = -\frac{1}{2}I$ and $R_p = 0$ reveals the positive real test for the system (5.8). On the other hand, for $Q_p = -\gamma I$, $S_p = 0$ and $R_p = \frac{1}{\gamma}I$ the $\mathscr{H}_\infty$ performance is recovered.

Theorem 5.4 *(LMI characterisation of Quadratic Performance) The system (5.8) is asymptotically stable and has quadratic performance with respect to the index (5.9) if and only if there exists a symmetric matrix $\mathcal{X}$ satisfying*

$$\mathcal{X} > 0 \ \textit{and} \ \left(\begin{array}{cc} I & 0 \\ \mathcal{A} & \mathcal{B} \\ \hline 0 & I \\ \mathcal{C} & \mathcal{D} \end{array}\right)' \left(\begin{array}{cc|cc} 0 & \mathcal{X} & 0 & 0 \\ \mathcal{X} & 0 & 0 & 0 \\ \hline 0 & 0 & Q_p & S_p \\ 0 & 0 & S_p' & R_p \end{array}\right) \left(\begin{array}{cc} I & 0 \\ \mathcal{A} & \mathcal{B} \\ \hline 0 & I \\ \mathcal{C} & \mathcal{D} \end{array}\right) < 0. \tag{5.11}$$

[Sch00, Theorem 3.3]

The inequality (5.11) however does not allow the direct computation of the $\mathscr{H}_\infty$ norm by minimisation of γ since the parameter does not enter affinely. An equivalent version with affine dependence on γ can be obtained by resorting to the Schur complement as

$$\left(\begin{array}{c|c} \left(\begin{array}{cc} I & 0 \\ \mathcal{A} & \mathcal{B} \\ \hline 0 & I \end{array}\right)' \left(\begin{array}{cc|c} 0 & \mathcal{X} & 0 \\ \mathcal{X} & 0 & 0 \\ \hline 0 & 0 & -\gamma I \end{array}\right) \left(\begin{array}{cc} I & 0 \\ \mathcal{A} & \mathcal{B} \\ \hline 0 & I \end{array}\right) & \begin{pmatrix} \mathcal{C} & \mathcal{D} \end{pmatrix}' \\ \hline \begin{pmatrix} \mathcal{C} & \mathcal{D} \end{pmatrix} & -\gamma I \end{array}\right) < 0$$

It can easily be shown that this condition is equivalent to the well-known Bounded Real Lemma condition [GA94, Lemma 4.1]

$$\begin{pmatrix} \mathcal{A}'\mathcal{X} + \mathcal{X}\mathcal{A} & \mathcal{X}\mathcal{B} & \mathcal{C}' \\ * & -\gamma I & \mathcal{D}' \\ * & * & -\gamma I \end{pmatrix} < 0$$

Remark 5.2 *Standard $\mathscr{H}_\infty$ or $\mathscr{H}_2$ optimal control problems as depicted in Figure 5.4 can be solved elegantly in terms of two Riccati equations [DGKF89]. However more complex control problems such as the structured controller design or LPV controller design have not been found to accept analytical solutions so far. For this reason all the analysis and synthesis conditions are given in terms of LMIs in this chapter. This will allow smooth extension of the LMI characterisation of the standard $\mathscr{H}_\infty$ control problems to more complicated LPV $\mathscr{H}_\infty$ control problems.*

Remark 5.3 *LMI techniques in control theory are an area of ongoing research with rapid development. Most results are only available in recently published articles in which different notations, terminology and methods are introduced. This is because there are several possible ways to express equivalent LMI conditions. The presentation of LMI techniques in this chapter closely follows the lines of [SW99, Sch00, Det01] and hopefully will provide a compact framework for the reader.*

5.2.1 Synthesis LMIs

A generic framework to design an LTI controller that satisfies an $\mathscr{H}_\infty$ performance is presented subsequently. Inequalities in terms of the unknown controller parameters and analysis variables $\mathcal{X}$ and γ are obtained by writing down the analysis LMIs for the closed-loop matrices. These inequalities are in general nonlinear since products among the variables appear. The conditions are rendered LMIs by either applying some invertible transformations of the controller parameters or eliminating the controller variables. After having solved the LMIs, if feasible, the original controller parameters are computed by either inverting the transformation or solving another LMI condition in the controller variables.

Consider the synthesis framework depicted in Figure 5.4 with the controller K given as

$$u = \left[\begin{array}{c|c} A_K & B_K \\ \hline C_K & D_K \end{array}\right] y, \tag{5.12}$$

and the generalised plant P as in (5.7). The state space matrices of the closed-loop system T can be computed as

$$\left[\begin{array}{c|c} \mathcal{A} & \mathcal{B} \\ \hline \mathcal{C} & \mathcal{D} \end{array}\right] = \left(\begin{array}{cc|c} A & 0 & B_w \\ 0 & 0 & 0 \\ \hline C_z & 0 & D_{zw} \end{array}\right) + \left(\begin{array}{cc} 0 & B_u \\ I & 0 \\ \hline 0 & D_{zu} \end{array}\right) \left(\begin{array}{cc} A_K & B_K \\ C_K & D_K \end{array}\right) \left(\begin{array}{cc|c} 0 & I & 0 \\ C_y & 0 & D_{yw} \end{array}\right) \tag{5.13}$$

A straightforward application of Theorem 5.4 to this closed-loop system reveals that T is asymptotically stable and has $\mathscr{L}_2$ gain from w to z less than γ, if and only if there exists a matrix $\mathcal{X}$ satisfying

$$\mathcal{X} > 0 \tag{5.14}$$

$$\begin{pmatrix} \mathcal{A}'\mathcal{X} + \mathcal{X}\mathcal{A} & \mathcal{X}\mathcal{B} \\ \mathcal{B}'\mathcal{X} & 0 \end{pmatrix} + \begin{pmatrix} 0 & I \\ \mathcal{C} & \mathcal{D} \end{pmatrix}' \begin{pmatrix} -\gamma I & 0 \\ 0 & \frac{1}{\gamma} I \end{pmatrix} \begin{pmatrix} 0 & I \\ \mathcal{C} & \mathcal{D} \end{pmatrix} < 0 \tag{5.15}$$

Unfortunately, (5.15) is not an LMI due to terms like $\mathcal{X}\mathcal{A}$ and $\mathcal{X}\mathcal{B}$. As mentioned above there are two different techniques to render this synthesis condition an LMI. The first technique, also first historically, uses the elimination lemma [GA94, Lemma 3.1] to recover the convexity. We will call this method "*synthesis via elimination of variables*" hereafter. The second technique uses some congruence transformations to obtain LMIs in some transformed controller variables [CG96,SGC97]. We will call this method "*synthesis via change of variables*" hereafter. In the following both techniques are presented for $\mathscr{H}_\infty$ controller design. The synthesis via change of variables method is presented first.

Controller Synthesis via Change of Variables

As a first step towards rendering the problem convex , partition $\mathcal{X}$ and $\mathcal{X}^{-1}$ as,

$$\mathcal{X} = \begin{pmatrix} X & U \\ U' & \bullet \end{pmatrix}, \ \mathcal{X}^{-1} = \begin{pmatrix} Y & V \\ V' & \bullet \end{pmatrix}, \tag{5.16}$$

where X, Y, U, V have same dimensions as A and $\bullet$ indicates entries that are not relevant for what follows. Consider

$$\mathcal{Y} = \begin{pmatrix} Y & I \\ V' & 0 \end{pmatrix} \tag{5.17}$$

with

$$\mathcal{Y}'\mathcal{X} = \begin{pmatrix} Y & V \\ I & 0 \end{pmatrix} \begin{pmatrix} X & U \\ U' & \bullet \end{pmatrix} = \begin{pmatrix} I & 0 \\ X & U \end{pmatrix} \tag{5.18}$$

Using $\mathcal{Y}$ and $\begin{pmatrix} \mathcal{Y} & 0 \\ 0 & I \end{pmatrix}$ to perform a congruence transformation on (5.14) and on (5.15) respectively, the following theorem is obtained.

Theorem 5.5 *(Synthesis via Change of Variables) There exist a controller* $\begin{pmatrix} A_K & B_K \\ C_K & D_K \end{pmatrix}$ *and a matrix* $\mathcal{X}$ *which satisfy (5.14) and (5.15) if and only if the following LMIs in* X, Y, K, L, M, N *admit a feasible solution,*

$$\begin{pmatrix} Y & I \\ I & X \end{pmatrix} > 0 \tag{5.19}$$

$$\left(\begin{array}{c|c} \begin{pmatrix} \mathbf{A}' + \mathbf{A} & \mathbf{B} \\ \mathbf{B}' & 0 \end{pmatrix} + \begin{pmatrix} 0 & I \\ \mathbf{C} & \mathbf{D} \end{pmatrix}' \begin{pmatrix} -\gamma I & 0 \\ 0 & 0 \end{pmatrix} \begin{pmatrix} 0 & I \\ \mathbf{C} & \mathbf{D} \end{pmatrix} & \begin{pmatrix} \mathbf{C} & \mathbf{D} \end{pmatrix}' T_p' \\ \hline T_p \begin{pmatrix} \mathbf{C} & \mathbf{D} \end{pmatrix} & -I \end{array} \right) < 0 \tag{5.20}$$

where $\frac{1}{\gamma} I = T_p' T_p$ *and*

$$\begin{pmatrix} \mathbf{A} & \mathbf{B} \\ \mathbf{C} & \mathbf{D} \end{pmatrix} = \left(\begin{array}{cc|c} AY + B_u M & A + B_u N C_y & B_w + B_u N D_{yw} \\ K & XA + LC_y & XB_w + LD_{yw} \\ \hline C_z Y + D_{zu} M & C_z + D_{zu} N C_y & D_{zw} + D_{zu} N D_{yw} \end{array} \right) \tag{5.21}$$

If a feasible solution exists, a controller and a matrix $\mathcal{X}$ that solve (5.14) and (5.15) can be computed as

i. *Compute two full-column rank matrices U and V such that $I - XY = UV'$.*

ii. *Construct controller matrices as*

$$\begin{pmatrix} A_K & B_K \\ C_K & D_K \end{pmatrix} = \begin{pmatrix} U & XB \\ 0 & I \end{pmatrix}^{-1} \begin{pmatrix} K - XAY & L \\ M & N \end{pmatrix} \begin{pmatrix} V' & 0 \\ CY & I \end{pmatrix}^{-1}. \tag{5.22}$$

iii. *Determine the Lyapunov matrix $\mathcal{X}$ as*

$$\mathcal{X} = \begin{pmatrix} Y & V \\ I & 0 \end{pmatrix}^{-1} \begin{pmatrix} I & 0 \\ X & U \end{pmatrix} \tag{5.23}$$

[Det01, Theorem 18]

Matrix inequality (5.20) does not allow direct minimisation of the $\mathscr{L}_2$ gain, since γ does not appear in an affine manner. An equivalent LMI condition, which is more user friendly, can be obtained through elementary matrix operations and Schur complement arguments as [SGC97]

$$\begin{pmatrix} XA + (*) + LC_y + (*) & * & * & * \\ K' + A + B_u N C_y & AY + (*) + B_u M + (*) & * & * \\ (XB_w + LD_{yw})' & (B_w + B_u N D_{yw})' & -\gamma I & * \\ C_z + D_{zu} N C_y & C_z Y + D_{zu} M & D_{zw} + D_{zu} N D_{yw} & -\gamma I \end{pmatrix} < 0 \tag{5.24}$$

The parameter transformation (5.21) plays a crucial role in several difficult synthesis problems such as the $\mathscr{H}_\infty$ control with pole placement constraints [CG96] or multi-objective output feedback control [SGC97].

Controller Synthesis via Elimination of Variables

The synthesis procedure via variable elimination is not as general as the synthesis via transformation of variables since the possibility of eliminating variables depends on the number and on the structure of the underlying LMIs. In problems in which the controller parameters appear in one LMI only it is possible to eliminate all the controller parameters. In the following controller synthesis by elimination of variables for the $\mathscr{H}_\infty$ performance is described.

Theorem 5.6 *(Synthesis via Elimination of Variables) There exists a stabilising controller that achieves $\|T\|_\infty < \gamma_0$ if and only if there exists X and Y that solve the following inequalities for $\gamma = \gamma_0$,*

$$\begin{pmatrix} Y & I \\ I & X \end{pmatrix} > 0 \tag{5.25}$$

$$\begin{pmatrix} \phi_1 \\ \phi_2 \end{pmatrix}' \left(\begin{array}{cc} I & 0 \\ 0 & I \\ \hline XA & XB_w \\ C_z & D_{zw} \end{array}\right)' \left(\begin{array}{cc|cc} 0 & 0 & I & 0 \\ 0 & -\gamma I & 0 & 0 \\ \hline I & 0 & 0 & 0 \\ 0 & 0 & 0 & \frac{1}{\gamma} I \end{array}\right) \left(\begin{array}{cc} I & 0 \\ 0 & I \\ \hline XA & XB_w \\ C_z & D_{zw} \end{array}\right) \begin{pmatrix} \phi_1 \\ \phi_2 \end{pmatrix} < 0 \tag{5.26}$$

$$\begin{pmatrix} \psi_1 \\ \psi_2 \end{pmatrix}' \left(\begin{array}{cc} -YA' & -YC_z' \\ -B_w' & -D_{zw}' \\ \hline I & 0 \\ 0 & I \end{array}\right)' \left(\begin{array}{cc|cc} 0 & 0 & I & 0 \\ 0 & -\frac{1}{\gamma} I & 0 & 0 \\ \hline I & 0 & 0 & 0 \\ 0 & 0 & 0 & \gamma I \end{array}\right) \left(\begin{array}{cc} -YA' & -YC_z' \\ -B_w' & -D_{zw}' \\ \hline I & 0 \\ 0 & I \end{array}\right) \begin{pmatrix} \psi_1 \\ \psi_2 \end{pmatrix} > 0 \tag{5.27}$$

where $\begin{pmatrix} \phi_1 \\ \phi_2 \end{pmatrix}$ *and* $\begin{pmatrix} \psi_1 \\ \psi_2 \end{pmatrix}$ *denote bases of the null spaces of (C_y, D_{yw}) and (B_u', D_{zu}') respectively* [Det01, Theorem 22].

In the present form the inequalities in Theorem 5.6 do not allow a direct minimisation of γ in order to determine the optimal $\mathscr{H}_\infty$ performance, since they do not depend affinely on this parameter. As usual, equivalent LMI conditions can be obtained via Schur complement arguments. In fact inequalities (5.26) and (5.27) can be rewritten in their more familiar form as [GA94]

$$\left(\begin{array}{c|c} \phi & 0 \\ \hline 0 & I \end{array}\right)' \left(\begin{array}{cc|c} XA + A'X & XB_w & C_z' \\ * & -\gamma I & D_{zw}' \\ \hline * & * & -\gamma I \end{array}\right) \left(\begin{array}{c|c} \phi & 0 \\ \hline 0 & I \end{array}\right) < 0 \tag{5.28}$$

$$\left(\begin{array}{c|c} \psi & 0 \\ \hline 0 & I \end{array}\right)' \left(\begin{array}{cc|c} YA' + AY & YC_z' & B_w \\ * & -\gamma I & D_{zw} \\ \hline * & * & -\gamma I \end{array}\right) \left(\begin{array}{c|c} \psi & 0 \\ \hline 0 & I \end{array}\right) < 0 \tag{5.29}$$

with $\phi = \begin{pmatrix} \phi_1 \\ \phi_2 \end{pmatrix}$ and $\psi = \begin{pmatrix} \psi_1 \\ \psi_2 \end{pmatrix}$.

Theorem 5.6 guarantees only the existence of a γ-suboptimal $\mathscr{H}_\infty$ controller, but it does not directly offer a way to compute it. There are several ways of computing the controller after having solved the above LMIs for X, Y and γ. One way is to compute $\mathcal{X}$ via the factorisation $I - XY = UV'$ and (5.23). Once $\mathcal{X}$ has been calculated, the controller parameters A_K, B_K, C_K, D_K can be obtained by directly solving (5.15). Another way is to use the explicit controller formulae given in [IS94, Gah96]

Remark 5.4 *The synthesis via elimination of variables requires the solution of two sequential systems of LMIs: one for computing X and Y, and one for computing the controller parameters. On the other hand the synthesis via transformation of variables requires the solution of only one system of LMIs, but with a larger number of decision variables. This makes the synthesis via elimination of variables the only method to obtain numerically tractable solutions for problems of large size.*

5.2.2 Example: LTI $\mathscr{H}_\infty$ Loop Shaping Controller Design

This example will demonstrate some features of the robust control system design in the $\mathscr{H}_\infty$ loop shaping paradigm which is described briefly in Appendix C for completeness and convenience of the reader. The plant considered is a simplified AFR path model with two sub-blocks. The LTI part of the model, denoted G_x, is the identified gas mixing and sensor dynamics at $P_m = 40kPa$, IVO=$-5°$, EVC=$10°$ ATDC,

$$G_x(z) = \frac{0.06273}{z^2 - 1.516z + 0.5792} \tag{5.30}$$

The time-varying part is an output delay that varies from 8 events at $30kPa$ to 2 events at $60kPa$ linearly. A second order approximation in LFT form is used to approximate the delay as suggested in Section 4.3. The overall plant G can be expressed as an upper LFT of the normalised manifold pressure ρ in the event based discrete-time as $G = \mathcal{F}_u(P, \Delta)$, where

$$P = \left[\begin{array}{cccc|ccc} 0 & 1 & 0 & 0 & 0 & 0 & 0 \\ -0.5792 & 1.5165 & 0 & 0 & 0 & 0 & 0.062728 \\ 0.57143 & 0 & 0.42857 & 0 & 0.85714 & 0 & 0 \\ -0.2449 & 0 & 0.81633 & 0.42857 & 0.4898 & 0.85714 & 0 \\ \hline 0.28571 & 0 & -0.28571 & 0 & 0.42857 & 0 & 0 \\ -0.12245 & 0 & 0.40816 & -0.28571 & 0.2449 & 0.42857 & 0 \\ 0.18367 & 0 & -0.61224 & 1.4286 & -0.36735 & 0.85714 & 0 \end{array}\right] \tag{5.31}$$

$\Delta = \begin{pmatrix} \rho & 0 \\ 0 & \rho \end{pmatrix}$ with $|\Delta| \leq 1$ and, ρ denotes the manifold pressure normalised to the range $-1 \leq \rho \leq 1$. Since this system is not LTI, the loop shaping controller is designed for the nominal plant $G_0 = \mathcal{F}_u(P, 0_2)$. The design objectives are twofold:

- Robust Stability: The LTI robust stability margin ϵ_{lti} is required to be higher than 0.19 for all frozen values of ρ.

- High Performance: A good disturbance rejection performance with zero steady state error and a bandwidth of no less than $0.1 rad/event$.

The magnitude of the open-loop plant (.- line) is plotted in Figure 5.5. As the system under consideration is in event based discrete-time, the frequency axis is in $rad/event$ and $w = \pi$ represents the Nyquist frequency. The second order Padé based approximation of the delay introduces RHP zeros at frequencies $0.8 rad/event$ and $2 rad/event$. Therefore, for a robust closed-loop system the loop bandwidth must be smaller than $0.8 rad/event$. This is compatible with the targeted closed-loop bandwidth of no less than $0.1 rad/event$. The design objectives can be achieved by appropriate choice of pre- and post-compensators. The pre-compensator W_1 is chosen as a PI weight. The integrator in W_1 is necessary for zero steady state error. It also improves the performance by boosting the low frequency gain. The proportional gain is used to reduce the phase lag introduced by the integrator around the cross-over frequency. The overall PI parameters of W_1, depicted in Figure 5.6,

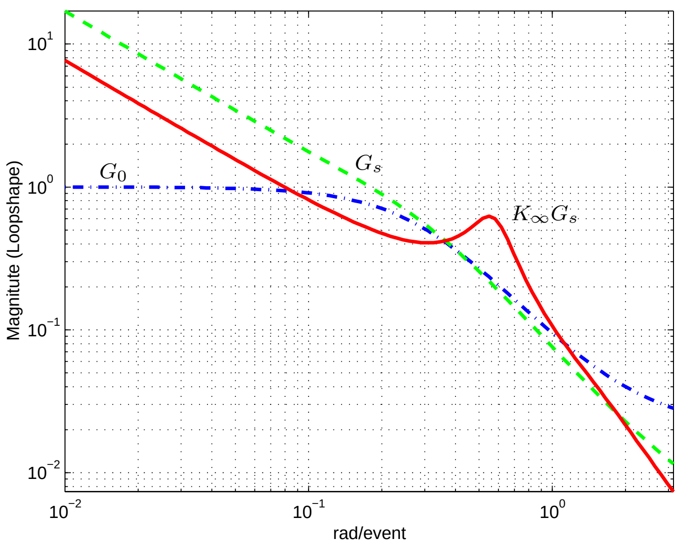

Figure 5.5 Singular values of nominal plant G_0, weighted plant G_s and $K_\infty G_s$

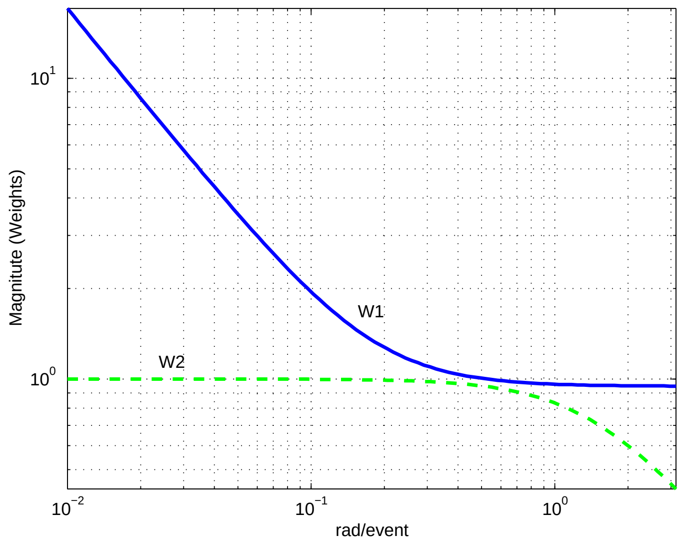

Figure 5.6 $\mathscr{H}_\infty$ loop shaping weights

are chosen to set the cross-over frequency of the weighted plant at $0.18 rad/event$

$$W_1(s) = \frac{0.9458s + 0.1703}{s}. \tag{5.32}$$

These parameters achieve smooth transition of the loop shape around the cross-over frequency. The post-compensator W_2, depicted in Figure 5.6, is chosen to ensure sufficient high frequency noise attenuation

$$W_2(s) = \frac{1.5}{s + 1.5}. \tag{5.33}$$

Once the weights are chosen and $G_s = W_2 G_0 W_1$ is formed, the sub-optimal $\mathscr{H}_\infty$ loop shaping controller K_∞ can easily be calculated using the μ-tools command "ncfsyn($\cdot$)" in MATLAB. This gives the value of the LTI robust stability margin for the closed-loop as $\epsilon_{\rm lti} = 0.411$ and also achieves $\epsilon_{\rm lti} \geq 0.19$ for all the frozen values of $|\rho| \leq 1$ as it can be seen in Figure 5.7.

5.3 Gain-scheduling and LPV Systems

Gain-scheduling is a popular design method often used by practical control engineers, when the controlled plant is so highly nonlinear that linear control techniques cannot be applied to it [SA91a,RS00]. Usually the designer selects the necessary number of operating points to cover the whole operating envelope, and then a controller is designed at each operating point using the linearised model of the plant at this operating point. In between

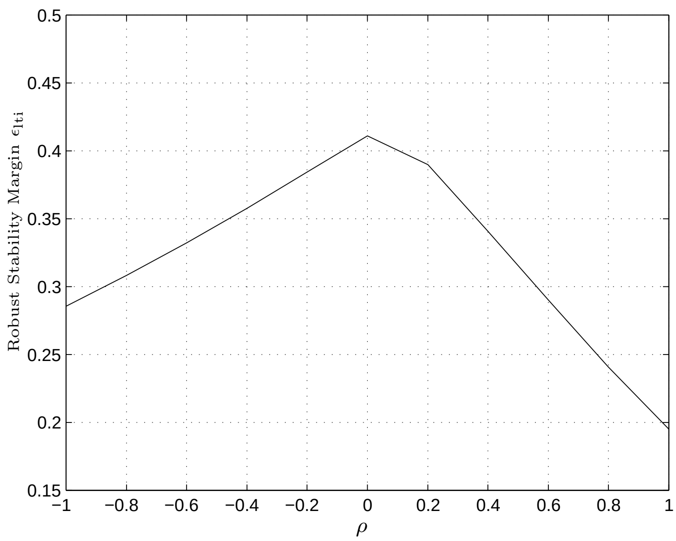

Figure 5.7 Robust Stability margin for the frozen values of ρ

the operating points, the parameters (gains) of the controllers are interpolated to cover the whole operating envelope. The result is a global feedback law obtained by gain-scheduling. The main drawback is the lack of guarantees that show that the interpolation of the LTI controllers will stabilise the nonlinear plant. This is because the global feedback law resulted from the gain-scheduling is a nonlinear controller and the guarantees of the linear synthesis methods do not hold anymore even though the gain scheduled controllers are known to work in practise. Hence, the designer spends most of his/her time to show that the gain-scheduling controller performs well by extensive computer simulations, as one cannot assess a priori the guaranteed stability, robustness, and performance properties of the gain-scheduled control law. Two prominent gain-scheduling guidelines are [SA90, SA91b]

- The scheduling variables should capture the plant's nonlinearities;

- The scheduling variables should vary slowly;

These guidelines also reveal the fundamental limitations on the achievable performance by the gain-scheduling design.

In contrast to the classical gain-scheduling techniques discussed above, the recently developed robust gain-scheduling methods [RS00] in the LPV framework provide systematic ways to design controllers that are scheduled on the operating point of the system. An LPV system is a linear system whose describing matrices depend on a time-varying parameter vector $\rho(t)$ as

$$\left(\begin{array}{c} \dot{x} \\ \hline z \\ y \end{array}\right) = \left(\begin{array}{c|cc} A(\rho(t)) & B_w(\rho(t)) & B_u(\rho(t)) \\ \hline C_z(\rho(t)) & D_{zw}(\rho(t)) & D_{zu}(\rho(t)) \\ C_y(\rho(t)) & D_{yw}(\rho(t)) & 0 \end{array}\right) \left(\begin{array}{c} x \\ \hline w \\ u \end{array}\right) \tag{5.34}$$

where $A(.)$, $B_w(.)$, $B_u(.)$, $C_z(.)$, $C_y(.)$, $D_{zw}(.)$, $D_{zu}(.)$, $D_{yw}(.)$ are continuous matrix valued functions of $\rho(t)$, which varies in the set of continuously differentiable parameter curves $\rho : [0, \infty) \to \mathbb{R}^k$. Both $\rho(t)$ and its rate of variation $\dot{\rho}(t)$ are contained in prespecified compact sets Γ and $\dot{\Gamma}$. The parameter vector ρ is composed of different real parameters ρ_i each one of them varying between $\underline{\rho}_i$ and $\overline{\rho}_i$

$$\rho(t) \in [\underline{\rho}_i, \overline{\rho}_i],\ \forall t \geq 0,\ \ i = 1, \cdots, k. \tag{5.35}$$

The rate of variation $\dot{\rho}_i$ is assumed to be well-defined at all times and satisfies

$$\dot{\rho}(t) \in [\underline{q}_i, \overline{q}_i],\ \forall t \geq 0,\ \ i = 1, \cdots, k. \tag{5.36}$$

LPV techniques do not require the heuristic interpolation of the locally designed controllers and allow designing a family of linear controllers with the theoretical guarantees of stability and performance for the whole operating envelope. Control design problems in the LPV framework are formulated as LMI optimisation problems which are then solved very efficiently using currently available semi-definite programming codes [GNLC95]. There are two different approaches for the LPV controller synthesis:

- **LFT/LPV Methods** It is assumed that the LPV plant accepts an LFT dependence on the scheduling parameters. Although the LFT/LPV controller design methods considered here all seek a single Lyapunov function that guarantees an $\mathscr{H}_\infty$ performance for the closed-loop system, they differ in terms of the techniques used in order to derive the synthesis conditions. The first method uses the optimally scaled small gain theorem to find a Lyapunov function [Pac94, AG95]. This method, we will call "*LFT/LPV synthesis with basic scalings*" hereafter, is very conservative due to the very special structure of the scalings introduced in order to render the synthesis conditions convex. These scalings do not take into account the realness of the scheduling parameter. A less conservative LFT/LPV method that employs scalings with skew-symmetric off-diagonal terms is proposed in [Hel95, SE95]. This method, we will call "*LFT/LPV design with skew-symmetric scalings*" hereafter, takes into account the realness of the scheduling parameters. The conservatism due to the use of the structured scalings in the LFT/LPV synthesis methods is reduced by introduction of full block scalings in [Sch01]. We will call this method "*LFT/LPV* *synthesis with full block scalings*" hereafter. The LFT/LPV methods provide a very attractive framework for searching a single Lyapunov function that establishes stability and performance bounds for the LPV system. The main drawback of these methods is that they cannot take into account the limits of the rates of variations of the scheduling parameters. This makes them very conservative when the scheduling parameters do not vary fast.

- **Grid/LPV Methods** These methods allow a general parameter dependence on the scheduling parameters in the LPV plant representation as in (5.37). The first Grid/LPV method seeks a single Lyapunov function by gridding the parameter space [BP94]. However it suffers from the same main drawback as the LFT/LPV synthesis methods, i.e. it allows for arbitrary rates of variation in the scheduled parameters. A significant improvement over the single Lyapunov function based techniques is obtained by introducing the concept of parameter-dependent Lyapunov functions [WYPB96, Bec96, AA98]. In this method parameter-dependent Lyapunov functions are searched by gridding both the parameter space and the limits of the parameter rates. Although this method leads to much less conservative designs, it also increases the computational complexity of the LMIs solved in the synthesis significantly.

The rest of the chapter presents both the LFT/LPV and Grid/LPV methods in a unified framework as much as possible. The reason for presenting both techniques is that they both have their advantages and disadvantages over each other and therefore depending on the control problem at hand one can decide which method to employ. These points will be made more clear in the following.

5.3.1 General Parameter Dependence

For an LPV system of the form,

$$\begin{pmatrix} \dot{x} \\ z \end{pmatrix} = \begin{pmatrix} \mathcal{A}(\rho(t)) & \mathcal{B}(\rho(t)) \\ \mathcal{C}(\rho(t)) & \mathcal{D}(\rho(t)) \end{pmatrix} \begin{pmatrix} x \\ w \end{pmatrix}, \tag{5.37}$$

where $\rho(t)$ and its rate of variation $\dot{\rho}(t)$ are contained in prespecified compact sets Γ and $\dot{\Gamma}$, the following theorem states the main analysis condition.

Theorem 5.7 *If there exists a continuously differentiable function $\mathcal{X}(\rho)$ defined on Γ and such that*

$$\mathcal{X}(\rho) > 0 \tag{5.38}$$

$$\left(\begin{array}{cc} I & 0 \\ \mathcal{A}(\rho) & \mathcal{B}(\rho) \\ \hline 0 & I \\ \mathcal{C}(\rho) & \mathcal{D}(\rho) \end{array}\right)' \left(\begin{array}{cc|cc} \dot{\mathcal{X}}(\rho) & \mathcal{X}(\rho) & 0 & 0 \\ \mathcal{X}(\rho) & 0 & 0 & 0 \\ \hline 0 & 0 & -\gamma I & 0 \\ 0 & 0 & 0 & \frac{1}{\gamma} I \end{array}\right) \left(\begin{array}{cc} I & 0 \\ \mathcal{A}(\rho) & \mathcal{B}(\rho) \\ \hline 0 & I \\ \mathcal{C}(\rho) & \mathcal{D}(\rho) \end{array}\right) < 0 \tag{5.39}$$

hold for all $(\rho, \dot{\rho}) \in \Gamma \times \dot{\Gamma}$, *then the system (5.37) is uniformly exponentially stable and the* L_2 *gain from* w *to* z *is smaller than* γ. [Det01, Theorem 24]

Note that $\dot{\mathcal{X}}(\rho)$ is a function of both $\rho(t)$ and $\dot{\rho}(t)$ as

$$\dot{\mathcal{X}}(\rho) = \sum_{i=1}^{k} \frac{\partial \mathcal{X}}{\partial \rho_i}(\rho(t))\dot{\rho}_i(t). \tag{5.40}$$

There are two main difficulties for the use of the above analysis theorem in the LMI framework. The first difficulty is that the inequalities must hold at an infinite number of points $(\rho, \dot{\rho}) \in \Gamma \times \dot{\Gamma}$. By observing that the parameter $\dot{\rho}$ enters the inequalities affinely, the test for all $\dot{\rho} \in \dot{\Gamma}$ can be reduced to only checking the extreme points of $\dot{\Gamma}$ as given in (5.36). Moreover by gridding the parameter space Γ, the infinite dimensional problem can be approximated with a finite problem. The second main difficulty is that the conditions in the theorem are functional inequalities and cannot be solved by the standard LMI algorithms. This can be alleviated by assigning a particular structure for $\mathcal{X}(\rho)$. These points will be further discussed in Section 5.3.3 in the context of LPV controller synthesis for general parameter dependence.

5.3.2 Rational Parameter Dependence

Instead of solving (5.38) and (5.39) directly there is an alternative way that leads to a finite number of LMIs with guaranteed validity over the whole parameter space, whenever the LPV system has a rational dependence on the parameter ρ. Such an LPV system can be expressed as an LFT

$$\left(\begin{array}{c} \dot{x} \\ \hline z_\Delta \\ z \end{array}\right) = \left(\begin{array}{c|cc} \mathcal{A} & \mathcal{B}_\Delta & B_w \\ \hline \mathcal{C}_\Delta & \mathcal{D}_\Delta & \mathcal{D}_{\Delta w} \\ C_z & \mathcal{D}_{z\Delta} & D_{zw} \end{array}\right) \left(\begin{array}{c} x \\ \hline w_\Delta \\ w \end{array}\right), \tag{5.41}$$

with

$$w_\Delta = \Delta(\rho) z_\Delta \tag{5.42}$$

where $\mathcal{A}$, $\mathcal{B}_\Delta$, B_w, $\mathcal{C}_\Delta$, C_z, $\mathcal{D}_\Delta$, $\mathcal{D}_{\Delta w}$, $\mathcal{D}_{z\Delta}$, D_{zw} are constant real matrices, and $\Delta(\rho)$ is a linear function of the parameter vector. Without loss of generality, it can always be chosen as $\Delta(\rho) = diag(\rho_1 I_1, ..., \rho_k I_k)$. A straightforward application of the full block S-procedure [Sch01] to (5.39) with the LPV system given by the LFT representation (5.41) leads to the following analysis characterisation for the LFT/LPV synthesis methods.

Theorem 5.8 *If there exists a symmetric matrix $\mathcal{X}$ and scalings $Q = Q'$, S, and $R = R'$ such that*

$$\mathcal{X} > 0 \tag{5.43}$$

and

$$\begin{pmatrix} I & 0 & 0 \\ \mathcal{A} & \mathcal{B}_w & \mathcal{B}_\Delta \\ \hline 0 & I & 0 \\ \mathcal{C}_z & \mathcal{D}_{zw} & \mathcal{D}_{z\Delta} \\ \hline 0 & 0 & I \\ \mathcal{C}_\Delta & \mathcal{D}_{\Delta w} & \mathcal{D}_\Delta \end{pmatrix}' \left(\begin{array}{cc|cc|cc} 0 & \mathcal{X} & 0 & 0 & 0 & 0 \\ \mathcal{X} & 0 & 0 & 0 & 0 & 0 \\ \hline 0 & 0 & -\gamma I & 0 & 0 & 0 \\ 0 & 0 & 0 & \frac{1}{\gamma} I & 0 & 0 \\ \hline 0 & 0 & 0 & 0 & Q & S \\ 0 & 0 & 0 & 0 & S' & R \end{array}\right) \begin{pmatrix} I & 0 & 0 \\ \mathcal{A} & \mathcal{B}_w & \mathcal{B}_\Delta \\ \hline 0 & I & 0 \\ \mathcal{C}_z & \mathcal{D}_{zw} & \mathcal{D}_{z\Delta} \\ \hline 0 & 0 & I \\ \mathcal{C}_\Delta & \mathcal{D}_{\Delta w} & \mathcal{D}_\Delta \end{pmatrix} < 0 \tag{5.44}$$

and

$$\begin{pmatrix} \Delta(\rho) \\ I \end{pmatrix}' \begin{pmatrix} Q & S \\ S' & R \end{pmatrix} \begin{pmatrix} \Delta(\rho) \\ I \end{pmatrix} > 0 \; for\, all\, \rho \in \Gamma \tag{5.45}$$

then the system in (5.41) is uniformly exponentially stable and $\mathscr{L}_2$ gain from w to z is smaller than γ for all $\rho(t)$ which is continuously differentiable and satisfies $\rho(t) \in \Gamma$ for all t [Det01, Theorem 26].

Note that the above theorem does not put any bounds on $\dot{\rho}$ and allows arbitrarly fast variations in the parameter vector ρ. Computationally tractable conditions for (5.45) are obtained through the choice of suitable sets of scalings. This will be discussed in Section 5.3.4 when the LMI synthesis conditions for the LFT/LPV methods will be presented.

Next we will show that $\mathscr{L}_2$ gain is preserved under the Tustin's transformation for an LFT/LPV system. Consider the matrix inequality (5.44), which can be rewritten as

$$\underbrace{\begin{pmatrix} I & 0 & 0 \\ \mathcal{A} & \mathcal{B}_w & \mathcal{B}_\Delta \\ \hline 0 & I & 0 \\ 0 & 0 & I \\ \hline \mathcal{C}_z & \mathcal{D}_{zw} & \mathcal{D}_{z\Delta} \\ \mathcal{C}_\Delta & \mathcal{D}_{\Delta w} & \mathcal{D}_\Delta \end{pmatrix}'}_{\begin{pmatrix} I & 0 \\ A & B \\ \hline 0 & I \\ C & D \end{pmatrix}'} \underbrace{\left(\begin{array}{cc|cc|cc} 0 & \mathcal{X} & 0 & 0 & 0 & 0 \\ \mathcal{X} & 0 & 0 & 0 & 0 & 0 \\ \hline 0 & 0 & -\gamma I & 0 & 0 & 0 \\ 0 & 0 & 0 & Q & 0 & S \\ \hline 0 & 0 & 0 & 0 & \frac{1}{\gamma} I & 0 \\ 0 & 0 & 0 & S' & 0 & R \end{array}\right)}_{\left(\begin{array}{cc|cc} 0 & \mathcal{X} & 0 & 0 \\ \mathcal{X} & 0 & 0 & 0 \\ \hline 0 & 0 & \mathbf{Q} & \mathbf{S} \\ 0 & 0 & \mathbf{S}' & \mathbf{R} \end{array}\right)} \underbrace{\begin{pmatrix} I & 0 & 0 \\ \mathcal{A} & \mathcal{B}_w & \mathcal{B}_\Delta \\ \hline 0 & I & 0 \\ 0 & 0 & I \\ \hline \mathcal{C}_z & \mathcal{D}_{zw} & \mathcal{D}_{z\Delta} \\ \mathcal{C}_\Delta & \mathcal{D}_{\Delta w} & \mathcal{D}_\Delta \end{pmatrix}}_{\begin{pmatrix} I & 0 \\ A & B \\ \hline 0 & I \\ C & D \end{pmatrix}} < 0 \tag{5.46}$$

Matrix inequalities (5.43), (5.46) represent the $\mathscr{L}_2$ γ-gain condition for a continuous-time LFT system described by (A, B, C, D). If the state space data (A, B, C, D) are actually obtained from a discrete-time state space data $(\hat{A}, \hat{B}, \hat{C}, \hat{D}, T_s)$ via Tustin's transformation, i.e.

$$\begin{bmatrix} A & B \\ C & D \end{bmatrix} = \begin{bmatrix} \frac{2}{T_s}(\hat{A}+I)^{-1}(\hat{A}-I) & \frac{2}{\sqrt{T_s}}(\hat{A}+I)^{-1}\hat{B} \\ \frac{2}{\sqrt{T_s}}\hat{C}(\hat{A}+I)^{-1} & \hat{D}-\hat{C}(\hat{A}+I)^{-1}\hat{B} \end{bmatrix}, \tag{5.47}$$

then, it can be shown after some simple matrix algebra that applying the following similarity and congruence transformations, $\mathcal{M}$ and $\mathcal{L}$, on (5.46) as suggested below

$$\left(\begin{array}{c|c} \mathcal{M} & 0 \\ \hline 0 & I \end{array}\right) \left(\begin{array}{cc} I & 0 \\ A & B \\ \hline 0 & I \\ C & D \end{array}\right) \mathcal{L} = \left(\begin{array}{cc} I & 0 \\ \hat{A} & \hat{B} \\ \hline 0 & I \\ \hat{C} & \hat{D} \end{array}\right), \tag{5.48}$$

$$\left(\begin{array}{c|c} \mathcal{M} & 0 \\ \hline 0 & I \end{array}\right)^{\prime -1} \left(\begin{array}{cc|cc} 0 & \mathcal{X} & 0 & 0 \\ \mathcal{X} & 0 & 0 & 0 \\ \hline 0 & 0 & \mathbf{Q} & \mathbf{S} \\ 0 & 0 & \mathbf{S}' & \mathbf{R} \end{array}\right) \left(\begin{array}{c|c} \mathcal{M} & 0 \\ \hline 0 & I \end{array}\right)^{-1} = \left(\begin{array}{cc|cc} -\hat{\mathcal{X}} & 0 & 0 & 0 \\ 0 & \hat{\mathcal{X}} & 0 & 0 \\ \hline 0 & 0 & \hat{\mathbf{Q}} & \hat{\mathbf{S}} \\ 0 & 0 & \hat{\mathbf{S}}' & \hat{\mathbf{R}} \end{array}\right), \tag{5.49}$$

with

$$\mathcal{L} = \begin{bmatrix} \frac{\sqrt{T_s}}{2}(A+I) & \frac{\sqrt{T_s}}{2}B \\ 0 & I \end{bmatrix} \tag{5.50}$$

$$\mathcal{M} = \begin{bmatrix} \frac{I}{\sqrt{T_s}} & -\frac{\sqrt{T_s}}{2}I \\ \frac{I}{\sqrt{T_s}} & \frac{\sqrt{T_s}}{2}I \end{bmatrix} \tag{5.51}$$

transforms (5.46) to the equivalent $\mathscr{L}_2$ γ-gain condition for the discrete-time system $(\hat{A}, \hat{B}, \hat{C}, \hat{D}, T_s)$ as

$$\hat{\mathcal{X}} > 0, \tag{5.52}$$

$$\left(\begin{array}{cc} I & 0 \\ \hat{A} & \hat{B} \\ \hline 0 & I \\ \hat{C} & \hat{D} \end{array}\right)' \left(\begin{array}{cc|cc} -\hat{\mathcal{X}} & 0 & 0 & 0 \\ 0 & \hat{\mathcal{X}} & 0 & 0 \\ \hline 0 & 0 & \hat{\mathbf{Q}} & \hat{\mathbf{S}} \\ 0 & 0 & \hat{\mathbf{S}}' & \hat{\mathbf{R}} \end{array}\right) \left(\begin{array}{cc} I & 0 \\ \hat{A} & \hat{B} \\ \hline 0 & I \\ \hat{C} & \hat{D} \end{array}\right) < 0 \tag{5.53}$$

where $\hat{\mathcal{X}} = \mathcal{X}$, $\hat{\mathbf{Q}} = \mathbf{Q}$, $\hat{\mathbf{S}} = \mathbf{S}$, $\hat{\mathbf{R}} = \mathbf{R}$. This concludes that analysing the $\mathscr{L}_2$ gain of a discrete-time LFT/LPV system $(\hat{A}, \hat{B}, \hat{C}, \hat{D}, T_s)$ is equivalent to first taking the Tustin's transform of the discrete-time system and then applying Theorem 5.8 on the transformed system state space data (A, B, C, D).

5.3.3 LPV Controller Synthesis for General Parameter Dependence

Consider the generalised LPV plant described in (5.34) with the state space realisation

$$\begin{pmatrix} \dot{x} \\ \hline z \\ y \end{pmatrix} = \left(\begin{array}{c|cc} A(\rho(t)) & B_w(\rho(t)) & B_u(\rho(t)) \\ \hline C_z(\rho(t)) & D_{zw}(\rho(t)) & D_{zu}(\rho(t)) \\ C_y(\rho(t)) & D_{yw}(\rho(t)) & 0 \end{array}\right) \begin{pmatrix} x \\ \hline w \\ u \end{pmatrix} \tag{5.54}$$

The analysis theorem 5.7 can be applied to the closed-loop LPV system to synthesise a controller of the form,

$$\begin{pmatrix} \dot{x}_K \\ u \end{pmatrix} = \begin{pmatrix} A_K(\rho(t),\dot{\rho}(t)) & B_K(\rho(t),\dot{\rho}(t)) \\ C_K(\rho(t),\dot{\rho}(t)) & D_K(\rho(t),\dot{\rho}(t)) \end{pmatrix} \begin{pmatrix} x_K \\ y \end{pmatrix}, \tag{5.55}$$

to ensure the internal stability and a guaranteed $\mathscr{L}_2$ gain bound γ from the disturbance signal w to the error signal z. The derivation of the LMI conditions for the LPV controller synthesis follows similar lines as in the case of the LTI controller synthesis in Section 5.2.1. Both the change of variables and elimination of variables techniques can be used to derive the LPV synthesis conditions. The synthesis via change of variables method is presented first. The dependence of the plant and controller parameters on ρ and $\dot{\rho}$ has been dropped for simplicity.

Theorem 5.9 *(Synthesis via Change of Variables) Consider the LPV plant governed by (5.54), with the parameter trajectories constrained by (5.35) ,(5.36). There exist a controller (5.55) enforcing internal stability and a bound γ on the $\mathscr{L}_2$ gain of the closed-loop system (5.54) and (5.55), whenever there exist parameter dependent symmetric matrices Y and X, and a parameter-dependent quadruple of state space data (K, L, M, N) such that for all $(\rho,\dot{\rho}) \in \Gamma \times \dot{\Gamma}$ the following infinite dimensional LMI problem holds*

$$\begin{pmatrix} X & I \\ I & Y \end{pmatrix} > 0 \tag{5.56}$$

$$\begin{pmatrix} \begin{matrix}\dot{X} + XA + (*) + \cdots \\ LC_y + (*)\end{matrix} & * & * & * \\ K' + A + B_uNC_y & \begin{matrix}-\dot{Y} + AY + (*) + \cdots \\ \cdots B_uM + (*)\end{matrix} & * & * \\ (XB_w + LD_{yw})' & (B_w + B_uND_{yw})' & -\gamma I & * \\ C_z + D_{zu}NC_y & C_zY + D_{zu}M & \begin{matrix}D_{zw} + \cdots \\ \cdots D_{zu}ND_{yw}\end{matrix} & -\gamma I \end{pmatrix} < 0 \tag{5.57}$$

If a solution exists, an LPV controller is readily obtained with the following two-step scheme

- *Solve for U, V, the factorisation problem $I - XY = UV'$.*
- *Compute A_K, B_K, C_K, and D_K with*

$$A_K = U^{-1}(X\dot{Y} + U\dot{V}' + K - X(A - B_uNC_y)Y - LC_yY - XB_uM)V^{-'} \quad (5.58)$$
$$B_K = U^{-1}(L - XB_uN) \quad (5.59)$$
$$C_K = (M - NC_yY)V^{-'} \quad (5.60)$$
$$D_K = N \quad (5.61)$$

[AA98, Theorem 2.1]

Alternatively, through the elimination lemma the controller variables can be eliminated leading to a characterisation involving the variables X and Y only. This is presented in the next theorem.

Theorem 5.10 *(Synthesis via Elimination of Variables) Consider the LPV plant governed by (5.54), with the parameter trajectories constrained by (5.35) ,(5.36). There exist a controller (5.55) enforcing internal stability and a bound γ on the $\mathscr{L}_2$ gain of the closed-loop system (5.54) and (5.55), whenever there exist parameter dependent symmetric matrices Y and X such that for all $(\rho, \dot{\rho}) \in \Gamma \times \dot{\Gamma}$ the following infinite dimensional LMI problem holds*

$$\begin{pmatrix} X & I \\ I & Y \end{pmatrix} > 0 \quad (5.62)$$

$$\left(\begin{array}{c|c} \phi & 0 \\ \hline 0 & I \end{array}\right)' \left(\begin{array}{cc|c} \dot{X} + XA + A'X & XB_w & C_z' \\ * & -\gamma I & D_{zw}' \\ \hline * & * & -\gamma I \end{array}\right) \left(\begin{array}{c|c} \phi & 0 \\ \hline 0 & I \end{array}\right) < 0 \quad (5.63)$$

$$\left(\begin{array}{c|c} \psi & 0 \\ \hline 0 & I \end{array}\right)' \left(\begin{array}{cc|c} -\dot{Y} + YA' + AY & YC_z' & B_w \\ * & -\gamma I & D_{zw} \\ \hline * & * & -\gamma I \end{array}\right) \left(\begin{array}{c|c} \psi & 0 \\ \hline 0 & I \end{array}\right) < 0 \quad (5.64)$$

where ϕ and ψ designate any bases of the null spaces of (C_y, D_{yw}) and (B_u', D_{zu}') respectively. If a feasible solution exists, an LPV controller can be constructed by the following sequential scheme

- *Compute N solution to*

$$\overline{\sigma}(D_{zw} + D_{zu}ND_{yw}) < \gamma \quad (5.65)$$

and set $D_{cl} := D_{zw} + D_{zu}ND_{yw}$.

- *Compute L and M*

$$\begin{pmatrix} 0 & D_{yw} & 0 \\ * & -\gamma I & D'_{cl} \\ * & * & -\gamma I \end{pmatrix} \begin{pmatrix} L' \\ \bullet \end{pmatrix} = \begin{pmatrix} C_y \\ B'_w X \\ C_z + D_{zu} N C_y \end{pmatrix} \tag{5.66}$$

$$\begin{pmatrix} 0 & D'_{zu} & 0 \\ * & -\gamma I & D_{cl} \\ * & * & -\gamma I \end{pmatrix} \begin{pmatrix} M \\ \bullet \end{pmatrix} = \begin{pmatrix} B_u \\ C_z Y \\ B_w + B_u N D_{yw} \end{pmatrix} \tag{5.67}$$

- *Compute*

$$\begin{aligned} K = -(A + B_u N C_y)' + \begin{pmatrix} X B_w + L D_{yw} & (C_z + D_{zu} N C_y)' \end{pmatrix} \\ \cdot \begin{pmatrix} -\gamma I & D'_{cl} \\ * & -\gamma I \end{pmatrix}^{-1} \begin{pmatrix} (B_w + B_u N D_{yw})' \\ C_z Y + D_{zu} M \end{pmatrix} \end{aligned} \tag{5.68}$$

- *Solve U, V as $I - XY = UV'$.*

- *Compute A_K, B_K, C_K, D_K with the help of (5.58)- (5.61).*

[AA98, Theorems 2.2 and 2.3]

Note that in spite of their different structures the characterisations given in Theorems 5.9-5.10, are equivalent and can be virtually used interchangeably for controller synthesis. However, in terms of the computational complexity or practical implementation these techniques exhibit significant differences. The first method, synthesis via change of variables, allows the incorporation of multiple specifications into the design problem such as mixed $\mathscr{H}_\infty$-$\mathscr{H}_2$ optimisation, pole clustering, or control effort constraints. However, it is computationally very intensive due to a much larger number of decision variables in the LMI constraints. The second method, synthesis via elimination of variables, although more restrictive, is computationally very attractive due to a much smaller number of decision variables. In terms of the practical implementation, controller equations resulting from the synthesis via change of variables method are significantly less complex than those resulting from the synthesis via elimination of variables method. At each sampling time the synthesis via change of variables method only requires one matrix inversion, whereas the synthesis via elimination of variables method requires two QR decompositions, three matrix inversions for (5.65) and two matrix inversions for the computation of A_K, B_K, C_K, D_K. Hence controllers resulting from the first technique are more easily implemented in real-time.

In the controller implementation, $I - XY$ should be well-conditioned to avoid the ill-conditioned inversions of the matrices U and V. Unfortunately, $I - XY$ will be nearly singular if the constraint (5.56) or (5.62) is saturated at the optimum. This can be prevented by choosing a suboptimal value of γ and including the following LMI

$$\begin{pmatrix} X & tI \\ tI & Y \end{pmatrix} > 0 \tag{5.69}$$

with the additional variable t in the synthesis LMIs and maximising t. This procedure maximises the minimal eigenvalue of XY and improves the conditioning of $I - XY$.

The LPV controllers derived from Theorems 5.9-5.10 are not gain-scheduled in the usual sense since they require not only the measurement of the parameters ρ but also of their time derivatives $\dot{\rho}$. As this is restrictive in many control problems, a simple but conservative approach is proposed in [Bec96, AA98]. Assuming either X or Y as parameter independent constant matrix variables drop the time derivative dependence in the above theorems. This can be seen by differentiating $I - XY = UV'$ and showing $X\dot{Y} + U\dot{V}' = \dot{X}Y - \dot{U}V'$. This equality can be used in (5.58) to show that A_K is indepedent of $\dot{\rho}$ whenever either $\dot{X} = 0$ or $\dot{Y} = 0$. Due to loss of duality in the variables X and Y, such choices are not equivalent. Therefore, the usual practice is to try both of the cases and use the less conservative one as the final controller.

The LMI conditions presented above cannot be solved due to two main difficulties. First, the functional dependence of X and Y on ρ has to be decided in order to render the conditions to standard LMIs. A useful guideline is to mimic the parameter dependence of the plant in the Lyapunov function variables X and Y. In the case of the synthesis via change of variables method, structures for the parameters K, L, M, N should also be assigned in a similar manner. Second, the synthesis LMIs, which have to be satisfied at an infinite number of points due to their dependence on $(\rho, \dot{\rho})$ ranging over $\Gamma \times \dot{\Gamma}$, have to be approximated with a finite problem. A simple remedy is to grid the parameter space $\rho \in \Gamma$. Since the derivative term $\dot{\rho}$ appears affinely in the LMIs there is only need to check the extreme points of the set $\dot{\Gamma}$ for all the admissible values of ρ. The overall procedure can be described as

i. Define a grid Γ_{grid} for the parameter space Γ and the extreme points of $\dot{\Gamma}$ as $\dot{\Gamma}_{ext}$

ii. Minimise γ subject to the LMI constraints associated with $\Gamma_{grid} \times \dot{\Gamma}_{ext}$

iii. Check the constraints with a denser Γ_{grid}

iv. If step 3 fails, increase the grid density and return to step 2

Remark 5.5 *Once the transformed controller parameters K, L, M, N are restricted to a specific structure the above techniques are no longer equivalent. Hence the synthesis via change of variables method, in which the controller parameters are restricted in structure, is expected to give more conservative results in general.*

Remark 5.6 *Since both methods offer complementary advantages, they can be used together to yield a more effective methodology. All the necessary tunings, requiring repeated computations should be based on the less costly synthesis via elimination of variables method. Once all the design requirements are satisfied, the final controller is calculated through the synthesis via change of variables method for implementation purposes.*

5.3.4 LPV Controller Synthesis for Rational Parameter Dependence

This section describes the formulation of the LPV synthesis problem for the LFT parameter dependence and presents the explicit LMI conditions for its solution. A full presentation of the subject can be found in [Sch00, Sch01]. Consider the following generalised plant with rational parameter dependence,

$$\begin{pmatrix} \dot{x} \\ \hline z_\Delta \\ z \\ y \end{pmatrix} = \left(\begin{array}{c|ccc} A & \mathcal{B}_\Delta & B_w & B_u \\ \hline \mathcal{C}_\Delta & \mathcal{D}_\Delta & \mathcal{D}_{\Delta w} & \mathcal{D}_{\Delta u} \\ C_z & \mathcal{D}_{z\Delta} & D_{zw} & D_{zu} \\ C_y & \mathcal{D}_{y\Delta} & D_{yw} & 0 \end{array}\right) \begin{pmatrix} x \\ \hline w_\Delta \\ w \\ u \end{pmatrix} \tag{5.70}$$

with

$$w_\Delta = \Delta(\rho) z_\Delta \tag{5.71}$$

where $\mathcal{A}$, $\mathcal{B}_\Delta$, B_w, B_u, $\mathcal{C}_\Delta$, C_z, C_y, $\mathcal{D}_\Delta$, $\mathcal{D}_{\Delta w}$, $\mathcal{D}_{\Delta u}$, $\mathcal{D}_{z\Delta}$, D_{zw}, D_{zu}, $\mathcal{D}_{y\Delta}$, D_{yw} are constant real matrices, and $\Delta(\rho)$ is a linear function of the parameter vector. For simplicity it is assumed that the scheduling function is a block-diagonal affine function of ρ, $\Delta(\rho) = diag(\rho_1 I_1, \cdots, \rho_k I_k)$, which causes no loss of generality if ρ enters the system description in a rational way.

The LFT/LPV controller design framework is depicted in Figure 5.8 with the controller given as

$$\begin{pmatrix} \dot{x}_K \\ \hline \begin{pmatrix} u \\ z_K \end{pmatrix} \end{pmatrix} = \begin{pmatrix} A_K & B_K \\ C_K & D_K \end{pmatrix} \begin{pmatrix} x_K \\ \hline \begin{pmatrix} y \\ w_K \end{pmatrix} \end{pmatrix} \tag{5.72}$$

and the scheduling function as

$$w_K = \Delta_K(\rho(t)) z_K \tag{5.73}$$

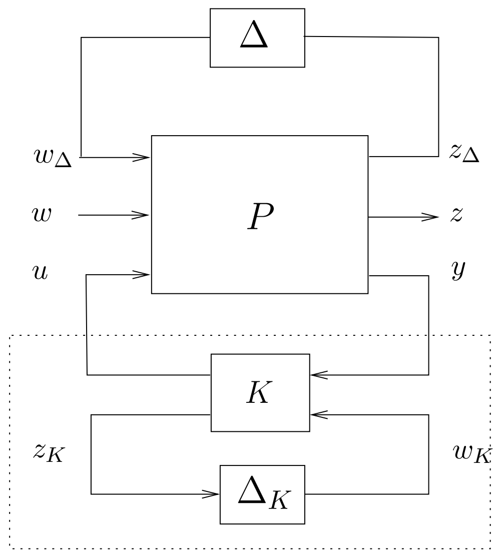

Figure 5.8 LFT control system synthesis framework

.

The aim is to design an LFT/LPV controller to achieve internal stability and $\mathscr{L}_2$ gain from w to z less than γ. This problem can be expressed as an $\mathscr{H}_\infty$ controller synthesis problem for the following generalised plant,

$$\begin{pmatrix} \dot{x} \\ \hline z_\Delta \\ z_K \\ \hline z \\ \hline y \\ w_K \end{pmatrix} = \left(\begin{array}{c|cc|c|cc} A & \mathcal{B}_\Delta & 0 & B_w & B_u & 0 \\ \hline \mathcal{C}_\Delta & \mathcal{D}_\Delta & 0 & \mathcal{D}_{\Delta w} & \mathcal{D}_{\Delta u} & 0 \\ 0 & 0 & 0 & 0 & 0 & I_{c_K} \\ \hline C_z & \mathcal{D}_{z\Delta} & 0 & D_{zw} & D_{zu} & 0 \\ \hline C_y & \mathcal{D}_{y\Delta} & 0 & D_{yw} & 0 & 0 \\ 0 & 0 & I_{r_K} & 0 & 0 & 0 \end{array}\right) \begin{pmatrix} x \\ \hline w_\Delta \\ w_K \\ \hline w \\ \hline u \\ z_K \end{pmatrix} \tag{5.74}$$

and,

$$\begin{pmatrix} w_\Delta \\ w_K \end{pmatrix} = \begin{pmatrix} \Delta(\rho(t)) & 0 \\ 0 & \Delta_K(\rho(t)) \end{pmatrix} \begin{pmatrix} z_\Delta \\ z_K \end{pmatrix}, \tag{5.75}$$

with an LTI controller of the form (5.72). Supposing that Δ_K is LTI, the synthesis of the LTI controller (5.72) is a robust control design problem for the plant (5.74) against the uncertainty (5.75). Due to this special structure of the generalised plant, the LFT/LPV synthesis problem can be reduced to a convex optimisation problem, which is not true in general.

Application of Theorem 5.8 to the closed-loop system formed by interconnection of the plant (5.74) with the controller (5.72) and together with the following scalings,

$$P = \begin{pmatrix} Q & S \\ S' & R \end{pmatrix} = \left(\begin{array}{cc|cc} Q_1 & Q_{12} & S_1 & S_{12} \\ Q_{12}' & Q_2 & S_{21} & S_2 \\ \hline S_1' & S_{21}' & R_1 & R_{12} \\ S_{12}' & S_2' & R_{12}' & R_2 \end{array}\right), \tag{5.76}$$

$$\tilde{P} = \begin{pmatrix} \tilde{Q} & \tilde{S} \\ \tilde{S}' & \tilde{R} \end{pmatrix} = \left(\begin{array}{cc|cc} \tilde{Q}_1 & \tilde{Q}_{12} & \tilde{S}_1 & \tilde{S}_{12} \\ \tilde{Q}_{12}' & \tilde{Q}_2 & \tilde{S}_{21} & \tilde{S}_2 \\ \hline \tilde{S}_1' & \tilde{S}_{21}' & \tilde{R}_1 & \tilde{R}_{12} \\ \tilde{S}_{12}' & \tilde{S}_2' & \tilde{R}_{12}' & \tilde{R}_2 \end{array}\right), \tag{5.77}$$

where $P^{-1} := \tilde{P}$, reveals the main synthesis theorem for the LFT/LPV synthesis.

Theorem 5.11 *(LFT/LPV Synthesis) There exists a controller (5.72), a scheduling function (5.73), a symmetric matrix $\mathcal{X}$ and a scaling P partitioned as in (5.76) satisfying* (5.43), (5.44), (5.45)*, if and only if there exist partial scalings*

$$P_1 = \begin{pmatrix} Q_1 & S_1 \\ S_1' & R_1 \end{pmatrix}, \text{ with } Q_1 < 0, \begin{pmatrix} \Delta(\rho) \\ I \end{pmatrix}' P_1 \begin{pmatrix} \Delta(\rho) \\ I \end{pmatrix} > 0, \forall \rho \in \Gamma \tag{5.78}$$

$$\tilde{P}_1 = \begin{pmatrix} \tilde{Q}_1 & \tilde{S}_1 \\ \tilde{S}_1' & \tilde{R}_1 \end{pmatrix}, \text{ with } \tilde{R}_1 > 0, \begin{pmatrix} I \\ -\Delta(\rho)' \end{pmatrix}' \tilde{P}_1 \begin{pmatrix} I \\ -\Delta(\rho)' \end{pmatrix} < 0, \forall \rho \in \Gamma \tag{5.79}$$

and matrices X and Y that satisfy the following conditions

$$\begin{pmatrix} Y & I \\ I & X \end{pmatrix} > 0 \tag{5.80}$$

$$\phi' \left(\begin{array}{c} * \\ * \\ * \\ \hline * \\ * \\ * \end{array}\right)' \left(\begin{array}{ccc|ccc} 0 & 0 & 0 & I & 0 & 0 \\ 0 & -\gamma I & 0 & 0 & 0 & 0 \\ 0 & 0 & Q_1 & 0 & 0 & S_1 \\ \hline I & 0 & 0 & 0 & 0 & 0 \\ 0 & 0 & 0 & 0 & \frac{1}{\gamma} I & 0 \\ 0 & 0 & S_1' & 0 & 0 & R_1 \end{array}\right) \left(\begin{array}{ccc} I & 0 & 0 \\ 0 & I & 0 \\ 0 & 0 & I \\ \hline XA & XB_w & X\mathcal{B}_\Delta \\ C_y & D_{zw} & \mathcal{D}_{z\Delta} \\ \mathcal{C}_\Delta & \mathcal{D}_{\Delta w} & \mathcal{D}_\Delta \end{array}\right) \phi < 0 \tag{5.81}$$

$$\psi' \left(\begin{array}{c} * \\ * \\ * \\ \hline * \\ * \\ * \end{array}\right)' \left(\begin{array}{ccc|ccc} 0 & 0 & 0 & I & 0 & 0 \\ 0 & -\frac{1}{\gamma} I & 0 & 0 & 0 & 0 \\ 0 & 0 & \tilde{Q}_1 & 0 & 0 & \tilde{S}_1 \\ \hline I & 0 & 0 & 0 & 0 & 0 \\ 0 & 0 & 0 & 0 & \gamma I & 0 \\ 0 & 0 & \tilde{S}_1' & 0 & 0 & \tilde{R}_1 \end{array}\right) \left(\begin{array}{ccc} -YA' & -YC_z' & -Y\mathcal{C}_\Delta \\ -B_w & -D_{zw}' & -\mathcal{D}_{\Delta w}' \\ -\mathcal{B}_\Delta' & -\mathcal{D}_{z\Delta} & -\mathcal{D}_\Delta' \\ \hline I & 0 & 0 \\ 0 & I & 0 \\ 0 & 0 & I \end{array}\right) \psi < 0 \tag{5.82}$$

[Det01, Theorem 28], [Sch01, Theorem 4]

Details of the derivation of the above theorem can be found in [Sch01,Det01]. In the light of this theorem the general design procedure for the LFT/LPV controller synthesis can be given as:

i. Find the partial scalings P_1, $\tilde{P}_1$ and matrices X and Y that minimise γ under the constraints (5.78)-(5.82)

ii. Extend the given P_1 to the full multiplier P as in (5.76) such that it satisfies

$$\left(\begin{array}{cc} \Delta(\rho) & 0 \\ 0 & \Delta_K(\rho) \\ \hline I & 0 \\ 0 & I \end{array}\right)' P \left(\begin{array}{cc} \Delta(\rho) & 0 \\ 0 & \Delta_K(\rho) \\ \hline I & 0 \\ 0 & I \end{array}\right) > 0 \ \forall \rho \in \Gamma \tag{5.83}$$

and such that in its inverse $\tilde{P} := P^{-1}$ the relevant submatrix is given by $\tilde{P}_1$ as in (5.77) and (5.79)

iii. Then compute the scheduling function $\Delta_K(.)$ from the constructed full multiplier P.

iv. Compute the controller matrices A_K, B_K , C_K and D_K by solving an LMI system.

It has been shown in [Sch01] that the use of the full block scalings P in the above construction leads to a less conservative design in general if compared to the LFT/LPV synthesis methods with the basic or skew-symmetric scalings. However, the controller reconstruction algorithm for the full block scalings necessitates that $\Delta_K \neq \Delta$. This leads to a scheduling function Δ_K that requires the inversion of a large matrix dependent on ρ. It is reported in [DS01] that this represents a problem in the real-time controller implementation. For this reason only the LFT/LPV synthesis methods with basic and skew-symmetric scalings will be discussed further in the rest of the chapter. Both of these LFT/LPV synthesis methods allow a linear scheduling function $\Delta_K(\rho) = \Delta(\rho) = diag(\rho_1 I_1, \cdots, \rho_k I_k)$ for the controller, whose implementation requires only simple multiplications. The LFT/LPV synthesis with basic scalings was first proposed in [Pac94, AG95] and shown to be quite conservative since it does not take into account the realness of the scheduling parameters. The LFT/LPV synthesis with skew-symmetric scalings employs both symmetric and skew-symmetric scalings that take into account the realness of the scheduling parameters. This method was first proposed in [Hel95,SE95]. Although in general the LFT/LPV synthesis with skew-symmetric scalings gives more conservative results than the LFT/LPV synthesis with full block scalings, it is shown in [DS01] that in the case of a one scheduling variable they are equally conservative.

The following matrices will be used in the exposition of the LMI conditions of both LFT/LPV synthesis methods

$$\Lambda_X = \begin{pmatrix} \begin{matrix} XA + A'X + \cdots \\ \cdots \mathcal{C}'_\Delta R_1 \mathcal{C}_\Delta \end{matrix} & X\mathcal{B}_\Delta + \mathcal{C}'_\Delta R_1 \mathcal{D}_\Delta + \mathcal{C}'_\Delta S_1 & \begin{matrix} XB_w + \cdots \\ \cdots \mathcal{C}'_\Delta R_1 \mathcal{D}_{\Delta w} \end{matrix} & C'_z \\ * & \begin{matrix} \mathcal{D}'_\Delta R_1 \mathcal{D}_\Delta - R_1 + \cdots \\ \cdots \mathcal{D}'_\Delta S_1 + S'_1 \mathcal{D}_\Delta \end{matrix} & \begin{matrix} \mathcal{D}'_\Delta R_1 \mathcal{D}_{\Delta w} + \cdots \\ \cdots S'_1 \mathcal{D}_{\Delta w} \end{matrix} & \mathcal{D}'_{z\Delta} \\ * & * & \begin{matrix} -\gamma I + \cdots \\ \cdots \mathcal{D}'_{\Delta w} R_1 \mathcal{D}_{\Delta w} \end{matrix} & D'_{zw} \\ * & * & * & -\gamma I \end{pmatrix}$$

$$\Lambda_Y = \begin{pmatrix} \begin{matrix} AY + YA' + \cdots \\ \cdots \mathcal{B}_\Delta \tilde{R}_1 \mathcal{B}'_\Delta \end{matrix} & Y\mathcal{C}'_\Delta + \mathcal{B}_\Delta \tilde{R}_1 \mathcal{D}'_\Delta + \mathcal{B}_\Delta \tilde{S}_1 & \begin{matrix} YC'_z + \cdots \\ \cdots \mathcal{B}_\Delta \tilde{R}_1 \mathcal{D}'_{z\Delta} \end{matrix} & B_w \\ * & \begin{matrix} \mathcal{D}_\Delta \tilde{R}_1 \mathcal{D}'_\Delta - \tilde{R}_1 + \cdots \\ \cdots \mathcal{D}_\Delta \tilde{S}_1 + \tilde{S}'_1 \mathcal{D}'_\Delta \end{matrix} & \begin{matrix} \mathcal{D}_\Delta \tilde{R}_1 \mathcal{D}'_{z\Delta} + \cdots \\ \cdots \tilde{S}'_1 \mathcal{D}'_{z\Delta} \end{matrix} & \mathcal{D}_{\Delta w} \\ * & * & \begin{matrix} -\gamma I + \cdots \\ \cdots \mathcal{D}_{z\Delta} \tilde{R}_1 \mathcal{D}'_{z\Delta} \end{matrix} & D_{zw} \\ * & * & * & -\gamma I \end{pmatrix}$$

LFT/LPV Synthesis with Basic Scalings

Theorem 5.12 *Consider the LPV plant governed by (5.70)-(5.71). There exist a controller (5.72), and scheduling function $\Delta_K = \Delta$ enforcing internal stability and a bound γ on the $\mathscr{L}_2$ gain of the closed-loop system, whenever there exist symmetric matrices Y and X, and symmetric block-diagonal partial scalings R_1, $\tilde{R}_1$ satisfying the following conditions*

$$\begin{pmatrix} \Phi & 0 \\ 0 & I \end{pmatrix}' \Lambda_X \begin{pmatrix} \Phi & 0 \\ 0 & I \end{pmatrix} < 0, \quad S_1 = 0 \tag{5.84}$$

$$\begin{pmatrix} \Psi & 0 \\ 0 & I \end{pmatrix}' \Lambda_Y \begin{pmatrix} \Psi & 0 \\ 0 & I \end{pmatrix} < 0, \quad \tilde{S}_1 = 0 \tag{5.85}$$

$$\begin{pmatrix} X & I \\ I & Y \end{pmatrix} > 0, \quad \begin{pmatrix} R_1 & I \\ I & \tilde{R}_1 \end{pmatrix} > 0, \tag{5.86}$$

where Φ, Ψ are any bases of the null spaces of $(C_y, \mathcal{D}_{y\Delta}, D_{yw})$ and $(B'_u, \mathcal{D}'_{\Delta u}, D'_{zu})$ respectively. If a solution exists, the LTI part of the LFT/LPV controller can be obtained as

- *Complete $\mathcal{X}$,*

$$\mathcal{X} = \begin{pmatrix} X & U \\ U' & E \end{pmatrix} = \begin{pmatrix} Y & \bullet \\ \bullet & \bullet \end{pmatrix}^{-1} \tag{5.87}$$

and scalings as

$$R = \begin{pmatrix} R_3 & R_2 \\ R_2' & R_1 \end{pmatrix} = \begin{pmatrix} \tilde{R}_3 & \tilde{R}_2 \\ \tilde{R}_2' & \tilde{R}_1 \end{pmatrix}^{-1} \tag{5.88}$$

- *Solve the following LMI for* $K = \begin{pmatrix} A_K & B_K \\ C_K & D_K \end{pmatrix}$,

$$\Lambda_K + P_{X_{cl}}' K Q_{cl} + Q_{cl}' K' P_{X_{cl}} < 0 \tag{5.89}$$

where

$$\Lambda_K = \begin{pmatrix} XA + (*) & A'U & 0 & X\mathcal{B}_\Delta & XB_w & 0 & \mathcal{C}_\Delta' & C_w' \\ * & 0 & 0 & U'\mathcal{B}_\Delta & U'B_w & 0 & 0 & 0 \\ * & * & -R_3 & -R_2 & 0 & 0 & 0 & 0 \\ * & * & * & -R_1 & 0 & 0 & \mathcal{D}_\Delta' & \mathcal{D}_{z\Delta}' \\ * & * & * & * & -\gamma I & 0 & \mathcal{D}_{\Delta w}' & D_{zw}' \\ * & * & * & * & * & -\tilde{R}_3 & -\tilde{R}_2 & 0 \\ * & * & * & * & * & * & -\tilde{R}_1 & 0 \\ * & * & * & * & * & * & * & -\gamma I \end{pmatrix} \tag{5.90}$$

$$P_{X_{cl}} = \begin{pmatrix} U' & E & 0 & 0 & 0 & 0 & 0 & 0 \\ B_u'X & B_u'U & 0 & 0 & 0 & 0 & \mathcal{D}_{\Delta u}' & D_{zu}' \\ 0 & 0 & 0 & 0 & 0 & I & 0 & 0 \end{pmatrix} \tag{5.91}$$

$$Q_{cl} = \begin{pmatrix} 0 & I & 0 & 0 & 0 & 0 & 0 & 0 \\ C_y & 0 & 0 & \mathcal{D}_{y\Delta} & D_{yw} & 0 & 0 & 0 \\ 0 & 0 & I & 0 & 0 & 0 & 0 & 0 \end{pmatrix} \tag{5.92}$$

LFT/LPV Synthesis with Skew-Symmetric Scalings

Theorem 5.13 *Consider the LPV plant governed by (5.70)-(5.71). There exist a controller (5.72), and a scheduling function $\Delta_K = \Delta$ enforcing internal stability and a bound γ on the $\mathscr{L}_2$ gain of the closed-loop system, whenever there exist symmetric matrices Y and X, symmetric block-diagonal partial scalings R_1, $\tilde{R}_1$, and skew-symmetric block-diagonal partial scalings S_1, $\tilde{S}_1$ satisfying the following conditions*

$$\begin{pmatrix} \Phi & 0 \\ 0 & I \end{pmatrix}' \Lambda_X \begin{pmatrix} \Phi & 0 \\ 0 & I \end{pmatrix} < 0 \tag{5.93}$$

$$\begin{pmatrix} \Psi & 0 \\ 0 & I \end{pmatrix}' \Lambda_Y \begin{pmatrix} \Psi & 0 \\ 0 & I \end{pmatrix} < 0 \tag{5.94}$$

$$\begin{pmatrix} X & I \\ I & Y \end{pmatrix} > 0, \quad R_1 > 0, \;\; \tilde{R}_1 > 0, \tag{5.95}$$

where Φ, Ψ *are any bases of the null spaces of* $(C_y, \mathcal{D}_{y\Delta}, D_{yw})$ *and* $(B_u', \mathcal{D}_{\Delta u}', D_{zu}')$ *respectively. If a solution exists, the LTI part of the LFT/LPV controller can be obtained as*

- *Construction of the full scalings* [DS01]*: Choose* $Q_1 = -R_1$, $\tilde{Q}_1 = -\tilde{R}_1$ *and form* P_1, $\tilde{P}_1$. *Define* $N_P := (P_1 - \tilde{P}_1^{-1})^{-1}$, *and* $Z = \begin{pmatrix} 0 \\ I \end{pmatrix}$. *Calculate* T,

$$T := \begin{pmatrix} -T_2 & T_{12} \\ -T_{12} & T_2 \end{pmatrix}, \tag{5.96}$$

such that

$$\begin{pmatrix} T_{12}' \\ T_2 \end{pmatrix}' (N_P - Z(Z'P_1Z)^{-1}Z') \begin{pmatrix} T_{12}' \\ T_2 \end{pmatrix} > 0. \tag{5.97}$$

In geometric terms this means that $(T_{12}' \, T_2')$ *should be chosen such that its columns span a positive subspace of* $(N_P - Z(Z'P_1Z)^{-1}Z')$ *of half of the dimension of the size* N_P. *Obtain* P_P *as,*

$$P_P := \begin{pmatrix} P_1 & T \\ T' & T'N_PT \end{pmatrix} = \begin{pmatrix} \tilde{P}_1 & \bullet \\ \bullet & \bullet \end{pmatrix}^{-1} \tag{5.98}$$

Finally form P *according to the following partition of* P_P

$$P_P = \left(\begin{array}{cc|cc} Q_1 & S_1 & Q_{12} & S_{12} \\ S_1' & R_1 & S_{12}' & R_{12} \\ \hline Q_{12}' & S_{21} & Q_2 & S_2 \\ S_{21}' & R_{12}' & S_2' & R_2 \end{array}\right) \tag{5.99}$$

- *Calculate the transformed controller parameters,*

$$\mathbf{K} = \left[\begin{array}{c|cc} K & L_1 & L_2 \\ \hline M_1 & N_{11} & N_{12} \\ M_2 & N_{21} & N_{22} \end{array}\right] \tag{5.100}$$

as a solution of the following LMI condition,

$$\left[\Gamma_{\mathbf{K}_{123}} \, \Gamma_{\mathbf{K}_4} \, \Gamma_{\mathbf{K}_5} \, \Gamma_{\mathbf{K}_6} \, \Gamma_{\mathbf{K}_{78}}\right] < 0 \tag{5.101}$$

where $R = \begin{pmatrix} R_1 & R_{12} \\ R_{12}' & R_2 \end{pmatrix} = T_p'T_p$ *with* $T_p = \begin{pmatrix} T_1 & T_{12} \\ T_{21}' & T_2 \end{pmatrix}$ *and matrices* $\Gamma_{\mathbf{K}_i}$ *defined as*

$$\Gamma_{\mathbf{K}_{123}} = \begin{pmatrix} AY + (*) + B_u M_1 + (*) & B_u N_{11} C_y + A + K' & B_u N_{11} D_{yw} + B_w \\ * & XA + (*) + L_1 C_y + (*) & L_1 D_{yw} + X B_w \\ * & * & -\gamma I \\ * & * & * \\ * & * & * \\ * & * & * \\ * & * & * \\ * & * & * \end{pmatrix} \tag{5.102}$$

$$\Gamma_{\mathbf{K}_4} = \begin{pmatrix} B_u N_{11} \mathcal{D}_{y\Delta} + \mathcal{B}_\Delta + M_1' \mathcal{D}_{\Delta u}' S_1' + Y \mathcal{C}_\Delta' S_1' + M_2' S_{12}' \\ L_1 \mathcal{D}_{y\Delta} + X \mathcal{B}_\Delta + C_y' N_{11}' \mathcal{D}_{\Delta u}' S_1' + \mathcal{C}_\Delta' S_1' + C_y' N_{21}' S_{12}' \\ D_{yw}' N_{11}' \mathcal{D}_{\Delta u}' S_1' + \mathcal{D}_{\Delta w} S_1' + D_{yw}' N_{21}' S_{12}' \\ Q_1 + S_1 \mathcal{D}_{\Delta u} N_{11} \mathcal{D}_{y\Delta} + (*) + S_1 \mathcal{D}_\Delta + (*) + S_{12} N_{21} \mathcal{D}_{y\Delta} + (*) \\ * \\ * \\ * \\ * \end{pmatrix} \tag{5.103}$$

$$\Gamma_{\mathbf{K}_5} = \begin{pmatrix} B_u N_{12} + M_1' \mathcal{D}_{\Delta u}' S_{21}' + Y \mathcal{C}_\Delta' S_{21}' + M_2' S_2' \\ L_2 + C_y' N_{11}' \mathcal{D}_{\Delta u}' S_{21}' + \mathcal{C}_\Delta' S_{21}' + C_y' N_{21}' S_2' \\ D_{yw}' N_{11}' \mathcal{D}_{\Delta u}' S_{21}' + \mathcal{D}_{\Delta w}' S_{21}' + D_{yw}' N_{21}' S_2' \\ Q_{12} + S_1 \mathcal{D}_{\Delta u} N_{12} + S_{12} N_{22} + \mathcal{D}_{y\Delta}' N_{11}' \mathcal{D}_{\Delta u}' S_{21}' + \mathcal{D}_\Delta' S_{21}' + \mathcal{D}_{y\Delta}' N_{21}' S_2' \\ Q_2 + S_{21} \mathcal{D}_{\Delta u} N_{12} + (*) + S_2 N_{22} + (*) \\ * \\ * \\ * \end{pmatrix} \tag{5.104}$$

$$\Gamma_{\mathbf{K}_6} = \begin{pmatrix} M_1'\mathcal{D}_{\Delta u}'T_1' + Y\mathcal{C}_\Delta' T_1' + M_2'T_{12}' \\ C_y'N_{11}'\mathcal{D}_{\Delta u}'T_1' + \mathcal{C}_\Delta'T_1' + C_y'N_{21}'T_{12}' \\ D_{yw}'N_{11}'\mathcal{D}_{\Delta u}'T_1' + \mathcal{D}_{\Delta w}'T_1' + D_{yw}'N_{21}'T_{12}' \\ \mathcal{D}_{y\Delta}'N_{11}'\mathcal{D}_{\Delta u}'T_1' + \mathcal{D}_\Delta'T_1' + \mathcal{D}_{y\Delta}'N_{21}'T_{12}' \\ N_{12}'\mathcal{D}_{\Delta u}'T_1' + N_{22}'T_{12}' \\ -I \\ * \\ * \end{pmatrix} \tag{5.105}$$

$$\Gamma_{\mathbf{K}_{78}} = \begin{pmatrix} M_1'\mathcal{D}_{\Delta u}'T_{21}' + Y\mathcal{C}_\Delta'T_{21}' + M_2'T_2' & M_1'D_{zu}' + YC_z' \\ C_y'N_{11}'\mathcal{D}_{\Delta u}'T_{21}' + \mathcal{C}_\Delta'T_{21}' + C_y'N_{21}'T_2' & C_yN_{11}'D_{zu}' + C_z' \\ D_{yw}'N_{11}'\mathcal{D}_{\Delta u}'T_{21}' + \mathcal{D}_{\Delta w}'T_{21}' + D_{yw}'N_{21}'T_2' & D_{yw}'N_{11}'D_{zu}' + D_{zw}' \\ \mathcal{D}_{y\Delta}'N_{11}'\mathcal{D}_{\Delta u}'T_{21}' + \mathcal{D}_\Delta'T_{21}' + \mathcal{D}_{y\Delta}'N_{21}'T_2' & \mathcal{D}_{y\Delta}'N_{11}'D_{zu}' + \mathcal{D}_{z\Delta}' \\ N_{12}'\mathcal{D}_{\Delta u}'T_{21}' + N_{22}'T_2' & N_{12}'D_{zu}' \\ 0 & 0 \\ -I & 0 \\ * & -\gamma I \end{pmatrix} \tag{5.106}$$

- *Calculate the original controller parameters as suggested in Theorem 5.5.*

5.3.5 Example: LPV $\mathscr{H}_\infty$ Loop Shaping Controller Design

This example presents a comparative study of the different LPV controller design methods introduced in this chapter in the $\mathscr{H}_\infty$ loop shaping paradigm. The plant in consideration is the one described in Example 5.2.2. In order to reveal the best performance of the LPV $\mathscr{H}_\infty$ loop shaping controllers a parameter-varying pre-compensator is used to shape the open loop plant. The PI parameters of $W_1(s,\rho)$ are chosen such that at $P_m = 60kPa$ the cross-over frequency of the weighted plant is placed at $0.27rad/event$ and at $P_m = 30kPa$ it is placed at $0.15rad/events$ in accordance with the variation of the delay in the loop. This provides a sensible change in the controller bandwidth with respect to the variations in the delay. The extreme values of the pre-compensator are given as

$$\overline{W}_1(s) = \frac{1.26s + 0.3401}{s}, \tag{5.107}$$

$$\underline{W}_1(s) = \frac{0.871s + 0.1306}{s}. \tag{5.108}$$

The parameter varying pre-compensator W_1 can be constructed as an LFT plant $W_1(s,\rho) = \mathcal{F}_l\left(P_{w_1},\rho\right)$ that varies linearly between $\overline{W}_1(s)$ and $\underline{W}_1(s)$ as a function of the scheduling

Method	Linearisation Technique	Number of Decision Variables	Number of LMIs	$\dot{\rho}$	ϵ_{lpv}	Time[1] (s)
LFT1	-	55	4	$\lvert\dot{\rho}\rvert \leq \infty$	0.2056	0.48
LFT2	-	61	5		0.2506	0.61
LPV1	elimi. of var.	43	123		0.2506	19.3
	chang. of var.	92	42		0.2394	34.8
LPV2	elimi. of var. $X = X(\rho), Y = Y(\rho)$	85	205	$\lvert\dot{\rho}\rvert \leq 0.6$	0.2657	77.7
	$X = X_0, Y = Y(\rho)$	64	205		0.2558	55.4
	$X = X(\rho), Y = Y_0$	64	205		0.2597	54.2
	chang. of var. $X = X(\rho), Y = Y_0$	162	123		0.2593	355.4

Table 5.1 Properties of the different LPV controller synthesis methods applied to a simplified AFR path model. LFT1 denotes the LFT/LPV synthesis method with basic scalings; LFT2 denotes LFT/LPV synthesis method with skew-symmetric scalings; LPV1 denotes the Grid/LPV method with a single Lyapunov function; LPV2 denotes the Grid/LPV method with a parameter-dependent Lyapunov function. For the Grid/LPV methods the grid length is chosen as 0.05 for $|\delta| \leq 1$

parameter (normalised manifold pressure). The post-compensator is chosen as before,

$$W_2(s) = \frac{1.5}{s + 1.5}. \tag{5.109}$$

The overall weighted plant can be expressed as,

$$\begin{aligned} G_s &= W_2 G W_1 \\ &= W_2 \mathcal{F}_l\left(P, \rho I_2\right) \mathcal{F}_l\left(P_{w_1}, \rho\right) \\ &= \mathcal{F}_u\left(P_s, \Delta\right), \end{aligned} \tag{5.110}$$

with $\Delta = \rho I_3$ and four states. Note that the LTI robust stability margin of the weighted plant at its extreme values is $\epsilon_{\text{lti}} = 0.379$ and $\epsilon_{\text{lti}} = 0.405$ for $P_m = 60kPa$ and $P_m = 30kPa$ respectively.

Table 5.1 reveals many important properties of the different LPV controller synthesis methods. The number of decision variables, number of LMIs and computation times are only given for the LMI conditions that need to be solved in order to compute the $\mathscr{L}_2$ gain γ $(= \epsilon_{\text{lpv}}^{-1})$ of the closed-loop system without considering the extra LMIs required for controller construction. Some important implications are:

- Among the methods that search for a single Lyapunov function (LFT1, LFT2, LPV1), the LFT/LPV synthesis with skew-symmetric scalings (LFT2) is the most attractive one since it is much less conservative than the LFT1 method and also significantly more computationally attractive than the LPV1 method.

- Both the LFT2 and LPV1 method with the elimination of variables technique give the same value of ϵ_{lpv} without any conservatism. However, when the LPV1 method with change of variables technique is employed, the achieved value of ϵ_{lpv} smaller, i.e. conservative as expected.

- The LPV2 method which searches for a parameter-dependent Lyapunov function, gives the best value of the ϵ_{lpv}. The price paid for this is the high computational cost as the number of decision variables and LMIs are significantly higher for this method.

As far as the computation time is concerned it can be seen that the number of decision variables is much more costly than the number of LMIs (number of decision variables and LMIs are defined according to the notation of [GNLC95]). For example, in the LPV1 method computing the achievable ϵ_{lpv} with the change of variables technique takes more time than computing it with the elimination of variables technique even though the latter has a larger number of LMIs.

Figure 5.9 shows the achieved ϵ_{lti} plots by each LPV $\mathscr{H}_\infty$ controllers together with the ϵ_{lti} plot achieved by the LTI $\mathscr{H}_\infty$ controller of Example 5.2.2 for the frozen values of $|\rho| \leq 1$. It can be seen that the value of the LPV robust stability margin ϵ_{lpv} is a lower bound for the ϵ_{lti} plot of an LPV controller, i.e. for a given LPV controller the ϵ_{lti} achieved for a frozen value of ρ is always greater or equal to the ϵ_{lpv} value of the LPV system.

Figure 5.10 shows the step disturbance rejection performance of the controllers when the scheduling parameter varies sinusoidally as depicted in Figure 5.11. An output step disturbance at event 5 and an input step disturbance at event 45 are applied to the closed-loop system. Although all of the controllers perform satisfactorily, the Erms values (root-mean-square (RMS) regulation error at the output) reveal that the ones with better ϵ_{lpv} values perform better. Note that the LPV2 and LFT2 controllers are the best and second-best performers in terms of the Erms performance respectively.

5.4 Comments

The $\mathscr{H}_\infty$ loop shaping design paradigm and a review of the LPV controller design methods have been presented in this chapter. The $\mathscr{H}_\infty$ loop shaping design has been applied to a variety of practical problems, such as flight control [Hyd91, Pap98] and automotive idle

[1]on an Athlon 1800+ PC with 1GB memory

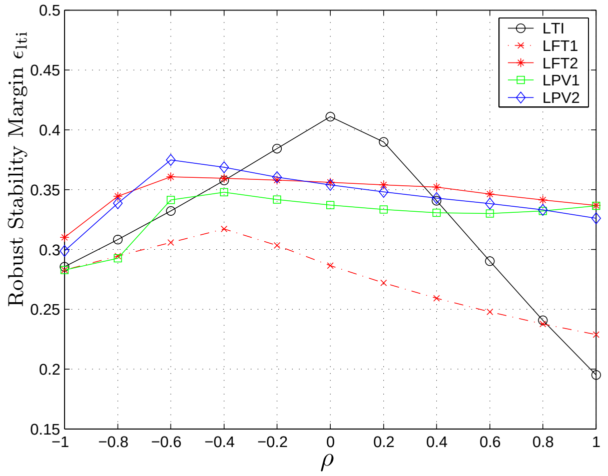

Figure 5.9 LTI robust stability margin for the frozen values of ρ

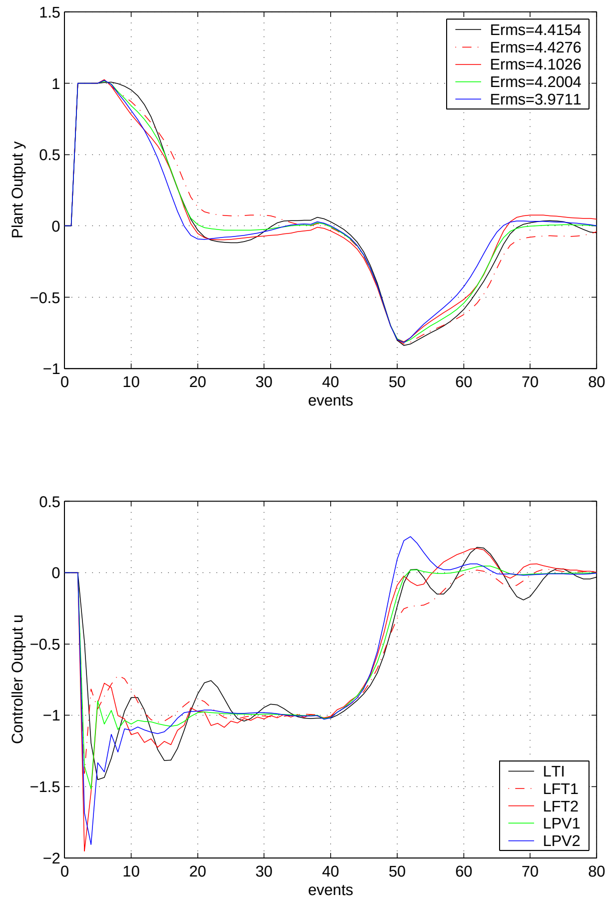

Figure 5.10 Disturbance rejection performances of the $\mathscr{H}_\infty$ *loop shaping controllers*

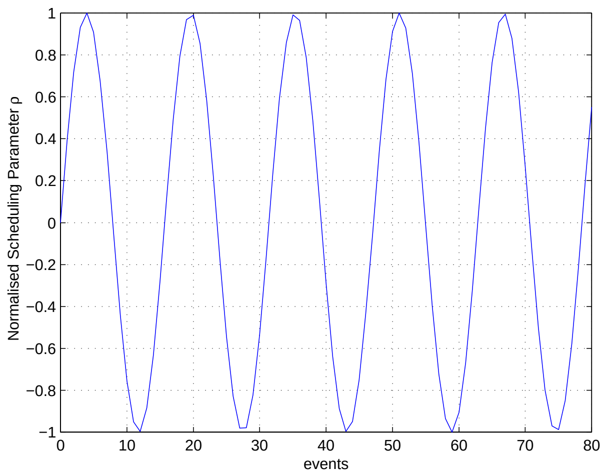

Figure 5.11 Variation of the normalised scheduling parameter

speed control [For00], and found to be performing well. The LPV controller design methods have been developed recently and are still an area of ongoing research. Although the review of the LPV methods in this chapter is not exhaustive, it is rather comprehensive. Moreover, a detailed comparison of the LFT/LPV and Grid/LPV controller design methods have been given through the design study presented in Example 5.3.5.

6

AFR Control System Design

This chapter presents the application of the $\mathscr{H}_\infty$ loop shaping controller design paradigm to the AFR control problem in the TI-VCT engines. An LTI $\mathscr{H}_\infty$ loop shaping controller is designed for the nominal LTI AFR path model. On the other hand, the LFT model of the AFR path developed in Chapter 4 is used to design LPV $\mathscr{H}_\infty$ loop shaping controllers. Although there are several methods for synthesising an LPV controller, as discussed in the previous chapter, Example 5.3.5 has revealed the best two candidates: the LFT/LPV synthesis method with skew-symmetric scalings and Grid/LPV synthesis method with a parameter-dependent Lyapunov function. The first method is computationally very attractive and gives non-conservative results (for a single quadratic Lyapunov function search) if there is only one scheduling parameter. However, it is conservative in the sense that it does not take into account the limits of the rate of the scheduling parameters. On the other hand, the second method can potentially give much less conservative results since it takes into account the limits of the rate of the scheduling parameters by searching for a parameter-dependent Lyapunov function. However, it is computationally very intensive and requires the measurement of the rate of the scheduling parameters in general. Note that the last requirement for the Grid/LPV controller can be dropped if either $X(\rho)$ or $Y(\rho)$ in the formulation of the parameter-dependent Lyapunov function is chosen as a constant matrix but this simplification produces sub-optimal controllers.

The designed controllers are first tested in simulations. Performance of the controllers are investigated both on the LFT AFR model of Chapter 4 and on the full nonlinear AFR path model of Chapter 3. Among the two LPV controllers the better performing one will be chosen for real-time implementation on the engine.

The final validation of the controllers are performed in the engine test cell through experiments. Both the LTI and LPV $\mathscr{H}_\infty$ loop shaping controllers are implemented through the MATLAB/Simulink/dSPACE suite in the event based discrete-time. Since the transport delays in the loop limit the achievable AFR regulation performance by feedback, further performance improvements are accomplished by including a feedforward element into the control systems. The engine tests are repeated for the feedback-plus-feedforward controllers and a comparison between the feedback and feedback-plus-feedforward controllers is presented at the end.

6.1 $\mathscr{H}_\infty$ Loop Shaping Controller Design

The $\mathscr{H}_\infty$ loop shaping controller design paradigm is an effective method for designing robust controllers and has been successfully used in a wide variety of applications. An AFR controller should have good robustness against system uncertainties and also good performance against the disturbances. These are usually conflicting requirements and a compromise has to be achieved. In the sequel an LTI $\mathscr{H}_\infty$ loop shaping controller with good robustness and performance properties ($\epsilon_{\mathrm{lti}} > 0.3$) is designed for the AFR control problem. This LTI controller is required to be robust to parameter variations in the AFR path. Further robustness and performance improvements are achieved by designing LPV controllers. The controller designs in this section follow the lines of Example 5.2.2 and Example 5.3.5.

6.1.1 LTI $\mathscr{H}_\infty$ Loop Shaping Controller

In order to design an LTI $\mathscr{H}_\infty$ loop shaping controller an LTI system model is required. Such a linear representation of the AFR path is obtained from the LFT model $G_\phi = \mathcal{F}_l(P_\phi, \Delta_\phi)$ developed in Chapter 4 by substituting $P_m = 50kPa$, EVC=10° and IVO=−5° in Δ_ϕ. This linear model is called the nominal representation of the system. The nominal model G_0 is a SISO transfer function with 14 states. Since the input to the model is the FPW in micro seconds and the output of the model is the normalised FAR the steady state gain of the system is much smaller than one. Therefore, as a common practice in loop shaping design , the nominal plant is scaled to have a unity steady state gain with a scaling factor $S_g = 4.2573 \times 10^3$. The scaled nominal plant is denoted as

$$\tilde{G}_0 = G_0 S_g.$$

The frequency response of the scaled nominal plant is plotted in Figure 6.1. As the system under consideration is in the event based discrete-time, the frequency axis is in $rad/event$ and $w = \pi$ represents the Nyquist Frequency. The second order Padé based approximation of the delay introduces RHP zeros at frequencies $0.94rad/event$ and $2rad/event$. Therefore, for a robust closed-loop system the loop bandwidth must be smaller than $0.94rad/event$. Good robustness and performance can be achieved by appropriate choices

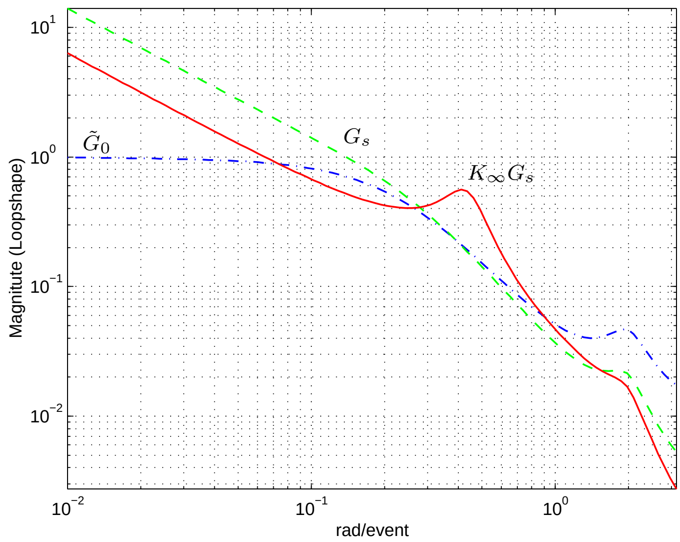

Figure 6.1 Singular values of scaled nominal plant $\tilde{G}_0$, weighted plant G_s and $K_\infty G_s$

of the pre- and post-compensators. The pre-compensator $W_1(s)$ is chosen as a PI weight as before. The integrator in the $W_1(s)$ is necessary to achieve zero steady state error and also improves the performance by boosting the low frequency gain. The proportional gain is used to reduce the phase lag introduced by the integrator around the cross-over frequency. The PI parameters of $W_1(s)$, shown in Figure 6.2, are chosen to set the cross-over frequency of the weighted plant at $0.14 rad/event$,

$$W_1(s) = \frac{1.008s + 0.1411}{s}. \tag{6.1}$$

These parameters achieve smooth transition of the loop shape around the cross-over frequency. The post-compensator $W_2(s)$, depicted in Figure 6.2, is chosen to ensure sufficient high frequency noise attenuation,

$$W_2(s) = \frac{1}{s+1}. \tag{6.2}$$

Once the weights are chosen and weighted plant $G_s = W_2\tilde{G}_0W_1$ is formed, the sub-optimal $\mathscr{H}_\infty$ loop shaping controller, K_∞ can be easily the calculated using the μ-tools command "ncfsyn($\cdot$)" in MATLAB. Note that the K_∞ has 16 states, same as the the weighted plant. The K_∞ produces a robust stability margin $\epsilon_{\text{lti}} = 0.4107$ for the closed-loop and also achieves $\epsilon_{\text{lti}} \geq 0.25$ for all the frozen values of the normalised MAP $|\rho| \leq 1$ as it will be shown in Figure 6.4. The final controller K, which has 18 states, can be implemented as $K = \tilde{W}_1K_\infty W_2$, where $\tilde{W}_1 = S_gW_1$.

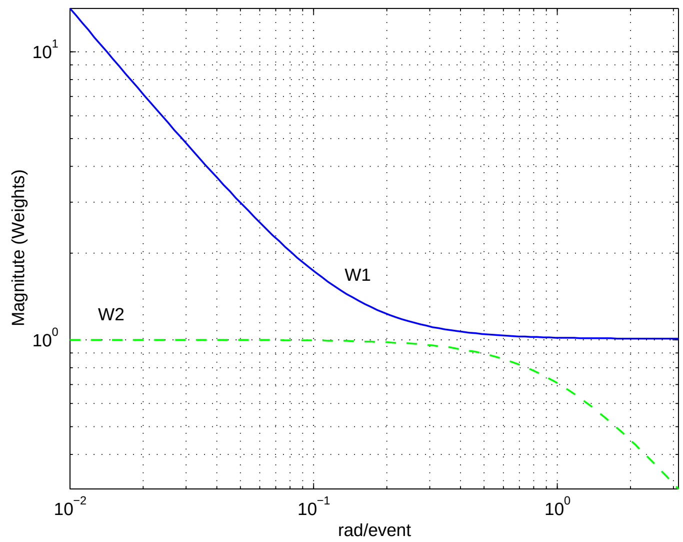

Figure 6.2 $\mathscr{H}_\infty$ loop shaping weights

6.1.2 LPV $\mathscr{H}_\infty$ Loop Shaping Controller

The LFT approximation of the AFR path can be used to design LPV controllers. Recall that the LFT model

$$G_\phi = \mathcal{F}_l\left(P_\phi, \Delta_\phi\right), \tag{6.3}$$

where $P_\phi \in \mathbb{R}^{30\times30}$, Δ_ϕ =diag[$P_m I_5$, EVCI_5,IVOI_5] $\in \mathbb{R}^{15\times15}$ has 3 scheduling parameters. Designing an LPV controller with 3 scheduling parameters would be computationally infeasible with the available LMI solvers. For this reason the LPV controllers are only designed for the MAP variations and the nominal values of the valve timings EVC=10° and IVO=$-5°$ are substituted in Δ_ϕ. Note that since MAP causes significant variations in the transport delay and cylinder MAF in the AFR path, it is aimed that the controller speed can be varied with respect to the MAP. The resulting LFT model is denoted as

$$G^p_\phi = \mathcal{F}_l\left(P^p_\phi, \Delta^p_\phi\right) \tag{6.4}$$

where $P^p_\phi \in \mathbb{R}^{20\times20}$ has 14 states, 6 inputs and 6 outputs, and $\Delta^p_\phi = P_m I_5 \in \mathbb{R}^{5\times5}$. In order to reveal the best performance of the LPV $\mathscr{H}_\infty$ loop shaping controllers a parameter-varying pre-compensator is designed to shape the open-loop plant. The PI parameters of $W_1(s,\rho)$ (ρ denotes the normalised MAP) is chosen such that at $P_m = 70kPa$ the cross-over frequency of the weighted plant is placed at $0.18 rad/event$ and at $P_m = 30kPa$ it is placed at $0.13 rad/events$ in accordance with the variation of the transport delay in the loop. This provides sensible variation of the controller bandwidth with respect to the variations in the delay. The extreme values of the pre-compensator and scaling are given as

$$\overline{W}_1(s) = \frac{1.13s + 0.2033}{s} \text{ and } \overline{S}_g = 6.0736 \times 10^3 \tag{6.5}$$

$$\underline{W}_1(s) = \frac{1.035s + 0.1346}{s} \text{ and } \underline{S}_g = 3.2772 \times 10^3 \tag{6.6}$$

The scaled parameter-varying pre-compensator $\tilde{W}_1 = W_1 S_g$ is constructed as an LFT model that varies linearly between $\overline{W}_1\overline{S}_g$ and $\underline{W}_1\underline{S}_g$ as a function of the normalised MAP

$$\tilde{W}_1 = \mathcal{F}_l\left(P_w, \rho\right), \; P_w \in \mathbb{R}^{3\times 3}. \tag{6.7}$$

The post-compensator is chosen as before,

$$W_2(s) = \frac{1}{s+1}. \tag{6.8}$$

The overall weighted plant can be expressed as an upper LFT,

$$G_s = \mathcal{F}_u\left(P_s, \Delta_s\right), \tag{6.9}$$

where $P_s \in \mathbb{R}^{23\times 23}$ has 16 states, 7 inputs and 7 outputs, and $\Delta_s = \rho I_6 \in \mathbb{R}^{6\times 6}$. Note that the LTI robust stability margins of the closed-loop system at its extreme values are $\epsilon_{\text{lti}} = 0.38$ and $\epsilon_{\text{lti}} = 0.39$ for $P_m = 70kPa$ and $P_m = 30kPa$ respectively.

Two different LPV $\mathscr{H}_\infty$ loop shaping controllers are synthesised for the weighted LFT plant in the following. The first LPV controller is designed via the LFT/LPV synthesis method with skew-symmetric scalings. The second LPV controller is designed via the Grid/LPV method with a parameter-depending Lyapunov function. In the rest of this chapter "the LFT controller" will denote the LPV controller designed via the LFT/LPV method with skew-symmetric scalings and "the LPV controller" will denote the LPV controller designed via the Grid/LPV method with a parameter-dependent Lyapunov function. Therefore, "the LPV controller" will refer to the LPV controller designed via the Grid/LPV method but "the LPV controllers" will refer to both the LFT controller and the LPV controller. The main advantage of the Grid/LPV method over the LFT/LPV method is that it can take into account the rate of variation of the scheduling parameters. Hence, it is important to get realistic estimates of the limits of the rate of the parameter variations in order to compute less conservative LPV controllers.

The global data used for the identification of the wall-wetting dynamics in Section 3.2.5 are investigated to obtain some realistic estimates for the limits of the rate of the MAP variations. Figure 6.3 shows the normalised MAP together with its time derivative in the event based discrete-time domain. The bottom plot gives an upper bound for the normalised $\dot{P}_m$ as $|\dot{\rho}| \leq 0.065$. However, since even more abrupt MAP variations are likely to occur during engine operation, it is assumed that $-0.1 \leq \dot{\rho} \leq 0.1$ in the synthesis of the LPV controller.

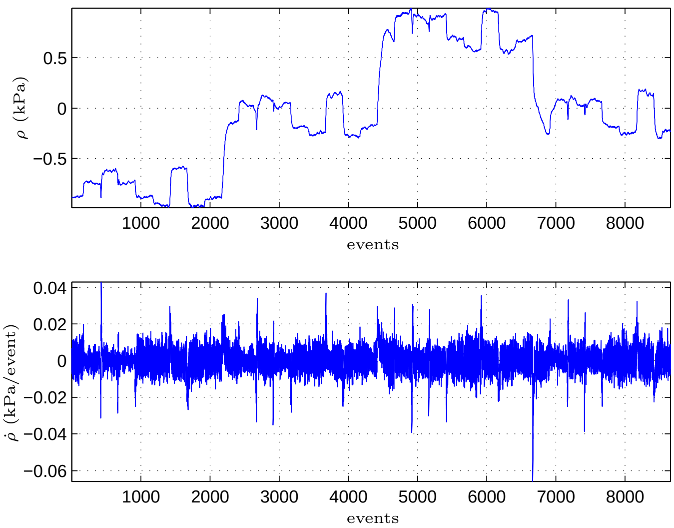

Figure 6.3 Sample data for normalised P_m and $\dot{P}_m$

Next some guidelines for designing LPV controllers will be presented. Table 6.1 summarises the properties of both the LFT/LPV and Grid/LPV methods. All synthesis LMIs are solved for the $\mathscr{H}_\infty$ loop shaping generalised plant which describes $T_{\left[\begin{smallmatrix} w_1 \\ w_2 \end{smallmatrix}\right] \to \left[\begin{smallmatrix} z_1 \\ z_2 \end{smallmatrix}\right]}$ for the weighted LFT plant (see Section C). The following design procedure is found to be adequate in order to compute numerically reliable solutions for the LFT/LPV method:

i. Minimise γ $(= \epsilon^{-1})$ over (5.93), (5.94) and (5.95), and compute γ_{opt} and X, Y, Q_1, S_1, R_1, $\tilde{Q}_1$, $\tilde{S}_1$, $\tilde{R}_1$ (this step is denoted as ϵ_{lpv} LMIs in Table 6.1).

ii. Having computed the full scaling P, choose a sub-optimal $\gamma > \gamma_{\text{opt}}$, and maximise t over (5.69) and (5.101) and compute X, Y, K, L_1, L_2, M_1, M_2, N_{11}, N_{12}, N_{21}, N_{22} (this step is denoted as Controller LMIs in Table 6.1).

iii. Calculate the original controller parameters as suggested in Theorem 5.5.

Maximising t improves the conditioning of X and Y as suggested in (5.69). If necessary further bounds can be placed also on the scalings. It is observed that 90 % of the total computation time is spent during the second step (controller construction) in the design of the LFT controller.

For the Grid/LPV method the following design procedure is found useful for getting numerically reliable solutions

i. Minimise γ for both the constant X/parameter-dependent Y and constant Y/parameter-dependent X cases using the elimination of variables technique (Theorem 5.9) in

<table>
<tr><th rowspan="2">Method</th><th rowspan="2">Notes</th><th colspan="2">Number of</th><th rowspan="2">$\dot{\rho}$</th><th rowspan="2">ϵ_{lpv}</th><th rowspan="2">Time[1] (hr)</th></tr>
<tr><th>Decision Variables</th><th>LMIs</th></tr>
<tr><td rowspan="2">LFT</td><td>ϵ_{lpv} LMIs</td><td>345</td><td>5</td><td rowspan="2">$|\dot{\rho}| \leq \infty$</td><td rowspan="2">0.2094</td><td rowspan="2">0.5</td></tr>
<tr><td>Cont. LMIs</td><td>802</td><td>2</td></tr>
<tr><td rowspan="3">LPV</td><td><u>elimi. of var.</u>
constant X</td><td>409</td><td>105</td><td rowspan="3">$|\dot{\rho}| \leq 0.1$</td><td>0.2236</td><td>8</td></tr>
<tr><td>constant Y</td><td>409</td><td>105</td><td>0.2099</td><td>8</td></tr>
<tr><td><u>chang. of var.</u>
constant X
(solved twice)</td><td>987</td><td>63</td><td>0.2236</td><td>29</td></tr>
</table>

Table 6.1 Comparison of the LPV synthesis methods for AFR controller design. For the Grid/LPV method the grid length is chosen as 0.1 for $|\rho| \leq 1$

order to find out the less conservative way of dropping the $\dot{\rho}$ dependence in the controller.

ii. For the less conservative case, minimise γ using the change of variables technique (Theorem 5.10) and compute the γ_{opt}, K, L, M, N.

iii. (This step is required for improving the conditioning of $I - XY$) Choose a sub-optimal $\gamma > \gamma_{\text{opt}}$, maximise t over (5.69) and the synthesis LMIs given in Theorem 5.10, and compute K, L, M, N.

iv. Compute A_K, B_K, C_K, D_K with the help of (5.58)- (5.61).

Solving the Grid/LPV method via the change of variable technique is much more computationally intensive as it can be seen in Table 6.1. It takes around 14.5 hours to solve the synthesis LMIs with this technique. Since they are solved twice to improve the conditioning of $I - XY$, the total computation time is around 29 hours. This is why most of the design iterations for the Grid/LPV method should be performed via the elimination of variables techniques which only takes 8 hours of computation time. However, the final controller should be computed via the the change of variable technique, since this computes a controller that is more suitable for real-time implementation.

The results show that the use of the Grid/LPV method improves the value of the $\epsilon_{\text{lpv}} =$ from 0.2094, obtained by the LFT/LPV method, to 0.2236, however at a cost of great increase of the computational complexity. Figure 6.4 compares the LTI robust stability

[1] on an Athlon 1800+ PC with 1GB memory

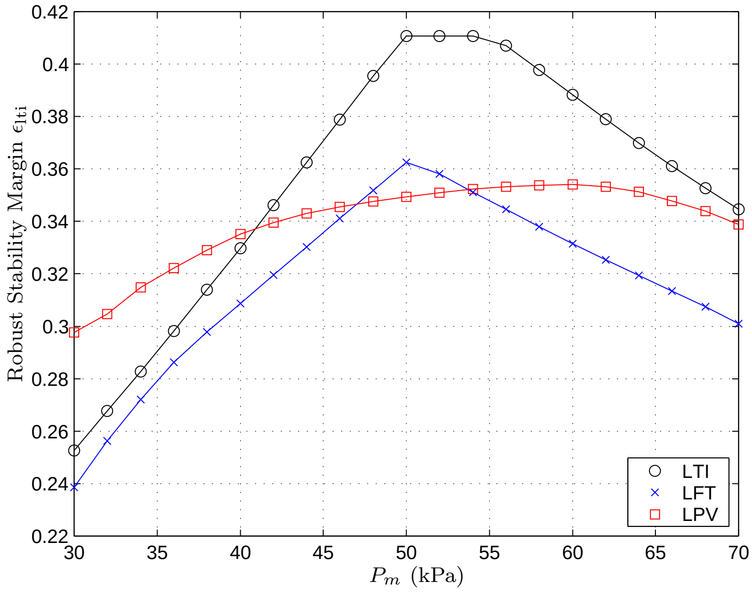

Figure 6.4 LTI robust stability margin for frozen values of P_m

margins of the LTI and LPV $\mathscr{H}_\infty$ loop shaping controllers for the frozen values of the MAP. All the controllers achieve satisfactory ϵ_{lti} values across the MAP envelope. The LPV controller produces higher ϵ_{lti} values as suggested by its higher ϵ_{lpv} value. Furthermore, it is observed the ϵ_{lpv} can be a very conservative lower bound for the ϵ_{lti}. For example, for the LPV controller the minimum value of the ϵ_{lti} is around 0.3, which is much larger than the value of achieved $\epsilon_{\mathrm{lpv}} = 0.2236$.

6.2 Controller Performance in Simulations

The controllers, implemented in MATLAB/Simulink environment, are tested in simulations. Since the AFR path model is developed in the event based discrete-time the simulations are also implemented in discrete-time. The controllers are first tested on the LFT AFR path model developed in Chapter 4. Since both of the LPV controllers are designed for this model, this simulation only validates the nominal performance of the LPV controllers. On the other hand, since the LTI controller is designed for a nominal model of the LFT plant, this simulation validates both the robust performance and stability properties of the LTI controller. Figure 6.5 shows the performances of the controllers and variation of the normalised MAP during the simulation. All the results are presented in the time domain so that the performances can be judged with ease. Note that the engine speed is fixed at 1500rpm in this simulation. A step disturbance is applied at the plant output at 0.2 seconds and another step disturbance is applied at the plant input at 0.9

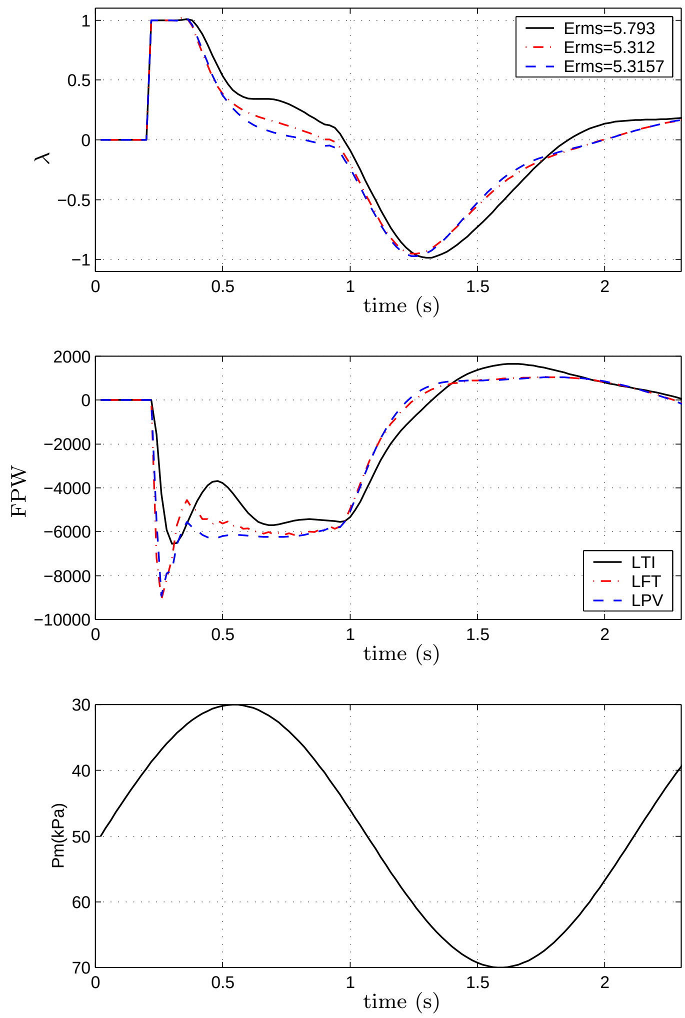

Figure 6.5 Performance of the controllers on the LFT model

seconds. Recall that "Erms" denotes the RMS regulation error at the plant output. The simulation results imply that the LTI controller is robust against the parameter variations in the model up to $|\dot{\rho}| \leq 0.06$. This also verifies the fact that $\epsilon_{\text{lti}} = 0.41$ is a good indication of the robust performance and stability. Furthermore, the LPV controllers perform better under the fast parameter variations as indicated by their $\epsilon_{\text{lpv}} \geq 0.2$. However, nothing can be said about their robustness properties at this stage since the LFT model is the nominal model for the LPV controllers.

In the next simulation, the controllers are tested on the full nonlinear AFR path model identified in Chapter 3. Neither the Padé based approximations of the delay nor the affine approximation of the cylinder MAF model are present in this simulation. Therefore, the following simulation will validate, up to a degree, the robust performance and stability of the LPV controllers as well as those of the LTI controller. A more realistic disturbance trajectory is designed for this simulation where all the disturbances for the AFR path, i.e. TP, EVC and IVO are excited. The engine speed is constant at $1500rpm$ for this simulation. Figure 6.6 shows the lambda regulation performances of the controllers together with the FPW, MAP, IVO and EVC traces. As MAP varies between the low and high loads, the valve timings are moved accordingly in some predetermined trajectories. The overlap is reduced to zero at very low loads and increased at mid and high loads. Plots show that all the $\mathscr{H}_\infty$ loop shaping controllers perform well under this aggressive disturbance scenario. Moreover, the LPV controllers improve the RMS performance levels almost up to 50%. It is also observed that the LFT and LPV controllers achieve almost the same RMS performances even though the LPV controller has a slightly higher ϵ_{lpv} value.

The simulations indicate that the designed controllers have the desired robustness and performance properties not only against the parameter variations but also against the uncertainties in the model.

6.3 Controller Performance in Experiments

Although the simulations indicate good performance of the designed controllers, the final validation of the controllers can only be performed on the real engine. Only one of the LPV controllers is tested on the engine for the following reasons:

Real-time implementation: The LFT controller has important advantages for the real-time implementation since 1) It requires only an LFT operation to get the state space matrices of the LFT controller at each sampling time 2) Due to its LFT structure its state space matrices can be discretised off-line. On the other hand, the LPV controller requires 1) computation of (5.58), (5.59), (5.60) , (5.61) at each sampling time 2) discretisation of the state space matrices of the controller at each sampling time. Therefore, it requires much less computing power to implement the LFT controller in real-time.

Performance: Although the LPV controller has a slightly better ϵ_{lpv} value than that of the LFT controller, the simulations have not shown that this leads to a performance improvement for the LPV controller.

For the above reasons the LFT/LPV controller is chosen for the engine tests together with the LTI controller.

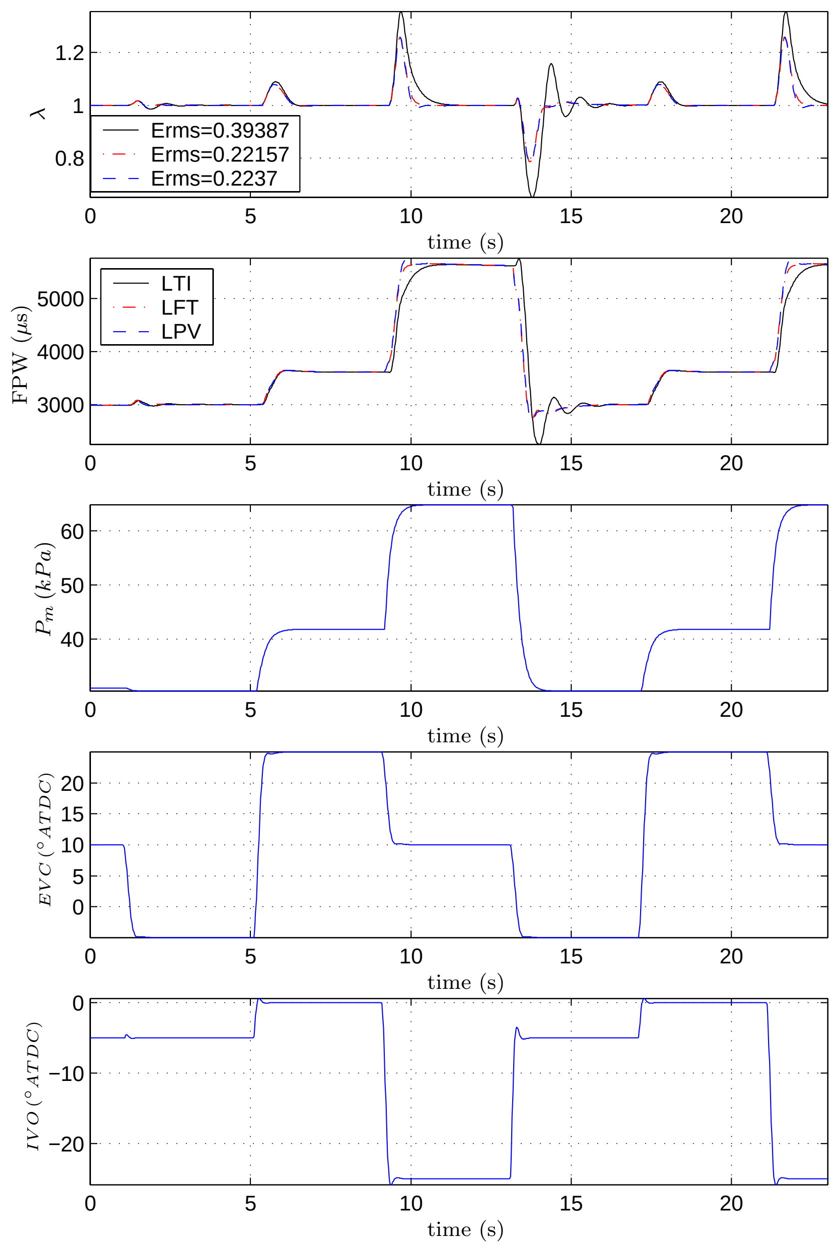

Figure 6.6 A realistic disturbance rejection test on the nonlinear model

6.3.1 Feedback Only

All the experimental data given in the following are averaged over several measurements (between 4 and 6) in order to improve the signal-to-noise ratio of the final results. Unless otherwise stated, all the experiments are performed at $1500rpm$. In a TI-VCT engine there are three main disturbances on the AFR signal at constant speed. The throttle position is a significant disturbance and fast variations in TP can cause large deviations in the lambda signal. Although not as severe as the TP, fast variations in the IVO and EVC timings also cause deviations of up to 5 % in the lambda. Moreover, since all the modelling were performed at $1500rpm$, any variations in the engine speed would test the robustness of the controllers to a significant change in the system dynamics. Therefore, the controllers are also tested against variations in the engine speed. In the following the disturbance rejection properties of the LTI and LFT feedback controllers are investigated against one disturbance at a time.

TP Disturbance

Figure 6.7 shows how the LTI and LFT $\mathscr{H}_\infty$ loop shaping controllers performs under an aggressive TP disturbance with EVC=10° and IVO=−5°. The MAP depicted in the bottom plot varies very fast between $40kPa$ and $58kPa$ due to the aggressive TP excitation. Initially the LTI controller is in the loop and lambda deviations up to 15% are visible. As

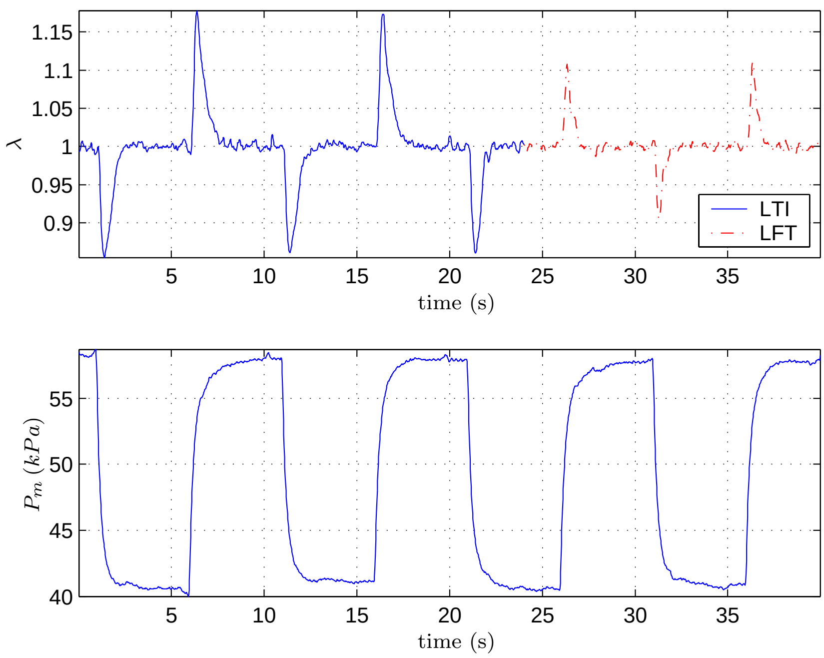

Figure 6.7 Aggressive TP disturbance rejection

soon as the LFT controller is switched on at around $24secs$, the peak of the lambda deviations are almost cut by half. Note that such a significant improvement in the performance is achieved without any feedforward action.

A more quantitative comparison of the controllers is given in Figure 6.8. It shows the RMS performance levels as well as the FPW, MAP and TP traces. This time a less aggressive but still significant TP disturbance is applied to the AFR loop. The MAP varies between $38kPa$ and $49kPa$ in a square wave manner. The top plot shows that the RMS error is almost halved (50 % improvement) by the LFT controller compared with that of the LTI controller. The faster response time of the LFT controller is visible in the FPW plot. This is because the LFT controller not only measures the lambda but also the MAP. Therefore, unlike the LTI controller it does not have to wait for the response of the lambda sensor in order to act against a significant variation in the MAP caused by the TP disturbance.

EVC Disturbance

This experiment is performed with constant TP and IVO=$-10°$. Figure 6.9 shows the EVC disturbance rejection performances of the LTI and LFT controllers. The valve overlap was changed from $0°$ to $30°$ by exciting the EVC timing. Although both controllers perform similarly, the LTI one has a slightly better performance. This can be analysed from the behaviour of the MAP shown in the third plot. Consider the first transient, when the MAP increases the gains of the LFT controller are also increased since the increase in the MAP would indicate a shorter transport delay. However, when an increase in the MAP is caused due to an increase in the overlap this would increase the transport delay. Thus, under the EVC excitation the MAP does not capture the dynamics of the system and using MAP as the scheduling variable misleads the LFT controller. Recall that for the success of the gain-scheduling the scheduling parameter should capture the dynamics of the system. Note that the performance of the LFT controller can be further enhanced by scheduling on the EVC timing as well as MAP.

The high frequency noise on the FPW output of the LFT controller can be seen in Figure 6.9. This noise is same as the engine noise present in the MAP measurements. Since the parameters of the LFT controller vary with the MAP, any noise on the MAP signal immediately affects the output of the LFT controller. This can be prevented by filtering the MAP measurements before the LFT controller, however this would slow down the controller response time.

IVO Disturbance

This experiment is performed with fixed TP and EVC=$10°$. Figure 6.10 shows the IVO disturbance rejection performance of the LTI and LFT controllers. The valve overlap was

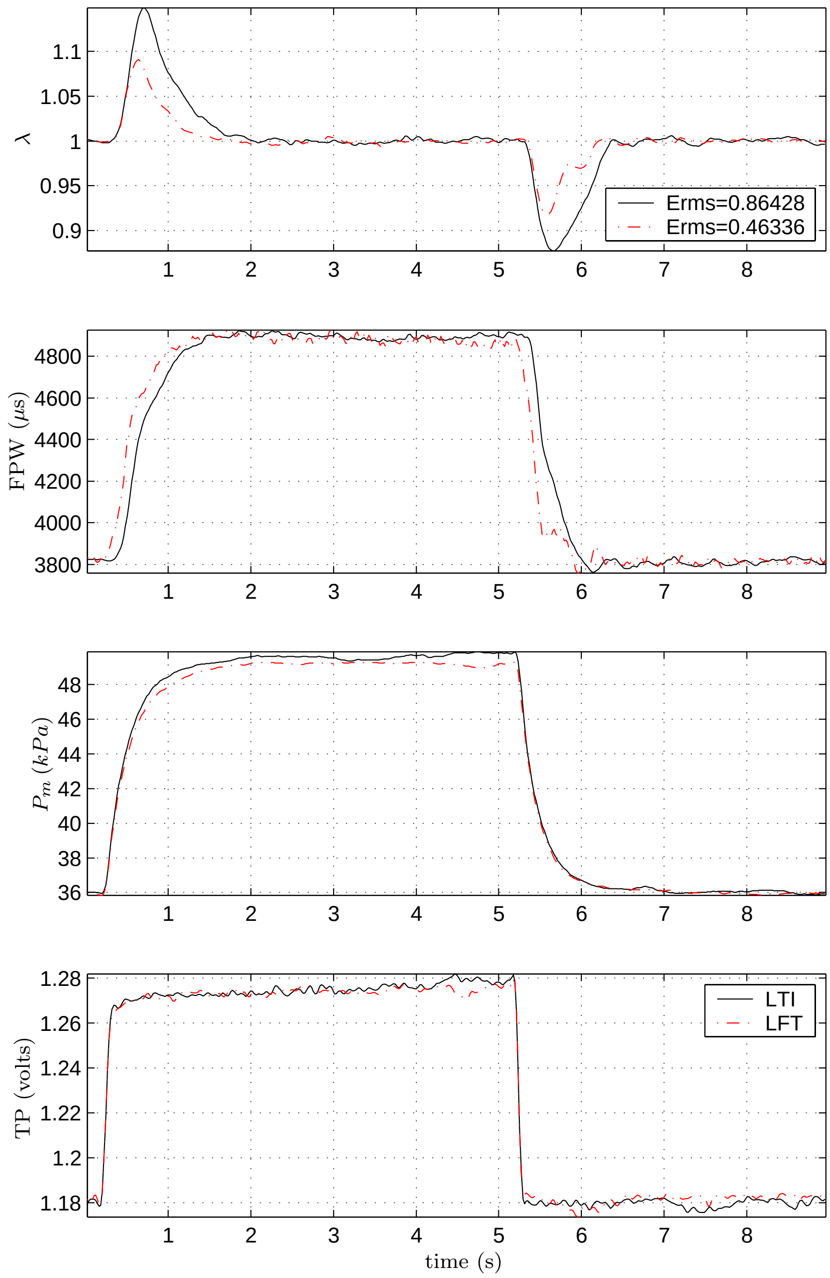

Figure 6.8 Moderate TP disturbance rejection

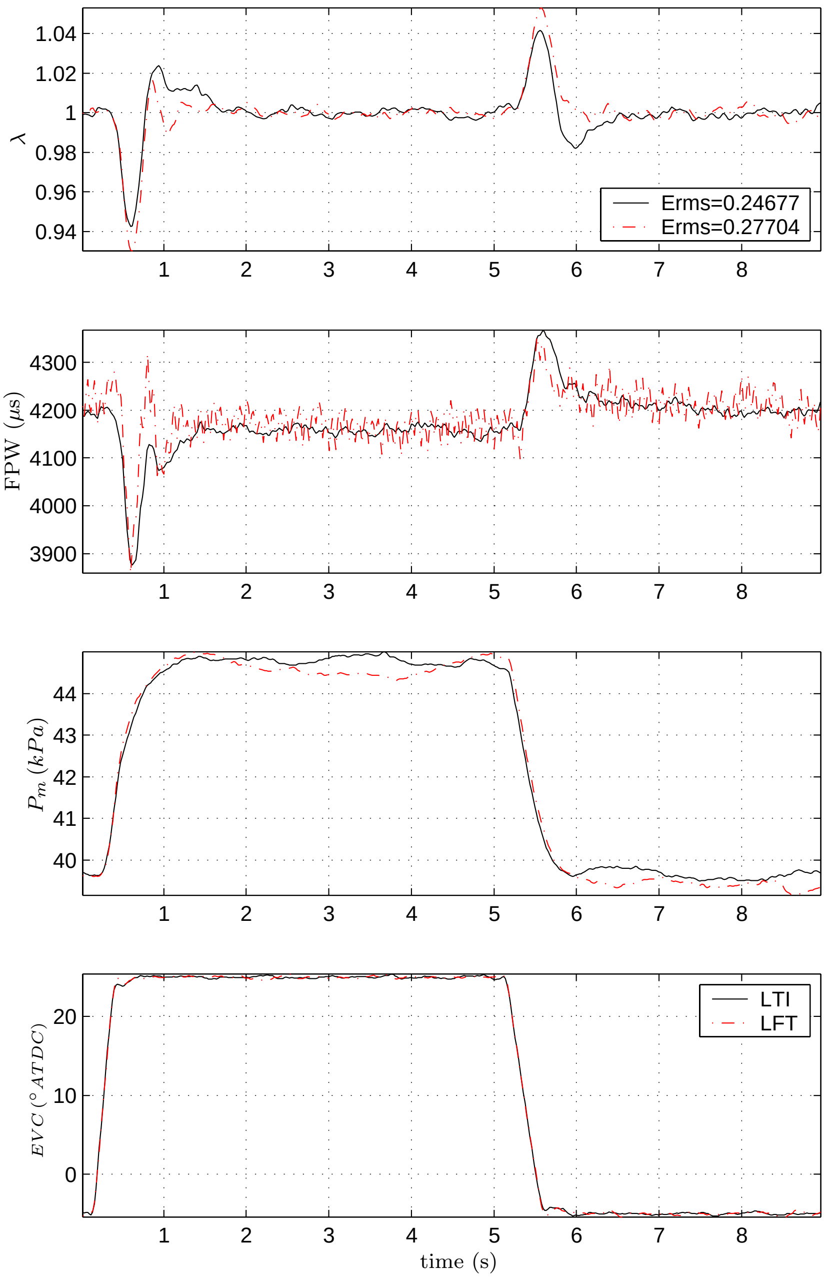

Figure 6.9 EVC timing disturbance rejection

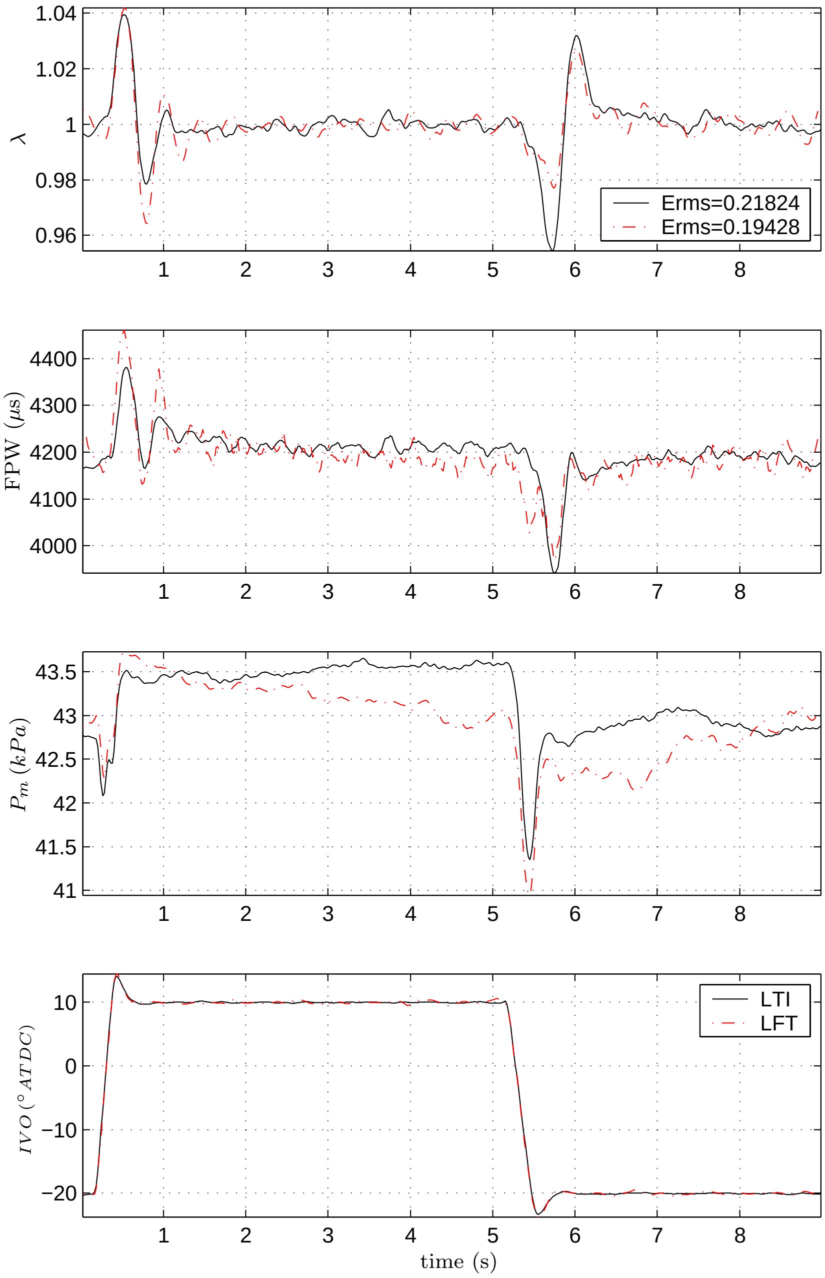

Figure 6.10 IVO timing disturbance rejection

changed from 0° to 30° by exciting the IVO timing. The achieved RMS errors show that this time the LFT controller performs slightly better, although the overall responses of the controllers are almost the same. The reason for the better performance of the LFT controller is that, the IVO timing affects the MAP in a similar manner to that of the TP excitation.

Speed Disturbance

This experiment is performed with constant TP, EVC=10° and IVO=−5°. Figure 6.11 shows the speed disturbance rejection properties of the LTI and LPV controllers. The engine speed is varied between 1300 and 1700 rpm through the dynamometer speed control loop. It is observed that although both controllers can handle the significant variations in the engine speed with ease, the LFT controller performs 50 % better than the LTI controller in terms of the RMS performance. This is because under the speed variations the MAP behaves similar to its behaviour under the TP variations for which the LFT controller is designed for. Note that such a large improvement in performance is achieved without any feedforward action.

6.3.2 Feedback-plus-Feedforward

The above experiments show that both the LTI and LFT controllers have good robustness properties. Furthermore, whenever a disturbance affects the AFR path in similar way to the TP disturbance (such as the engine speed) the LFT controller offers significant improvements in the RMS performance. However, whenever a disturbance affects the MAP in a way that was not considered during the design of the LFT controller such as the EVC timing, the LTI controller may perform slightly better. On the other hand, performances of the feedback controllers are limited due to the transport delays present in the AFR path. Further improvements are possible by introducing a feedforward element in the AFR control system. It is common practice in the AFR control applications to use the cylinder MAF estimation in a feedforward sense in order to improve the disturbance rejection performance. However, the cylinder MAF is not the only disturbance acting on the AFR signal in a TI-VCT engine. Variations in the valve timings also cause significant changes in the fuel puddle size disturbing the cylinder fuel flow. Therefore, a feedforward element should employ not only the air path models but also the wall-wetting model in order to achieve superior AFR regulation in a TI-VCT engine. The overall structure for a feedback-plus-feedforward controller (also called two degree-of-freedom (2DOF) controller) is depicted in Figure 6.12. Note that in the case of the LFT feedback controller, MAP is also fed back into the feedback controller.

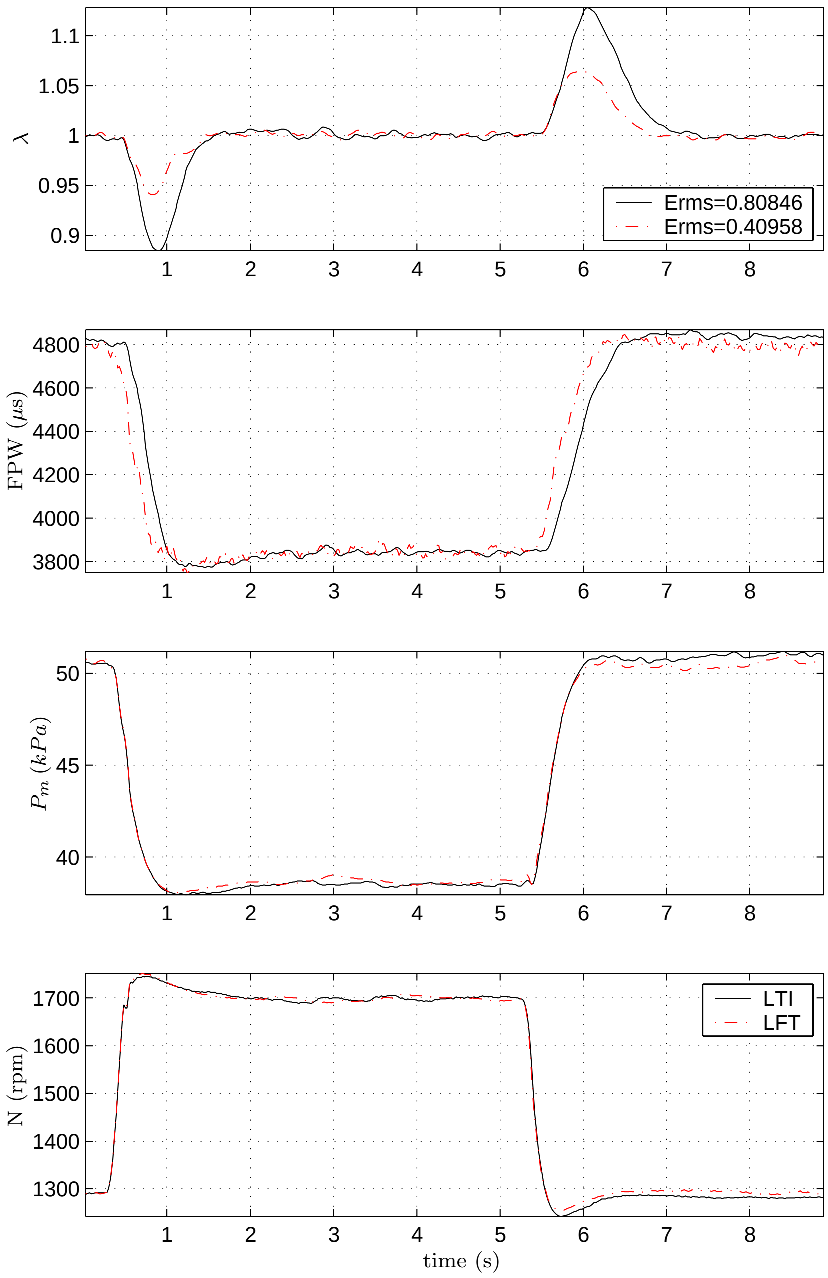

Figure 6.11 Engine speed disturbance rejection

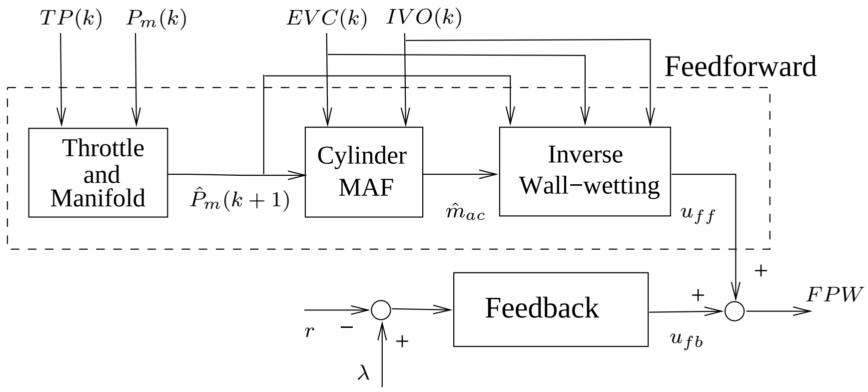

Figure 6.12 Feedback-plus-Feedforward Control System Structure

The feedforward controller is a nonlinear parameter-varying function consisting of the throttle MAF model (3.2), cylinder MAF model (3.3), manifold pressure model (3.4) and the inverse of the 4-cylinder wall-wetting model (3.20). The measured values of TP, P_m, IVO and EVC are used to estimate the value of P_m in the next event

$$\hat{P}_m(k+1) = P_m(k) + K_{man}\left(\hat{\dot{m}}_{at}(k) - \hat{\dot{m}}_{ac}(k)\right) \tag{6.10}$$

where $K_{man} = 300$ is the manifold gain defined in (3.4). The estimated value $\hat{P}_m(k+1)$ is used together with the valve timings to predict the cylinder MAF and fuel puddle parameters in the next event. Note that the feedforward controller does not have any robustness properties and its performance is only as good as the accuracy of the models used in its design. If the models used are poor, the feedforward action may even degrade the overall performance of the control system. The feedback-plus-feedforward controllers are constructed by combining the LTI and LFT feedback controllers with the feedforward controller as suggested in Figure 6.12 without any modifications. Note that this is a very crude way of designing 2DOF controllers. A more proper way would be to integrate the feedforward controller into the $\mathscr{H}_\infty$ loop shaping design framework and redesign the feedback controllers to make sure that the feedback and feedforward controller work together seamlessly. A well-known guideline for assuring satisfactory performance of a 2DOF controller is to make sure that the feedback and feedforward parts are active on different frequency ranges. In general feedback controllers are active in the low frequencies and provide robustness. The feedforward controllers are active at mid-high frequencies and provide performance. Filtering can be used to decouple the frequency ranges of the controllers.

In the following the disturbance rejection tests of Section 6.3.1 are repeated in order to investigate and compare the properties of the 2DOF controllers with the feedback only controllers. In the sequel "LTI+FF" will denote the 2DOF controller consisting of the LTI $\mathscr{H}_\infty$ loop shaping feedback controller and the feedforward controller, and "LFT+FF" will denote the 2DOF controller consisting of the LFT $\mathscr{H}_\infty$ loop shaping feedback controller and the feedforward controller. Note that the LTI+FF and LFT+FF controllers have exactly the same feedforward controllers.

TP Disturbance

Introducing a well designed feedforward action improves the performance of the controllers significantly compared to the feedback only controllers as shown in Figure 6.13. The 2DOF controllers perform four times better relative to the LTI controller and two times better relative to the LFT controller in terms of the RMS performance. The LTI+FF performs slightly better than the LFT+FF controller. This is because the LTI controller and the feedforward controller are almost decoupled due to the slow response time of the LTI controller. However, since the LFT controller has a much faster response time than the LTI controller, it interacts with the feedforward controller. This interaction reduces the performance of the LFT+FF controller slightly. However, the robustness guarantees under the fast parameter variations given by the LFT+FF controller are much greater than those of the LTI+FF controller. Superior robustness properties become crucial for the 2DOF controllers whenever the feedforward part of the controller produces poor predictions.

EVC Disturbance

This experiment is performed with constant TP and IVO$=-10°$. Figure 6.14 shows the EVC disturbance rejection properties of the four controllers. The EVC disturbance rejection capabilities of the feedback controllers are enhanced visibly by the introduction of the feedforward controller. The peak deviations are reduced from 6 % to 2 % and the RMS errors are more than halved. As before the LTI+FF controller performs slightly better than the LFT+FF controller due to the undesired interaction between the LFT controller and the feedforward part in the 2DOF control system.

IVO Disturbance

This experiment is performed under constant TP and EVC$=10°$. Figure 6.15 shows the IVO disturbance rejection properties of the designed controllers when the valve overlap is changed from $0°$ to $30°$ via IVO. Significant improvements are achieved in the performance by the feedforward scheme. Peak deviations are reduced from 4 % to 2 % and the RMS errors are improved by almost 50 %. Recall that the rapid IVO variations cause changes in the fuel puddle size. The superior performances of the 2DOF controllers are another indication that the identified wall-wetting model can predict changes in the fuel puddle

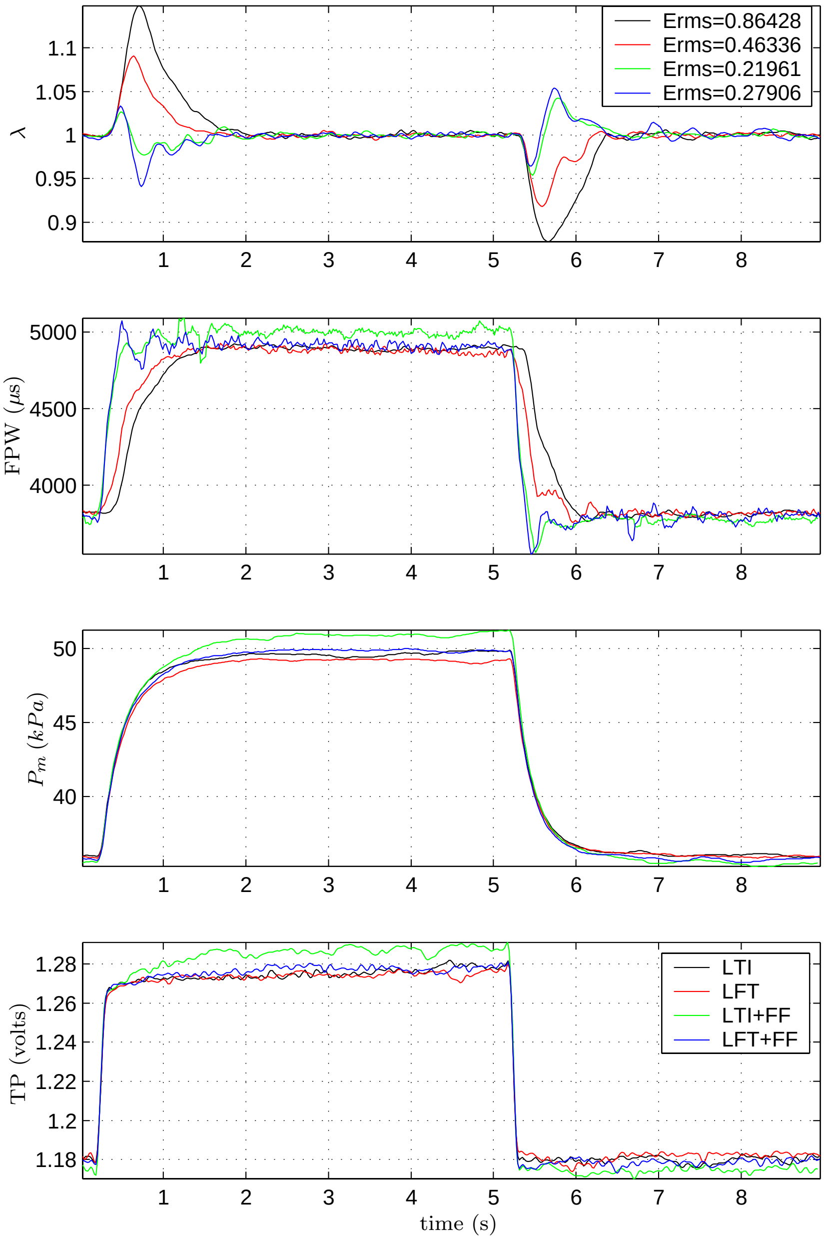

Figure 6.13 TP disturbance rejection (Feedback-plus-Feedforward)

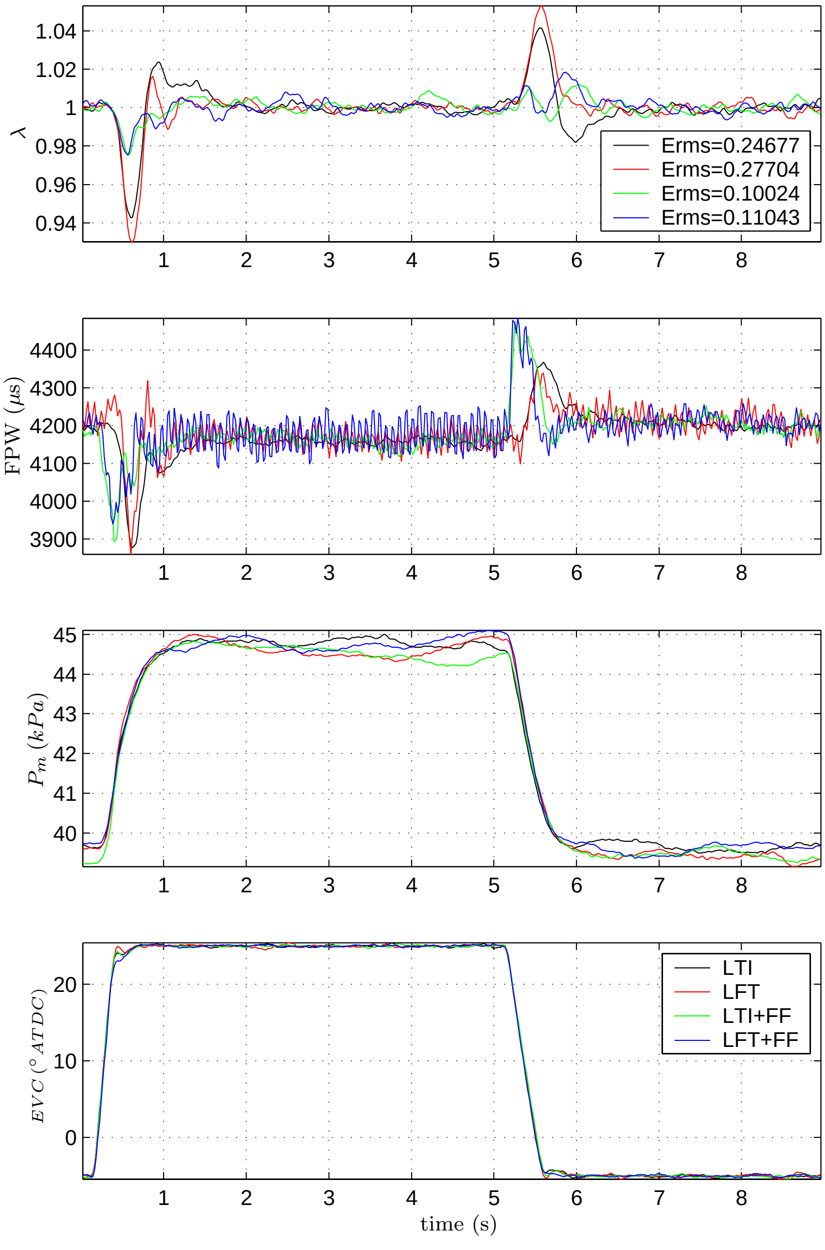

Figure 6.14 EVC disturbance rejection (Feedback-plus-Feedforward)

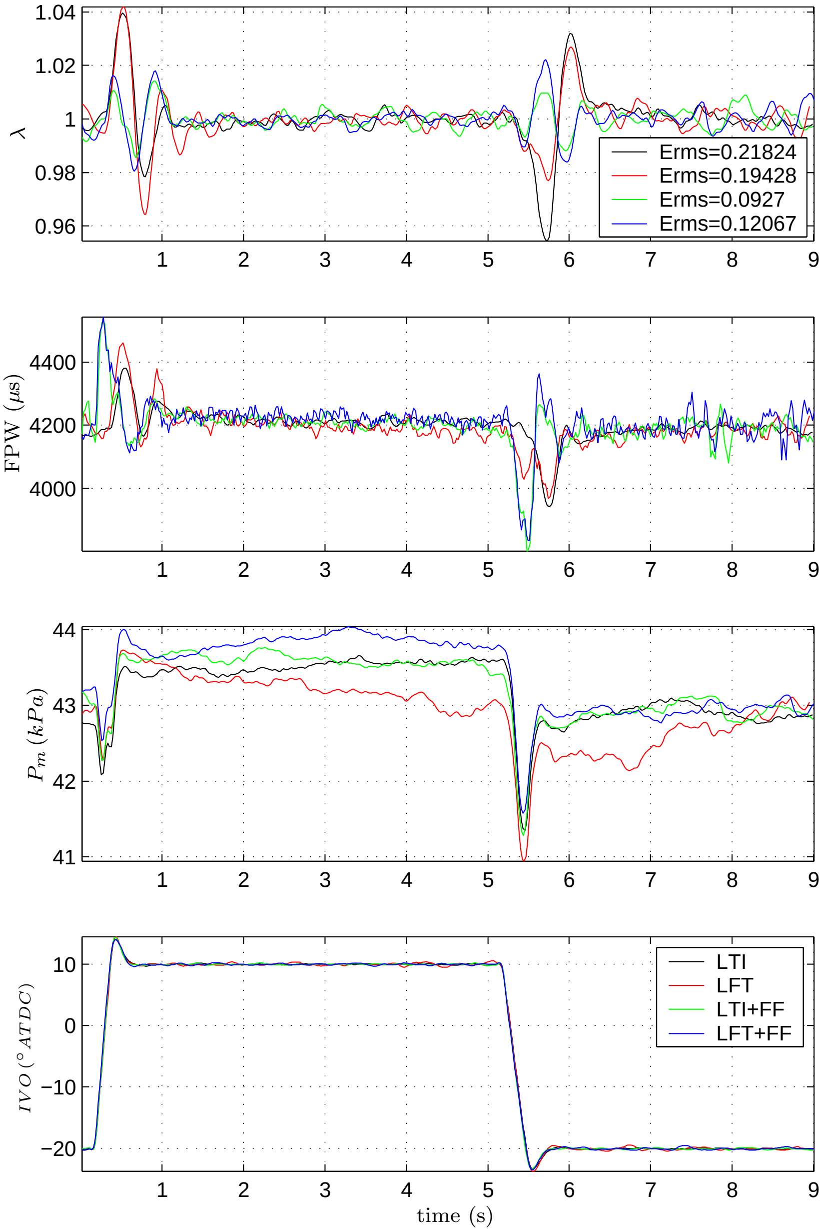

Figure 6.15 IVO disturbance rejection (Feedback-plus-Feedforward)

size. As before there is a slight degradation in the performance of LFT+FF compared to that of the LTI+FF controller.

Speed Disturbance

This experiment is performed with constant TP, EVC=10° and IVO=-5°. Figure 6.16 shows the speed disturbance rejection properties of the designed controllers. It can be seen that the 2DOF controllers improve the performance significantly compared with that of the LTI or LFT controller. It is interesting that the feedforward controller can still produce accurate predictions even though it is designed from models identified only at 1500rpm. Note that the feedforward controller does not have the engine speed as a parameter in its model. As before, the LTI+FF controller performs slightly better than the LFT+FF controller.

Above engine tests have shown that all the designed controllers have good robustness properties against all the major disturbances and parameter variations in the AFR path. Furthermore, disturbance rejection performances can be significantly improved when the feedforward controller is used together with the feedback controllers.

6.3.3 More Realistic Disturbance Scenarios

So far all of the engine tests have been performed with only one disturbance acting on the AFR path. It is likely that under realistic driving conditions several disturbances would act on the AFR path at the same time. The following experiments are performed in order to assess the performance of the controllers under severe transients that are induced by several disturbances acting together on the system. Only the 2DOF controllers are tested under these severe transients since the feedback-only controllers cannot maintain the exhaust lambda in a region that is required for the safe operation of the engine. The first test is performed under the constant engine speed at 1500rpm. The TP is varied rapidly to reach low, mid and high loads while the overlap is changed via EVC and/or IVO timing every time the TP is moved to a new position. Note that the operating conditions for this test are very similar to those of the nonlinear simulation shown in Figure 6.6.

Figure 6.17 shows the performances of the 2DOF controllers under these severe transients at constant speed. Both controllers perform satisfactorily in terms of stability, even though significant deviations in lambda, up to 10%, are seen during the large TP transients. This deviations could be further reduced if a predictor that predicts the cylinder MAF several events (not only one) ahead would be included into the feedforward controller [CVH00]. Without a predictor such deviations cannot be prevented due to the

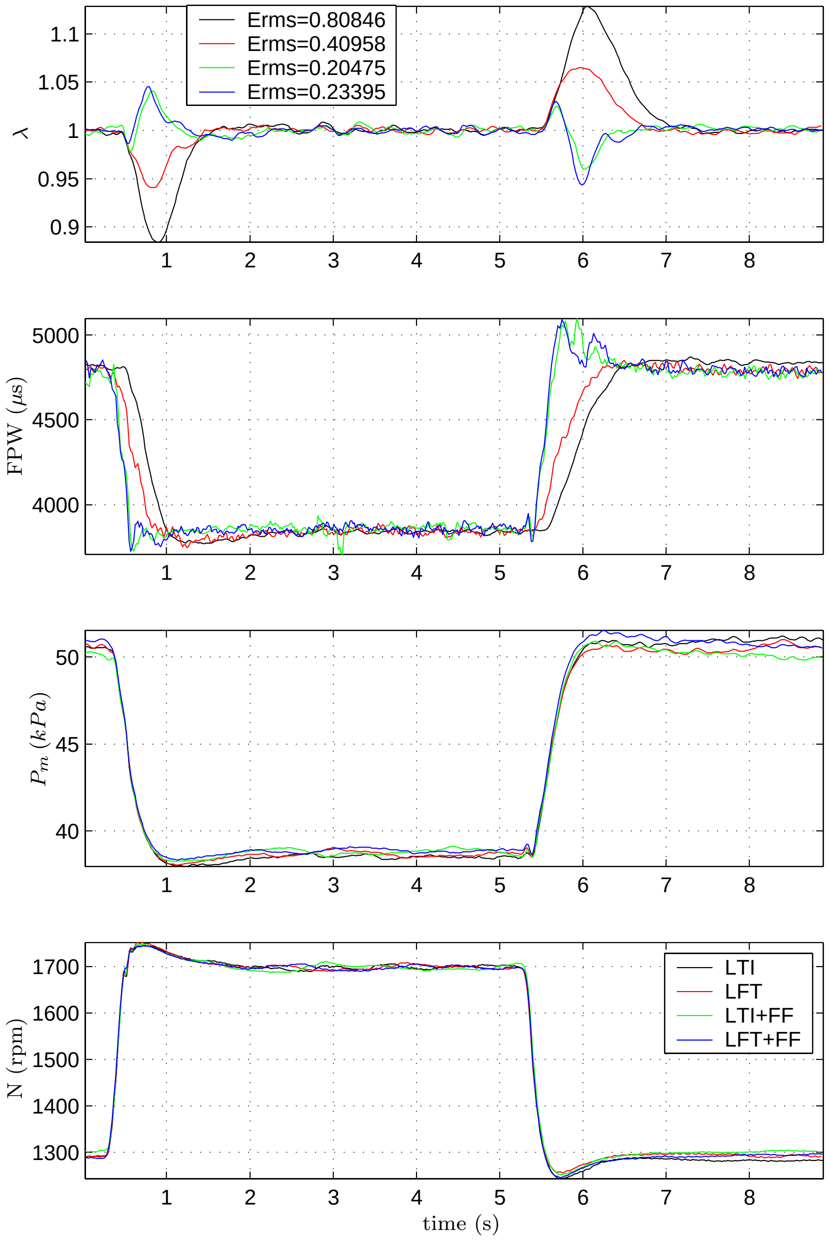

Figure 6.16 Engine speed disturbance rejection (Feedback-plus-Feedforward)

injection delay in the AFR path. Note that the LTI+FF controller again slightly outperforms the LFT+FF controller.

A more severe transient scenario is tested repeating the above transient under varying engine speed conditions. The performances of the controllers are depicted in Figure 6.18. The engine speed takes values between 1300 and 2000*rpm* in accordance with the TP variations, i.e. as the TP increases (decreases) the engine speed increases (decreases). Note that the engine speed is controlled by the dynamometer during this test according to a predetermined trajectory so this is not an engine test under constant load, i.e. engine speed is independent of the engine operating conditions. Results are rather interesting: the LFT+FF controller can handle these quite severe transients better than the LTI+FF controller. Especially, LFT+FF controller performs better during an unusual transient taking place around 6.5*secs*: when the TP moves from 1.21 to 1.27*volts*, the engine speed rises from 1500 to 2000*rpm* and the valve timings are advanced, an unusual transient MAP behaviour occurs. This interesting observation deserves a closer look. Note that since both controllers share exactly the same feedforward parts this difference in performance should be due to a difference between the responses of the feedback parts of the controllers.

In order to check the repeatability of this unusual response the same experiment is repeated twice. Figure 6.19 shows the controllers' responses (feedback and feedforward responses) and the measured lambda for all of the three experiments. The first row displays the measurements of the first experiment shown in Figure 6.18, second and third row display the second and third experiment respectively. From the feedforward responses and lambda measurements it can be seen that all three experiments are performed under very similar conditions even though there is a slight difference between the first and the rest of the experiments. This is because the TP is under open loop control only and applying the same reference does not lead to the same TP in general. What is certainly common in all of the experiments is that the LFT+FF controller outperforms the LTI+FF controller in terms of AFR regulation. In order to see the difference in feedback responses of the LTI+FF and LFT+FF controllers, the first column of Figure 6.19 is zoomed in around 6.5*sec* in Figure 6.20. All three measurements suggest that LFT feedback controller can respond faster during this fast transient without degrading its performance (rapidness of the LFT response is more clear in experiments two and three). This supports the view that the superior robustness properties of the LFT+FF controller can give it a performance lead whenever there are very fast parameter variations in the system.

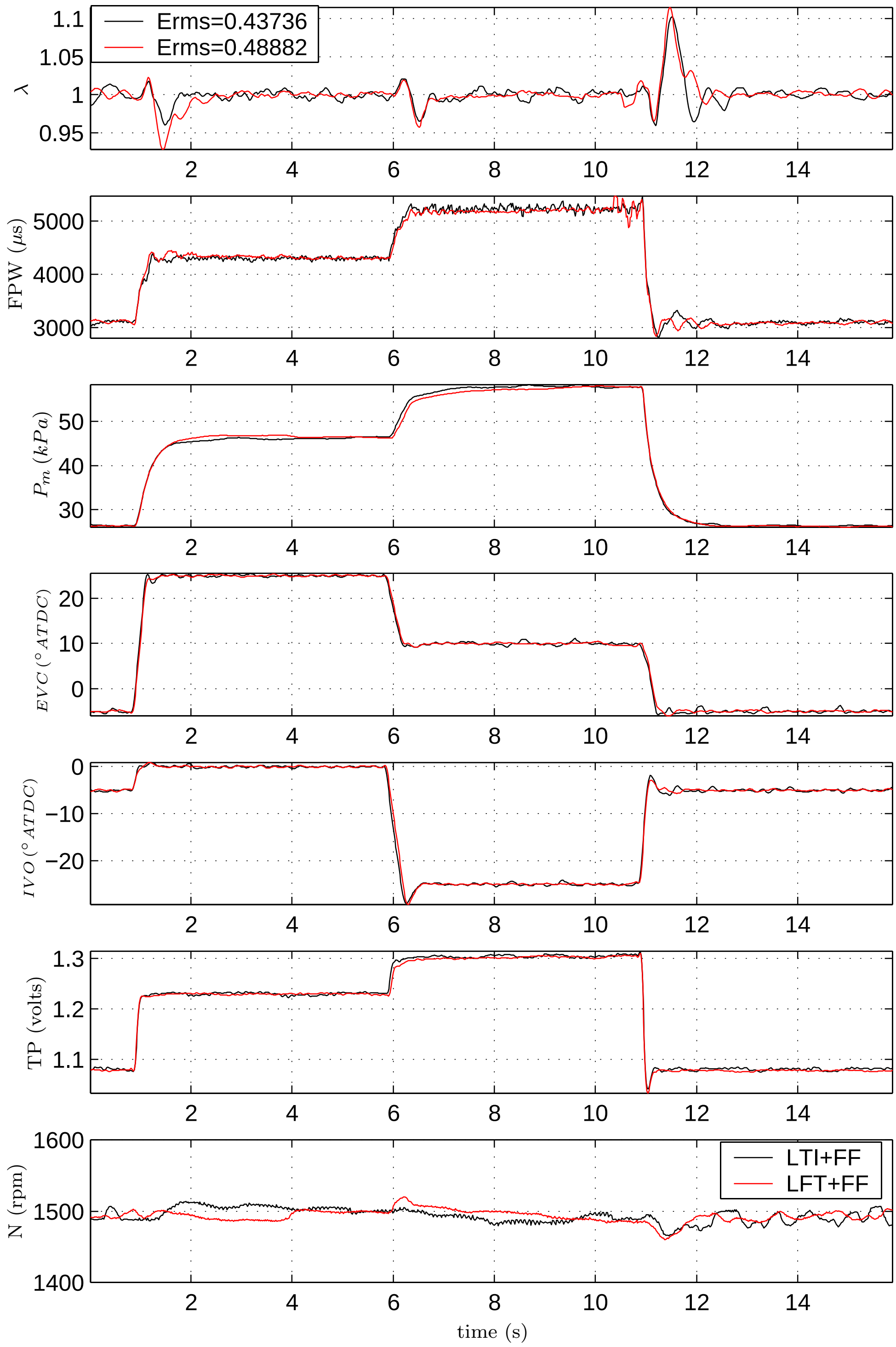

Figure 6.17 A realistic disturbance rejection test (constant speed)

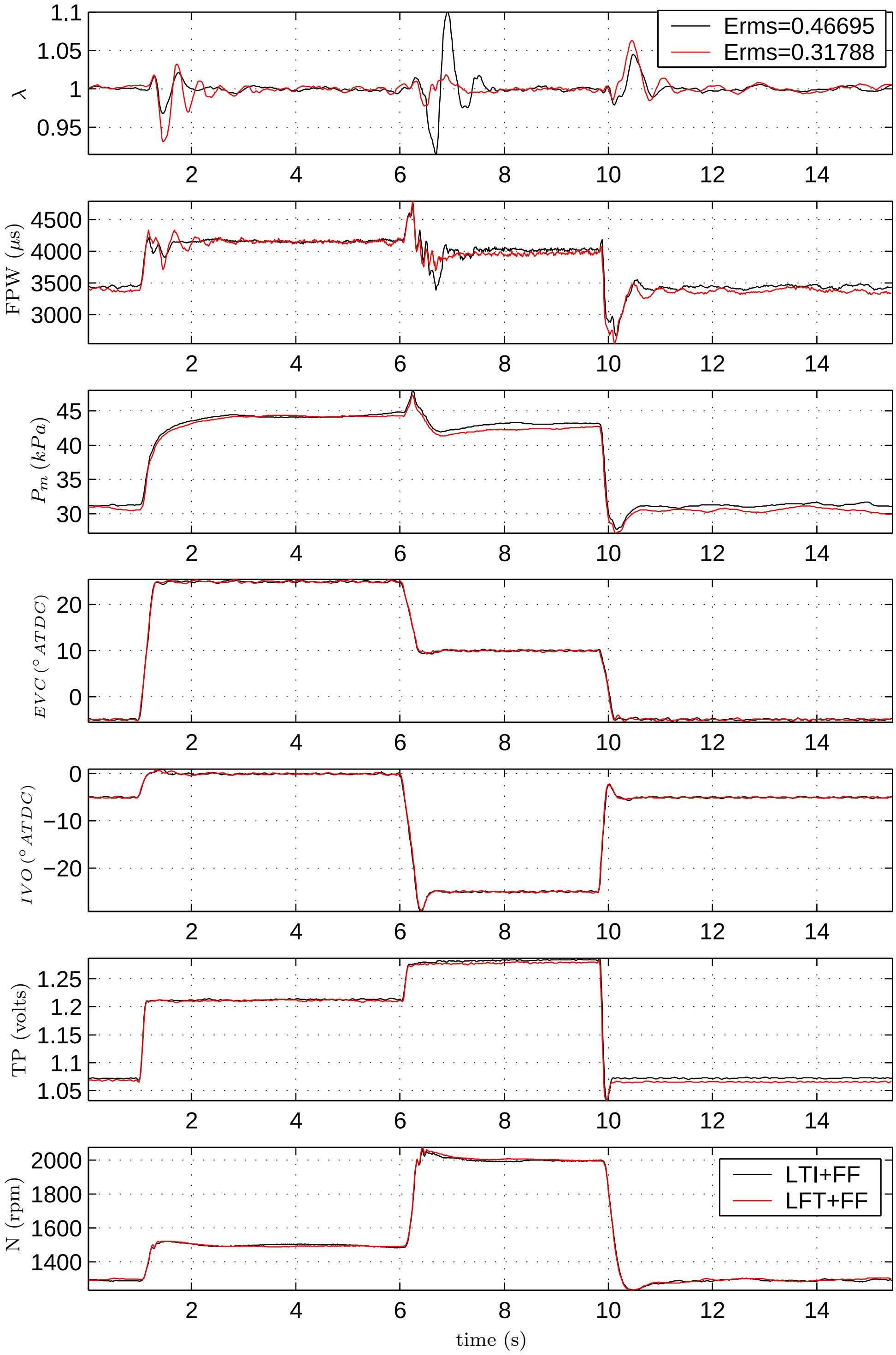

Figure 6.18 A realistic disturbance rejection test (varying speed)

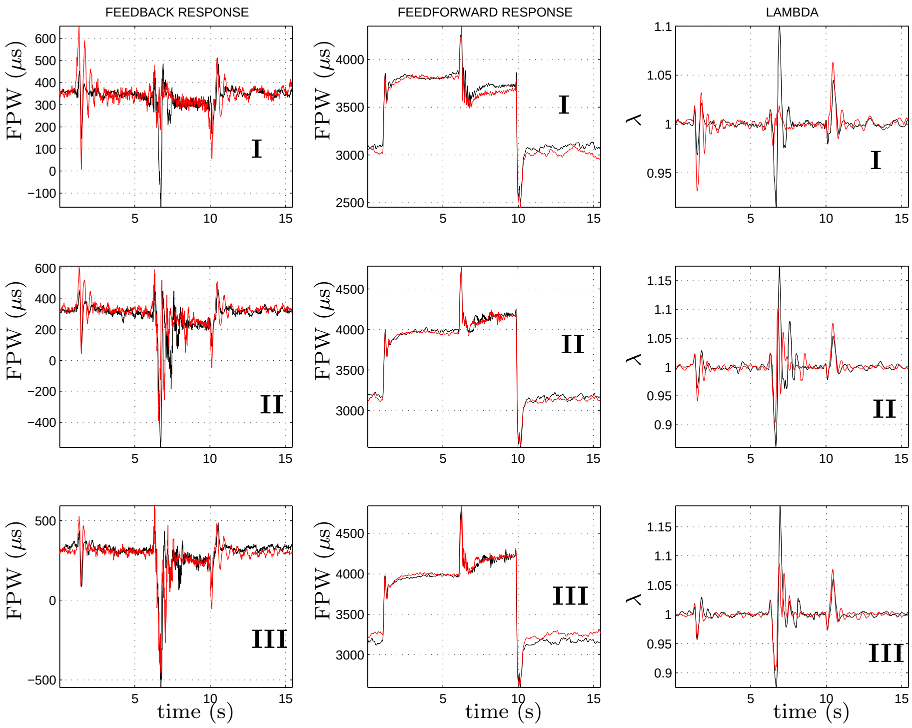

Figure 6.19 Feedback and feedforward responses of the controllers

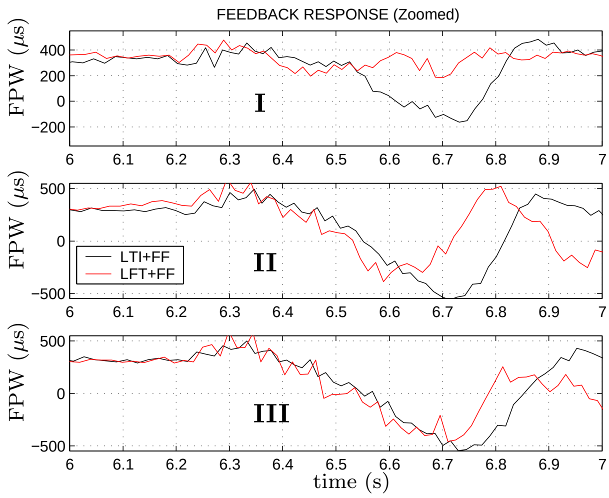

Figure 6.20 Feedback responses of the controllers (zoomed)

6.4 Comments

The LTI and LFT/LPV $\mathscr{H}_\infty$ loop shaping controllers have been successfully designed and implemented on a TI-VCT engine for AFR control. The designed controllers have undergone extensive engine tests under various conditions. The experiments show that the LFT/LPV controller offers significant improvements in the AFR regulation performance as far as a feedback-only controller is concerned. When complemented with a well designed feedforward controller both the LTI and LFT controllers (LTI+FF and LFT+FF) perform almost equally well, beating even the performance of the LFT feedback-only controller easily. However, due to the undesired interactions between the LFT and feedforward controller a slight degradation in the performance is observed for the LFT+FF controller. Although a possible remedy would be to incorporate the feedforward controller into the LFT/LPV controller design framework, this could not be done during this study due to lack of time. On the other hand, the LFT+FF controller is observed to handle an unusual fast transient better than the LTI+FF controller. This might be contributed to the LFT controller's good robustness and performance properties against fast parameter changes. This is the first time an LFT/LPV AFR controller is designed and tested in real-time on an automotive engine to the author's knowledge as far as the published literature is concerned.

Note that since a reduced LFT model (varying only with MAP) of the identified AFR path model has been used in this chapter to design the LPV feedback controllers, the feedback synthesis did not take the full advantage of the identification performed in Chapter 3. Although it was desirable to use the full knowledge of the system, i.e. schedule on at least two parameters (MAP, IVO and maybe even EVC), this was not accomplished due to lack of time and computation issues as discussed before.

7

Conclusions

Modelling, identification and control of the AFR path in a TI-VCT engine have been investigated in this thesis. The TI-VCT mechanism induced variations in the wall-wetting dynamics have been verified and modelled with the help of gaseous fuel experiments. Both the LTI and LPV AFR controllers have been designed in the $\mathscr{H}_\infty$ loop shaping framework. Moreover, they have been implemented on the TI-VCT engine and tested successfully in a variety of different transient conditions. The experimental evaluation of the controllers has revealed that the LFT/LPV feedback controller offers up to 50 % improvements in AFR regulation performance compared to that of the LTI controller. Further improvements in the controllers' performances have been achieved by including a feedforward controller into the AFR control systems. The success of the feedforward controller in disturbance rejection is considered as another indication of the quality of the identified AFR path model. On the other hand it has been observed that when complemented with the feedforward controller both the LTI+FF and LFT+FF controllers perform almost equally well. Finally the good performance of the controllers on the engine without any fine tuning shows that the $\mathscr{H}_\infty$ loop shaping framework produces high performance robust controllers even for an environment as complex and uncertain as the TI-VCT engine as long as a reliable model is available.

7.1 Main Contributions

A parameter-varying AFR path model. A parameter-varying mean value TI-VCT engine model has been identified for the AFR control problem. An alternative cylinder MAF model has been proposed and identified for VCT engines. Furthermore, it has been observed that some nonlinear dynamics such as the wall-wetting in the VCT engine cannot be identified satisfactorily via linear (local) identification methods.

An LPV wall-wetting model. Variations in the wall-wetting dynamics under the TI-VCT excitations have been observed with the help of gaseous fuel experiments. A global identification framework is proposed for the identification of the wall-wetting dynamics which are modelled as a slow and a fast first order fuel puddles. The LPV wall-wetting model have been shown to predict the fuel film size variations accurately through validation and also through the good performance of the feedforward controller during the engine tests.

A comprehensive review of the LPV controller design methods. Several different LPV controller design methods have been presented in a unified and systematic framework. Whenever possible coding friendly forms of the LMI conditions are provided for ease of numerical implementation of the methods. A detailed comparison of the different LPV methods is provided through the illustrative examples and design of the final AFR controllers.

Design and experimental implementation of the LPV $\mathscr{H}_\infty$ loop shaping AFR controllers. The LTI and LPV $\mathscr{H}_\infty$ loop shaping AFR controllers have been designed and successfully implemented on the TI-VCT engine. It is shown that the LPV controller offers significant improvements in the feedback-only performance as long as the scheduling parameter captures the nonlinear dynamics of the system.

7.2 Further Work

Results of this thesis can be further developed and enhanced in several ways:

Expansion of the AFR path model to different engine speeds. The AFR path model has been developed at $1500rpm$. Even though the experiments have shown that the designed controllers are robust against the variations in the engine speed, further improvements in performance can be realised if the model would also include the engine speed as a parameter. It is believed that the proposed identification methods can easily be extended to include the engine speed into the AFR path model.

Enhancement of the LPV controller performance and robustness by scheduling on two or even three parameters The designed LPV controller is only scheduled on the MAP. Further improvements in the performance can be achieved if the controller is gain-scheduled with the valve timings as well as the MAP. A second scheduling parameter would be the IVO timing since it affects the wall-wetting dynamics significantly. If computationally found feasible, the EVC timing can also be included as a scheduling parameter to realise an LPV controller with 3 scheduling parameters. Note that only the LFT/LPV methods are suitable for design of the LPV controllers with several scheduling parameters due to the intensive computational requirement of the Grid/LPV methods.

Integration of feedforward controllers into the LPV $\mathscr{H}_\infty$ loop shaping design framework. It has been observed that there are some undesired interactions between the feedforward and LPV controller which cause slight degradations in the 2DOF LPV controller's performance. This problem can be alleviated by incorporating the feedforward controller into the LPV $\mathscr{H}_\infty$ loop shaping design framework.

Designing a MIMO control system that controls not only the AFR but also the valve timings. Only SISO controllers have been designed in this thesis. Since there is high interaction between the valve timings and AFR path dynamics, the overall performance can be further improved if a MIMO control system that controls not only the AFR but also the valve timings is designed for the TI-VCT engine.

A

Facilities

The Engineering Department at Cambridge University has two state of the art transient engine test cells. These facilities were jointly funded by the Engineering and Physical Sciences Research Council (EPSRC) and the Ford Motor Company, with approximately 65 % of the funding from the latter.

This appendix describes the facilities available in the first of the two cells where the AFR control investigation in a TI-VCT engine was carried out.

A.1 Dynamometer

The dynamometer used in the gasoline cell is a low inertia 103kW d.c. electric motor. The drive unit enables transient capabilities by controlling a fast thyristor bridge network which controls the field and armature currents in the motor. The dynamometer is used to absorb energy from, or to motor, the engine. Typically the dynamometer will be in speed control mode. If the engine is generating net positive torque at the reference speed the dynamometer will absorb energy from the shaft (and generate electricity which is fed back into the grid). Conversely if net negative torque is generated by the engine then the dynamometer will motor the engine to keep the speed at the desired value. The low system inertia and fast control loop enable relatively fast transient response characteristics.

A.2 Engine

The engine is a prototype Ford TI-VCT 1.6l 16 valve gasoline engine. It is connected to the dynamometer via a clutch which can be used to accurately duplicate gear change events, and also to allow the engine to idle disconnected from the dynamometer.

Board	Function	Specification
DS1005	processor board	Motorola PowerPC750 at 480MHz
DS2003	Analog input board	32 × 16bit channels
DS2101	Analog output board	5 × 12bit channels
DS2201	multi purpose board	20 × 12bit ADC 8 × 12 bit DAC
		16 × DIO channels
DS4001	Digital I/O	32 × DIO with timing
DS4301	CAN interface	

Table A.1 dSPACE boards

A.3 Software

The MATLAB®/Simulink®/dSPACE® suite of rapid controller prototyping tools is the main software environment used in the engine test cell. The suite extends the powerful set of MATLAB and Simulink tools that are familiar to most control engineers. The Real-Time Workshop® (a Mathworks product) translates the Simulink diagram into compilable C code which can be used by a third party supplier. The dSPACE organisation takes this code and compiles it to run on its dedicated real time processor. dSPACE provides various interfacing cards and Simulink blocks to represent them. The compiled code then runs independently on the dSPACE hardware. Data is passed to and from the main computer where software enables display and control of variables in the code on the real time processor.

The dSPACE facilities are summarised in table A.1. In addition to those described, custom hardware and software from Ford enables control of engine actuators via the Simulink model.

A.4 Actuators and Sensors

The throttle is controlled via an electronic throttle controller. The spark timing and fuel injectors are controllable on an event by event, cylinder by cylinder basis. The air bypass valve (ABV) are also directly controllable. The clutch is controlled from dSPACE via a pneumatic actuator.

All standard engine sensors are monitored, throttle MAF, MAP, air charge temperature (ACT) as shown in Figure A.1. These are augmented with various research sensors as indicated in table A.2. The sensors are nonlinear to varying degrees and the specifications given are an indication only of their response characteristics.

Signal	Sensor	Specification
cylinder pressure	Kistler 6123	100kHz corner frequency
general pressure	strain gauge bridge	$\approx$ 1ms
temperatures	0.5mm tip K-type	25ms t_{0-63} in water
engine position	optical encoder	1 degree resolution
HC	Cambustion fast FID HC sensor	5ms t_d, 5ms t_{10-90}
NO	Cambustion fast CLD NO sensor	5ms t_d, 5ms t_{10-90}
AFR	UEGO sensors (Horiba, ETAS, NTK)	various
AFR, O_2, HC, NO_x, CO, CO_2	Horiba EXSA 1500	5-10s t_d, 5-10s t_{10-90}
engine torque	piezo load cell & reaction arm	

Table A.2 Sensors in engine test cell

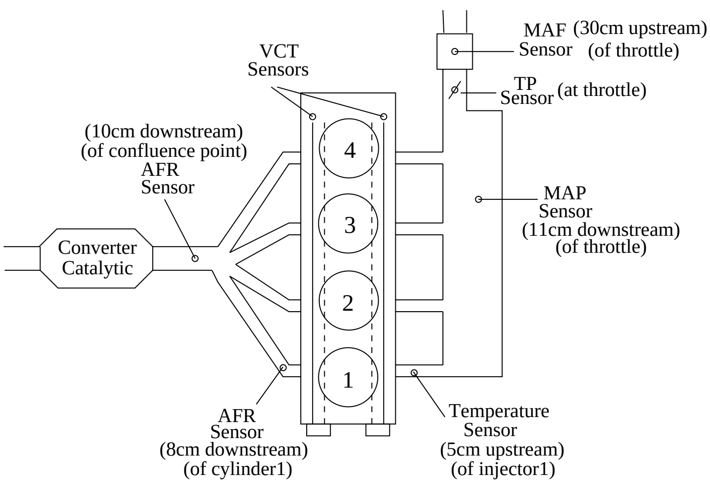

Figure A.1 Locations of the main sensors used in the AFR path identification

B

Input Excitations for Linear Identification

In order to have an informative identification data the input should be persistently exciting, i.e. it should contain sufficiently many distinct frequencies. This remains enough freedom for choice of the input excitation. The common input signals for linear identification are filtered Gaussian white noise, random binary signals, pseudo-random binary signal (PRBS), multi-sines and chirp signal (swept sinusoids). Two of the above inputs will be defined in the following.

B.1 PRBS

A PRBS is periodic, deterministic signal with white-noise-like properties. It is generated by the difference equation

$$u(t) = rem(A(q)u(t), 2) = rem(a_1u(t-1) + ... + a_nu(t-n), 2) \tag{B.1}$$

Here rem(x,2) is the remainder as x is divided by 2. If the polynomial $A(q)$ is chosen such that *Maximum length PRBS* is obtained [Lju99, p. 419], the PRBS has the following properties:

- period of the sequence is $T_{prbs} = (2^n - 1)T_c$ where n is the number of registers and T_c is period of the clock generating PRBS
- the mean of the PRBS is given by $\frac{\overline{u}}{2^n-1}$ when is its magnitudes shifts between $\pm\overline{u}$
- Its frequency response has $(2^n-2)/2$ frequency peaks for positive frequencies(excluding 0 frequency).

Figure B.1 shows one period of a PRBS with it frequency response. The Nyquist frequency is labelled as $f_n = \pi/T_s$. This shows that maximum length PRBS with $T_s = T_c$

behaves like periodic white noise. Notice that it is essential to perform these calculations over whole periods.

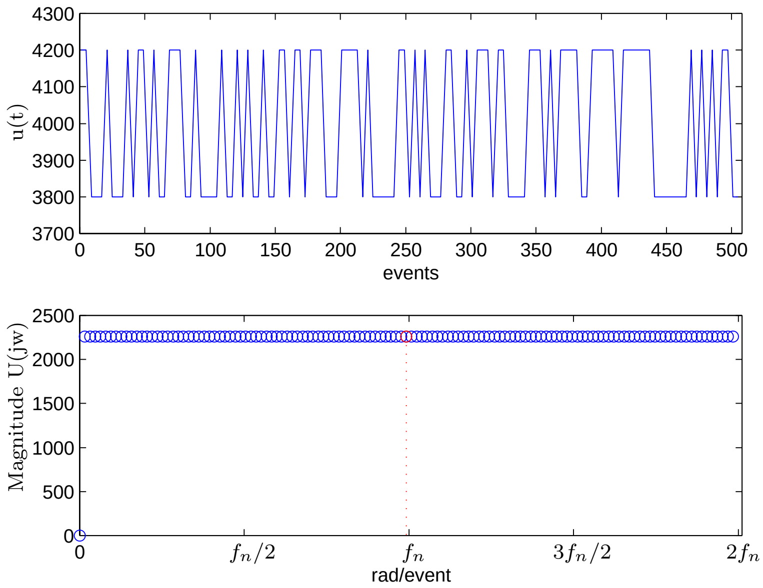

Figure B.1 A PRBS signal with $n = 7$, $2^n - 1 = 127$, $T_c = T_s = 4$

B.2 Multi-Sine

Another natural choice of input for wide-range frequency identification is sum of sinusoids [Lju99, p. 423]:

$$u(k) = \sum_{h=1}^{n} A_h \cos(w_h k + \phi_h) \tag{B.2}$$

With n, A_h, w_h the signal power can be placed precisely to desired frequencies. The phase ϕ_h should be chosen to have the cosines as much out of phase as possible. A simple solution is the so-called Schroeder phase choice

$$\begin{aligned} &\phi_1 \;\text{ arbitrary} \\ &\phi_h = \phi_1 - \frac{h(h-1)}{n}\pi, \; 2 \leq h \leq n \end{aligned} \tag{B.3}$$

Finally, a periodic multi-sine with period $\mathcal{T}_{max}$ can be obtained by choosing the frequencies w_h from the following grid

$$w_h = \frac{2\pi h}{\mathcal{T}_{max}}, \quad h = 1, 2, ..., \frac{\mathcal{T}_{max}}{\mathcal{T}_{min}} \tag{B.4}$$

Such a periodic input excites $\mathcal{T}_{max}/\mathcal{T}_{min}$ equally distanced frequencies between $2\pi/\mathcal{T}_{max}$ and $2\pi/\mathcal{T}_{min}$ with increments of $2\pi/\mathcal{T}_{max}$. The main advantage of having a periodic input is that the signal-to-noise-ratio can be improved by averaging the measurement over the period. For the identification tests in this study $\mathcal{T}_{max} = 684$ and $\mathcal{T}_{min} = 9$ are chosen.

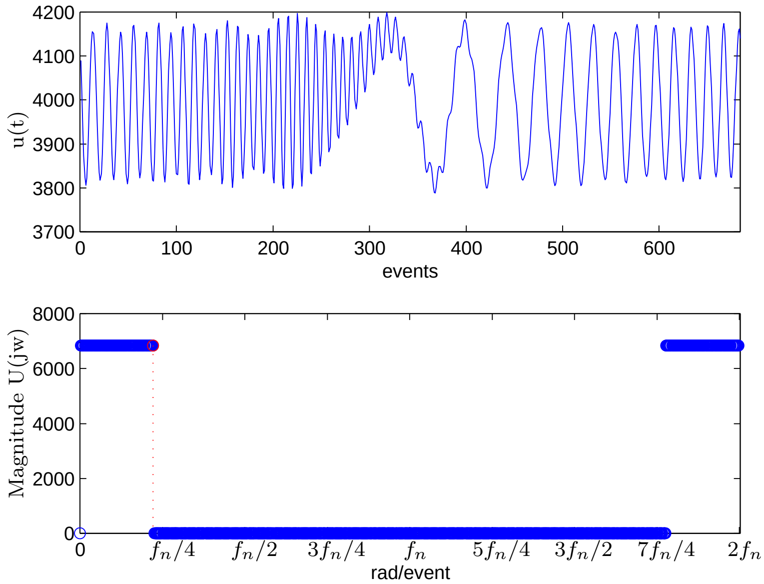

Figure B.2 A multi-sine signal with $\mathcal{T}_{max} = 684$, $\mathcal{T}_{min} = 9$ and $T_s = 1$

C

$\mathscr{H}_\infty$ Loop Shaping

The $\mathscr{H}_\infty$ loop shaping design procedure, which is the main synthesis technique used in this thesis, is a powerful method for designing robust controllers. It combines the classical ideas of loop shaping, as discussed in Section 5.1, with the modern ideas of robust control [MG92]. The motivation for the $\mathscr{H}_\infty$ loop shaping can be presented either from a classical perspective or from a robust control perspective. Consider the closed-loop system shown in Figure C.1. The transfer matrix

$$\begin{aligned} T_{\left[\begin{smallmatrix} w_1 \\ w_2 \end{smallmatrix}\right] \to \left[\begin{smallmatrix} z_1 \\ z_2 \end{smallmatrix}\right]} &= \begin{bmatrix} (I + G_s K_\infty)^{-1} G_s & (I + G_s K_\infty)^{-1} \\ -K_\infty (I + G_s K_\infty)^{-1} G_s & -K_\infty (I + G_s K_\infty)^{-1} \end{bmatrix} \\ &= \begin{bmatrix} I \\ -K_\infty \end{bmatrix} (I + G_s K_\infty)^{-1} \begin{bmatrix} G_s & I \end{bmatrix} \end{aligned} \tag{C.1}$$

represents the important requirements of the system in terms of robustness and disturbance rejection as it bounds all the transfer functions from the input and output disturbances to the plant input and output. The $\mathscr{H}_\infty$ loop shaping controller K_∞ is calculated as a result of the following optimisation

$$K_\infty = \arg \min_{\text{stab}\, K} \left\| T_{\left[\begin{smallmatrix} w_1 \\ w_2 \end{smallmatrix}\right] \to \left[\begin{smallmatrix} z_1 \\ z_2 \end{smallmatrix}\right]} \right\|_\infty \tag{C.2}$$

Alternatively, consider the left coprime factorisation of a perturbed plant interconnected with a controller depicted in Figure C.2, where $G_s = \tilde{M}^{-1}\tilde{N}$ with $\tilde{M}, \tilde{N} \in \mathscr{RH}_\infty$ and the perturbed plant is given by $G_{s_\Delta} = (\tilde{M} + \tilde{\Delta}_M)^{-1}(\tilde{N} + \tilde{\Delta}_N)$. The coprime factor uncertainty has characteristics of both the multiplicative and inverse multiplicative uncertainty, i.e. it represents uncertainty due to both the high frequency dynamics and low frequency errors. Furthermore, the perturbed plant and the nominal plant model are not required to have the same number of RHP poles and zeros. The stability of such a perturbed system

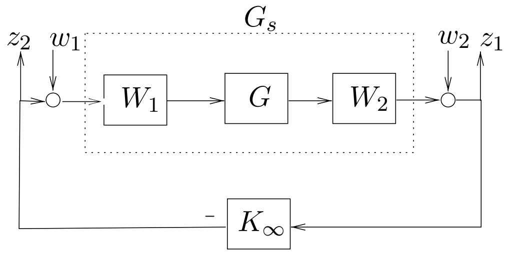

Figure C.1 The $\mathscr{H}_\infty$ loop shaping typical block diagram

depends on the following transfer function,

$$T_{w \to \left[\begin{smallmatrix} z_1 \\ z_2 \end{smallmatrix}\right]} = \begin{bmatrix} -K_\infty \\ I \end{bmatrix} (I + G_s K_\infty)^{-1} \tilde{M}^{-1}. \tag{C.3}$$

Using a small gain argument it can be shown that the perturbed system is internally stable with a controller K_∞ if and only if

$$\left\| \begin{bmatrix} -K_\infty \\ I \end{bmatrix} (I + G_s K_\infty)^{-1} \tilde{M}^{-1} \right\|_\infty < \beta, \text{ given } \left\| \begin{bmatrix} \tilde{\Delta}_N & \tilde{\Delta}_M \end{bmatrix} \right\|_\infty \leq \frac{1}{\beta}. \tag{C.4}$$

The equivalence of these two different approaches can be shown by the following equality [ZDG96, Lemma 18.4]

$$\left\| \begin{bmatrix} -K_\infty \\ I \end{bmatrix} (I + G_s K_\infty)^{-1} \tilde{M}^{-1} \right\|_\infty = \left\| \begin{bmatrix} I \\ -K_\infty \end{bmatrix} (I + G_s K_\infty)^{-1} \begin{bmatrix} G_s & I \end{bmatrix} \right\|_\infty \tag{C.5}$$

Thus, the $\mathscr{H}_\infty$ loop shaping optimisation (C.2) produces a controller that has optimal disturbance properties and is optimally robust to the coprime factor perturbations of the plant. The success of the optimisation can be judged by the value of the robust stability margin ϵ

$$\epsilon = \left\| T_{\left[\begin{smallmatrix} w_1 \\ w_2 \end{smallmatrix}\right] \to \left[\begin{smallmatrix} z_1 \\ z_2 \end{smallmatrix}\right]} \right\|_\infty^{-1} \tag{C.6}$$

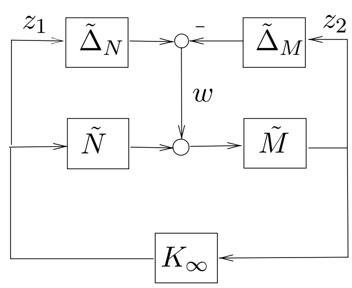

Figure C.2 Left coprime factor uncertain plant

An $\mathscr{H}_\infty$ loop shaping design which achieves a robust stability margin $\epsilon = \epsilon_0$ will be robustly stable to coprime factor perturbations in the plant of size $\left\| \begin{bmatrix} \tilde{\Delta}_N & \tilde{\Delta}_M \end{bmatrix} \right\|_\infty < \epsilon_0^{-1}$. The value of ϵ is always between 0 and 1, and a value closer to unity indicates a loop shape which has good robust stability properties.

C.1 McFarlane and Glover's Design Procedure

i. For an appropriately scaled system, shape the singular values of the nominal plant G using a pre-compensator W_1 and/or a post-compensator W_2 to get the desired loop shape as shown in Figure 5.3. The weighted plant is given by $G_s = W_2 G W_1$.

ii. Calculate ϵ_{max}, where

$$\epsilon_{max}^{-1} = \inf_{\text{stab } K_\infty} \left\| T_{\left[\begin{smallmatrix} w_1 \\ w_2 \end{smallmatrix}\right] \to \left[\begin{smallmatrix} z_1 \\ z_2 \end{smallmatrix}\right]} \right\|_\infty \tag{C.7}$$

If $\epsilon_{max} < 0.25$ return to 1) and adjust W_1 and W_2. If $\epsilon_{max} > 0.25$ select $\epsilon \leq \epsilon_{max}$, then synthesise a controller K_∞, which satisfies

$$\left\| T_{\left[\begin{smallmatrix} w_1 \\ w_2 \end{smallmatrix}\right] \to \left[\begin{smallmatrix} z_1 \\ z_2 \end{smallmatrix}\right]} \right\|_\infty \leq \epsilon^{-1} \tag{C.8}$$

iii. The final controller K is constructed by combining the $\mathscr{H}_\infty$ controller K_∞ with the weighting matrices W_1 and W_2 such that $K = W_1 K_\infty W_2$.

The theoretical basis for the $\mathscr{H}_\infty$ loop shaping is that K_∞ does not modify the desired loop shape significantly at low and high frequencies, if ϵ_{max} is not too small. Thus, shaping the open loop plant G corresponds to shaping the loop gains GK and KG. In contrast with the conventional loop shaping, the control engineer does not need to shape the phase of G explicitly. It can be shown that a value of $\epsilon_{max} > 0.2 - 0.3$ is satisfactory, in the same way that a gain margin of ± 6 dB, and phase margin of $45°$ are for a SISO system. If ϵ_{max} is small, then the desired loop shape is incompatible with the robust stability requirements and should be adjusted accordingly (note that the calculation of ϵ_{max} is routine). It is shown that all the closed-loop objectives are guaranteed to have bounded magnitudes. Moreover, the bounds depend only on ϵ_{max}, W_1, W_2 and G (see [ZDG96, Section 18.3] for further discussion).

The most crucial part of the design procedure is to find the appropriate weighting matrices. The shape of the weights is determined by the closed-loop design specifications. The general trends to be followed are high low frequency gain so that the disturbance rejection at both the input and the output of the plant, as well as output decoupling are achieved; low high frequency gain for noise rejection; and a smooth transition around the loop cross-over frequency, i.e. the loop gain should not decrease faster than 20dB/decade, in order to achieve the desired robust stability and performance such as good gain and phase margins. A fast rise time can be achieved with a high loop cross-over frequency and a good ϵ. High low frequency gain can be achieved with a PI weight. Low high frequency gain can be realized with a low-pass filter. A lead-lag filter can provide the smooth transition around the loop cross-over frequency.

C.2 ν-Gap Metric

The ν-gap metric indicates how close two systems are to each other in terms of their closed-loop behaviour. The distance between two plants as measured by the ν-gap metric is a measure of alikeness of their closed loop behaviour. The gap between two plants G_0 and G_1 is defined as the smallest value of $\|[\Delta_N, \Delta_M]\|_\infty$, coprime factor perturbation, that perturbs G_0 into G_1 and is denoted by $\delta_\nu(G_0, G_1)$. In this framework the robust stability margin ϵ gives the radius, in terms of the distance in the gap metric, of the largest *ball* of plants stabilised by K as shown in Figure C.3.

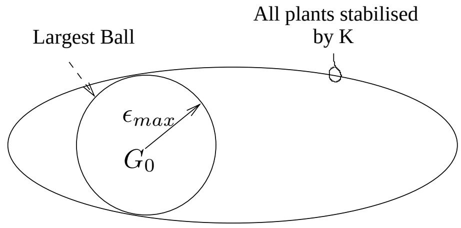

Figure C.3 Interpretation of robust stability margin ϵ in the gap metric

Theorem C.1 *Let G_0 be a nominal plant and $\beta \leq \alpha < \epsilon_{max}$.*

i. For a given controller K,

$$\text{arcsin}\epsilon > \arcsin\alpha - \arcsin\beta$$

for all G satisfying $\delta_\nu(G_0, G) \leq \beta$ if and only if $\epsilon > \alpha$.

ii. For a given plant G,

$$\text{arcsin}\epsilon > \arcsin\alpha - \arcsin\beta$$

for all K satisfying $\epsilon > \alpha$ if and only if $\delta_\nu(G_0, G) \leq \beta$ [Vin99, Theorem 3.10].

The preceding theorem shows that any plant at a distance less than β from the nominal will be stabilised by any controller stabilising the nominal with a robust stability margin of at least β. Moreover, any plant at a distance greater than β from the nominal will be destabilised by some controller that stabilises the nominal with a performance measure of β.

Bibliography

[AA98] P. Apkarian and R.J. Adams. Advanced Gain-Scheduling Techniques for Uncertain Systems. *IEEE Transactions on Control Systems Technology*, 6(1):21–32, January 1998.

[AG95] P. Apkarian and P. Gahinet. A Convex Chracterization of Gain-Scheduled $\mathscr{H}_\infty$ Controllers. *IEEE Transactions on Automatic Control*, 40:853–864, 1995.

[Aqu81] C.F. Aquino. Transient A/F Control Characteristics of the 5 Liter Central Fuel Injection Engine. *SAE*, (810494), 1981.

[Asm82] T.W. Asmus. Valve Events and Engine operation. *SAE*, (820749), 1982.

[AT00] P. Apkarian and H.D.. Tuan. Parameterized LMIs in Control Theory. *SIAM Journal of Control Optimization*, 38(4):1241–1264, 2000.

[Bau99] H. Bauer, editor. *Gasoline-Engine Management.* Robert Bosch GmbH, SAE Books, 1999.

[BBC95] P. Bidan, S. Boverie, and V. Chaumerliac. Nonlinear Control of a Spark-Ignition Engine. *IEEE Transactions on Control Systems Technology*, 3(1):4–13, 1995.

[BBFE93] S. Boyd, V. Balakrishnan, E. Feron, and L. El Ghaoui. Control System Analysis and Synthesis via Linear Matrix Inequalities. In *Proceedings of the American Control Conference*, pages 2147–2154, 1993.

[Bec96] B. Becker. Additional Results on Parameter-Dependent Controllers for LPV Systems. In *IFAC, 13th Triennial World Congress*, pages 351–356, 1996.

[BF94] S. Boyd and E. Feron. History of Linear Matrix Inequalities in Control Theory. In *Proceedings of the American Control Conference*, San Diego, California, June 1994.

[BP94] G. Becker and A. Packard. Robust Performance of Linear Parameter Varying Systems Using Parametrically-Dependent Linear Feedback. *Systems & Control Letters*, 23:205–215, 1994.

[Bra96] M. Brandstetter. *Robust Air-Fuel Ratio Control For Combustion Engines.* PhD thesis, University of Cambridge, Department of Engineering, December 1996.

[CC86] Y. Chin and F.E. Coats. Engine Dynamics:Time-Based Versus Crank-Angle Based. *SAE*, (860142), 1986.

[CG96] M. Chilali and P. Gahinet. $\mathscr{H}_\infty$ Design with Pole Placement Constraints: An LMI Approach. *IEEE Transactions on Automatic Control*, 41(3):358–367, March 1996.

[CH88] D. Cho and J.K. Hedrick. A Nonlinear Controller Design Method for Fuel-Injected Automotive Engines. *Journal of Engineering for Gas Turbines and Power*, 110:313–320, 1988.

[CH98] S.B. Choi and J.K. Hedrick. An Observed-Based Controller Design Method for Improving Air/Fuel Ratio Chracteristics of Spark Ignition Engines. *IEEE Transactions on Control Systems Technology*, 6(3):325–334, 1998.

[CM00] A. Chevalier and M. Muller. On the Validity of Mean Value Engine Models during Transient Operation. *SAE*, (2000-01-1261), 2000.

[CVH00] A. Chevalier, C.W. Vigild, and E. Hendricks. Predicting the Port Air Mass Flow of SI Engines in Air/Fuel Ratio Control Applications. *SAE*, (2000-01-0260), 2000.

[Det01] M. Dettori. *LMI Techniques for Control with Application to a Compact Disc Player Mechanism.* PhD thesis, Delft University of Technology, Mechanical Engineering Systems and Control Group, Netherlands, February 2001.

[DGKF89] J. C. Doyle, K. Glover, P. P. Khargonekar, and B. A. Francis. State-space solutions to the standard $\mathscr{H}_2$ and $\mathscr{H}_\infty$ control problems. *IEEE Transactions on Automatic Control*, 34(8):831–847, August 1989.

[DLM98] K. Donaldson, X.Y. Li, and W. MacNee. Ultrafine (Nanometer) Particle Mediated Lung Injury. *Journal of Aerosol Science*, 29(5/6):553–560, 1998.

[Dob80] D.J. Dobner. A Mathematical Engine Model for Development of Dynamic Engine Control. *SAE*, (800054), 1980.

[DPZ91] J. C. Doyle, A. Packard, and K. Zhou. Review of LFTs, LMIs and μ. In *Proceedings of the 30th IEEE Conference on Decision and Control*, pages 1227–1232, England, 1991.

[DS01] M. Dettori and C.W. Scherer. LPV Design for a CD player: an experimental evaluation of performance. *Selected Topics in Signal, Systems and Control*, 12:15–22, September 2001.

[For00] R.G. Ford. *Robust Automotive Idle Speed Control in a Novel Framework*. PhD thesis, University of Cambridge, Department of Engineering, September 2000.

[GA94] P. Gahinet and P. Apkarian. A Linear Matrix Inequality Approach to $\mathscr{H}_\infty$ Control. *International Journal of Robust and Nonlinear Control*, 4:421–448, 1994.

[Gah96] P. Gahinet. Explicit Controller Formulas for LMI-based $\mathscr{H}_\infty$ Synthesis. *Automatica*, 32(7):1007–1014, 1996.

[GCFV99] D. Gorinevsky, J. Cook, L. Feldkamp, and G. Vukovich. Predictive Design of Linear Feedback/Feedforward Controller for Automotive VCT Engines. In *ACC*, volume 1, pages 207–211, June 1999.

[GFGC02] A.U. Genç, R. Ford, K. Glover, and N. Collings. Experimental Investigation of Changing Fuel Path Dynamics in Twin-Independent Variable Cam Timing Engines. *SAE*, (2002-01-2752), 2002.

[GGF01] A.U. Genç, K. Glover, and R. Ford. Nonlinear Control of Hydraulic Camshaft Actuators in Variable Cam Timing Engines. In *MECA International Workshop*, pages 49–54, University of Salerno,Italy, September 2001.

[GNLC95] P. Gahinet, A. Nemirovski, A. J. Laub, and M. Chilali. *LMI control toolbox*. The MathWorks, Inc., 1995. For use with Matlab.

[Guz95] L. Guzzella. Models and Modelbased Control of IC-Engines A Nonlinear Approach. *SAE*, (950844), 1995.

[Hel95] A. Helmersson. *Methods for Robust Gain Scheduling.* PhD thesis, Linköping University, Sweden, 1995.

[Hen01] E. Hendricks. Isothermal vs. Adiabatic Mean Value SI Engine Models. In *Advances in Automotive Control*, Karlsruhe,Germany, March 2001. 3rd IFAC Workshop.

[Hey88] J.B. Heywood. *Internal Combustion Engine Fundamentals.* McGraw-Hill, 1988.

[HFS99] C.S. Hsieh, S.J. Freudenberg, and A.G. Stefanopoulou. Multivariable Controller Structure in a Variable Cam Timing Engine with Electronic Throttle and Torque Feedback. In *Conf. on Control Appl.*, pages 465–470, Hawai, 1999.

[HL01] E. Hendricks and J.B. Luther. Model and Observer Based Control of Internal Combustion Engines. In *MECA International Workshop*, pages 9–20, University of Salerno,Italy, September 2001.

[HO81] S.D. Hires and M.T. Overington. Transient Mixture Strength Excursions - An Investigation of Their Causes and the Development of a Constant Mixture Strength Fueling Strategy. *SAE*, (810495), 1981.

[HS90] E. Hendricks and S.C. Sorenson. Mean Value Modelling of Spark Ignition Engines. *SAE*, (900616), 1990.

[HSFB97] S.C. Hsieh, A.G. Stefanopoulou, J.S. Freudenberg, and K.R. Butts. Emissions and Drivability Tradeoffs in a Variable Cam Timing SI Engine with Electronic Throttle. In *ACC*, pages 284–288, Albuquerque, New Mexico, June 1997.

[HVK+93] E. Hendricks, T. Vesterholm, P. Kaidantzis, P. Rasmussen, and M. Jensen. Nonlinear Transient Fuel Film Compensation (NTFC). *SAE*, (930767), 1993.

[Hyd91] R.A. Hyde. *The Application of Robust Control to VSTOL Aircraft.* PhD thesis, University of Cambridge, Department of Engineering, August 1991.

[IS94] T. Iwasaki and R.E. Skelton. All Controllers for the General $\mathscr{H}_\infty$ Control Problem: LMI Existence Conditions and State Space Formulas. *Automatica*, 30(8):1307–1317, 1994.

[JF97] M. Jankovic and F. Frischmuth. Disturbance Rejection in SI Engines with Variable Cam Timing. In *ACC*, pages 289–293, Albuquerque, New Mexico, June 1997.

[JFSC98] M. Jankovic, F. Frischmuth, A.G. Stefanopoulou, and J.A. Cook. Torque Management of Engines with Variable Cam Timing. *IEEE Control Systems*, 18(5):34, 1998.

[JM02] M. Jankovic and S.W. Magner. Variable Cam Timing: Consequences to Automotive Engine Control Design. In *IFAC, 15th Triennial World Congress*, 2002.

[Jur95] R. Jurgen. *Automotive Electronics Handbook*. McGraw-Hill, 1995.

[KG00] J.M. Kang and J.W. Grizzle. Dynamic Control of a SI Engine with Variable Valve Timing. *IEEE Transactions on Control Systems Technology*, 2000.

[Kie88] U. Kiencke. A View of Automotive Control Systems. *IEEE Control Systems Magazine*, pages 11–18, August 1988.

[KRU98] Y. Kim, G. Rizzoni, and V. Utkin. Automotive Engine Diagnosis and Control via Nonlinear Estimation. *IEEE Control Systems Magazine*, 18(3):84–99, 1998.

[LCS96] T.G. Leone, E.J. Christenson, and R.A. Stein. Comparison of Variable Camshaft Timing Strategies at Part Load. *SAE*, (960584), 1996.

[Lju99] L. Ljung. *System Identification-Theory for the User, 2nd Edition*. Prentice Hall, 1999.

[LP96] L. H. Lee and K. Poolla. Identification of linear parameter-varying systems via lfts. In *Proceeding of the 35th IEEE Conference on Decision and Control*, Kobe, Japan, December 1996.

[Ma88] T.H. Ma. Effect of Variable Engine Valve Timing on Fuel Economy. *SAE*, (880390), 1988.

[MG92] D. McFarlane and K. Glover. A Loop Shaping Design Procedure Using $\mathscr{H}_\infty$ Synthesis. *IEEE Transactions on Automatic Control*, 37(6):759–769, June 1992.

[MH92] J.J. Moskwa and J.K. Hedrick. Modeling and Validation of Automotive Engines for Control Algorithm Development. *Journal of Dynamic Systems, Measurement, and Control*, 114:278–285, 1992.

[MMP99] M.C. Mazzaro, B.A. Movsichoff, and R.S.S. Pena. Robust Identification of Linear Parameter-Varying Systems. In *Proceedings of the American Control Conference*, June 1999.

[MWU+96] Y. Moriya, A. Watanabe, H. Uda, H. Kawamura, M. Yoshioka, and M. Adachi. A Newly Developed Intelligent Variable Valve Timing System-Continuously Controlled Cam Phasing as Applied to a New 3 Liter Inline 6 Engine. *SAE*, (960579), 1996.

[OG93] C.H. Onder and H.P. Geering. Model-Based Multivariable Speed and Air-to-Fuel Ratio Control of an SI Engine. *SAE*, (930859):1142–1153, 1993.

[OG94] C.H. Onder and H.P. Geering. Measurement of the Wall-Wetting Dynamics of a Sequential Injection Spark Ignition Engine. *SAE*, (940447), 1994.

[Oga87] K. Ogata. *Discrete-time Control Systems.* Prentice-Hall, 1987.

[ORG97] C.H. Onder, C.A. Roduner, and H.P. Geering. Model Identification for the A/F Path of an SI Engine. *SAE*, (970612), 1997.

[ORSG98] C.H. Onder, C.A. Roduner, M.R. Simons, and H.P. Geering. Wall-Wetting Parameters Over the Operating Region of a Sequential Fuel-Injected SI Engine. *SAE*, (980792), 1998.

[Pac94] A. Packard. Gain scheduling via Linear Fractional Transformations. *Systems & Control Letters*, 22:79–92, 1994.

[Pap98] G. Papageorgiou. *Robust Control System Design: $\mathscr{H}_\infty$ Loop Shaping and Aerospace Applications.* PhD thesis, University of Cambridge, Department of Engineering, July 1998.

[PC87] B.K. Powell and J.K. Cook. Nonlinear Low Frequency Phenomenological Engine Modeling and Analysis. In *American Control Conference*, pages 332–340, Minneapolis,USA, June 1987.

[PD93] G.R. Purdy and R. Douglas. Wall-Wetting Theories Applied to the Transient Operation of a Single Cylinder Four-Stroke Gasoline Engine. *SAE*, (932446), 1993.

[Pea01] J.K. Pearson. *Improving Air Quality: Progress and Challenges for the Auto Industry.* SAE Books, 2001.

[PFC98] J.D. Powell, N.P. Fekete, and C. Chang. Observer-Based Air-Fuel Ratio Control. *IEEE Control Systems Magazine*, 18(3):72–83, 1998.

[Pow87] J.D. Powell. A Review of IC Engine Models for Control System Design. In *10th World Congress on Automatic Control*, volume 3, pages 233–238, Munich,Germany, 1987. IFAC.

[PZPB91] A. Packard, K. Zhou, P. Pandey, and B. Becker. A Collection of Robust Control Problems Leading to LMI's. In *Proceedings of the 30th Conference on Decision and Control*, pages 1245–1250, December 1991.

[RS00] W.J. Rugh and J.S. Shamma. Research on Gain Scheduling. *Automatica*, 36:1401–1425, 2000.

[SA90] J.S. Shamma and M. Athans. Analysis of Gain Scheduled Control for Nonlinear Plants. *IEEE Transactions on Automatic Control*, 35(8):898–907, 1990.

[SA91a] J.S. Shamma and M. Athans. Gain Scheduling: Potential Hazards and Possible Remedies. In *Proceedings of the American Control Conference*, pages 516–521, June 1991.

[SA91b] J.S. Shamma and M. Athans. Guaranteed Properties of Gain Scheduled Control for Linear Parameter-Varying Plants. *Automatica*, 27(3):559–564, 1991.

[SCGF98] A.G Stefanopoulou, J.A. Cook, J.W. Grizzle, and J.S. Freudenberg. Control-Oriented Model of a Dual Equal Variable Cam timing Spark Ignition Engine. *Journal of Dynamic Systems, Measurement, and Control*, 120:257–266, 1998.

[Sch00] C.W. Scherer. Robust Mixed Control and LPV Control with Full Block Scalings. *Advances in Linear Matrix Inequality Methods in Control*, pages 187–207, SIAM 2000.

[Sch01] C.W. Scherer. LPV Control and Full Block Multipliers. *Automatica*, 37:361–375, 2001.

[SE95] G. Scorletti and L. El Ghaoui. Improved Linear Matrix Inequality Conditions for Gain Scheduling. In *Proceedings of the 34th Conference on Decision and Control*, pages 3626–3631, December 1995.

[SGC97] C.W. Scherer, P. Gahinet, and M. Chilali. Multiobjective Output-Feedback Control via LMI Optimization. *IEEE Transactions on Automatic Control*, 42(7):896–911, 1997.

[SGL95] R.A. Stein, K.M. Galietti, and T.G. Leone. Dual Equal VCT - A Variable Camshaft Timing Strategy for Improved Fuel Economy and Emissions. *SAE*, (950975), 1995.

[SLOG00] M.R. Simons, M. Locatelli, C.H. Onder, and H.P. Geering. A Nonlinear Wall-Wetting Model for the Complete Operating Region of a Sequential Fuel Injected SI Engine. *SAE*, (2000-01-1260), 2000.

[ST95] P.J. Shayler and Y.C. Teo. Fuel Transport Characteristics of Spark Ignition Engines for Transient Fuel Compensation. *SAE*, (950067), 1995.

[SW99] C.W. Scherer and S. Weiland. *Lecture Notes DISC Course on Linear Matrix Inequalities in Control.* Dutch Instutite of Systems and Control, Delft, Netherlands, April 1999.

[TCG94] R.C. Turin, E.G.B. Casartelli, and H.P. Geering. A New Model for Fuel Supply Dynamics in an SI Engine. *SAE*, (940208), 1994.

[TG93] R.C. Turin and H.P. Geering. On-Line Identification of Air-to-Fuel Ratio Dynamics in a Sequentially Injected SI Engine. *SAE*, (930857), 1993.

[Vin99] G. Vinnicombe. *Uncertainty and Feedback:*$\mathscr{H}_\infty$ *loop-shaping and the* ν*-gap metric.* Imperial College Press, London, 1999.

[WYPB96] F. Wu, X. H. Yang, A. Packard, and G. Becker. Induced $\mathscr{L}_2$-Norm Control for LPV Systems with Bounded Parameter Variation Rates. *International Journal of Robust and Nonlinear Control*, 6:983–998, 1996.

[XYM98] W. Xu, V.W.K. Yuen, and J.K. Mills. Application of Nonlinear Transformations to A/F Ratio and Speed Control in an IC Engine. *SAE*, (199-01-0858), 1998.

[ZDG96] K. Zhou, J.C. Doyle, and K. Glover. *Robust and Optimal Control.* Prentice-Hall, 1996.